FAA-RD-82/19

**Project Report**
**ATC-116**

# L-Band DME Multipath Environment in the Microwave Landing System (MLS) Approach and Landing Region

**J. E. Evans**

**13 April 1982**

**Lincoln Laboratory**
MASSACHUSETTS INSTITUTE OF TECHNOLOGY
*LEXINGTON, MASSACHUSETTS*

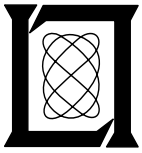

Prepared for the Federal Aviation Administration,
Washington, D.C. 20591

Technical Report Documentation Page

| 1. Report No. | 2. Government Accession No. | 3. Recipient's Catalog No. |
|---|---|---|
| FAA-RD-82/19 | | |

| 4. Title and Subtitle | 5. Report Date |
|---|---|
| L-Band DME Multipath Environment in the Microwave Landing System (MLS) Approach and Landing Region | 13 April 1982 |
| | 6. Performing Organization Code |
| 7. Author(s) | 8. Performing Organization Report No. |
| James E. Evans | ATC-116 |
| 9. Performing Organization Name and Address | 10. Work Unit No. |
| Lincoln Laboratory, M.I.T.<br>P.O. Box 73<br>Lexington, MA 02173-0073 | 11. Contract or Grant No.<br>DOT-FA74-WAI-461 |
| | 13. Type of Report and Period Covered |
| 12. Sponsoring Agency Name and Address | Project Report |
| *Department of Transportation*<br>Federal Aviation Administration<br>Systems Research and Development Service<br>Washington, D.C. 20591 | 14. Sponsoring Agency Code |

15. Supplementary Notes

The work reported in this document was performed at Lincoln Laboratory, a center for research operated by Massachusetts Institute of Technology, under Air Force Contract F19628-80-C-0002.

16. Abstract

The multipath environment in the approach and landing region represents an important factor in the optimization and ultimate performance of the Microwave Landing System (MLS) Precision Distance Measuring Equipment (DME/P). Various types of multipath are assessed in the context of the proposed DME/P implementation error characteristics to ascertain the principal challenges. It is shown (analytically and experimentally) that specular reflections from buildings represent a significant challenge, particularly at low altitudes (e.g., category II decision height and below) where terrain lobing can cause the effective multipath levels to exceed the effective direct signal level. However, the time delay discrimination capabilities of the proposed DME/P should effectively eliminate the bulk of such multipath.

Limited S-band (3 GHz) measurements of diffuse reflections from nominally flat terrain indicated very low levels. However, specular reflections from bare, hilly terrain may present problems in some cases.

| 17. Key Words | | 18. Distribution Statement |
|---|---|---|
| Air Traffic Control | Moving Target Indicator | Document is available to the public through the National Technical Information Service, Springfield, Virginia 22161 |
| Radar Signal Processor | Doppler Processor (FIR Filtering) | |
| Moving Target Detection | Adaptive Thresholding | |
| Airport Surveillance Radar | Parallel Processor | |

| 19. Security Classif. (of this report) | 20. Security Classif. (of this page) | 21. No. of Pages | 22. Price |
|---|---|---|---|
| Unclassified | Unclassified | 270 | |

Form DOT F 1700.7 (8-72) Reproduction of completed page authorized

## ABSTRACT

The multipath environment in the approach and landing region represents an important factor in the optimization and ultimate performance of the Microwave Landing System (MLS) Precision Distance Measuring Equipment (DME/P). Various types of multipath are assessed in the context of the proposed DME/P implementation error characteristics to ascertain the principal challenges. It is shown (analytically and experimentally) that specular reflections from buildings represent a significant challenge, particularly at low altitudes (e.g., category II decision height and below) where terrain lobing can cause the effective multipath levels to exceed the effective direct signal level. However, the time delay discrimination capabilities of the proposed DME/P should effectively eliminate the bulk of such multipath.

Limited S-band (3GHz) measurements of diffuse reflections from nominally flat terrain indicated very low levels. However, specular reflections from bare, hilly terrain may present problems in some cases.

ACKNOWLEDGMENTS

Several sections of this report draw heavily on earlier work by R.S. Orr. J. Yaeger-Charriere coded the computer programs used to assess relative likelihood of multipath as well as generating much of the airport geometry data base from maps provided by the FAA.

A. Vierstra was the principal engineer for the PDME multipath measurement system used in the Quonset State Airport field tests summarized in Chapter V. J. Bertram, W. Crowder, and D. Hamilton assisted in those measurements. The cooperation of the Quonset State Airport manager's office enabled us to execute the measurement program in a very short time period. P. Swett was the principal engineer for the major airport tests summarized in Chapter V. A. Gregory, J. Kalil and T. Magnan assisted in the measurements while J. Yaeger-Charriere and K. Roberts reduced the data. C. Catalano assisted in the software development.

J. Austin was the principal engineer of the S-band channel sounding system used for the high resolution time measurements at L.G. Hanscom airfield presented in Chapter VI. P. Murray made logistical arrangements for the experiments and reduced the data.

Concurrent studies carried out by a number of people in connection with the AWOP WG/M multipath subgroup were of considerable help for the work reported here. Particular thanks are due to Robert Kelly (Bendix/USA), T. Koshino (N.E.C./Japan), A. Becker (DFVLR/W. Germany), and M. Gori (Electronica/Italy).

The report was ably typed by C. Carter-Likas, D. Young and N. Campbell.

TABLE OF CONTENTS

LIST OF ILLUSTRATIONS

# METRIC CONVERSION FACTORS

## Approximate Conversions to Metric Measures

| Symbol | When You Know | Multiply by | To Find | Symbol |
|---|---|---|---|---|
| | **LENGTH** | | | |
| in | inches | *2.5 | centimeters | cm |
| ft | feet | 30 | centimeters | cm |
| yd | yards | 0.9 | meters | m |
| mi | miles | 1.6 | kilometers | km |
| | **AREA** | | | |
| $in^2$ | square inches | 6.5 | square centimeters | $cm^2$ |
| $ft^2$ | square feet | 0.09 | square meters | $m^2$ |
| $yd^2$ | square yards | 0.8 | square meters | $m^2$ |
| $mi^2$ | square miles | 2.6 | square kilometers | $km^2$ |
| | acres | 0.4 | hectares | ha |
| | **MASS (weight)** | | | |
| oz | ounces | 28 | grams | g |
| lb | pounds | 0.45 | kilograms | kg |
| | short tons (2000 lb) | 0.9 | tonnes | t |
| | **VOLUME** | | | |
| tsp | teaspoons | 5 | milliliters | ml |
| Tbsp | tablespoons | 15 | milliliters | ml |
| fl oz | fluid ounces | 30 | milliliters | ml |
| c | cups | 0.24 | liters | l |
| pt | pints | 0.47 | liters | l |
| qt | quarts | 0.95 | liters | l |
| gal | gallons | 3.8 | liters | l |
| $ft^3$ | cubic feet | 0.03 | cubic meters | $m^3$ |
| $yd^3$ | cubic yards | 0.76 | cubic meters | $m^3$ |
| | **TEMPERATURE (exact)** | | | |
| | Fahrenheit temperature | 5/9 (after subtracting 32) | Celsius temperature | °C |

*1 in = 2.54 (exactly). For other exact conversions and more detailed tables, see NBS Misc. Publ. 286, Units of Weights and Measures. Price $2.25, SD Catalog No. C13.10:286

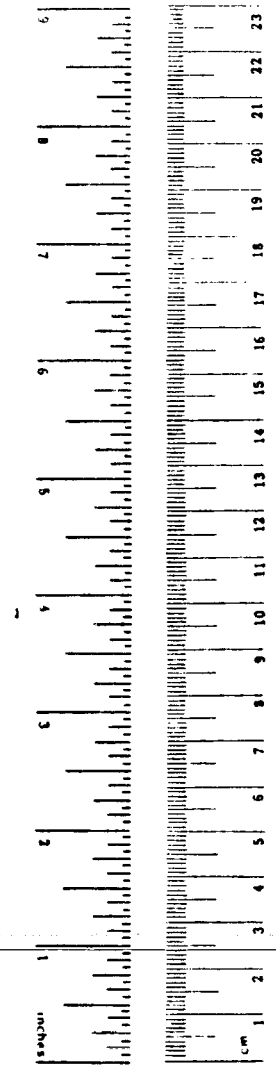


## Approximate Conversions from Metric Measures

| Symbol | When You Know | Multiply by | To Find | Symbol |
|---|---|---|---|---|
| | **LENGTH** | | | |
| mm | millimeters | 0.04 | inches | in |
| cm | centimeters | 0.4 | inches | in |
| m | meters | 3.3 | feet | ft |
| m | meters | 1.1 | yards | yd |
| km | kilometers | 0.6 | miles | mi |
| | **AREA** | | | |
| $cm^2$ | square centimeters | 0.16 | square inches | $in^2$ |
| $m^2$ | square meters | 1.2 | square yards | $yd^2$ |
| $km^2$ | square kilometers | 0.4 | square miles | $mi^2$ |
| ha | hectares (10,000 $m^2$) | 2.5 | acres | |
| | **MASS (weight)** | | | |
| g | grams | 0.035 | ounces | oz |
| kg | kilograms | 2.2 | pounds | lb |
| t | tonnes (1000 kg) | 1.1 | short tons | |
| | **VOLUME** | | | |
| ml | milliliters | 0.03 | fluid ounces | fl oz |
| l | liters | 2.1 | pints | pt |
| l | liters | 1.06 | quarts | qt |
| l | liters | 0.26 | gallons | gal |
| $m^3$ | cubic meters | 35 | cubic feet | $ft^3$ |
| $m^3$ | cubic meters | 1.3 | cubic yards | $yd^3$ |
| | **TEMPERATURE (exact)** | | | |
| °C | Celsius temperature | 9/5 (then add 32) | Fahrenheit temperature | |

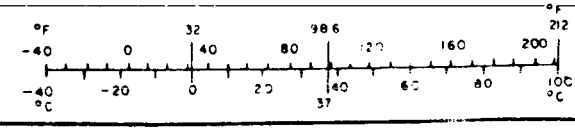

# I. INTRODUCTION

This report summarizes a study of the multipath environment for the Microwave Landing System (MLS) precision Distance Measuring Equipment (DME/P) subsystem. The study objectives were to determine a quantitative statement of the anticipated environment as a guide to DME/P system optimization and performance assessment. In particular, we have sought to consider the multipath environment features which will be of greatest concern for the L-band DME/P implementations currently under consideration by the International Civil Aviation Organization (ICAO) All Weather Operations Panel (AWOP).

The present hope is that an L-band DME which is fully compatible with current VOR/DME navigation and/or RNAV requirements can provide range guidance which is adequate for all the MLS needs (e.g., RNAV to MLS transition, complex terminal maneuvers for curved approach, flare initiation and the flare maneuver itself, etc.). Typical DME/P requirements are shown in Table 1-1.

There is at this time a limited L-band DME data base which can be directly applied to the DME/P. All of the precision DME's testing in the U.S. during the MLS phase II program used fast rise time pulses at C-band. Performance extrapolation of these C-band results to the L-band DME/P is unlikely due to the differences in pulse rise time, carrier frequency and the unrepresentative reflector geometry of the multipath tests in the US MLS phase II assessment. Subsequent L-band DME tests conducted [23,30] at the FAA Technical Analysis Center (Atlantic City N.J.), Crows Landing, Calif. and Wallops Island, Va. used runways which have few if any sizable scatterers.

The L-band DME testing by the Federal Republic of Germany (FRG) at Braunschweig, W. Germany associated with the DLS proposal [13] encountered a certain degree of "indigenous" multipath from buildings, houses, etc. [13], however, the airport geometry was not typical of normal airports. The limited United Kingdom (UK) DME trials at RAE Bedford using an L-band DME with a fast (100 nsec) risetime apparently encountered only ground reflection lobing [14].

---

*Minimum Decision Altitude

TABLE 1-1

DME/P ACCURACY REQUIREMENTS

-maximum error (95% probability)
-calculations based upon a 1768 m (5800ft) DME to runway threshold distance
-NA for "non applicable"

| Function | | Typical distance from the reference datum (NM) | Path Following Error | Control Motion Error |
|---|---|---|---|---|
| Segmented approach | -extended runway centerline | 20 | 250m (800ft) | 68m (173ft) |
| | -at 40° azimuth | | 375m (1200ft) | 68m (220ft) |
| Segmented approach | -extended runway centerline | 5 | 85m (210ft) | 34m (50ft) |
| | -at 40° azimuth | | 127m (330ft) | 34m (63ft) |
| Marker replacement | -Outer marker | 5 | 800m (2400ft) | NA |
| | -middle marker | 0.57 | 400m (1200ft) | NA |
| Cat II Decision Height | -CTOL | 0.3 | 30m (100ft) | NA |
| | -STOL | | 15m (50ft) | NA |
| Flare initiation over uneven terrain | -CTOL | 0 | 30m (100ft) | 18m (100ft) |
| | -STOL | | 12m (40ft) | 12m (40ft) |
| Sensitivity Modifications (Autopilot gain scheduling) | | 20 to 0 | 240m (770ft) | NA |
| Flare Maneuver with MLS Flare Antenna | - CTOL | 0 | 30m (100ft) | 12m (40ft) |
| | - STOL | | 12m (40ft) | 12m (40ft) |
| Long Flare Alert | | 1 | 30m (100ft) | NA |
| CTOL High Speed Rollout/Turnoffs | | 0 | 12m (40ft) | 30m (100ft) |
| Departure Climb and Missed Approach | | 0 to -5 | 100m (328ft) | 68m (250ft) |
| Windshear Detection | | 5 | NA | 3.25m |
| VTOL Decelerated Approach | | 0.5 to 0 | 12m (40ft) | 1.3m (4.3ft) |
| Coordinate Translations and Conversions | | | 12m to 30m (40ft) (100ft) | 12m (40ft) |

Multipath affects the DME signal-in-space in much the same way that it does the MLS angle guidance scanning beam signal, i.e., by additive distortion of the received pulse envelope. An important distinction, however, is the following: for DME, multipath returns are one-sided in time, that is, they always arrive late with respect to the direct component due to the longer paths they traverse. This is in contrast to the situation in scanning beam in which multipath arrival time is a function of scan direction and the angular location of the scatterer, and in fact, multipath which leads the direct on the "TO" scan will trail it on the "FRO" scan and vice versa. This observation has important implications on processor implementation for both interrogator and transponder.

Figure 1-1 illustrates the effect of a single multipath component on a typical DME waveform. The multipath signal is a delayed replica of the received direct signal s(t); in general, the multipath amplitude and phase will differ from the direct. In terms of $\tau$, $\rho$, and $\phi$, the (relative) delay, amplitude, and phase, the complex envelope of the multipath can be written $\rho e^{j\phi} s(t - \tau)$. Figures 1-1(a) and (b) show the direct and multipath waves, respectively. The total received envelope is simply the magnitude of the sum of the two complex waveforms. This is illustrated by Fig. 1-1(c) for the in-phase ($\phi$=0°) case. One can note that the trailing edge suffers far greater displacement than the leading edge for a fixed -6 dB threshold.

Further on, we shall see that multipath delay is a key factor in DME performance, and that each DME implementation has a region of what are called "critical delays," that is, values of differential delay for which the net range error is largest. For some, typically the slow risetime pulses associated with present day L-band DME practice, the critical delays are on the order of several hundred ns to more than one μs. Figure 1-2 illustrates elliptical contours of constant delay of this order of magnitude on an airport plan view. It is assumed that the DME transponder is 1,000 ft behind the stop end of a 10,000 ft runway, and that the receiving aircraft is over threshold. One can easily see that the 1μs - 2μs time delay contours extend well back into portions of the airport which could be occupied by buildings or other structures (the nominal 700 ft obstacle clearance line is sketched for

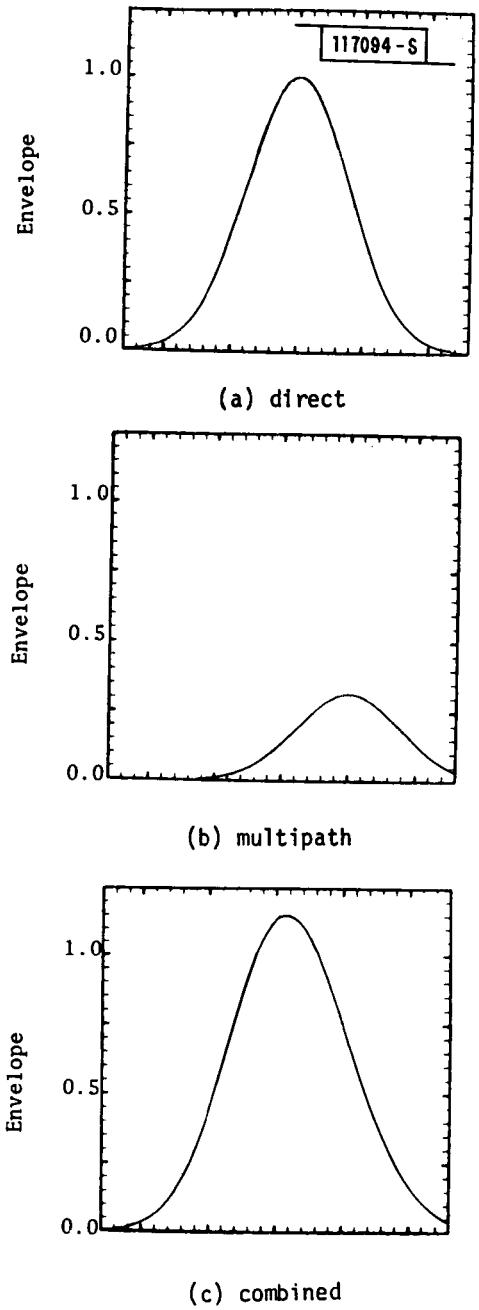


Fig.1-1. Effect of a single multipath component on DME pulse.

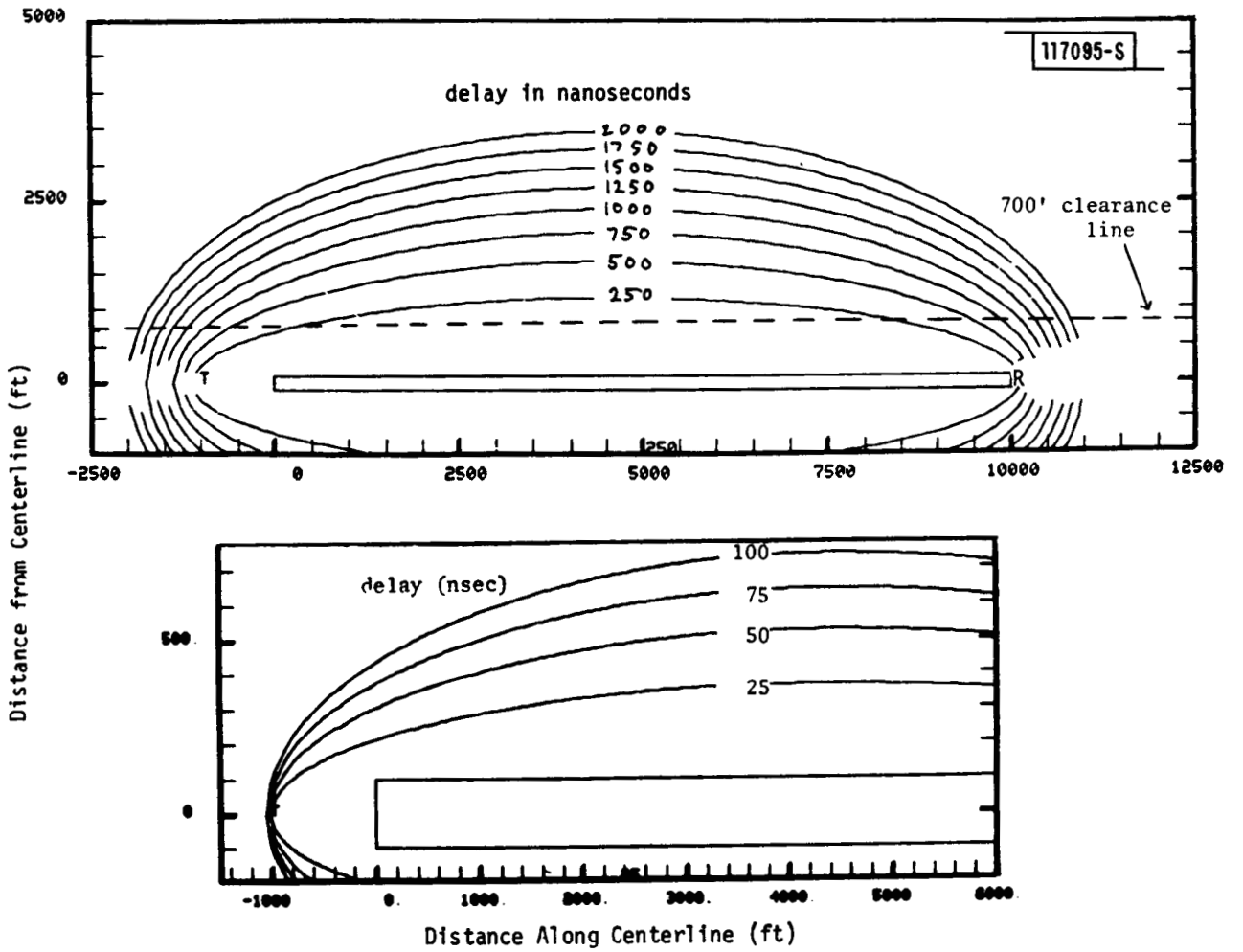


Fig.1-2. Constant delay contours on airport surface.

reference). Thus, for such DMEs, numerous potential multipath sources can exist at an airport.

Other DMEs (fast risetime pulses and improved processors) have much smaller critical delays, e.g., less than 200 ns. The contours in Fig. 1-2 indicate that these DMEs are largely immune to reflections from permanent obstacles on the airport surface. They may be susceptible to reflections from parked or taxiing aircraft and service vehicles which can be found inside the obstacle clearance limits. The extent of these susceptibilities is discussed in Section IV, where the critical/sensitive area problem is addressed. For the present, it suffices to note that differential delay provides one handy rule-of-thumb for assessing potential DME multipath hazards.

A number of ideas were put forth regarding the achievement of suitably small ranging errors with a signalling scheme compatible with the present day navigation DME. These ranged all the way from no pulse modification at all to the design of special waveforms which marginally satisfy ICAO Annex 10 and will provide enough accuracy for the most demanding applications (Cat III flare initiation through rollout and turnoff) when processed by appropriate receiver techniques. The approach recently adopted by Working Group "M" (WGM) of AWOP uses pulses which have significantly faster rise times than the previous ICAO DME pulse, but still meet the ICAO Annex 10 spectrum occupancy requirements.

The principal burden of achieving good DME/P multipath performance is divided more or less equally between <u>waveform design</u> and <u>processor technique</u>. Both of these factors must be examined to ascertain which multipath parameters are of greatest concern. Section II describes the three receiver processing techniques (fixed thresholding, real time thresholding, and delay-and-compare) to be studied and qualitatively identifies some of their performance characteristics which are somewhat waveform-independent. Also considered in Section II are some additional available means of multipath suppression, primarily transponder antenna pattern shaping and motion averaging.

Section III considers the DME multipath environment with particular emphasis on those types of multipath which are likely to be of greatest concern for representative optimized waveform/processor designs. It is seen that lateral multipath from buildings or aircraft are of greatest concern from the viewpoint of relative time delays. Terrain reflections are seen to also be important as a contributing factor in that they will cause substantial decreases in the direct signal strength and, may not cause as large a decrease in the multipath signal levels.

Section IV considers DME multipath simulation studies results to date. Reflections from aircraft, truck type objects, and buildings are examined by the approach used to assess MLS angle guidance critical/sensitive areas [8]. Next, building reflections are examined in the context of the multipath levels and spatial variation as exemplified in two multipath scenarios developed by AWOP. It is shown that lateral multipath from buildings represents a significant challenge to successful DME/P operation.

Section V examines the experimental studies to date regarding L-band lateral multipath in representative geometries. These include both work directly aimed at DME/P multipath and related work in the context of airport surveillance. It is shown that very high M/D levels (e.g., in excess of 0 dB) can be encountered at low interrogator (i.e., aircraft) heights as a result of differential ground lobing effects.

Another important issue is the relative likelihood of multipath with various characteristics (e.g., relative time delay, multipath region, scalloping frequency). To assess this, a building location data base derived from maps for some 24 U.S. and foreign airports has been analyzed to determine empirical probabilities of encountering specular building reflections with a given characteristic value. Results of this analysis are presented in Section VI.

Section VII summarizes the results of the various studies and presents a preliminary quantitative asessment of the expected multipath environment as well as identifying several issues requiring further study.

## II. PRINCIPAL DME/P MULTIPATH REJECTION FEATURES

Our objective in this section is to examine the principal DME/P multipath rejection features with the objective of defining the characteristics of the principal multipath threats. It is unfortunate that no simple rule-of-thumb relationship exists between multipath level and delay and DME error*. Error behavior is strongly dependent upon the signal design as well as the processing at both the transponder and interrogator. Dependence on multipath amplitude is fortunately somewhat simpler. In order to convey some understanding of what is involved, the following two sections examine common DME pulse shapes and pulse arrival time estimation techniques and some of their qualitative performance characteristics. Following that, several additional multipath features are examined.

### A. Signal Waveform

The signal waveform utilized for the DME/P can make a major impact on multipath performance to the extent that it permits one to make a distance measurement at reasonable signal-to-noise ratio (SNR) soon after the pulse has arrived. A variety of pulse shapes have been proposed over the past two years. We will consider here two of the most common proposals.

#### 1. Gaussian Pulse

Figure 2-1 illustrates the basic Gaussian pulse on a time scale measured in 10-90% risetime units. We use the Gaussian pulse as the model for present

---

*The Radio Technical Commission for Aeronautics RTCA Special Committee No. 117 (SC-117) [15] used the relationship

$$\epsilon = 0.29\ t_r$$

where $t_r$ is the pulse risetime as a guideline for its DME design. This particular relationship would suggest significant multipath problems for many of the current DME pulse shape proposals. Fortunately, the physical/mathematical basis for applying this relationship to all pulse shape/processor combinations is highly suspect.

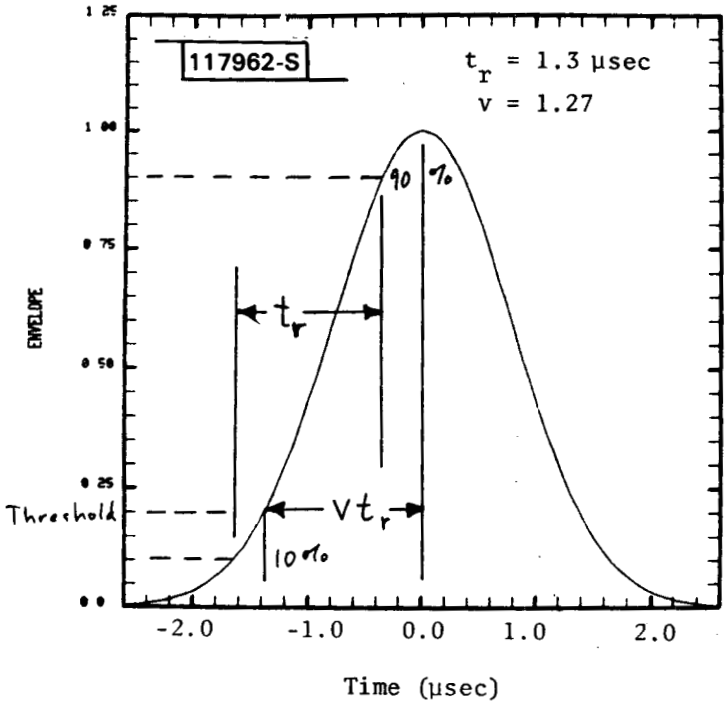


Fig.2-1. Gaussian DME waveform illustrating the definition of risetime and nominal threshold crossing time.

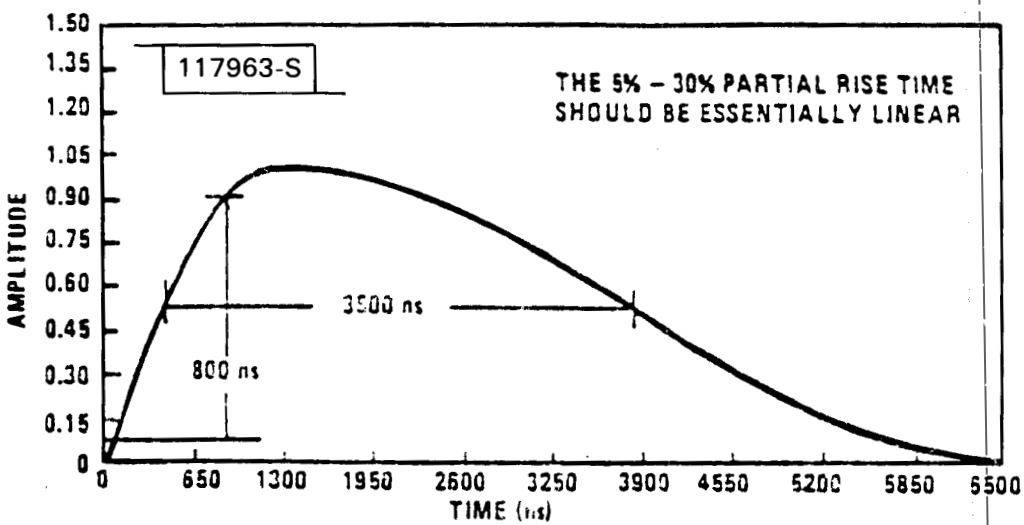


Fig.2-2. DME/P cos-cos$^2$ waveform.

day DME waveform. Thus, it is relevant to the use of a nonprecision DME (DME/N) as a part of MLS as well as the DME based azimuth system (DAS) under study by the FRG [13].

The ICAO standard pulse width (measured between the -6 dB envelope points) is 3.5 μs, which corresponds to a 2.5 μs risetime [1]. The 2.5 μs risetime pulse meets the ICAO spectrum requirements with room to spare. R.P. Crow has calculated that the pulse will still meet the ICAO specifications if the risetime is decreased to 1.3 μs [15]. For our purposes, the Gaussian pulse will be described by the equation:

$$s(t) = e^{-\beta(t/t_r)^2} \qquad (2\text{-}1)$$

where $t_r$ is the risetime and $\beta = 1.423$ so that the $t_r$ satisfies the ICAO 10% - 90% definition.

2. $\cos/\cos^2$ Pulse

This waveform was designed in an attempt to find a suitable compromise between

i) a pulse shape usable at L-band whose spectrum adheres to ICAO Annex 10 and is thus compatible with present DME, and

ii) a sharp leading edge suitable for low level thresholding and good multipath rejection.

The $\cos/\cos^2$ pulse adopted by WG-M[50] as the precision measurement waveform for DME/P is shown in Fig. 2-2. This pulse shape satisfies the basic requirements above. The leading edge has a much sharper rise than the Gaussian-type pulse. Its initial slope is such that the risetime would be 0.78 μs if it continued linearly.

## B. Receiver Pulse Processors

All the DME performance results found in the ensuing discussion are based on the assumption of one of three canonical receiver processing techniques; fixed threshold, real time threshold, or delay-and-compare. Each of these can be used with any of the pulse types, and their performance characteristics are more or less independent of the details of the pulse shape. In this section, a description of each processor is given. This is supplemented by an explanation of its important performance characteristics; the explanation is done with the aid of an analytical formula which predicts range error vs. multipath and processor parameters.

A collection of such formulas is derived in Appendix A. These formulas have been validated against computer simulation data; the principal restriction on their use is that they apply for small-to-moderate multipath levels. From among these, the results which apply to a Gaussian pulse will be used as illustrations.

All the DME performance results found in the ensuing discussion are based on the assumption of one of three canonical receiver processing techniques; fixed threshold, real time threshold, or delay-and-compare. Each of these can be used with any of the pulse types, and their performance characteristics are more or less independent of the details of the pulse shape. In this section, a description of each processor is given. This is supplemented by an explanation of its important performance characteristics; the explanation is done with the aid of an analytical formula which predicts range error vs. multipath and processor parameters.

All three techniques are leading edge processors, that is, time of arrival is determined from measurements made on the leading edge of the first pulse. The objective is to defeat multipath by detecting the pulse prior to contamination by the delayed reflections. In general, the earlier the detection can be made, the greater the multipath suppression. Of course, the extent to which this can be carried out is limited by the receiver noise level and the available signal power.

1. Fixed Threshold Receiver

In this receiver, time of arrival is estimated by detecting the time at which the leading edge of the first pulse crosses a threshold level $\alpha$. The interpretation of "fixed" threshold is that the threshold voltage remains a constant fraction of the peak direct signal level*. For some of the performance results, it is convenient to express the threshold in terms of "risetime" units. The parameter, v, expresses the time elapsed between the nominal (no multipath) threshold crossing and the waveform peak as a function of the risetime $t_r$ (see Fig. 2-1). For small multipath to direct signal ratios (M/D), the following expression is an accurate approximation to the static arrival time estimation error for fixed thresholding on a Gaussian pulse:

$$\varepsilon_{fix} \approx \frac{\rho t_r}{2\beta v} e^{-\beta\left(\frac{\tau}{t_r}\right)\left(\frac{\tau}{t_r} + 2v\right)} \cos\phi \qquad (2\text{-}2)$$

where

$$\alpha = e^{-\beta v^2}. \qquad (2\text{-}3)$$

$\rho$ = voltage M/D ratio

$\phi$ = relative rf phase between direct and multipath signals

$\tau$ = relative time delay between direct and multipath signals

An appreciation of the utility of this formula can be gained by making some simple observations. First of all, note that in-phase multipath ($\cos\phi > 0$) causes negative errors. The multipath signal reinforces the direct signal, increasing the envelope and causing a late threshold crossing. Similarly, out-of-phase multipath will result in an early crossing.

---

*The notion of an absolutely fixed threshold is convenient for analytic purposes, but does not necessarily correspond to what happens in a real receiver. The threshold could be a fixed voltage, in which case the threshold crossing point drops as the aircraft nears the transponder, or the threshold voltage could be range scaled to keep it a fixed number of dB below the nominal direct signal level.

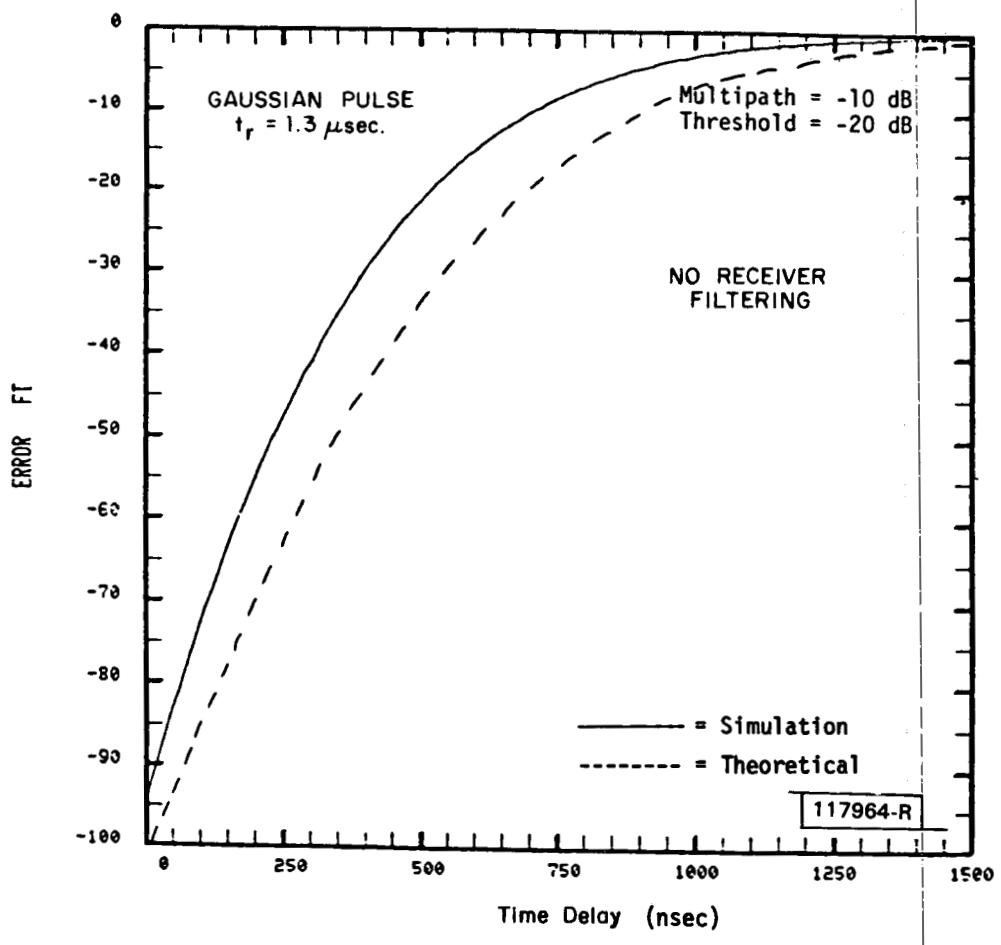


Fig.2-3. Fixed thresholding error vs. multipath delay.

As a function of multipath delay, the error magnitude is monotone decreasing. At zero delay, the multipath amplitude modulates the direct pulse, causing a large error since the threshold is fixed. As the delay increases, correspondingly less of the multipath pulse influences the leading edge and smaller errors result. This behavior illustrates one favorable aspect of fixed thresholding, which is insensitive to late multipath resulting from the decoupling of threshold level and variations in received signal level. Of course, this feature comes at the price of large errors for early multipath and considerable sensitivity to signal level changes characteristic of ground lobing and airborne antenna gain variations*. Neither of these traits is inherent in either of the other processors to be considered.

Formula (2-2) clearly shows that multipath performance is improved by using short risetimes and low thresholds (large values of v). The latter observation, interestingly, is opposite to what is found for MLS angle system multipath when a dwell gate processor is used. There, the problem is to minimize the maximum dwell gate displacement, which is achieved by using a high threshold value.

Figure 2-3 illustrates the fixed thresholding behavior in a plot of error vs. multipath delay. A second curve, which is the comparable simulation data, is plotted for comparison. In both cases, the multipath parameters are $\rho$ = -10 dB, $t_r$ = 1.3 $\mu$sec, $\phi$ = 0°. The threshold setting is -20 dB (v = 1.27).

Real Time Threshold Receivers

This processor makes use of a technique employed in the MLS angle processors. The threshold voltage is set a specified number of dB below a reference value related to peak pulse amplitude. The reference could be taken from the present pulse, the previous pulse, or it could be a smoothed average of several past pulses (motion averaging properties will differ slightly depend-

*For example, Lincoln measurements [18-20] of L-band airborne antenna gain for typical DME locations show variations of as much as 10 dB near the forward direction when the wheels are down [18-20].

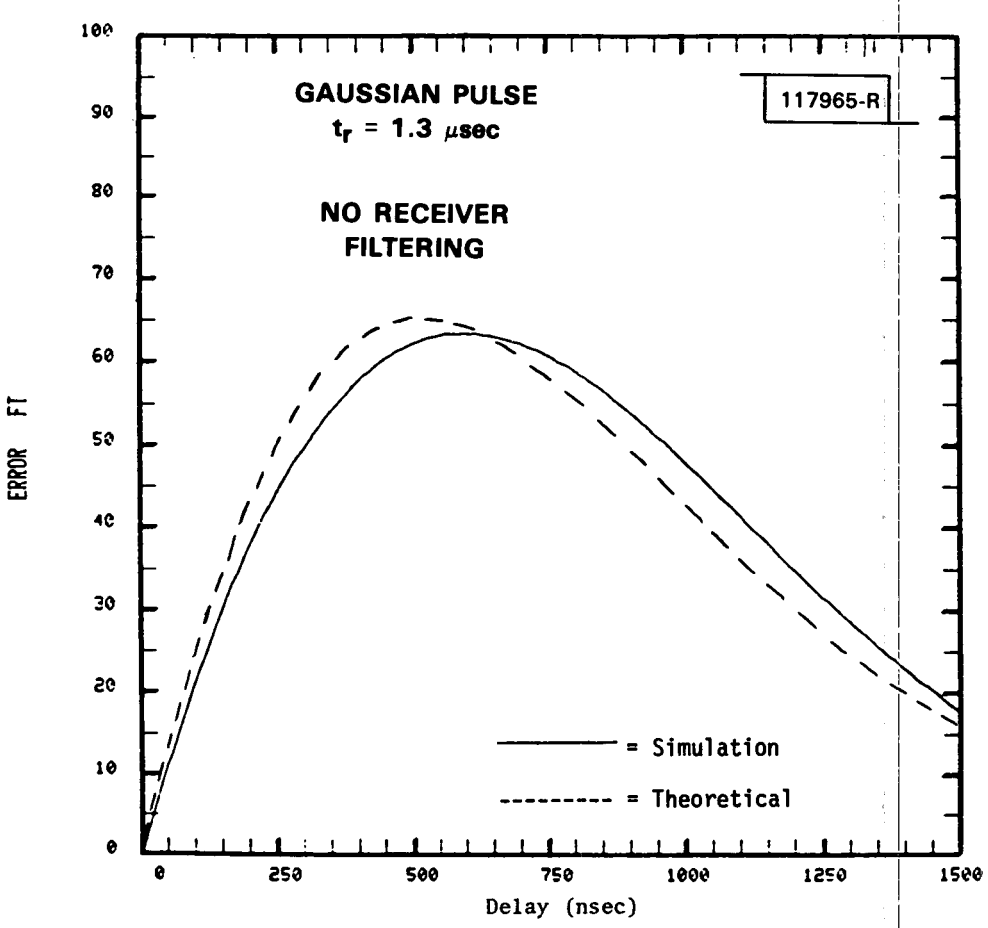


Fig.2-4. Adaptive thresholding error vs. multipath delay.

ing on the choice of reference). For the following, the threshold is referred to the present pulse amplitude.

As the following formula illustrates, adaptive thresholding induces a somewhat different error behavior from that seen previously:

$$\varepsilon_{rt} \simeq \rho\tau e^{-\beta\left(\frac{\tau}{t_r}\right)\left(\frac{\tau}{t_r}+v\right)} \frac{\sinh\frac{\beta v\tau}{t_r}}{\frac{\beta v\tau}{t_r}} \cos\phi \qquad (2\text{-}4)$$

The major difference between this and the previous formula is the multiplicative term in $\tau$, indicating that as multipath delay increases from zero, error increases from zero to a maximum and subsequently decreases. For example, using a -20 dB threshold, the maximum error is found to occur at a delay equal to 35% of the risetime and the corresponding error is roughly $0.28\ \rho t_r$. This behavior can be explained in terms of the processor operation. Close-in multipath scales the leading edge and peak in proportion, inducing little error. For longer delays (e.g., those in the maximum error vicinity), the peak is displaced while the leading edge is relatively clean. The resulting incorrect threshold setting causes an error. As delay further increases, the error does not fall off as fast as for the fixed threshold processor due to the residual errors in peak amplitude. This can be seen by comparing the exponential terms in (2-4) and (2-2). The dependence upon $\rho$ and $\phi$ is essentially the same as for fixed thresholding, except now in-phase multipath tends to delay the threshold crossing and produce a positive error.

Figure 2-4 shows analytical and simulation results of error vs. delay for real time thresholding. The multipath and processor parameters are the same as in Fig. 2-3 (fixed thresholding).

### 3. Delay-and-Compare Receivers (DAC)

A block diagram of a delay-and-compare processor is shown in Fig. 2-5. Arrival time is detected by coincidence of the leading edges of the delayed and undelayed pulses. This processor is self-AGC'd with regard to the threshold setting, since the comparator inputs are scaled replicas. This feature

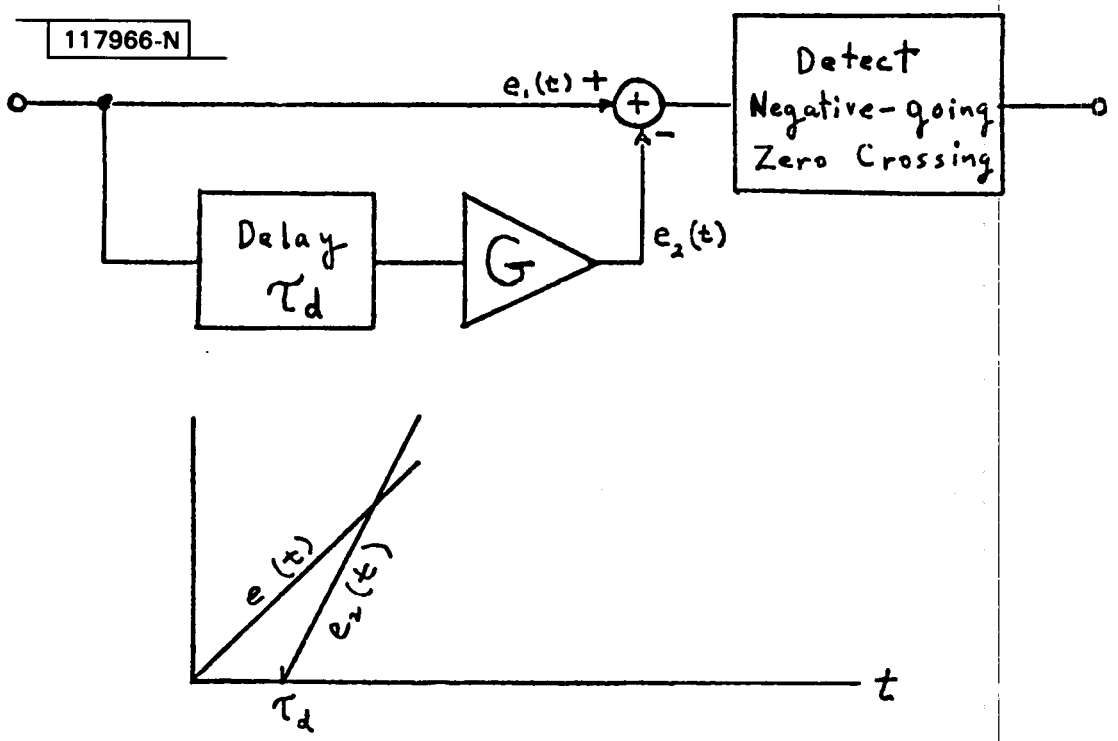


Fig.2-5. DME leading edge comparator circuit.

provides a measure of level insensitivity similar to adaptive thresholding.

The combined choice of processor gain (G) and comparator delay ($\tau_d$) fixes the effective threshold level by determining the point on the input waveform at which the coincidence nominally occurs. Various combinations of G and $\tau_d$ yield equivalent thresholds. The gain required to achieve a threshold crossing $vt_r$ sec before the waveform peak of a Gaussian pulse is (as a function of $\tau_d$)

$$G = e^{\left(\frac{\tau_d}{t_r}\right)\left(\frac{\tau_d}{t_r} + 2v\right)} \tag{2-5}$$

Equation (2-6) below gives the arrival time error for a DAC processor with Gaussian pulses. It is written in a form which places in evidence the half-width at threshold parameter (v) used previously and the delay $\tau_d$; explicit dependence on the gain has been suppressed through use of (2-5):

$$\varepsilon_{dc} \simeq \rho\,\tau\left\{\exp\left[-\beta\left(\frac{\tau}{t_r}\right)\left(\frac{\tau}{t_r} + \frac{\tau_d}{t_r} + 2v\right)\right]\right\}\left\{\frac{\sinh\frac{\beta\tau_d\tau}{2}}{\frac{\beta\tau_d\tau}{t_r^2}}\right\}\cos\phi \tag{2-6}$$

The above form allows direct comparison with the previous error expression. The behavior is qualitatively identical to that of adaptive thresholding, differing only in its detailed dependence on the processing parameters. The exponential decay is essentially the same as for fixed thresholding, as is more easily seen in the following rewrite of (2-6):

$$\varepsilon_{dc} = \frac{\rho t_d^2}{2\beta\tau_d} e^{-\beta\left(\frac{\tau}{t_r}\right)\left(\frac{\tau}{t_r} + 2v\right)} \left[1-\exp \frac{-2\beta\tau_d\tau}{t_r^2}\right] \cos\phi \qquad (2\text{-}7)$$

For large multipath delays, both are superior to real time thresholding. Delay-and-compare has a clear advantage over fixed thresholding, however, for small values of $\tau$.

A further advantage of DAC processing is that it effectively eliminates all multipath components whose delay exceeds some small multiple of the comparator delay*. Thus, by decreasing $\tau_d$ at fixed gain (equivalently, dropping the threshold), better multipath immunity is obtained.

A number of studies of DAC processing for cos - $\cos^2$ pulses have been carried out [3,34,37,40-43]. Appendix A derives the error formula for a cosine leading edge of duration D:

$$\varepsilon_{dc} = \begin{cases} \left(\frac{3}{2\pi}\right) \rho \sin w\tau \cos\phi & \tau < t_d \\ \left(\frac{3}{2\pi}\right) \sin \frac{w(t_c - \tau_d)}{w \sin w\tau_d} \sin w(t_c - \tau) \cos\phi & t_d < \tau < t_c \\ 0 & \tau > t_c \end{cases} \qquad (2\text{-}8)$$

where $w = \pi/2T$ and $t_c$ is the DAC decision time.

---

*A similar statement is true of fixed thresholding. The assumption of a Gaussian pulse disguises these facts, since the leading edge extends infinitely into the past. The results are easier to see for a pulse that rises from zero amplitude, e.g., a cos-$\cos^2$ pulse.

Unfortunately, eq. (2-8) is not appropriate for practical DME/P implementations due to the influence of the receiver IF filter. Figures 2-6 and 2-7 show DAC curves for Gaussian and cos - $\cos^2$ pulses. In Fig. 2-7, we see that the region of errors with the IF considered is approximately 50% greater than suggested by the pulse shape alone. However, the peak error is reduced. Also note that the region of noticeable errors lengthens slightly at high M/D ratios. This is due to the IF filter output starting out at zero slope as opposed to a finite slope (Fig. 2-8).

The commentary concerning the most critical path delays for adaptive thresholding applies to the present case as well. The delay-and-compare error vs. delay curve peaks earlier than the adaptive thresholding curve, so the critical path differences lie in a somewhat smaller range.

It is possible to exercise partial control over the DME multipath environment by means other than signal and receiver thresholding circuit design. Five such means are now discussed: antenna pattern shaping, motion averaging, lateral diversity, uplink/downlink error averaging, and mismatched receiver filtering.

## C. Transponder Antenna Pattern Shaping

It is generally assumed that the DME transponder will be located with or near the MLS azimuth ground antenna and will have at least the same coverage. The pattern of the ground-based antenna is a key factor in maintaining sufficiently high quality range guidance throughout the coverage volume. Since the coverage is wide in azimuth (40°), the azimuth pattern cannot roll off appreciably off centerline without exaggerating the problems of direct signal shadowing and multipath enhancement for aircraft on curved or dog-leg approaches. However, it is certainly possible to use an azimuth pattern with centerline emphasis such as that shown in Fig. 2-9 which was proposed by Hazeltine [11]. A pattern such as Fig. 2-9 typically requires an array phased to yield the desired pattern. The use of a simple reflector can yield a degree of centerline emphasis (Fig. 2-10). The range accuracy requirements for an aircraft executing a terminal maneuver off centerline are

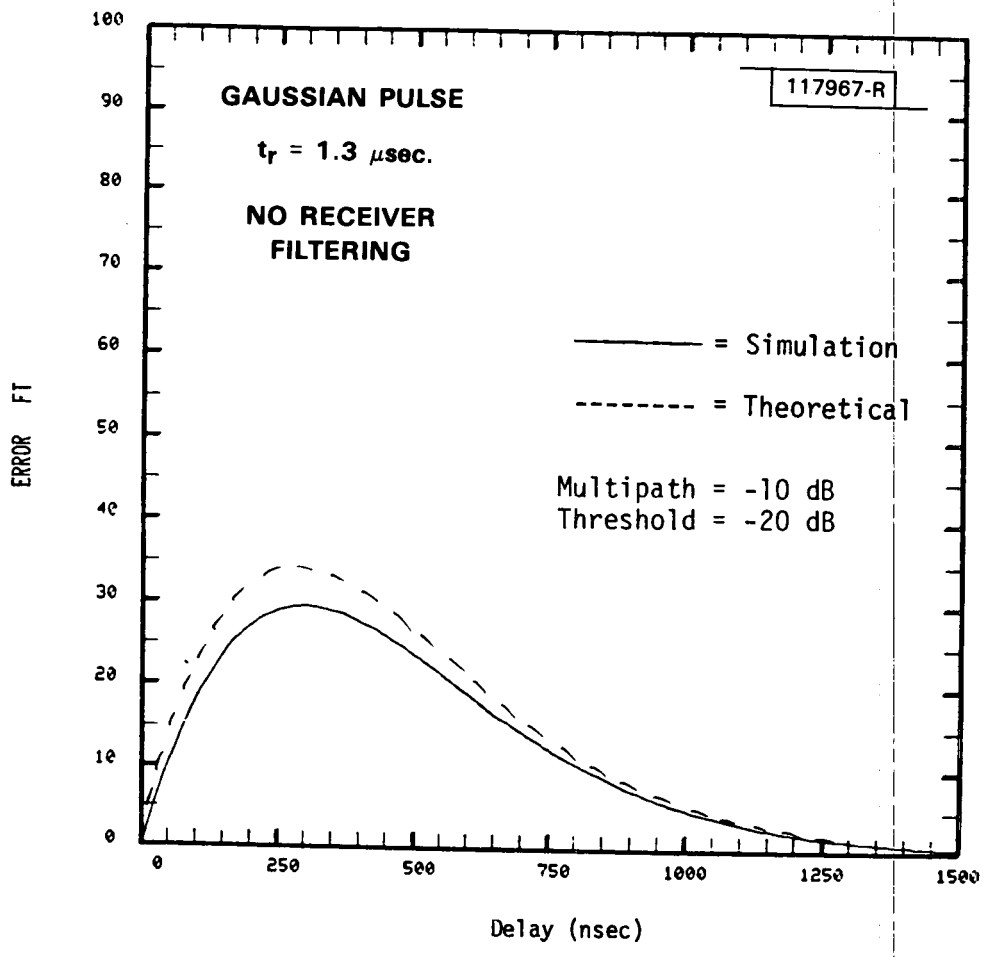


Fig.2-6. Delay-and-compare error vs. multipath delay.

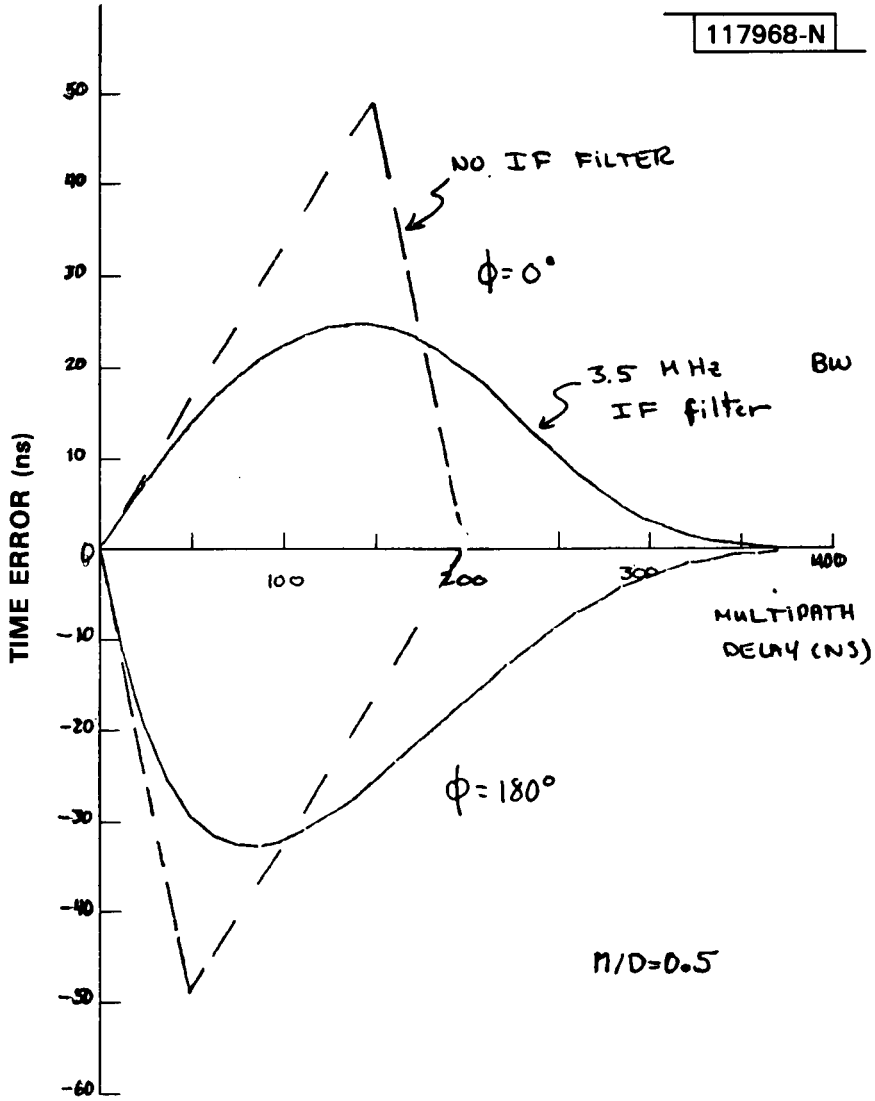


Fig.2-7. Comparison of DAC error characteristic with and without IF filtering.

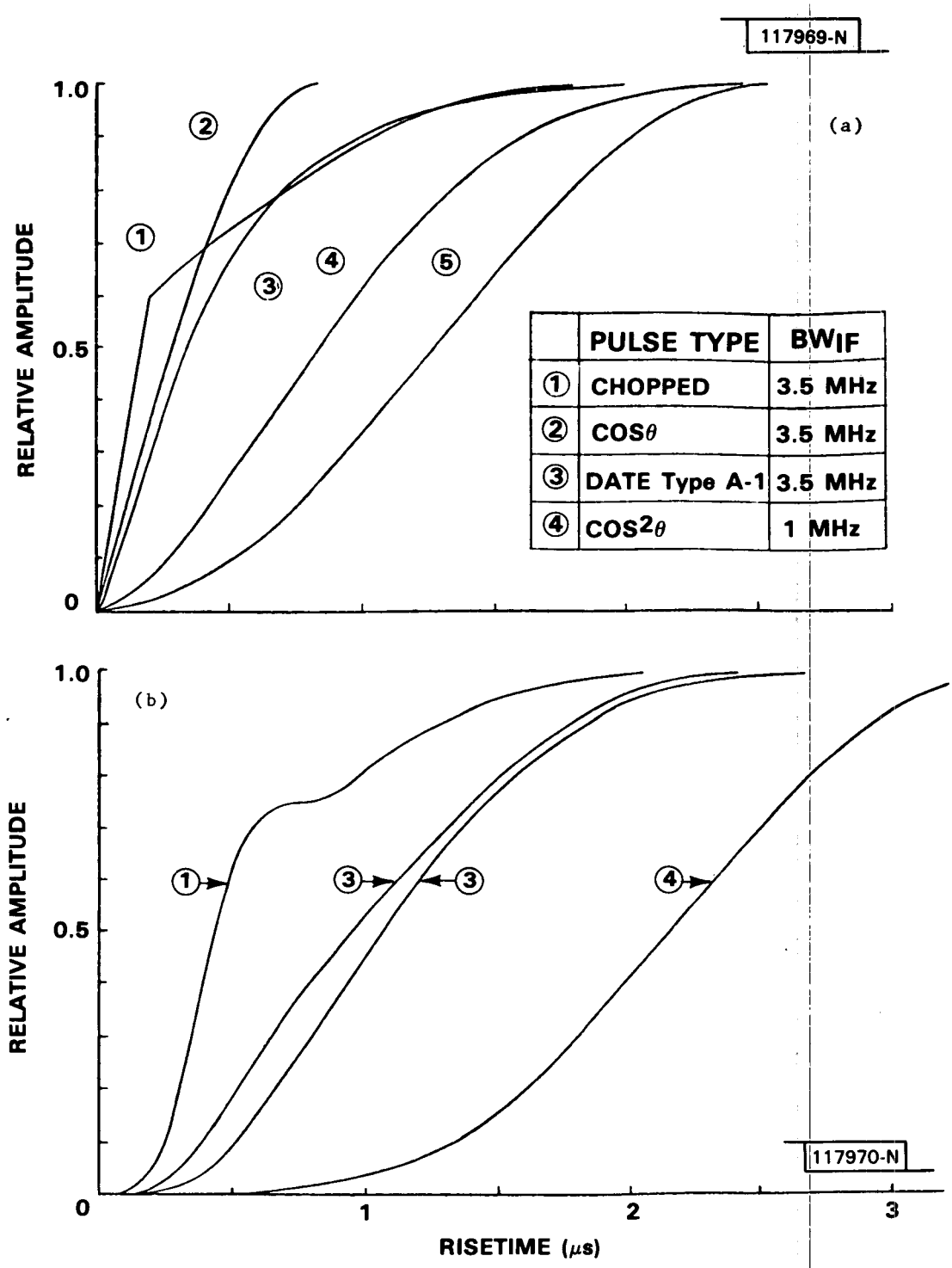


Fig.2-8. (a) Leading edge comparison of various proposed pulse shapes for air to ground (from [12]) and (b) leading edge characteristics of various proposed ground to air pulse shapes including IF filter effect (from [12]).

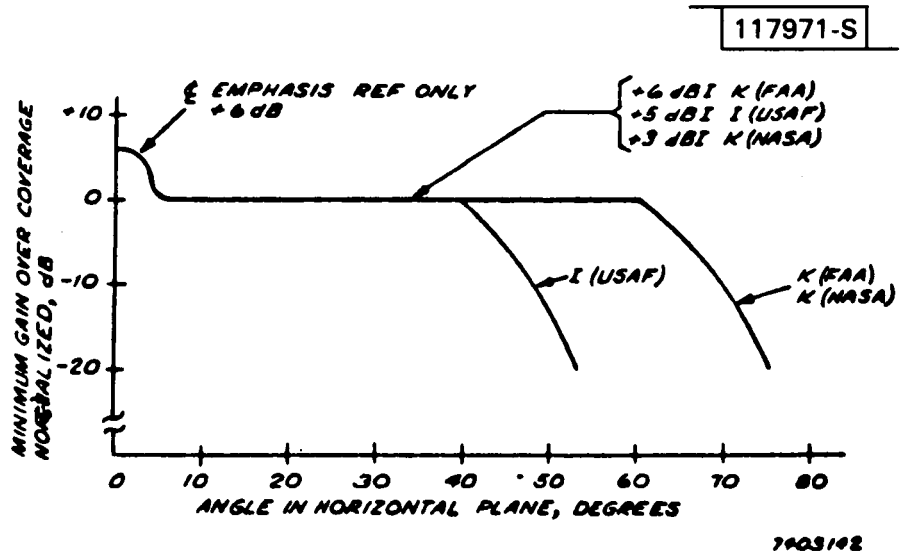


Fig.2-9. Hazeltine AZ antenna azimuth pattern showing centerline emphasis.

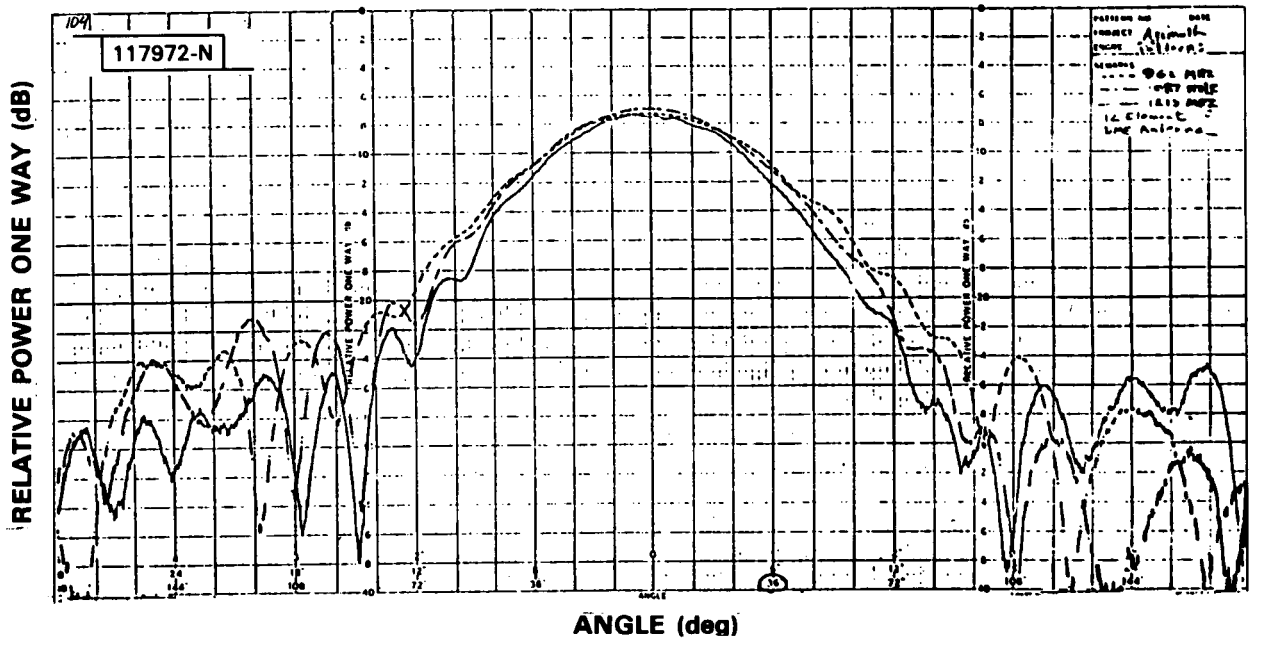


Fig.2-10. Measured horizontal pattern of ground antenna (from [37]).

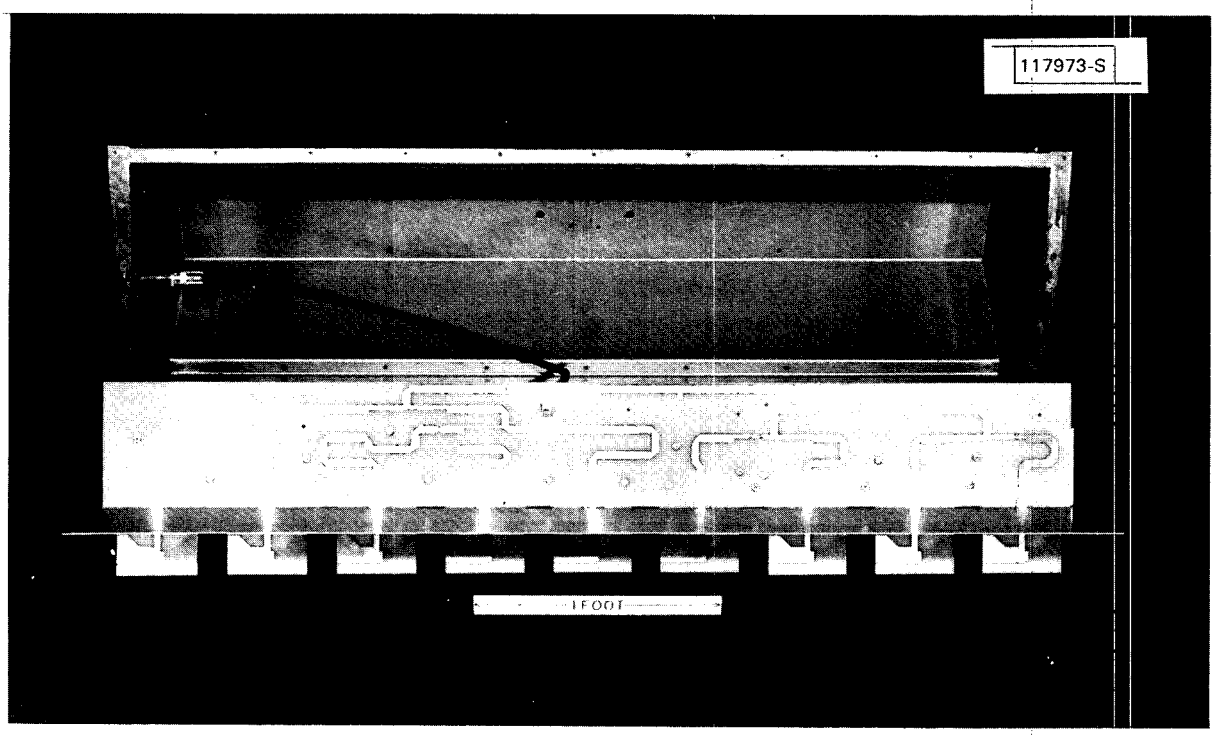


Fig.2-11(a). PALM dipole array.

sufficiently lax to tolerate a decreased signal level. The reflection multipath risk when off centerline is not increased very much by the use of centerline emphasis since it is unlikely that significant scatterers will lie in the emphasis region.

In elevation, the antenna pattern can be designed to ameliorate some of the reflection multipath problems cited earlier. Specular reflections from flat or tilted terrain will usually intercept the transponder at negative or low (relative to the glideslope) elevation angles. Each of the processors discussed in the previous section, especially fixed threshold, has a certain susceptibility to such multipath and would benefit from low elevation cutoff in the elevation pattern. The design of L-band patterns to yield a maximal rolloff at the horizon was the object of considerable study in the PALM program [9]; Fig. 2-11 shows representative PALM patterns.

### D. Aircraft Antenna Pattern Shaping

Onboard the aircraft, wide azimuth coverage is required for guidance during complex prefinal maneuvers, so that little multipath suppression can be achieved by airborne antenna azimuth shaping if a single airborne antenna is used for DME. Similarly, except for the cases of tilted terrain or tilted scatters (such as aircraft fuselages) below the aircraft, the multipath arrival angles at the aircraft are not widely dispersed in elevation and cannot be significantly reduced by the elevation pattern of the aircraft antenna.

### E. Motion Averaging

Like the MLS angle functions, the DME is a multi-scan system and can benefit from motion averaging. Since the interrogation rate (40 Hz) is typically eight times the MLS data rate (5 Hz), eight replies can be averaged per output range reading. The averaging improvement varies with scalloping frequency in a manner dependent upon the single-scan error vs relative rf phase function. All the error formulas presented above show the error is proportional to cos $\phi$, where $\phi$ is the differential phase angle between direct

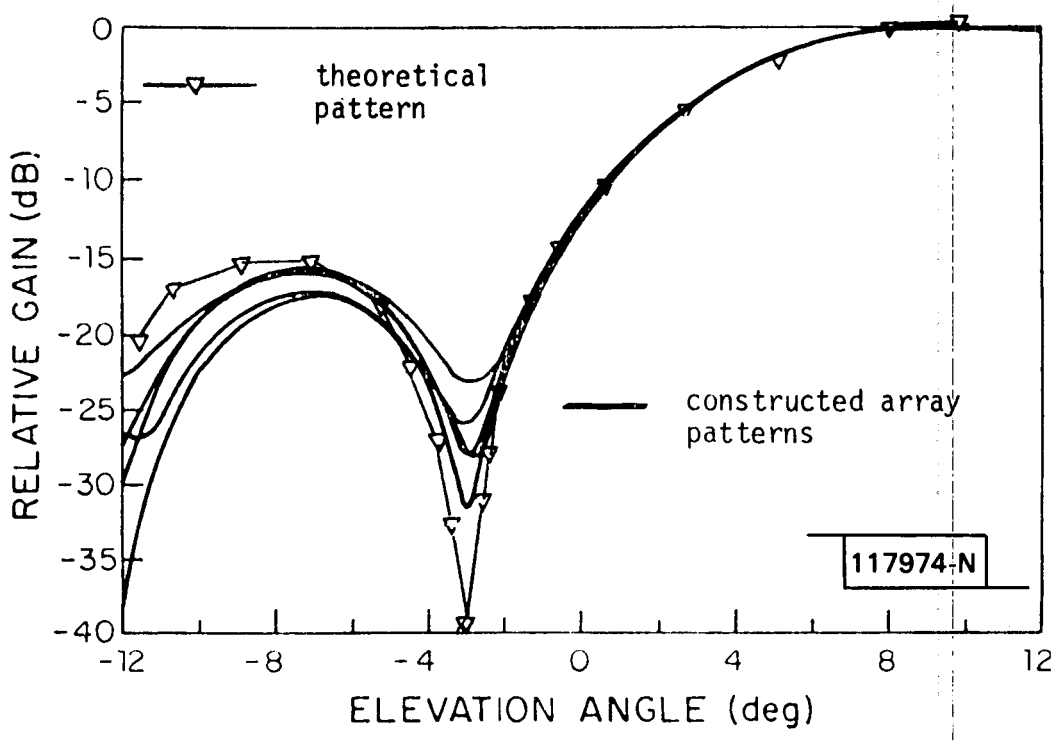


Fig.2-11(b). Patterns of five PALM elements.

and multipath. Differential phase advances by an amount $\omega_s T$ between interrogations separated by T sec when the scalloping frequency is $\omega_s$ rad/sec, and the consequent reduction in error obtained by averaging M consecutive scans is given by the averaging factor [8]

$$A(\omega_s) = \frac{\sin \frac{M\omega_s T}{2}}{M \sin \frac{\omega_s T}{2}} \qquad (2\text{-}9)$$

Because the phase behavior of DME error is not truly sinusoidal, it is more conservative to assume that the actual error improvement is the maximum of (2-9) and $1/\sqrt{M}$ (the improvement to be expected from averaging independent errors). This function is plotted vs. $f_s (=\omega_s/2\pi)$ in Fig. 2-12 for M=8 and an interrogation rate of 40 Hz. The grating lobes (points of poor motion averaging) are at multiples of 40 Hz, and the points of maximum improvement are at multiples of 5 Hz which are not harmonics of 40 Hz. In Section IV, the effects of this type of motion averaging upon DME/P sensitivity to aircraft and vehicle reflections are studied.

An informative way to look at motion averaging results is from relating the scalloping frequency to the multipath geometry. For an aircraft on centerline approach, multipath arriving at conical angle $\beta$ (relative to the A/C heading) has scalloping frequency [9]

$$f_s = \frac{v}{\lambda} (1 - \cos \beta) \qquad (2\text{-}10)$$

where v = A/C speed and $\lambda$ = wavelength. If this expression is substituted into (2-9), the averaging factor can be graphed in a polar plot showing averaging improvement as a function of arrival angle. The scalloping frequency formula inverts to give

$$\beta = \cos^{-1} \left(1 - \frac{\lambda f_s}{v}\right) \qquad (2\text{-}11)$$

$$\simeq \frac{2\lambda f_s}{v} \quad ; \quad \text{small } \beta$$

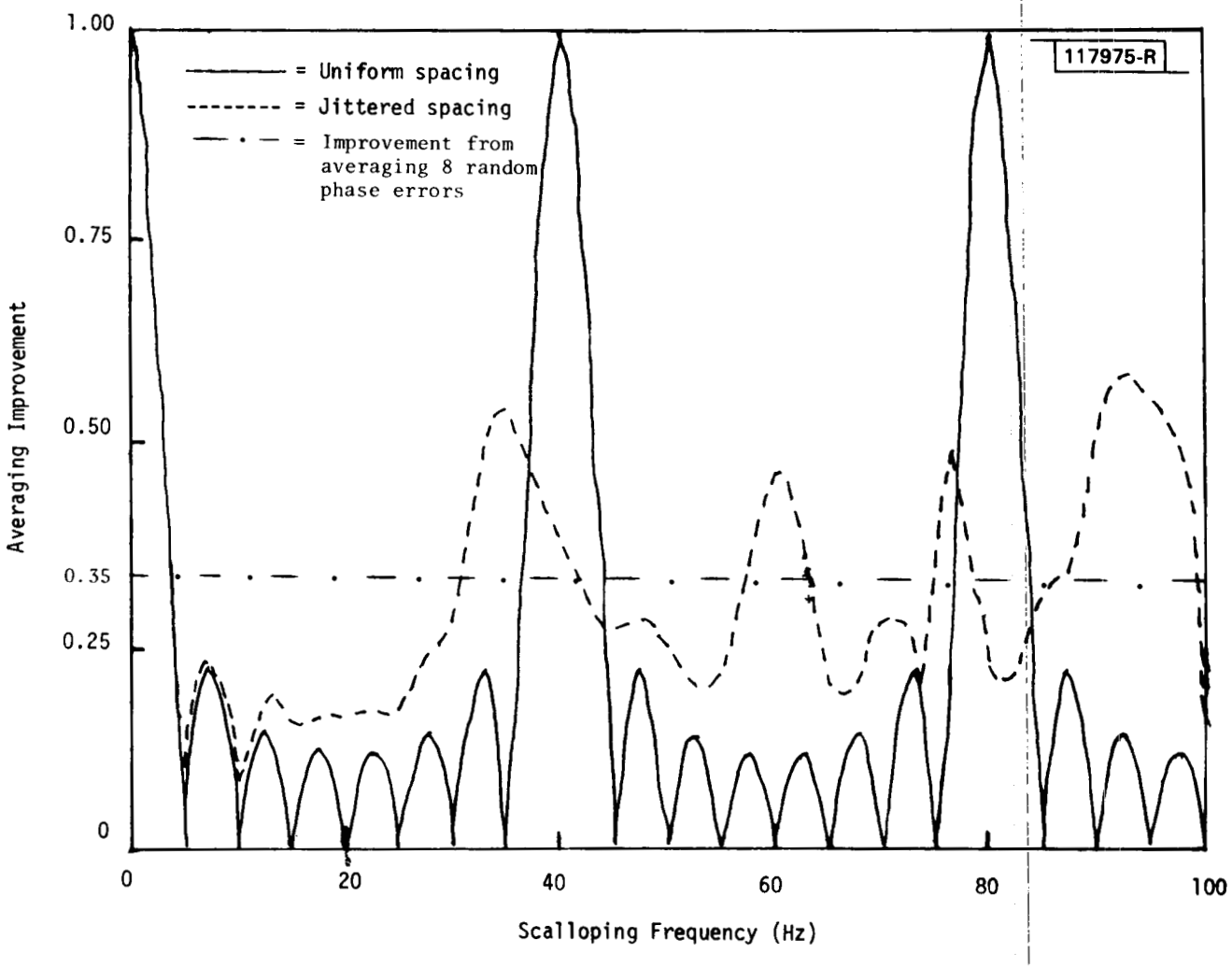


Fig.2-12. Averaging factor for uniform and jittered spacing (TRSB).

The angles at which greatest averaging improvement can be expected are those where $f_s = n/MT$, $n \neq$ multiple of M. The first grating lobe angle is 36.9° at L-band. Figure 2-13 shows these angular directions. Outside the first grating lobe, the scalloping persistance [8] may be too short for coherent averaging. Denoting by Y the distance normal to centerline to the specular point on the scatterer, motion averaging becomes ineffective at ranges (measured from the centerline projection of the specular point)

$$R >> Y \frac{2vT}{\lambda} \qquad (2\text{-}12)$$

At L-band, $2vT/\lambda = 3.16$ for our example.

Further improvement can be obtained using a non-uniformly spaced (jittered) interrogation sequence. This principle was demonstrated in the MLS Phase II EL-1 tests, and for the ICAO submission a more elaborate jitter sequence was devised which has better averaging improvement than the Phase II sequence. Figure 2-12 shows the averaging factor for one phase of the latter jitter sequence, again for 8 pulses. Although jittered pulse sequences have not been proposed for the MLS DME, it can be seen by comparing the two curves in Fig. 2-12 that jitter can substantially reduce the error in the vicinity of the grating lobes (multiples of 1/T, e.g., multiples of 40 Hz for the cases cited).

### F. Lateral Diversity

Another means of obtaining a phase change between the direct and reflected signals is to utilize spatial diversity at the ground station. Figure 2-14 illustrates the principle. Two modes of operation have been suggested [32]:

(a) simultaneous averaging of the received interrogation by N antennas and receivers, whereby N pulse reception times s are averaged to yield a starting point for the transponder delay circuit, and

(b) sequential reception/transmission, where the ordinary DME transponder is connected to an array of N antennas by a single pole N throw switch. In this case, the averaging

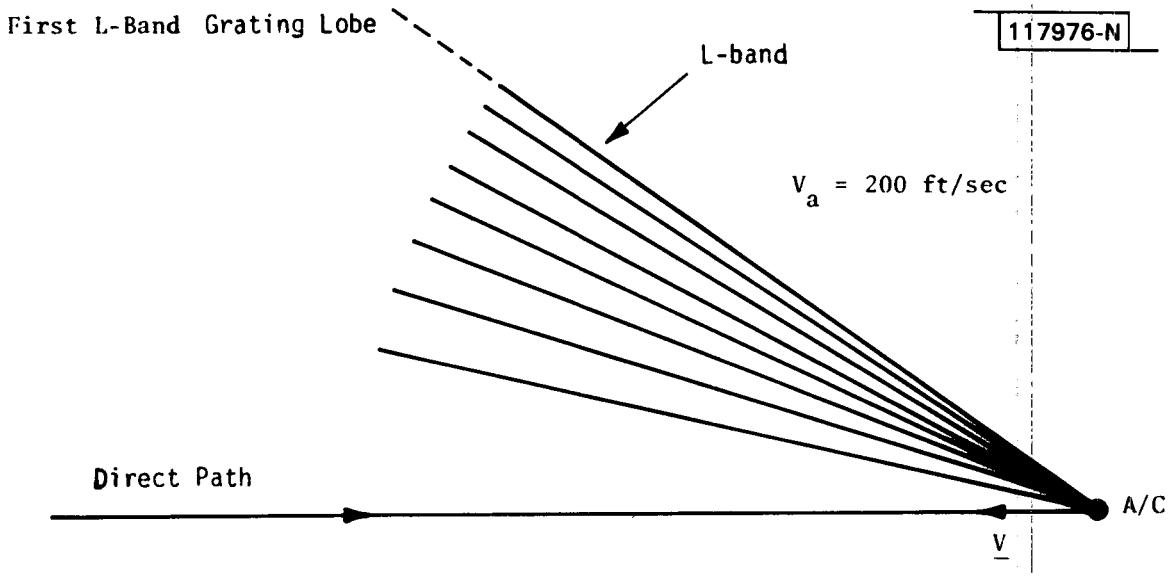


Fig.2-13. Multipath arrival directions for maximum motion averaging and first grating lobe.

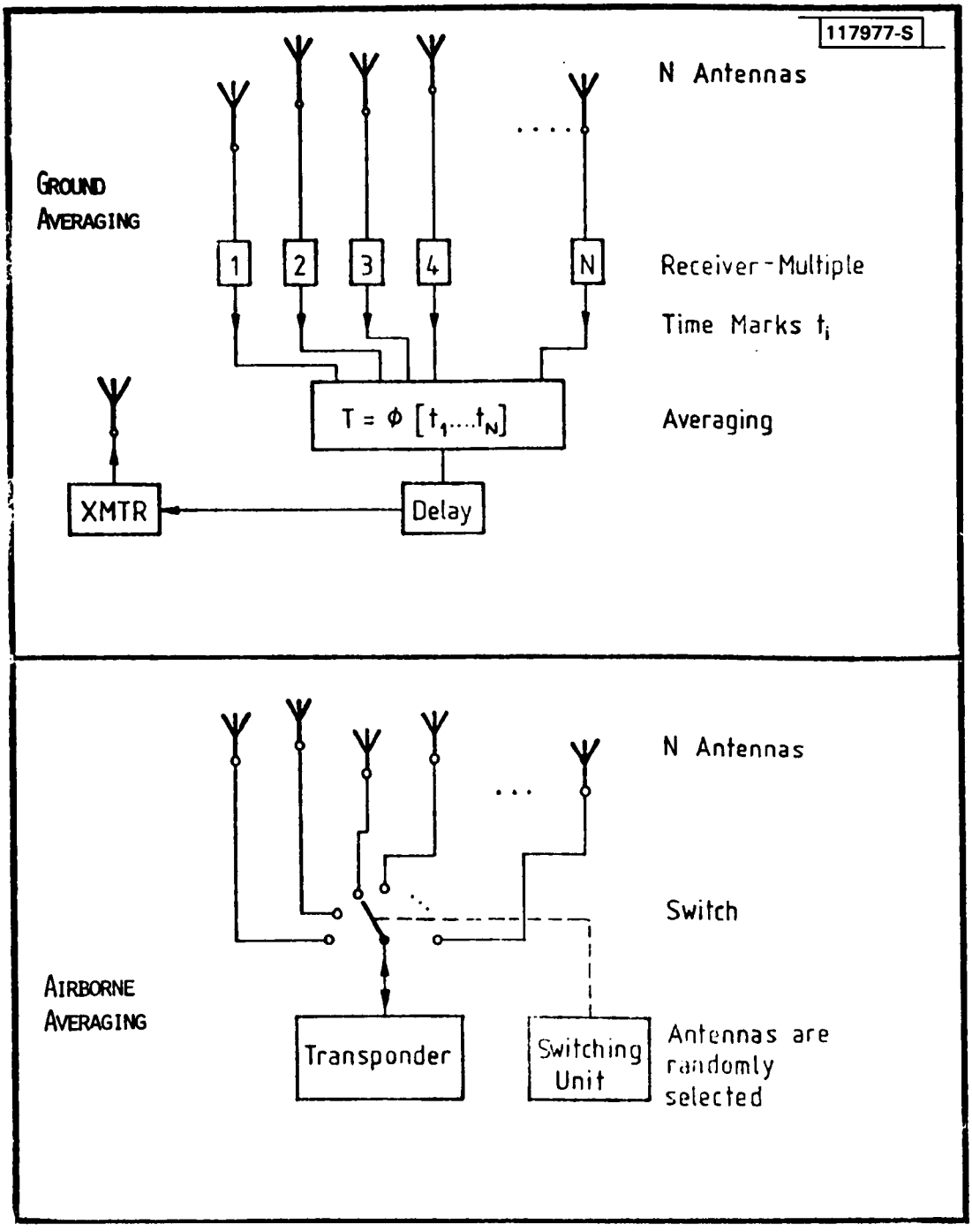


Fig.2-14. Lateral diversity DME/P transponder.

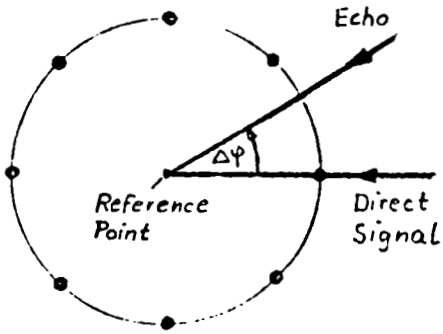


Pulse : $\cos^2$-$\cos^2$, $t_r$ = 1,5 µs
Trigger: DAC, 25 %/50%
A Antenna: 23 Elements (Example)
Diameter 3,5 λ
M/D: 0,5
τ : 0,4 µs

RF-Phase at reference point:
ψ = 0 or ψ = 180°

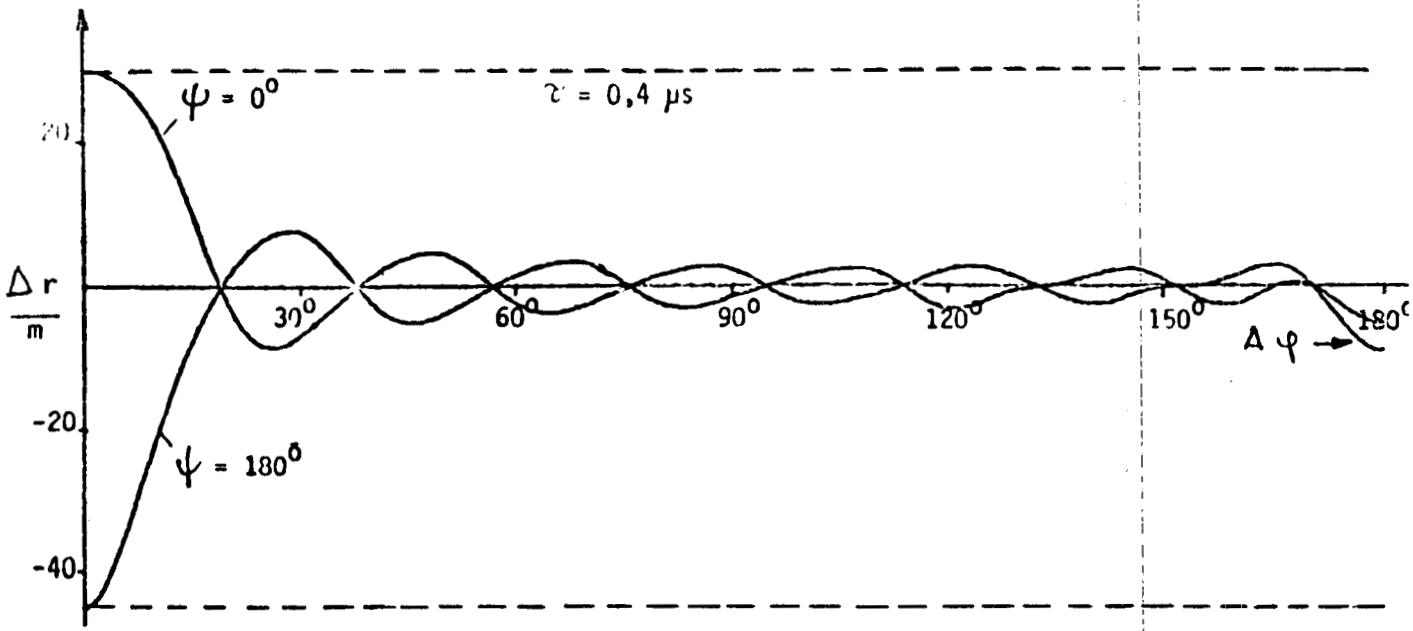


Fig.2-15. DME/P multipath error reduction via ground averaging lateral diversity (from [32]).

over phase changes is obtained by the airborne data processing.

Method (a) has the advantage of reducing the downlink error significantly on each interrogation, as shown in Fig. 2-15. Moreover, motion averaging may reduce the residual error yet further. However, the cost is high, and uplink errors are not affected. Method (b) has a much smaller cost impact and does reduce uplink errors as well. However, it:

(1) does not yield as significant an error reduction on single interrogation and

(2) acts in parallel with motion averaging.

One significant difficulty with both lateral diversity modes (and, motion averaging) is that the fractional error reduction decreases with increased M/D level ($\rho$), since the bias error typically is proportional to $\rho^2$. Consequently, in situations where improvement is most needed, the amount of improvement decreases.

G. Uplink/Downlink Error Combining

The aircraft interrogation of a ground transponder and the ground transponder reply are at different carrier frequencies which typically differ by 63 MHz. Consequently, the relative phase, $\phi$, of the multipath signal on the uplink will differ from that on the downlink by

$$\Delta\phi = 2\pi (\Delta f \ \tau + f_s \ t_r) \qquad (2\text{-}13)$$

where $\Delta f$ = uplink/down link channel frequency offset (typically 63 MHz).

$t_r$ = time interval between transmitting the interrogation and receiving a reply.

= 50 ns + 2 x aircraft to ground propagation time.

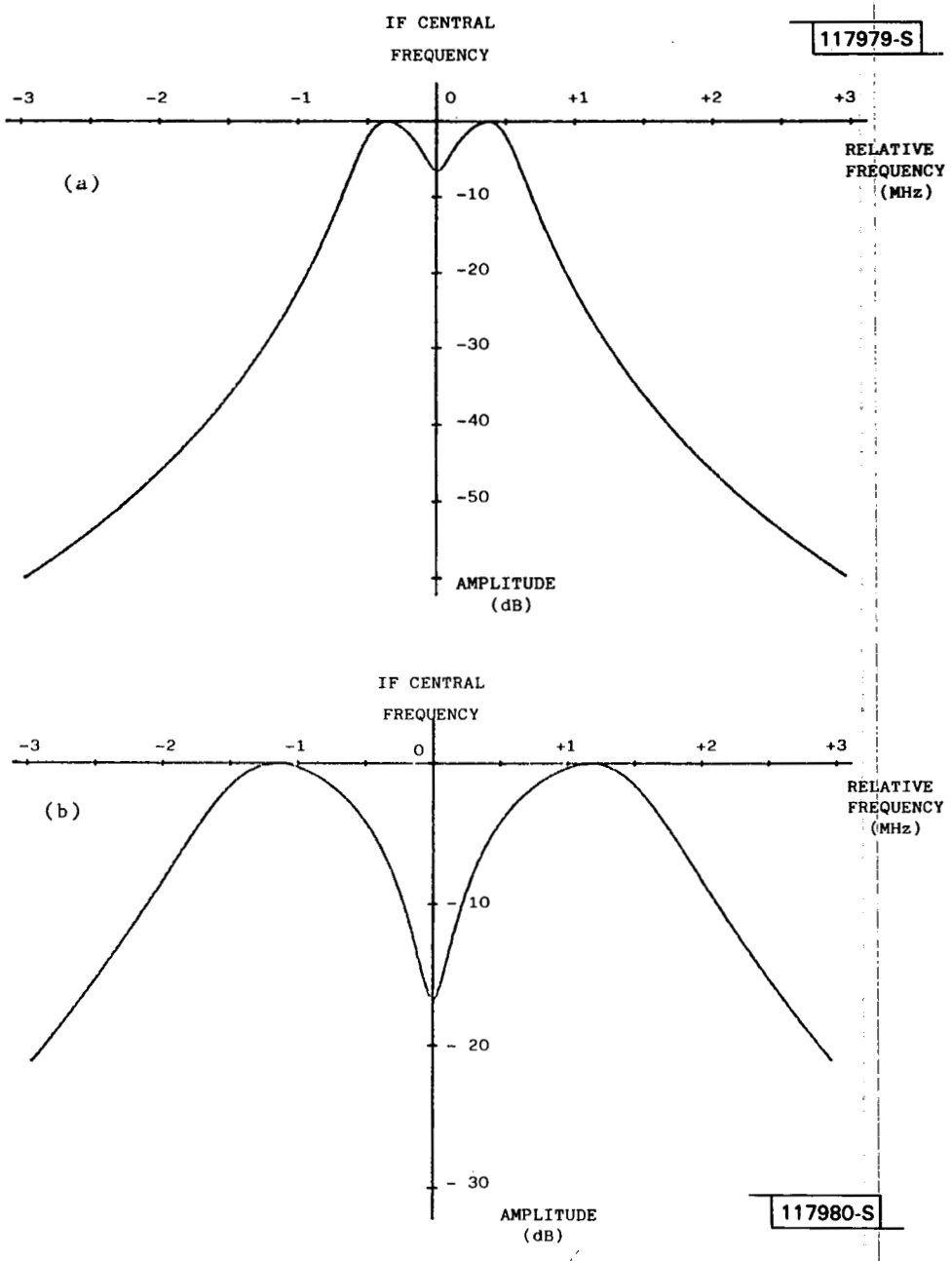


Fig.2-16. (a) Characteristic of the CTOL/STOL system receiver filter and (b) characteristic of the VTOL system receiver filter.

The error reduction due to the $f_s\ t_r$ term is neglible in virtually all situations. Consequently, we may focus our attention on the $\Delta f\tau$ term. If the M/D ratio is such that the errors are proportional to $\cos\phi$ , the resulting distance error will be changed by a factor

$$B(\tau) = \cos\ 2\pi\Delta f\tau \qquad (2\text{-}14)$$

over the one way error at a frequency midway between the uplink and downlink frequencies. This uplink/downlink error factor is periodic in $\tau$ at intervals of $1/\Delta f = 16$ ns. Since practical multipath delays are generally large multiples of this period, it is reasonable to assume that uplink/downlink error combining will on the average decrease the rms range error by $\sqrt{2}$ over that for the one way pulse reception.

H. Receiver Mismatched IF Filtering

The problem of pulse arrival time estimation in Gaussian noise alone has been a standard radar problem for years [33,35]. The received signal is passed through a matched filter and the range is estimated from the centroid of the peak filter output.

However, this procedure is <u>not</u> optimal in the presence of multipath. The standard approach to DME multipath mitigation has been to use one of the leading edge thresholding methods together with a filter which is more or less matched to the leading edge of the pulse, e.g. , a Butterworth IF filter whose bandwidth is approximately the reciprocal of the leading edge equivalent rise time.

Recently, it has been suggested by M. Gori of Italy [43] that yet further improvement in DME multipath performance can be achieved by using a receiver filter which is significantly mismatched with respect to the received pulse waveform. Figure 2-16 shows representative mismatched filters suggested for CTOL and V/STOL applications. The filter emphasis at frequencies off center frequency is intended to yield a faster pulse risetime at the filter output and hence improved multipath rejection. Figure 2-17 shows the IF filter input and output waveforms for a cos-$\cos^2$ 2 ns risetime pulse with mismatched

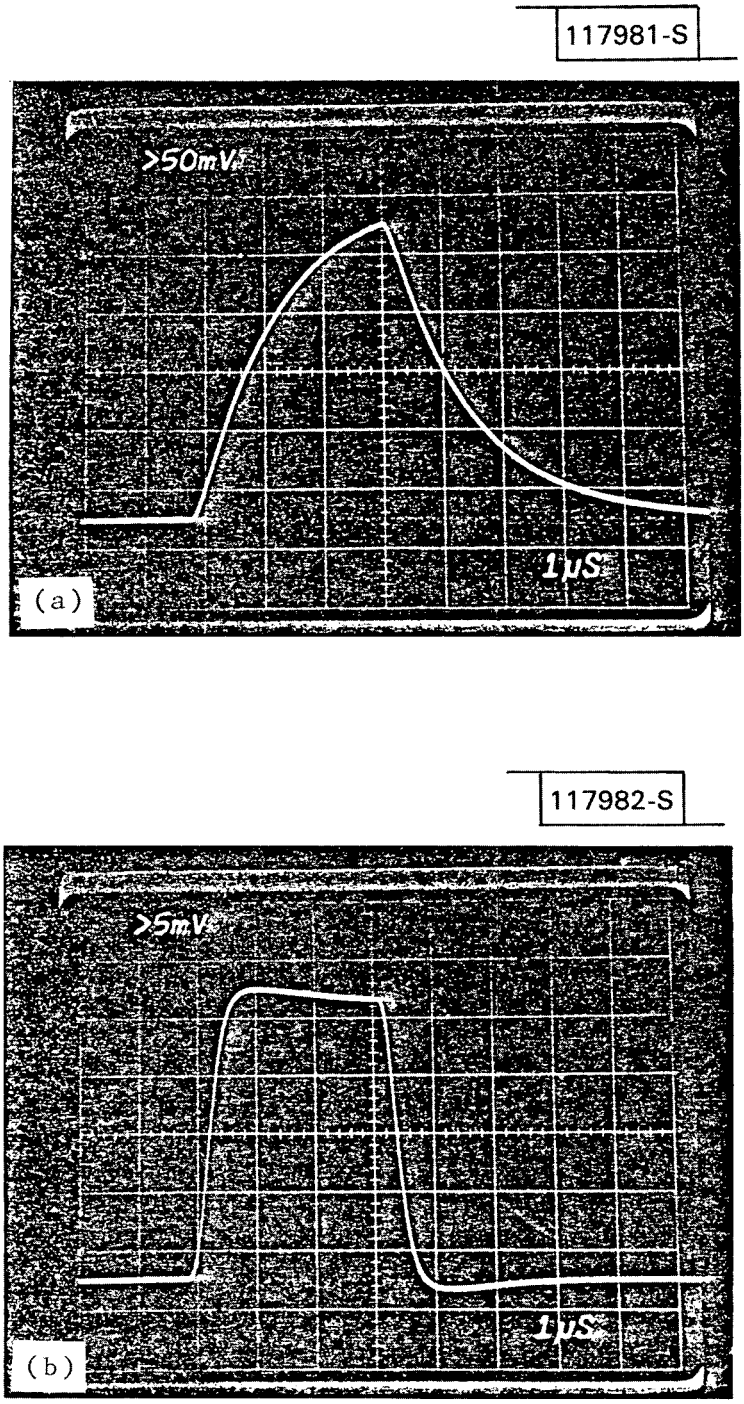


Fig.2-17. Experimental first defined pulses (from [43]): (a) transmitted and (b) received.

filter. The rise time of the pulse at the mismatched output filter is faster than that for a matched filter. This yields improved multipath performance. On the other hand, the mismatch does adversely effect performance against receiver noise and/or adjacent channel interference.

One difficulty associated with the use of a mismatched filter is the need to utilize it on all airborne DME/P receivers if it is felt that the improved performance on the interrogator reply will be required at some airport runway. By contrast, some of the other multipath reduction techniques such as centerline emphasis need only be incorporated in the ground equipment for "difficult" sites.

## III. DME/P MULTIPATH SOURCES AND CHARACTERISTICS

Figure 3-1 shows the principal multipath sources considered to date in MLS studies. Our objective in this chapter is to ascertain which sources are of greatest concern for DME/P operation and to bound the expected multipath effects.

The two principal parameters of concern here are the level ($\rho$) and time delay ($\tau$). The time delay is strictly a function of scatterer location, and can thus be characterized geometrically by ellipses of constant delay such as were shown in Fig. 1-2. The peak relative multipath level is more complicated since it represents the product of several factors:

$$\rho = \rho_{size}\, R_{eq}\, \rho_R\, \rho_r\, \rho_{sec}\, \rho_{div} \qquad (3\text{-}1)$$

where

$\rho_{size}$ = size factor

$R_{eq}$ = equivalent Fresnel reflection coefficient which takes into account the surface dielectric and conductivity

$\rho_R$ = distance factor (= direct path distance/multipath path distance)

$\rho_r$ = surface roughness factor (also, mode loss factor in case of periodically corrugated surfaces)

$\rho_{sec}$ = factor corresponding to various secondary paths involving terrain reflections as illustrated in Fig. 3-2.

$\rho_{div}$ = divergence factor for curved surfaces

Since the various factors in (3-1) are a strong function of scatterer type, one must consider each particular scatterer shown in Fig. 3-1 separately.

### A. Reflections from Terrain in Front of Transponder Array

The principal effect of these reflections is to change the effective direct signal level since the multipath delay turns out to be so small that the two pulses completely overlap. The effective direct signal is given by:

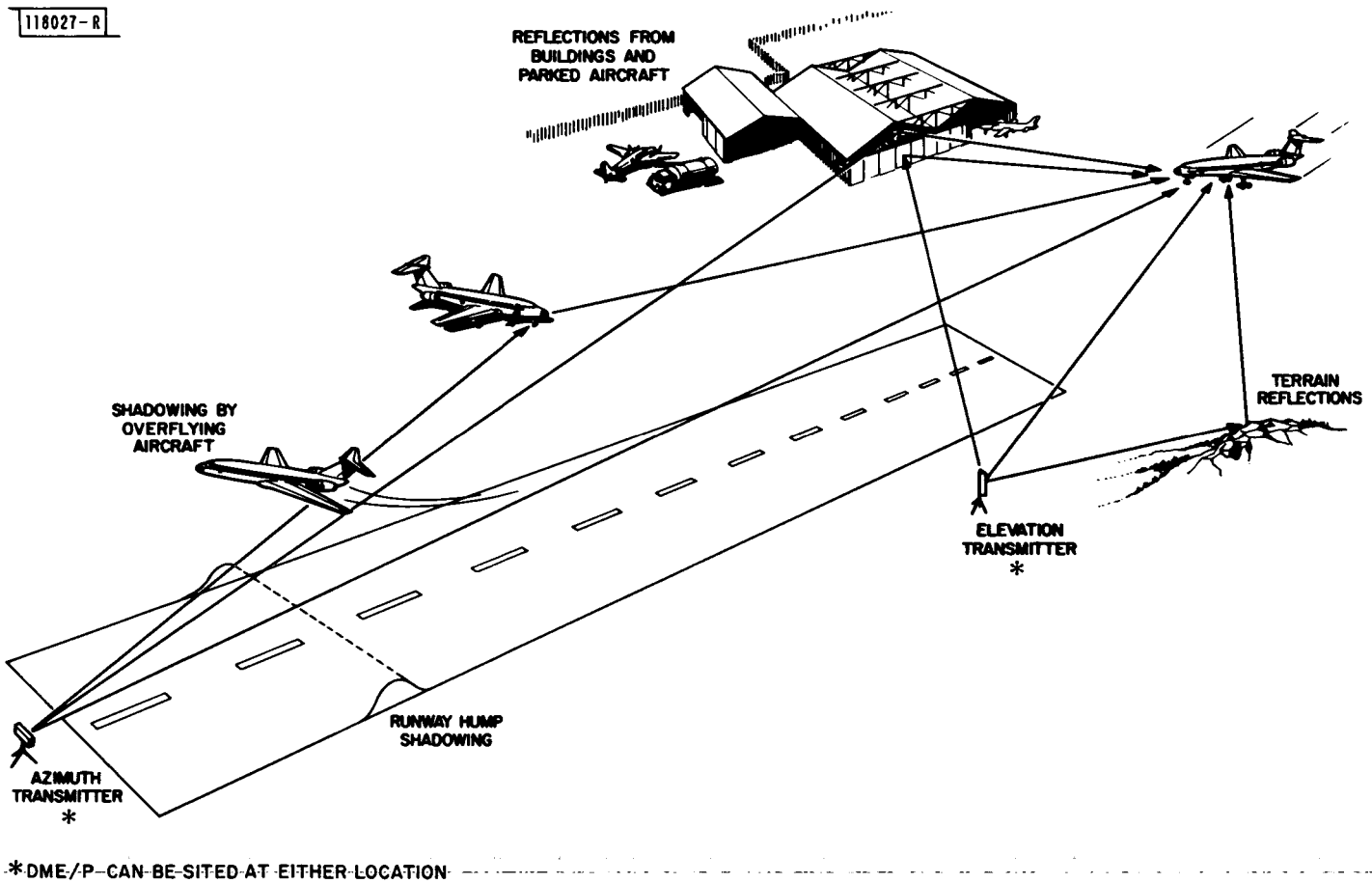


Fig.3-1. MLS multipath phenomena.

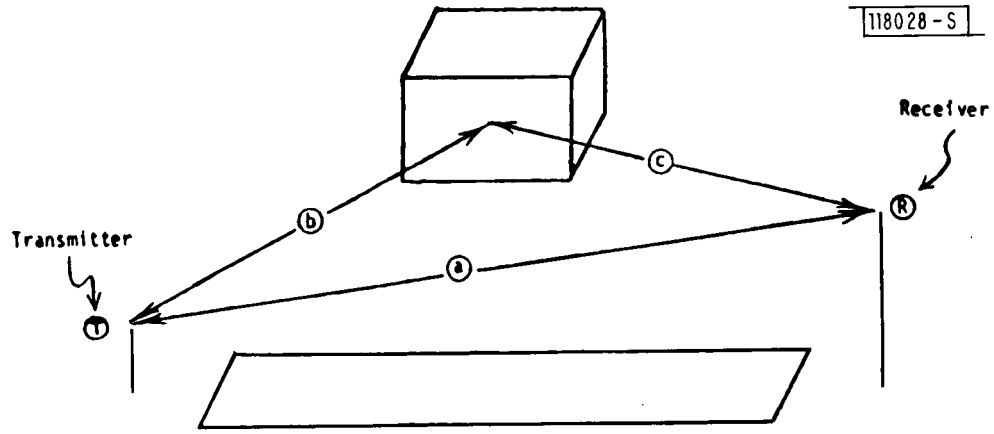


(a)

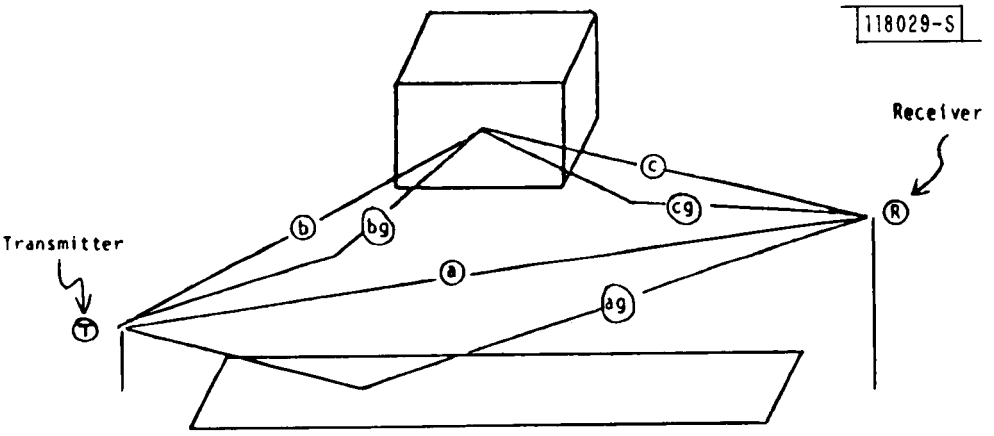


Measured "DIRECT" signal level depends on paths a and ag

Measured "MULTIPATH" signal level depends on paths b, bg, c, cg

(b)

Fig.3-2. (a) Signal paths considered in "naive" DME multipath analysis and (b) role of ground reflections in determining DME multipath/direct amplitude ratio.

$$E \cong G(\theta_1, E_1)\frac{e^{jkr_1}}{r_1} + G(\theta_2, E_2)\rho_g\frac{e^{j(kr_2 + j\phi)}}{r_2} \qquad (3\text{-}2)$$

where $r_1$ is the direct path length, $r_2$ the ground reflected path length; k, the wavenumber equals $2\pi/\lambda$, where $\lambda$ is the wavelength; $\rho_g$ is the effective terrain reflection coefficient, $\phi$ the rf phase change due to reflection and $G(\theta_i, E_i)$ the antenna (voltage) gain at azimuth $\theta_i$ and elevation $E_i$.

Using the standard approximations we can show that the received power is:

$$P_r \cong \frac{\lambda^2 G^2(\theta_1,E_1)\ P_o}{(4\pi\ r_1)^2}\ [1 + \rho_o^2 + 2\rho_o \cos\left(\frac{2\pi\Delta r}{\lambda} + \phi\right)] \qquad (3\text{-}3)$$

where $\rho_o$ is the effective reflection coefficient $[\rho G(\theta_2,\phi_2)/G(\theta_1,\phi_1)]$ and $\Delta r$ is the range difference $(r_2-r_1)$. It is easily shown that

$$\Delta r = c\tau \approx \frac{2z_1 z_2}{r_1}$$

where $z_2$ is the transmitter height and $z_1$ the receiver height. The term $P_o$ is the power of the transmitter. The term in the brackets is usually termed the pattern propagation factor . When $z_1$ and $z_2 << r_1$, we have the case most often found in the MLS DME environment when near runway threshold. Furthermore, in this case $\rho_o \to 1.0^*$ and $\phi \to \pi$ because the grazing angle is small, so that

$$F \cong 2 - 2\cos\left(\frac{4\pi\ z_1 z_2}{\lambda r_1}\right) \approx 0.5\left(\frac{4\pi z_1 z_2}{\lambda r_1}\right)^2 .$$

Thus, for the transmitter and the receiver both at low altitudes, the received power becomes

---

*As will be discussed below.

$$P_r = G^2(\theta_1, E_1) P_o \frac{(z_1 z_2)^2}{r_1^4} \qquad (3\text{-}4)$$

i.e., $P_r$ depends on $r_1^{-4}$. This is the statement of the $R^4$ law in propagation theory. At this point, the effective direct signal amplitude with respect to (wrt) the free space direct signal level is

$$D = \sqrt{F} = 4\pi\, z_1 z_2 / \lambda r_1 \qquad (3\text{-}5)$$

As the aircraft nears the runway $z_2 \to 0$, and the null becomes much deeper. These low angle relationships [(3-4) and (3-5)] are reasonably accurate for

$$\Delta r < \lambda/8$$

corresponding to an aircraft height

$$z_2 < \frac{\lambda}{16} \frac{r_1}{h_1} \qquad (3\text{-}6)$$

Assuming $r_1 \sim 16{,}000$ feet and a DME phase center height $h_1 \sim 10$ feet at L-band ($\lambda = 1$ foot), equation (3-6) yields $z_2 < 100$ feet, which shows that the ground reflection null is of greatest concern at and below the cat II decision height. Next, we consider the possibility that vertical polarization and/or ground antenna elevation pattern shaping will yield $\rho_o \ll 1$. These two factors are related in that over flat terrain:

$E_1 - E_2 \triangleq \Delta$ difference in elevation angle between direct and reflected signals

$\sim$ grazing angle of ground reflection

$\sim \frac{z_1+z_2}{r_1} \leq 0.04°$ for the numerical parameters above

At such a low angle, the terrain reflection coefficient $\rho_g$ is essentially unity (even for vertical polarization) and the ground antenna vertical pattern

Details taken from FAA Order 6750.16A

118030-R

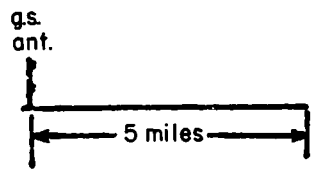


SITE #1: IDEAL.

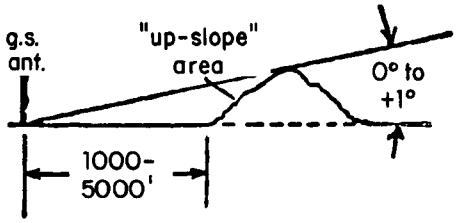


SITE #2: TERRAIN SLOPES UPWARD ABOVE INITIAL TERRAIN PROJECTED.

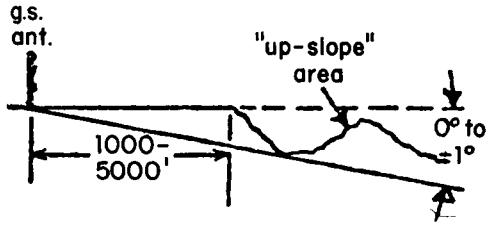


SITE #3: TERRAIN SLOPES UPWARD BELOW INITIAL TERRAIN PROJECTED.

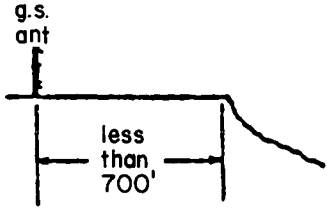


SITE #4: NO UP-SLOPE AREA: LIMITED TERRAIN IN FRONT OF ARRAY.

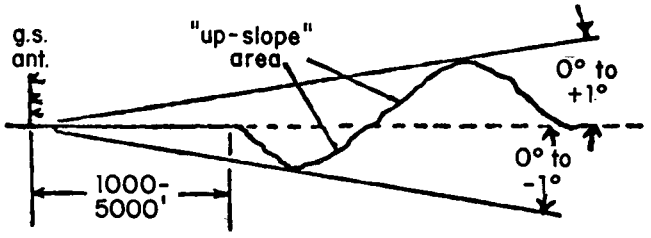


SITE #5: COMBINATION OF SITES #2 AND 3.

| | SITE #1 | SITE #2 | SITE #3 | SITE #4 | SITE #5 |
|---|---|---|---|---|---|
| PERCENT OF TOTAL SITES | 5% | 20% | 15% | 15% | 45% |

Fig.3-3. Expected siting conditions for glide slope systems.

discrimination is very small ($\lesssim$ 1.2 dB for a 3 dB/degree pattern slope at the horizon).

At L-band, the $\tau$ corresponding to $\lambda/8$ is on the order of 0.1 nsec. We see from Figs. 2-3 to 2-7 that the corresponding error is quite small. To summarize, the effective DME/P direct signal level is reduced significantly as the aircraft nears the threshold with the greatest loss occurring at the lowest heights. However, the error directly introduced by this terrain reflection is very small.

B. Reflections from Terrain in the Approach Sector

Significant reflections from terrain along the extended runway centerline can arise only when the terrain is visible from the transponder site. This virtually necessitates that the terrain be upsloping as illustrated by sites #2 and #3 in Fig. 3-3. The L-band multipath levels from such rising terrain can exceed -6 dB [27, 44].

However, one must also consider the time delays. If the terrain is gradually upsloping (e.g., local slopes of 1°-2°), the delays will be quite small (< 5 nsec at the category 1 decision height).* More abrupt slopes (e.g., 20°) will yield larger $\tau$ (e.g., 100-200 nsec at the category 1 decision height), but should have significantly lower levels due to the reduced terrain reflectivity and depolarization.

In either case, the errors due to such terrain will disappear as the aircraft nears the runway threshold since the upsloping terrain will then be to the rear of the aircraft.

Diffuse reflections from rough terrain to the side of the runway could have a wide variety of multipath delays (recall Fig. 1-2). The propagation models to data for such multipath suggest that the principal contributions must come from the so called "glistening" surface which is in front of the array as shown in Fig. 3-4 [10,17,36]. The diffuse reflection power from a

---

* By the same token, runways which upslope in the vicinity of the threshold will generate reflection multipath with a small $\tau$.

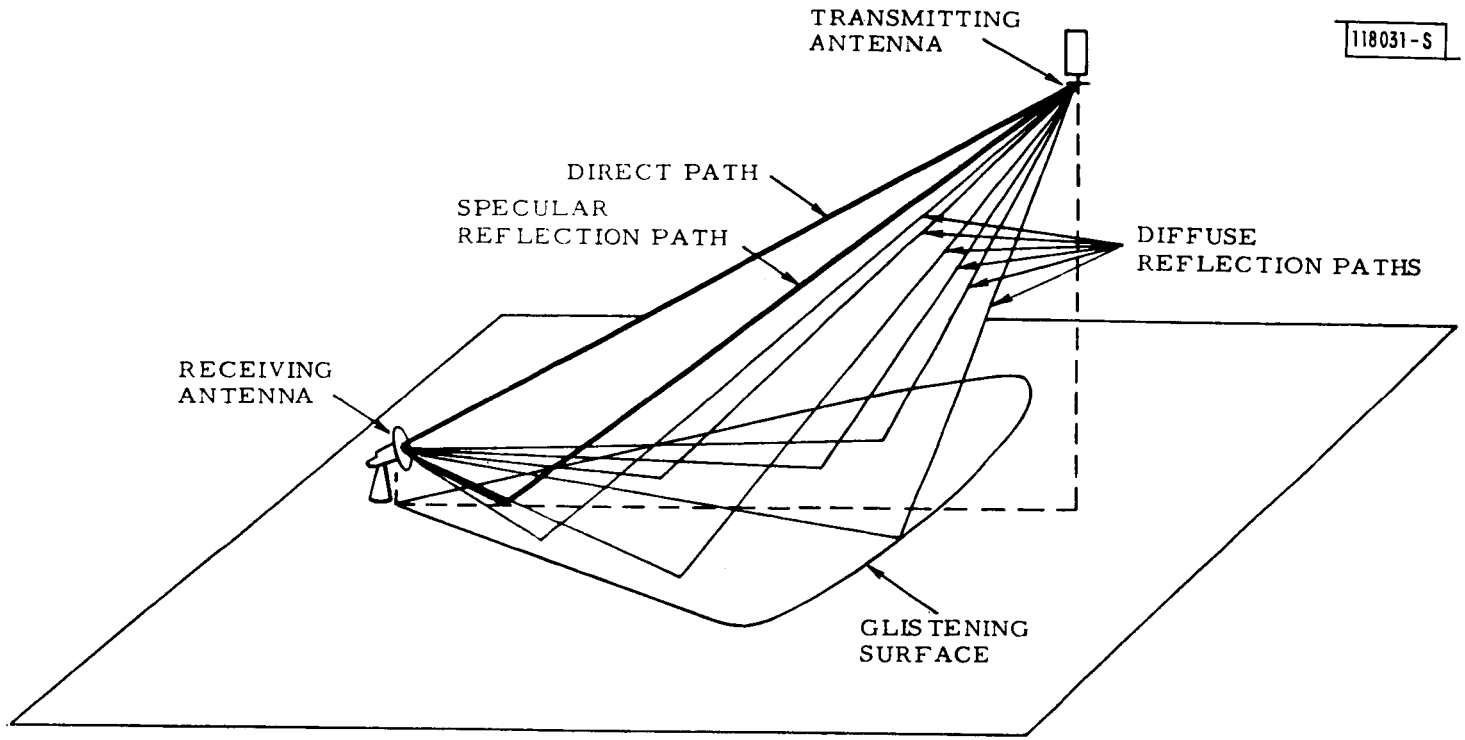


Fig.3-4. Multipath propagation over rough surfaces.

Gaussian distributed randomly rough (in two dimensions) surface depends on the surface roughness as indicated in Fig. 3-5. Also shown in Fig. 3-5 is a typical glistening surface distribution in azimuth and elevation angle as seen from the ground antenna. We see that much of the diffuse power appears near the horizon. It must be noted that the homogeneous Gaussian randomly rough surface model assumed in most diffuse multipath studies is probably unrealistic for most airport environments* due to:

(1) marked differences in terrain characteristics as a function of range

(2) shadowing by intervening terrain and/or

(3) absorption by vegetation

Thus, experimental measurements of diffuse multipath in representative environments were essential.

Some high time resolution measurements of diffuse multipath at X band had been made by Raytheon at Fort Devens, Mass. [36]. The measured data for elevation angles in the range 0.5° to 2.0° shows low level multipath (e.g., less than -25 dB M/D ratio) with delays typically less than 6 ns. Such multipath would not be a significant threat to DME/P. Similarly, significant diffuse multipath has not been evident in the high angular resolution C- and L-band angular spectrum measurements made to date by Lincoln [27,44].

However recent DME/P field measurements [30] suggest that a substantial error component may be due to diffuse reflections from irregular terrain and/or small objects (e.g., posts, signs, etc.) on the airport surface. Consequently, a set of experimental measurements were carried out at S-band (3 GHz) on two runways at L.G. Hanscom airport (Bedford, Mass). Results of these measurements are presented in Chapter V and Appendix C.

C. Shadowing by Overflying or Taxiing Aircraft

The diffraction signals which arise when the line of sight is blocked (or

---

*With the exception of approaches over a water body (e.g., as in helicopter operations from oil platforms in the ocean).

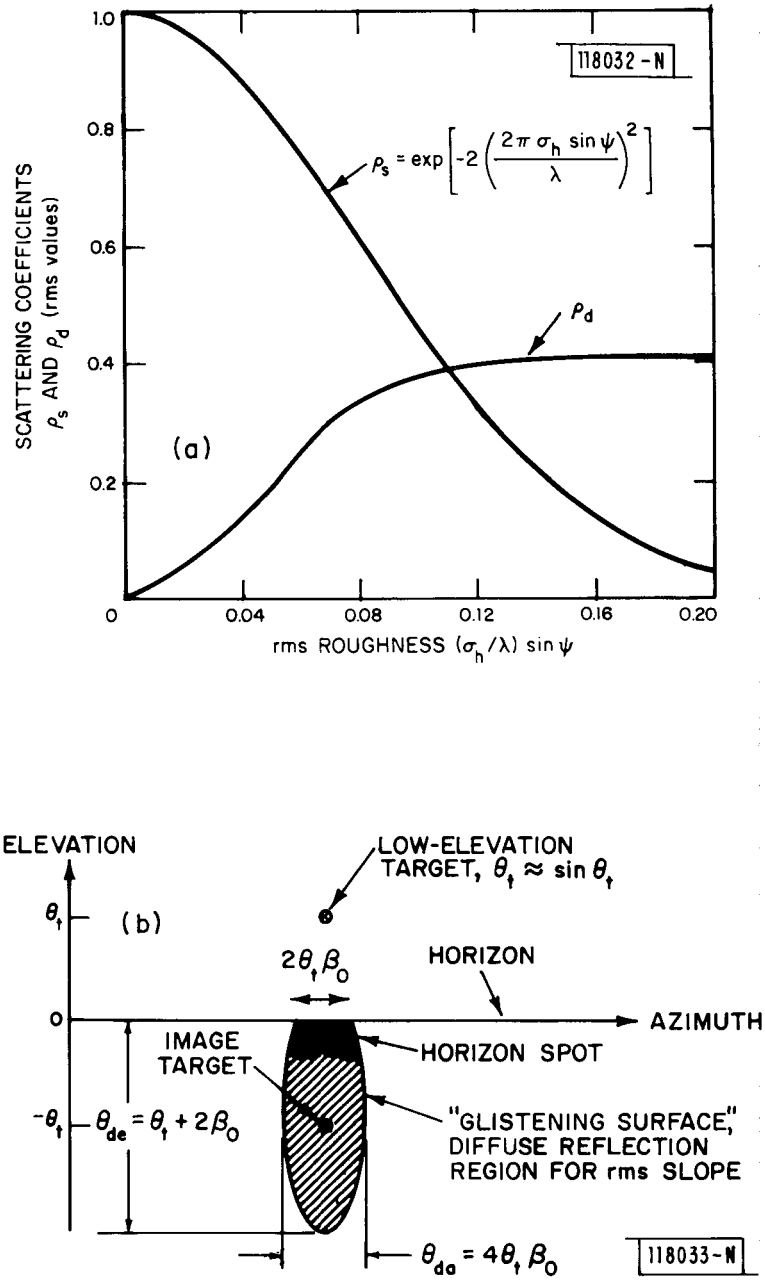


Fig.3-5. Diffuse multipath level and spatial distribution: (a) specular and diffuse scattering coefficient vs. roughness factor and (b) angular extent of glistening surface for rough surface scattering.

nearly blocked) by an intervening obstacle (e.g., an overflying or taxiing aircraft) can have levels comparable to that of the direct signal [17, 27]. However, the associated multipath delays are typically less than 2 wavelengths (i.e., 2 ns). Consequently, the errors directly induced by shadowing will be very small.

D. Reflections from Parked or Taxiing Aircraft

Parked or taxiing aircraft will be found at locations well inside the delay contours of concern (e.g., $\tau < 300$ nsec). Consequently, one must consider the reflected signals from such aircraft.

Several of the factors in eq. (3-1) have worst case values:

| | |
|---|---|
| $\rho_{size} \sim 1$ | aircraft fuselages are long and tail fins high, especially on wide body aircraft |
| Req $\rho_r \sim 1$ | the reflecting surface is smooth metal |
| $\rho_R \sim 1$ | aircraft are near the runway |

Fortunately, the curvature of the aircraft surfaces will yield a divergence factor ($\rho_{div}$) which is significantly less (e.g., -10 dB) than unity. Although experimental measurements of aircraft reflectivity at L-band were not carried out as a part of the MLS propagation validation, the physical mechanisms are such that L-band levels (ignoring secondary paths) should be comparable to or smaller than the C-band levels (which were experimentally validated [17]).

The terrain reflection secondary paths can in some circumstances increase the effective aircraft reflection levels. This typically occurs when the fuselage is higher then the line of sight corresponding to the same X-coordinate, i.e., when the scattering aircraft is near the transponder or near a landing aircraft. Otherwise, the secondary paths serve to reduce the effective levels.

In the next section, we present some simulation results for the expected error due to reflections from widebody aircraft as a function of the widebody aircraft location. These results include the effects of divergence and secondary reflection effects.

E. Reflections from Buildings

Reflections from buildings are viewed as the principal multipath threat to DME/P operation due to the potentially high levels and time durations of the multipath. If a fast rise time pulse (e.g., 100 nsec) were used for DME/P together with delay and compare thresholding, few buildings would be of concern since the corresponding $\tau$ values (see Fig. 1-2) typically are greater than the upper limit of the corresponding error region ($\sim$ 40 ns). Unfortunately, the rise times compatible with the ICAO Annex 10 specifications will be affected by multipath with delays as great as 200-400 nsec. The corresponding ellipses include a significant portion of the airport region in which buildings may be found. Thus, we must consider the expected building reflection amplitudes.

Size factor constraints require that the building subtend a significant fraction of a Fresnel zone about the specular point. For a building some R feet from the transponder or landing aircraft, the Fresnel zone extents are approximately $\sqrt{R}$ feet vertically and $\sqrt{R}/\sin \theta g$ feet horizontally where $\theta g$ is the grazing angle. Thus, for R $\sim$ 2500 feet, and $\theta g = 10°$, we are concerned about building heights on the order of 50 feet and widths of 290 feet. These values correspond to typical hangars, but not to small office buildings or vehicle shelters.

The product Req $\rho_r \rho_{div}$ is likely to be near unity since the walls of most large airport buildings are corrugated metal with a corrugation period $< \lambda$ [29]. Such buildings scatter much like perfectly smooth metal. For building reflections where $\tau$ is of concern to PDME, $\rho_R$ (= $1 + c\tau/r_1$) is essentially unity.

The principal uncertainties associated with the building reflection level are concerned with blockage of the reflections by intervening obstacles (e.g., fences, parked aircraft or small structures) and the secondary paths associated with ground reflections. Statistics on blockage by intervening obstacles is not available and probably would have to be assessed on a case by case basis.

The influence of the secondary ground reflection paths is amenable to a more quantitative analysis. The various paths involving ground bounces can be related to the canonical problem shown in Fig. 3-4 by the use of appropriately located image transmitters and/or receivers (see Chapter III in Ref. [17]). From Fig. 3-6 we may write the received multipath signal amplitude as:

$$M_o \approx \frac{e^{jk(r_1 + r_2)}}{(r_1 + r_2)} \rho_f \rho_{size} ( H, W, \underline{r}_B) \qquad (3\text{-}7)$$

where

$\rho_f$ = effective reflection coefficient of building surface material

$\rho_{size}$ = building size factor which depends on building size, orientation and specular reflection point location (= 1 for infinitely large building)

H,W = building height and width

$\underline{r}_B$ = denotes transmitter-building-receiver geometry

For the case of the specular point located at the building midpoint, the building size factor can generally be written as a product of height and width factors

$$\rho_{size} = K\, A(W)\, B(H,z_s) \qquad (3\text{-}8)$$

where

$A(W)$ = width factor = $F(\tilde{W}/2) - F(-\tilde{W}/2)$

$B(H,z_s)$ = height factor = $F(\tilde{H} - \tilde{z}_s) - F(-\tilde{z}_s)$

F = Fresnel integral

K = normalizing constant

$\tilde{W}$, $\tilde{H}$ = projected building width and height (in Fresnel zone radii)

$\tilde{z}_s$ = specular point height on an infinite plane coplanar with building wall (in Fresnel zone radii)

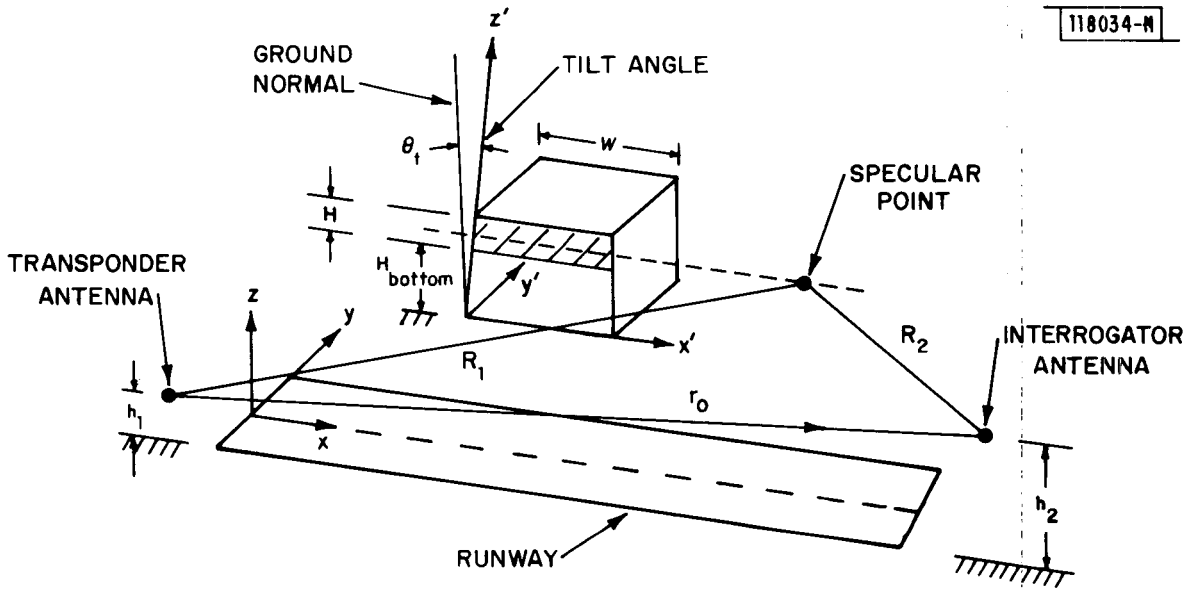


Fig.3-6. Configuration used to determine multipath parameters due to scattering from building.

For a transmitter (actual or image) at height $h_1$ and receiver (actual or image) at height $h_2$, it is easy to show that the specular point height is given by

$$z_s = \frac{r_1}{r_1+r_2} h_2 + \frac{r_2}{r_1+r_2} h_1 \qquad (3\text{-}9)$$

Let us now consider the case of flat terrain and no transmitter antenna directivity. In this case, the net received multipath signal can be shown to be

$$M_{eff} \sim \{B_{XOR} + \rho_g^2 B_{XGOGR} - \rho_g e^{jk\Delta r_m}[B_{XGOR}+B_{XOGR}]\}\rho_f A(W) \frac{e^{jk(r_1+r_2)}}{(r_1+r_2)} \qquad (3\text{-}10)$$

where

$B_{XOR}$ = height factor for path b-c in Fig. 3-2 = $B(H,z_{s1})$

$B_{XGOGR}$ = height factor for path bg-cg in Fig. 3-2 = $B(H,-z_{s1})$

$B_{XGOR}$ = height factor for path bg-c in Fig. 3-2 = $B(H,z_{s2})$

$B_{XOGR}$ = height factor for path b-cg in Fig. 3-2 = $B(H,-z_{s2})$

$$z_{s1} = \frac{r_1}{r_1+r_2} h_r + \frac{r_2}{r_1+r_2} h_t$$

$$z_{s2} = -\frac{r_1}{r_1+r_2} h_r + \frac{r_2}{r_1+r_2} h_t$$

$$\Delta r_m = 2h_t h_r/(r_1+r_2)$$

$h_t, h_r$ = actual transmitter and receiver heights

$\rho_g$ = terrain reflection coefficient magnitude (reflection coefficient phase assumed to be 180°)

We note that the XGOR and XOGR terms cancel the XOR and XGOGR terms as $\Delta r_m \to 0$.

If the factors $B_{XOR}$, $B_{XOGR}$, and $B_{XGOGR}$ were all approximately equal, then as the aircraft approached the ground $\rho_g \to 1$ and

$$|M_{eff}| \rightarrow \frac{4\pi\ h_t\ h_r}{(r_1 + r_2)}\ M_o \qquad (3\text{-}11)$$

which is of the same form as eq. (3-5), i.e., the effective multipath level would decrease in a manner similar to that of the effective direct signal.

However, since the specular point heights are different, the various B terms are <u>not</u> equal (except when $h_r = 0$) and the effective multipath signal does not decrease near the ground as suggested by eq. (3-11). The exact decrease is a complicated function of the particular values of H and $z_{si}$; and, one must take into account the ground antenna elevation pattern. Thus, the most straight-forward approach is to simply compute the received levels for relevant geometries and building sizes. This is done in the next section, where it is shown that in a number of cases the effective multipath level exceeds the effective direct signal level due to the interactions between the B terms.

## IV. SIMULATION STUDIES OF DME/P MULTIPATH EFFECTS

In this section, we summarize the results of various simulation studies to assess the DME/P multipath environment. The first two sections are concerned with reflection effects from aircraft, surface vehicles, and buildings, with the principal objective being to locate the "worst case" regions for such scatterers on the airport surface. The third section describes simulation results for two scenarios which were designed to explore DME/P behavior in the presence of high level multipath with delays less than 300 ns.

### A. Reflections from Aircraft and Surface Vehicles

In the preceding section, we noted that aircraft and surface vehicles can commonly be found within the delay contours of concern for current DME/P pulse waveform/signal processing proposals. The approach used here was to consider the worst case error due to surface vehicles (modeled as 6m wide by 5m high rectangular plates) and taxiing wide body aircraft (B747) as a function of the scatterer location as was done earlier in assessing TRSB azimuth/elevation sensitive areas [31].

Briefly, the program calculates the worst case error which can be caused by a given scatterer as it is moved over a grid of points in the plane of the runway and plots contours of constant error. At each point, the obstacle is oriented for specular (i.e., maximum) reflection. The multipath calculations are made by the appropriate programs in the full Lincoln Laboratory MLS simulation [17]. The results are substituted into one of the formulas given in Appendix A for the peak error computation*.

In all cases to be considered, plots of peak error contours (in ft) are shown for a landing aircraft over threshold on a 10,000 ft runway. The

---

* The WGM cos - $\cos^2$ waveform /DAC results are based on a lookup table derived from simulation results which account for IF filter effects.

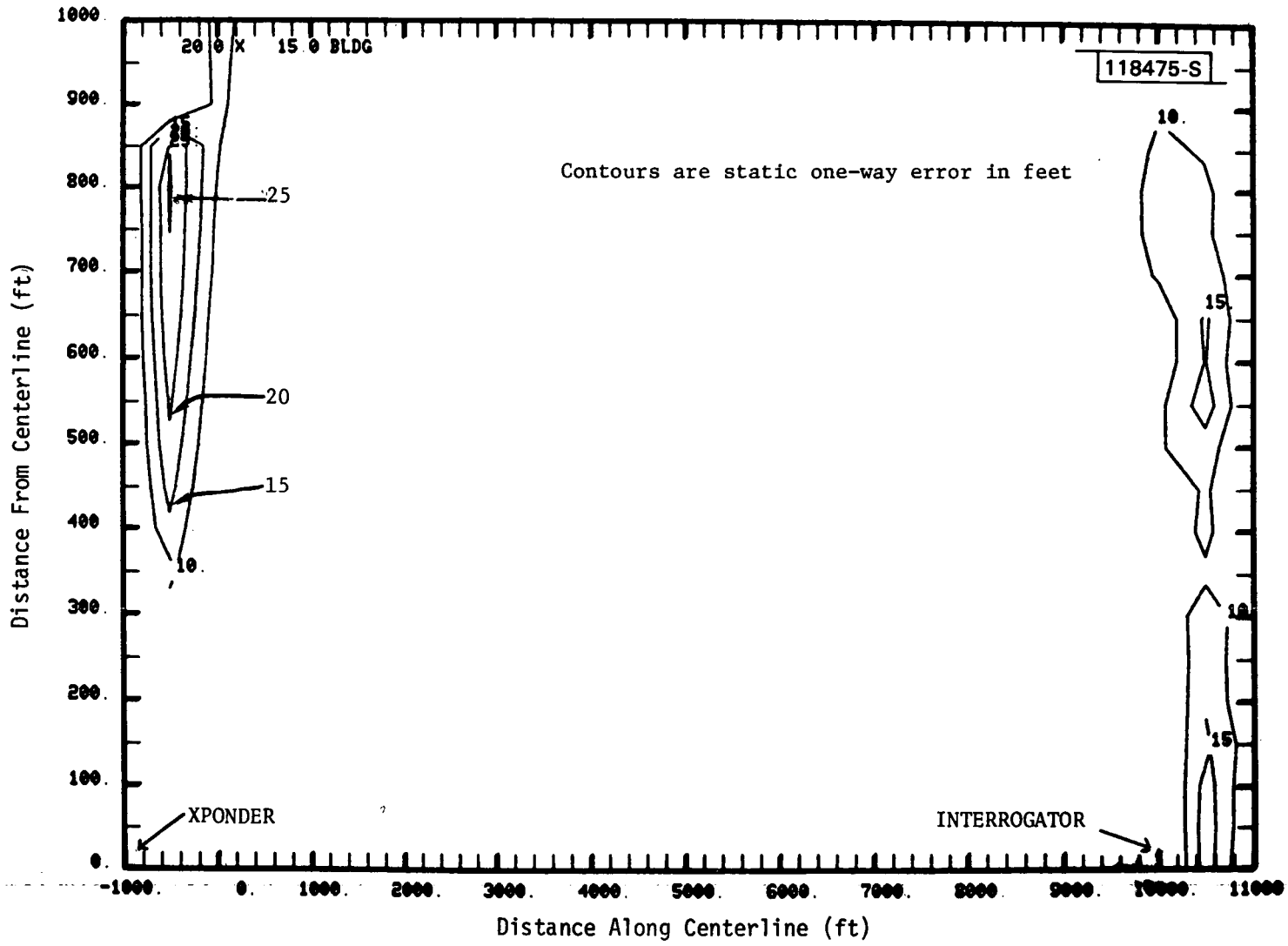


Fig.4-1. Present-day L-band DME waveform/real time thresholding receiver: surface vehicle reflections.

transponder is 1000 or 2000 ft behind the runway stop end and has a phase center height of 10 or 30 ft.

### 1. Present-Day L-Band DME Waveform/Real Time Thresholding

Figure 4-1 shows static uplink (or downlink) error contours for an interrogator at the runway threshold for the 10 ft. height/1000 ft. back transponder siting using the current ICAO Gaussian waveform and a real time (-6 dB) thresholding (RTT) receiver when the scatterer is a "surface vehicle". The largest error* observed is 25 ft, well within tolerance of all but the most stringent criterion. No motion averaging or aircraft antenna directivity is needed to decrease the error. If a delay-and-compare (DAC) receiver were used, the errors would have been even smaller, since the DAC errors are approximately 1/2 those of the RTT receiver for the delays of concern here.

Reflections from a B747 could pose a more severe threat to this system, as Fig. 4-2 indicates. At the transponder end, the threat locations are roughly 45° from centerline and can be reduced by the use of centerline emphasis transponder antennas. At the other end, the threats are at least 45° from the nose. For these threat locations near the threshold, Fig. 4-3 shows that motion averaging provides a substantial reduction in the error.

If a delay-and-compare receiver were utilized here, the errors for aircraft near the transponder would be significantly reduced (e.g., by a factor of 2 or 3) as would the errors near the interrogator corresponding to scattering aircraft locations > 300 feet from the (extended) runway centerline.

---

* Error here is the one way timing error converted to feet. This is also the peak distance error in feet.

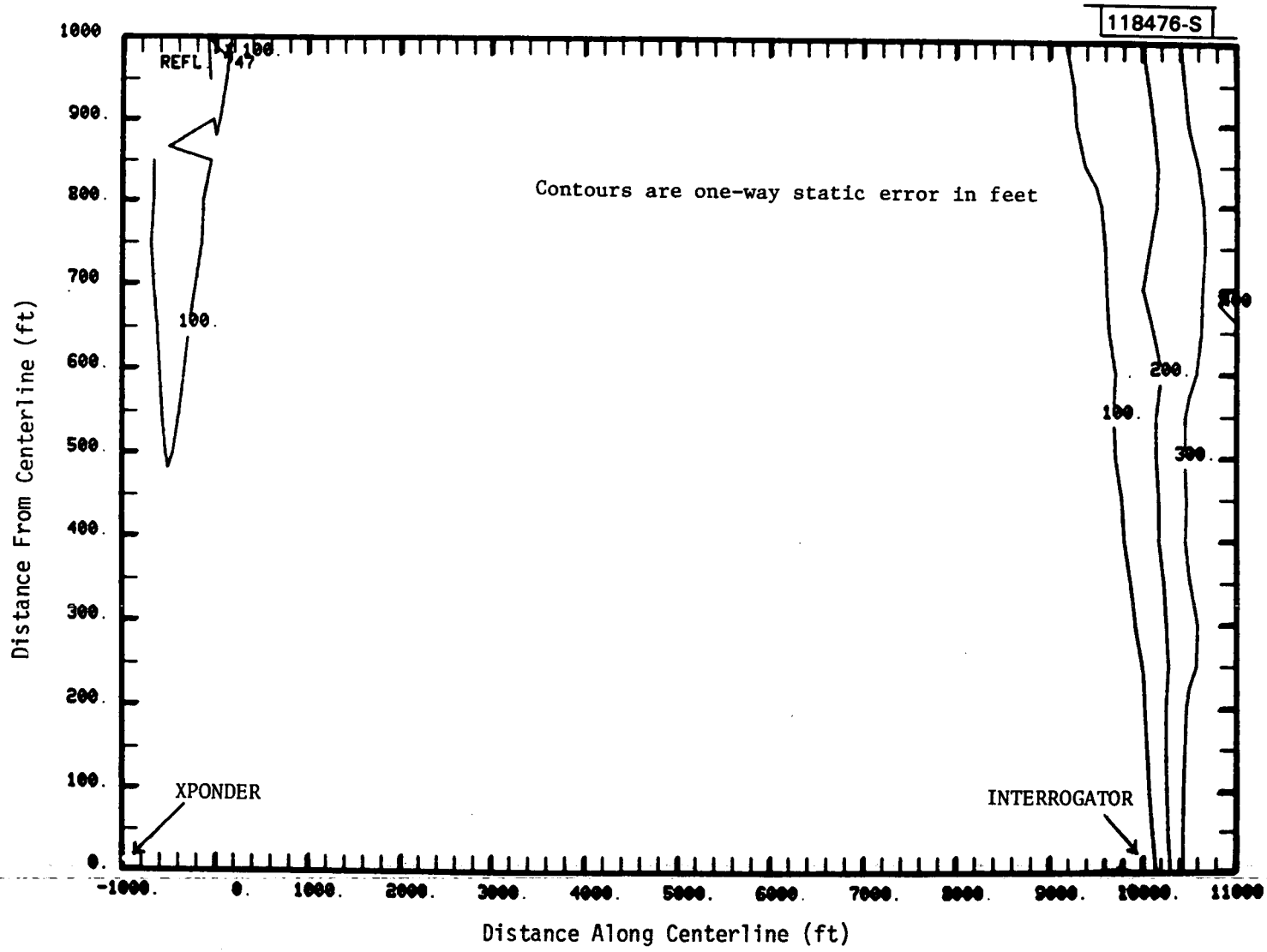


Fig.4-2. Present-day L-band DME waveform/real time thresholding receiver: B747 reflections.

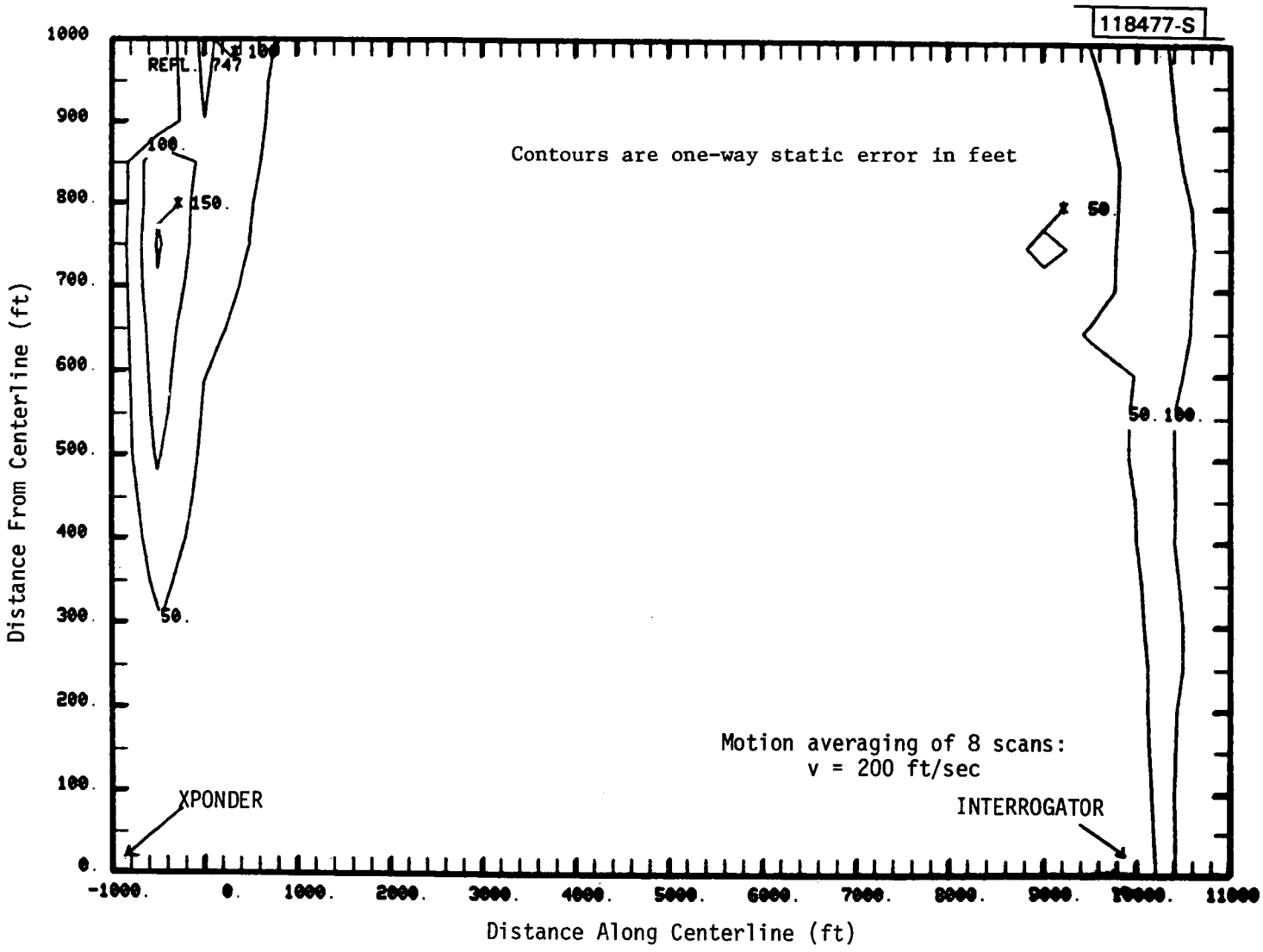


Fig.4-3. Present-day L-band DME waveform/real time thresholding receiver: B747 reflections.

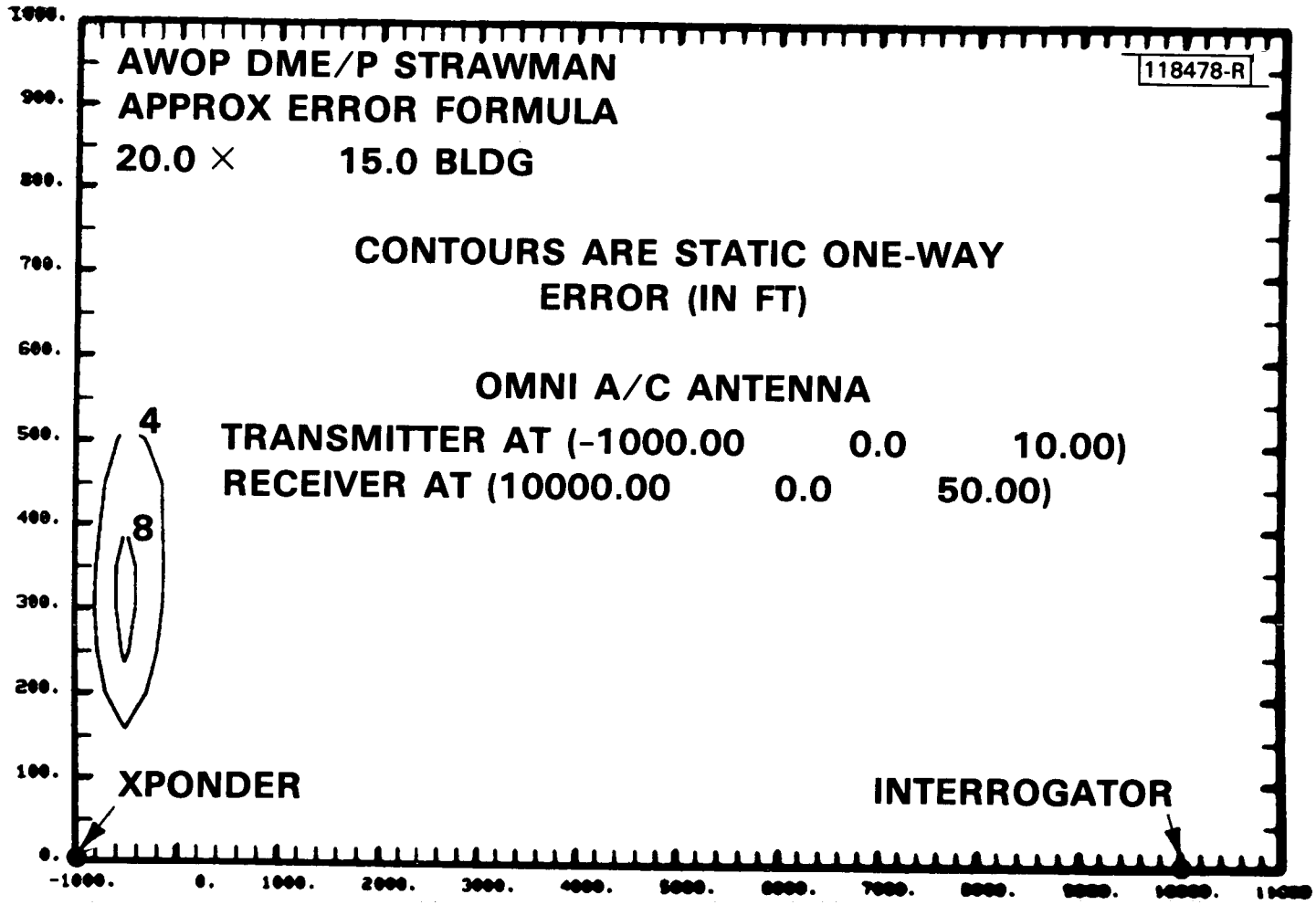


Fig.4-4. AWOP WG-M DME/P Strawman: "surface vehicle" reflections at threshold.

## 2. Cos/Cos$^2$ Waveform/Delay and Compare Receiver

Figure 4-4 shows the "surface vehicle" error contours for an interrogator at the runway threshold using the WG-M cos - cos$^2$ pulse waveform and nominal DAC parameters (G=2, $\tau_d$ = 100 ns ). The errors here are seen to be substantially lower than the corresponding results in Fig. 4-1. Figures 4-5 and 4-6 show the "surface vehicle" static and dynamic error contours for an interrogator in the final portion of the flare maneuver. Sizable static errors arise; however, motion averaging sharply reduces the errors. Additionally, the vehicle geometry here is such that the spatial extent of the error region is approximately 15 ft corresponding to less than 0.1 second of flight time. We conclude from the above that surface vehicles are not a threat to DME/P.

Figure 4-7 shows the static error contours for a B747 aircraft scatterer when the interrogator is at the runway threshold. The errors here are seen to be substantially smaller than those of Fig. 4-3 and, well within the error requirements indicated in Table 1-1. Figures 4-8 and 4-9 show the error contours when the interrogator is in the final stages of flare. The errors are considerably higher here because the reflections from the B747 fuselage have a height gain which is approximately 6 dB above that of the direct signal. The "worst case" B747 orientation here is such that the duration of significant errors would be approximately 150 ft, which corresponds to approximately 0.75 sec of flight time. If this error duration is excessive, it might be necessary to restrict taxiing aircraft orientations in the vicinity of the flare region (e.g., to be parallel to the runway) and to keep large aircraft away from the transponder array.

For interrogator heights above the height of a widebody aircraft, the computed errors for a B747 near the runway approach end are low as illustrated in Fig. 4-10. This is because:

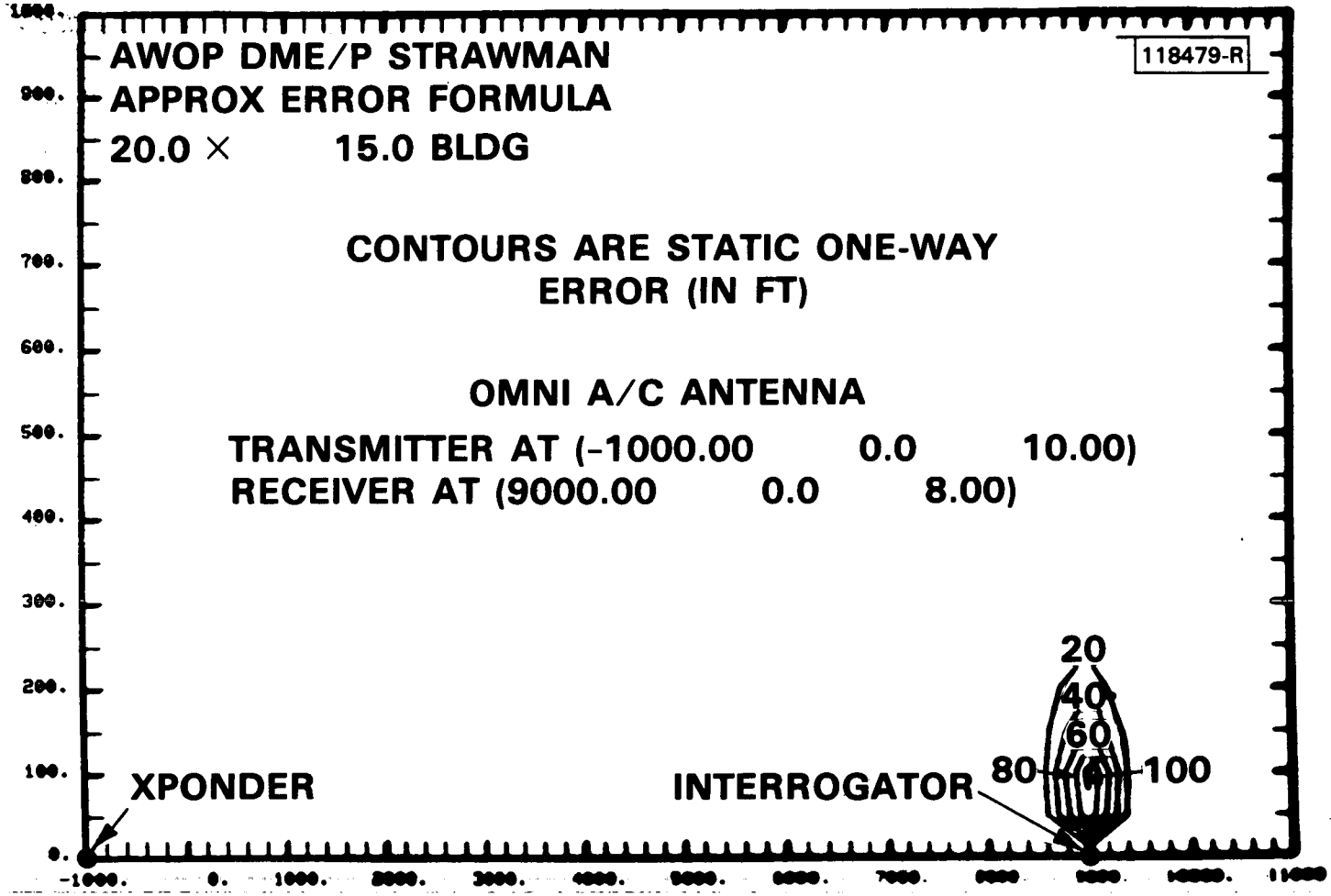


Fig.4-5. AWOP WG-M DME/P Strawman: "surface vehicle" reflections near touchdown.

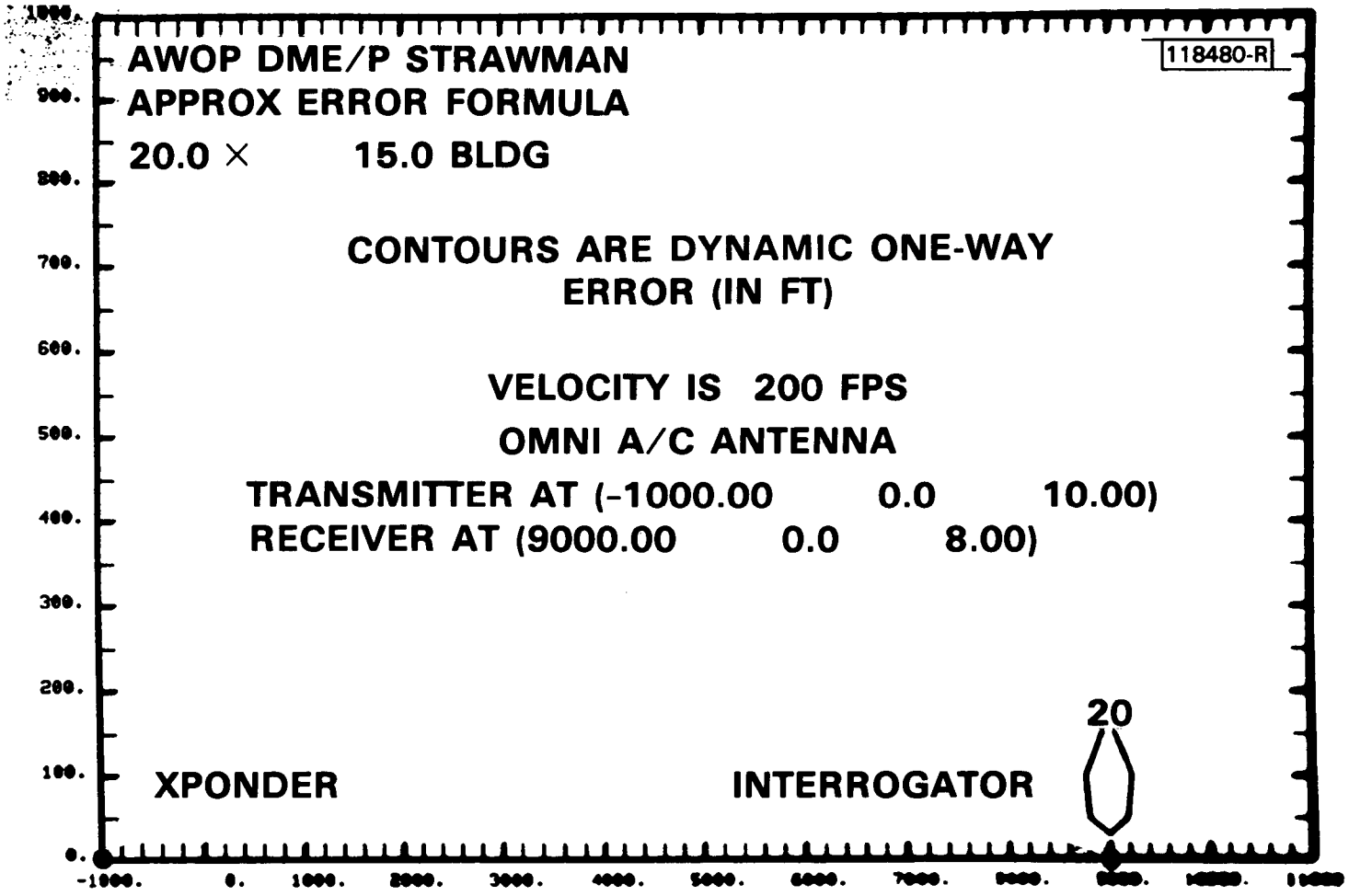


Fig.4-6. AWOP WG-M DME/P Strawman: "surface vehicle" reflections near touchdown.

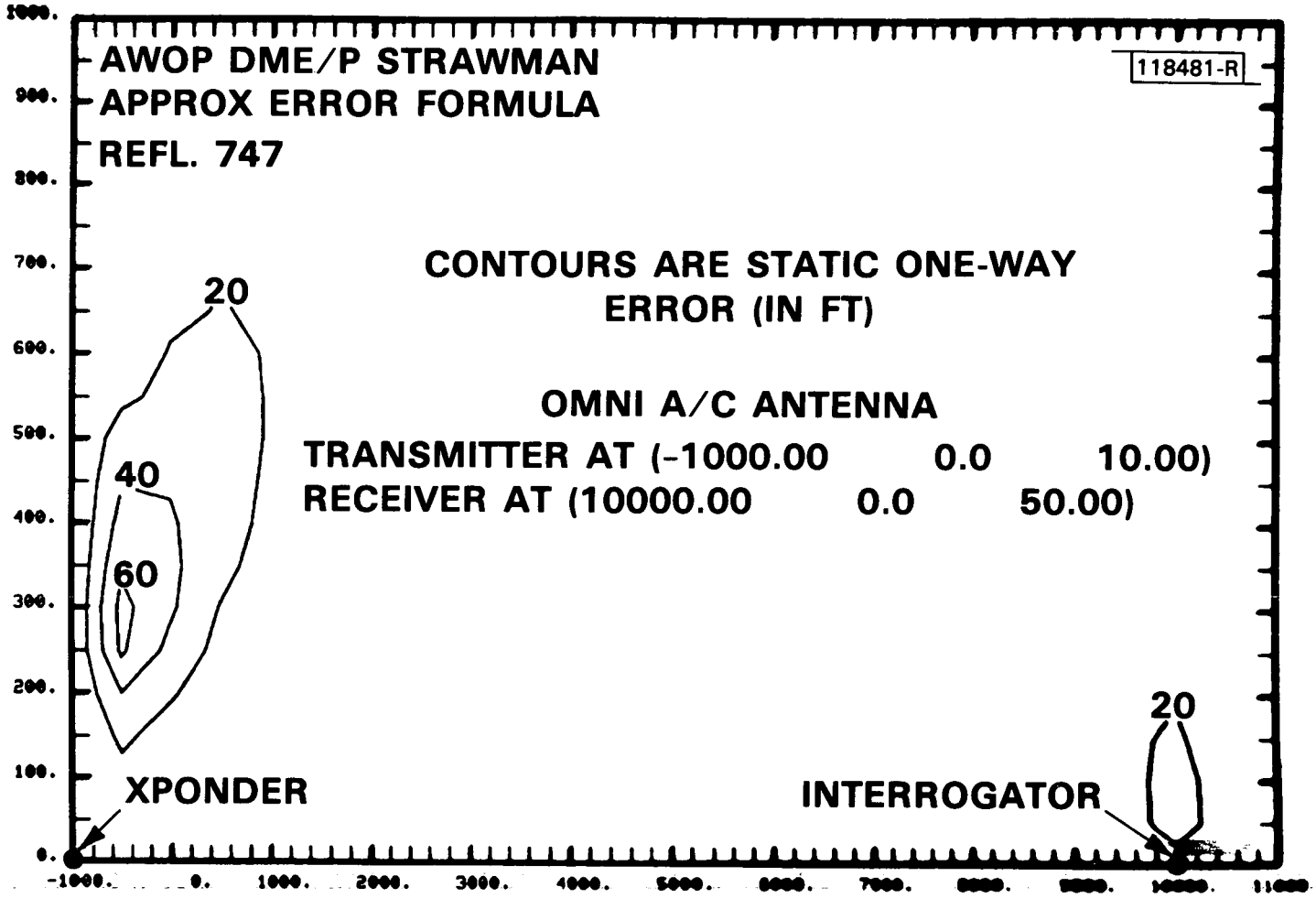


Fig.4-7. AWOP WG-M DME/P Strawman: B747 reflections at threshold.

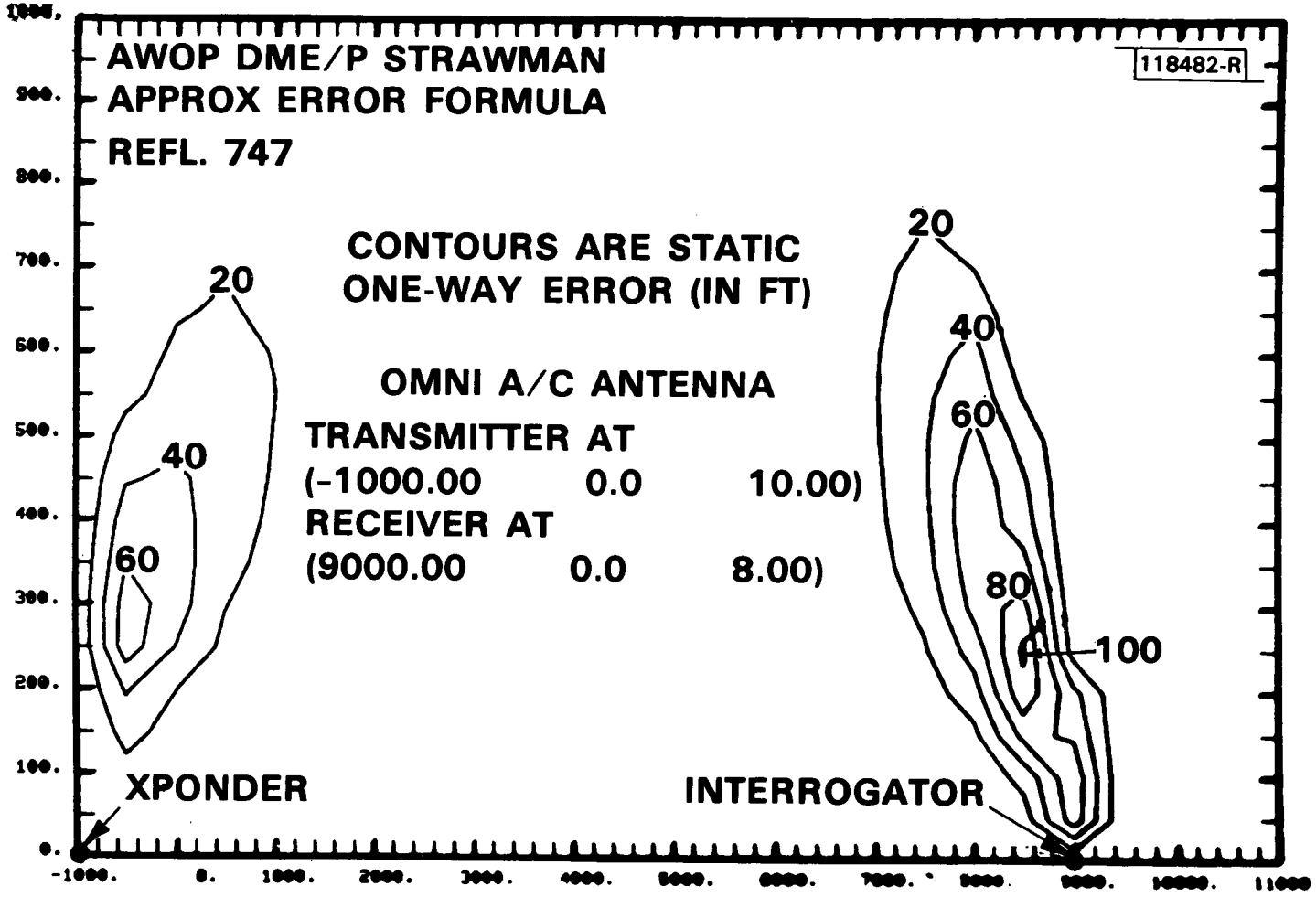


Fig.4-8. AWOP WG-M DME/P Strawman: B747 reflections near touchdown.

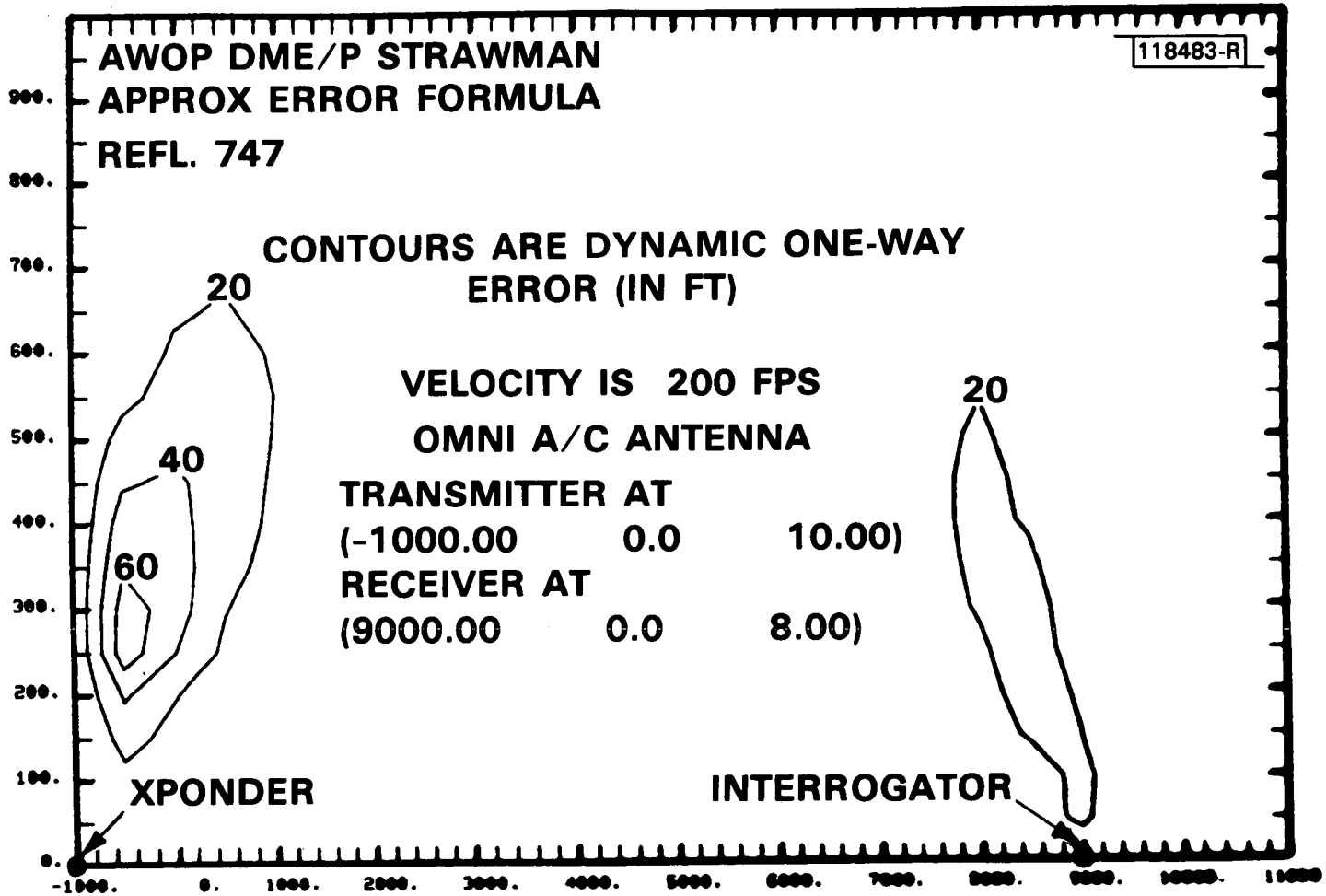


Fig.4-9. AWOP WG-M DME/P Strawman: B747 reflections near touchdown.

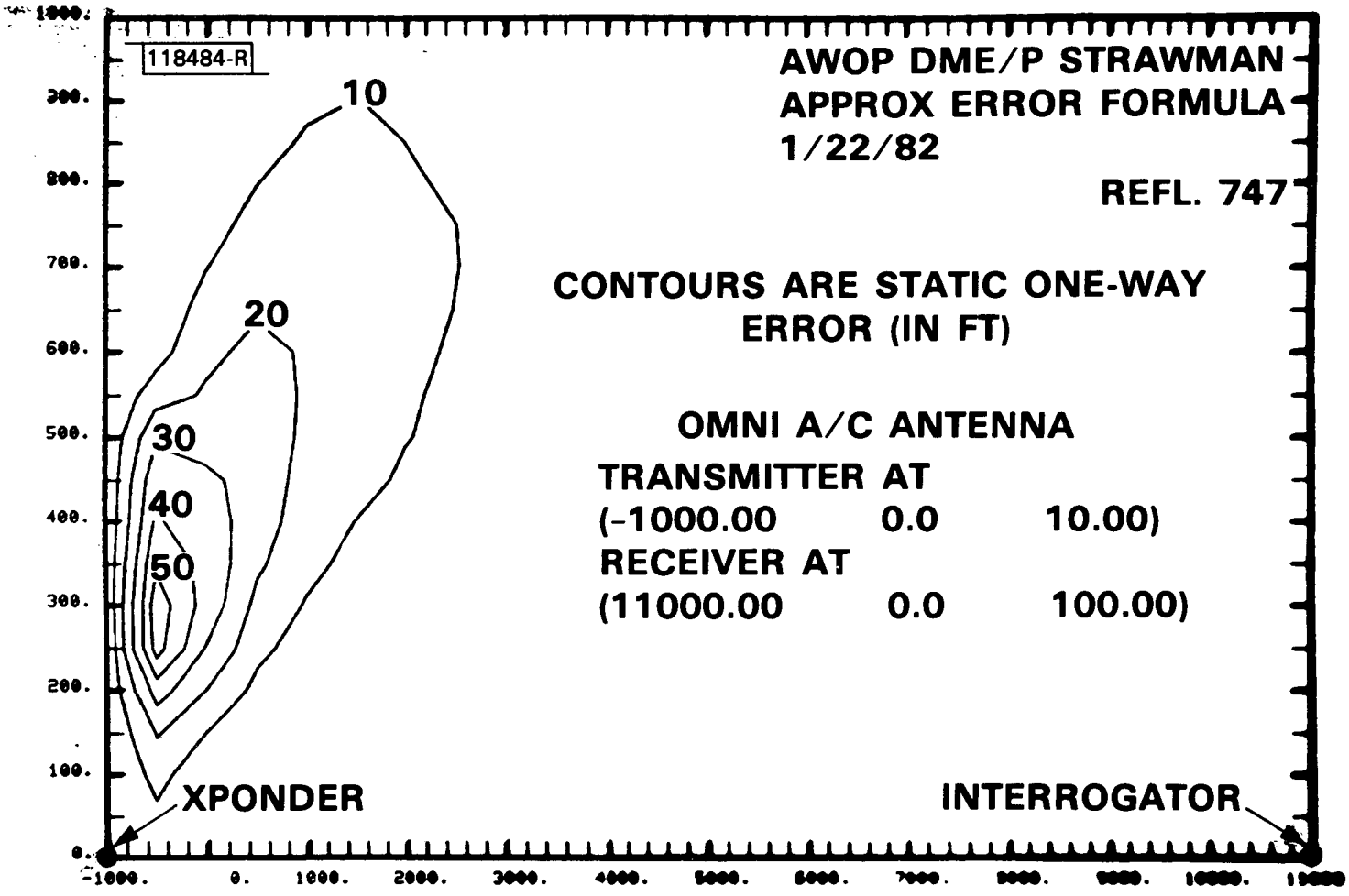


Fig.4-10. AWOP WG-M DME/P Strawman: B747 reflections near Cat II decision height.

(1) the tail fin model no longer yields specular reflections*, and
(2) lobing of the direct signal is much lower than was the case in the flare region.

We conclude that in the initial MLS implementation for cat I and II service, the DME/P should not impose any restrictions on surface aircraft movements on the aircraft surface other than to avoid physical blockage of the signals.

B. Effective M/D Levels Due to Building Reflections

Whereas with aircraft reflections, the errors are generally small enough such that the final conclusions are not very sensitive to the exact DME/P waveform or processor, the same is not true for high level multipath such as can be associated with building reflections. Additionally, there are several transponder antenna options which could be utilized to reduce the errors for a given waveform/receiver combination. Therefore, it was felt that contours of effective M/D level would be the most meaningful parameter to plot since error curves such as were given in Chapter II could then be used to bound the error for a given implementation.

In computing the effective signal levels, it is necessary to make some assumptions about the antenna gain pattern $G(\theta,E)$ . For the results here, it was assumed that $G(\theta,E)$ is omnidirectional in azimuth and decreases at a slope of 2 dB/degree in elevation near the horizon. This slope assumption corresponds roughly to the horizon slopes achievable by a good elevation pattern design [9] for a 4-foot vertical aperture.

The specific numerical values for airport geometry were chosen as follows:

---

* There is a tilt to aircraft tail surfaces which may result in slightly higher levels than predicted by the simulation model in cases where the interrogator is above the tail fin.

1. transmitter-receiver locations are based on a 20:1 glideslope to a 12,000 foot runway with the DME/P located on the extended centerline a distance $x_o$ beyond the runway stop end where $x_o$ = 1000 ft. for a transponder height of $z_r$ = 10 ft and $x_o$ = 2000 ft when $z_r$ = 30 ft.

2. buildings are located along the runway 800 to 3000 feet off the runway centerline. The minimum distance was dictated by obstruction clearance surface limits, while the maximum distance corresponds to only considering time delays which are less than the current DME pulse risetime. Building locations near the transmitter or beyond the runway threshold were not considered as the time delays of the resulting reflections tend to be quite large. At each location (the building wall center), the building is rotated so as to yield a maximum specular reflection for the given transmitter-receiver geometry

3. building sizes were chosen so as to represent large aircraft hangars (100 ft high by 400 ft long) as well as smaller "general" buildings (50 ft high by 100 ft long), and

4. the building surface material reflection coefficient was assumed to be -1 dB for grazing angles below 20° and -3 dB otherwise. This is consistent with the AWOP WG-A analysis of building reflectivity [21].

The contouring program utilized prefers the variable to be positive quantity which is numerically greater than one. Since only M/D levels in excess of -20 dB were of interest, we decided to plot 10 times the voltage M/D ratio in the contour plots (thus, the value 30 on the contour corresponds to M = 3D where M and D are linear envelope values). The x and y axes in the plot represent the (x,y) coordinates to the center of the "optimally oriented" buildings. Shown at the bottom of each plot are the (x,y,z) coordinates in feet of transponder and interrogator, respectively.

Figures 4-11 to 4-16 show the computed effective levels as a function of building location at several receiver heights for the 100 foot high, 400 foot

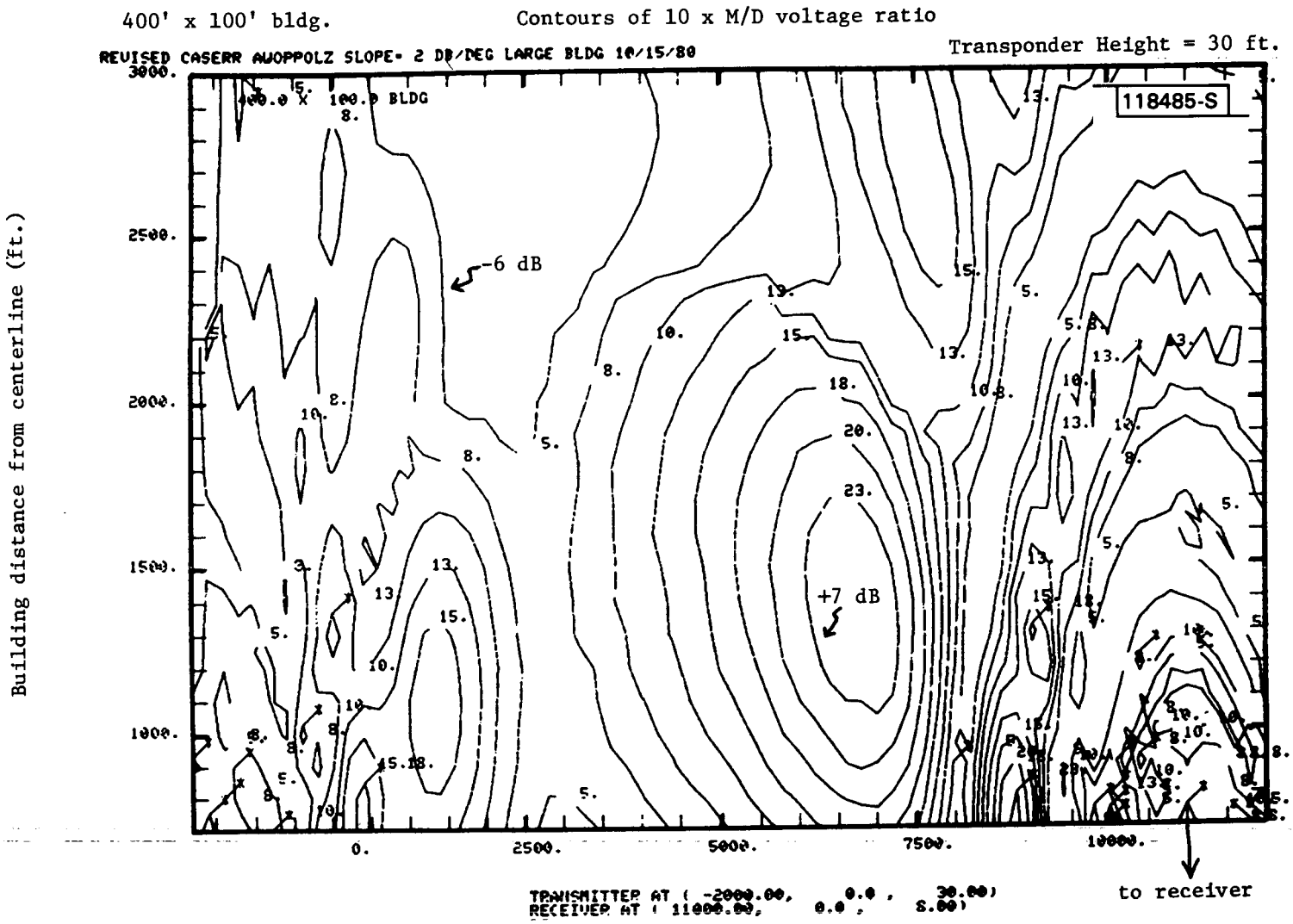


Fig.4-11(a). Effective L-band M/D level from large building for receiver near touchdown.

400' x 100' bldg. Contours of 10 x M/D (voltage) ratio

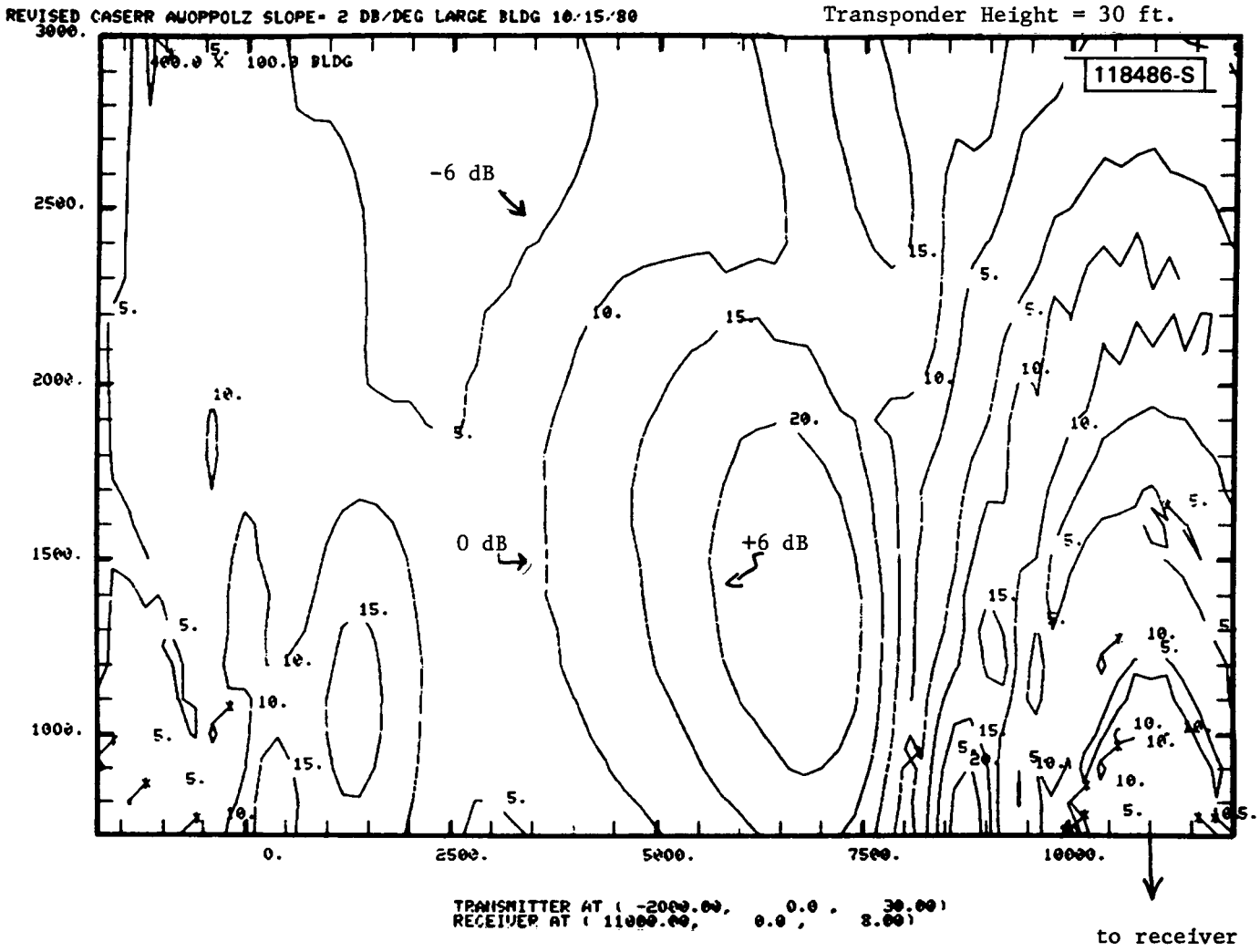


Building distance from centerline (ft.)

Fig.4-11(b). Effective L-band M/D ratio from large building for receiver near touchdown.

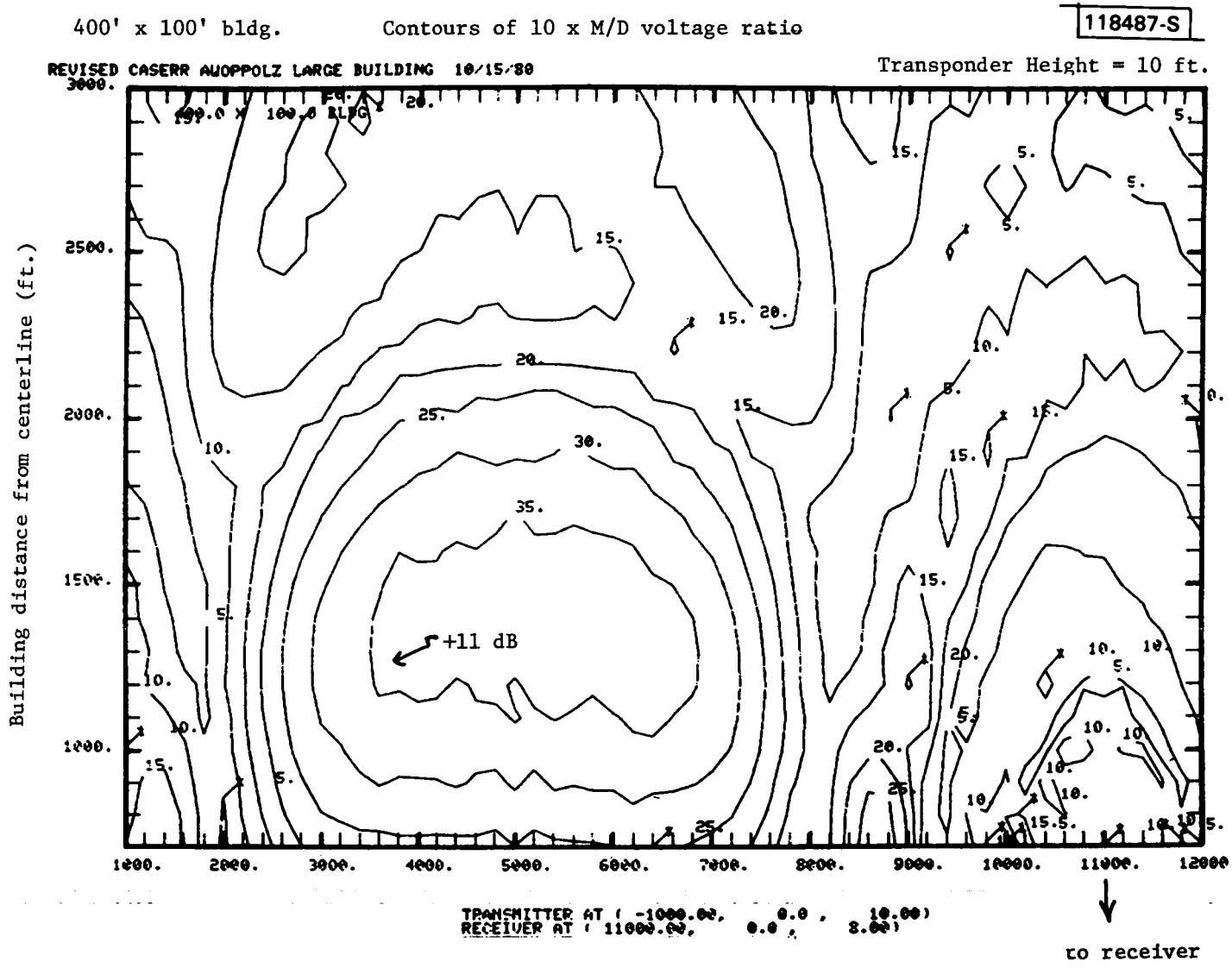


Fig.4-12(a). Effective L-band M/D level from large building for receiver near touchdown.

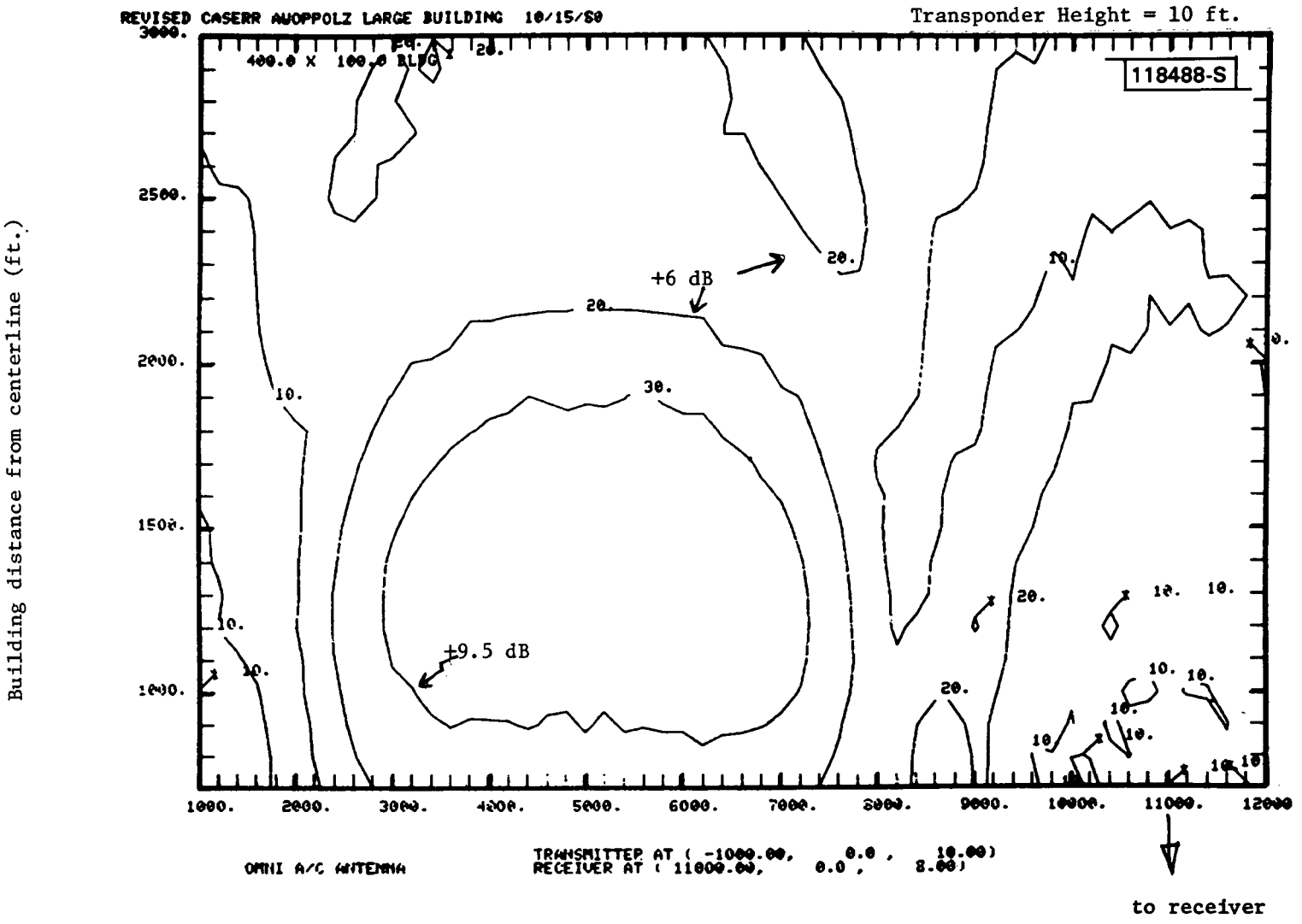


Fig.4-12(b). Effective L-band M/D level from large building for receiver near touchdown.

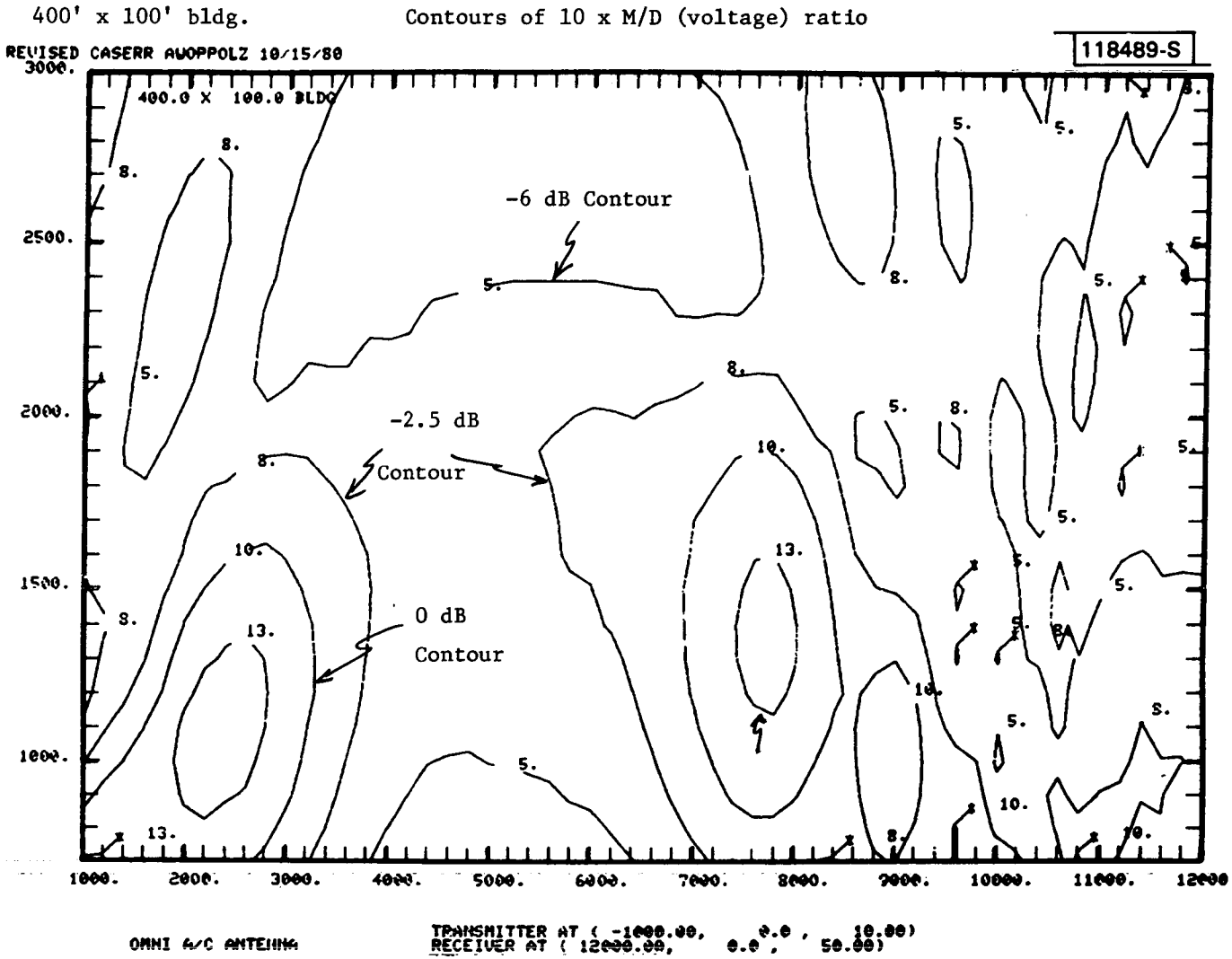


Fig.4-13. Effective M/D levels from large building with receiver at runway threshold.

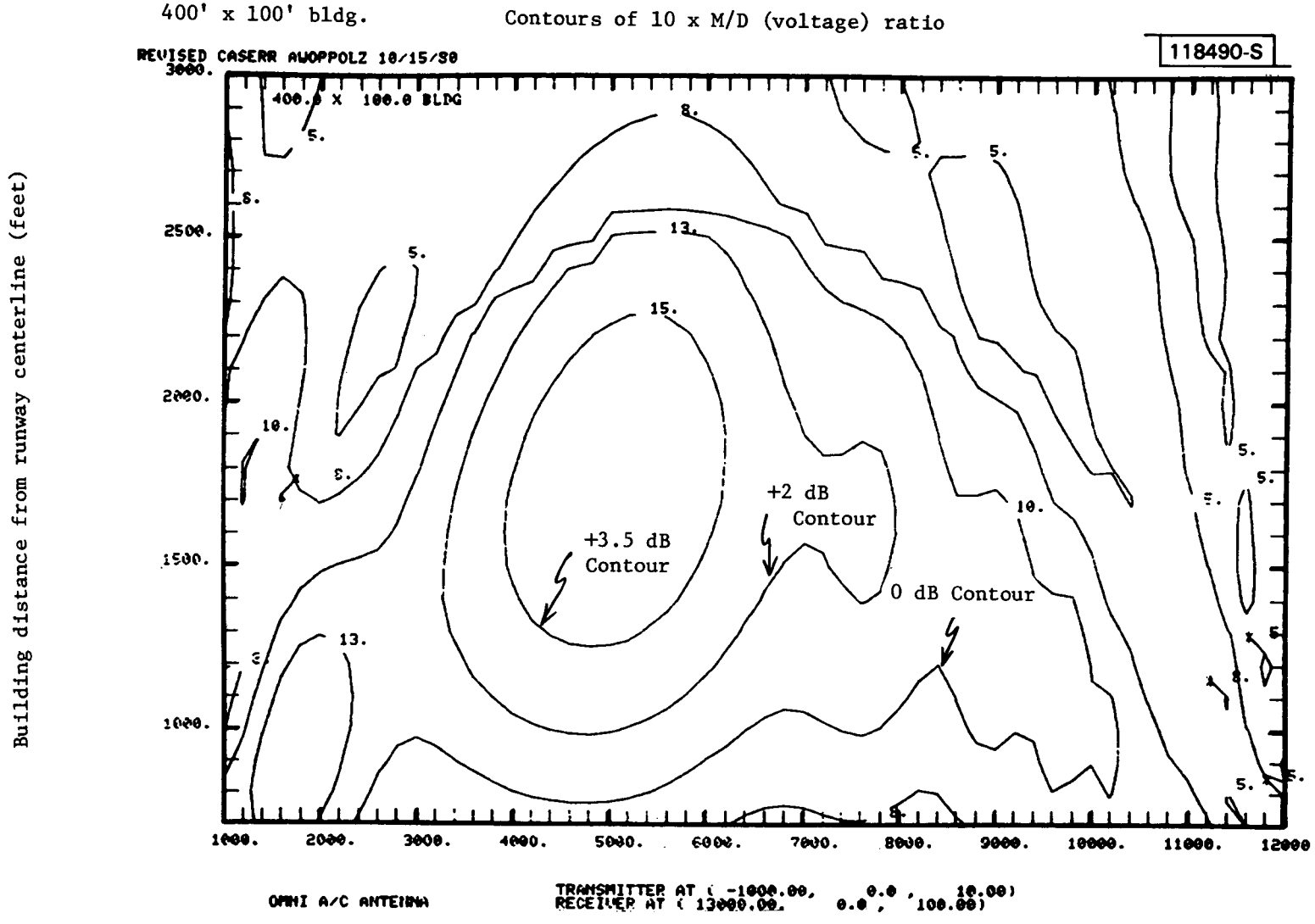


Fig.4-14. Effective M/D levels from large building with receiver near Cat II decision height.

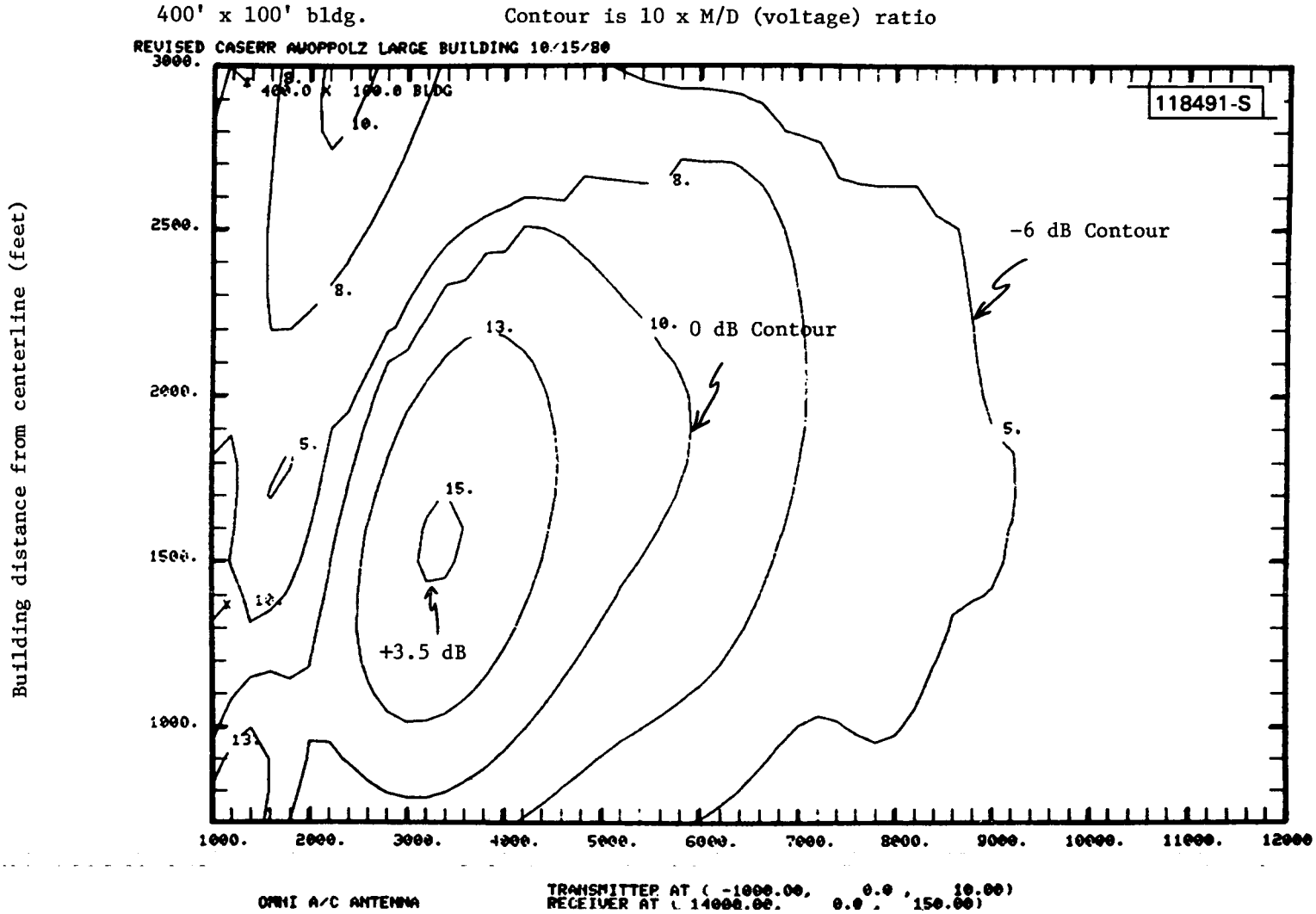


Fig.4-15. Effective M/D levels from large building with receiver between Cat I and Cat II decision heights.

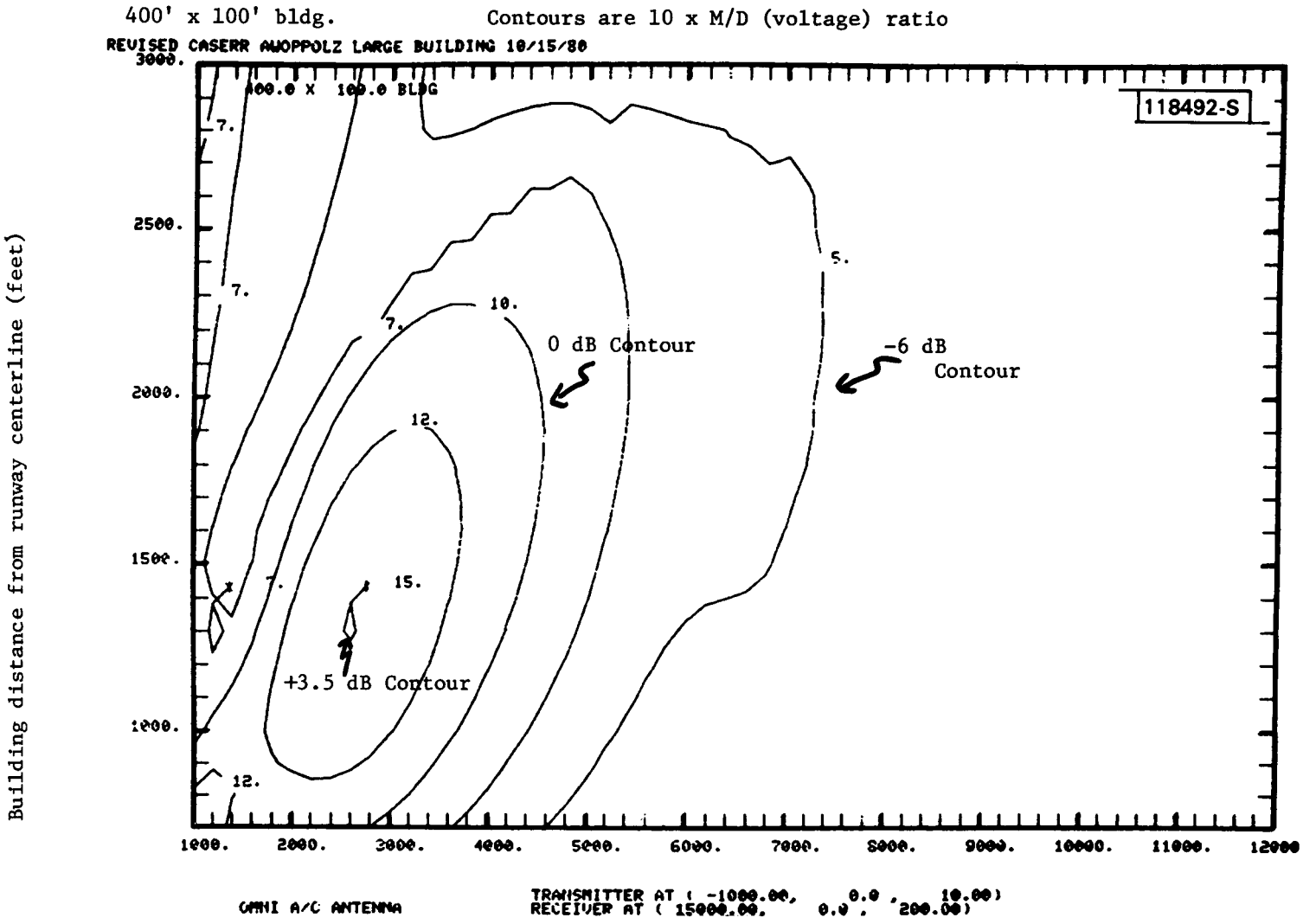


Fig.4-16. Effective M/D levels from large building with receiver at Cat I decision height.

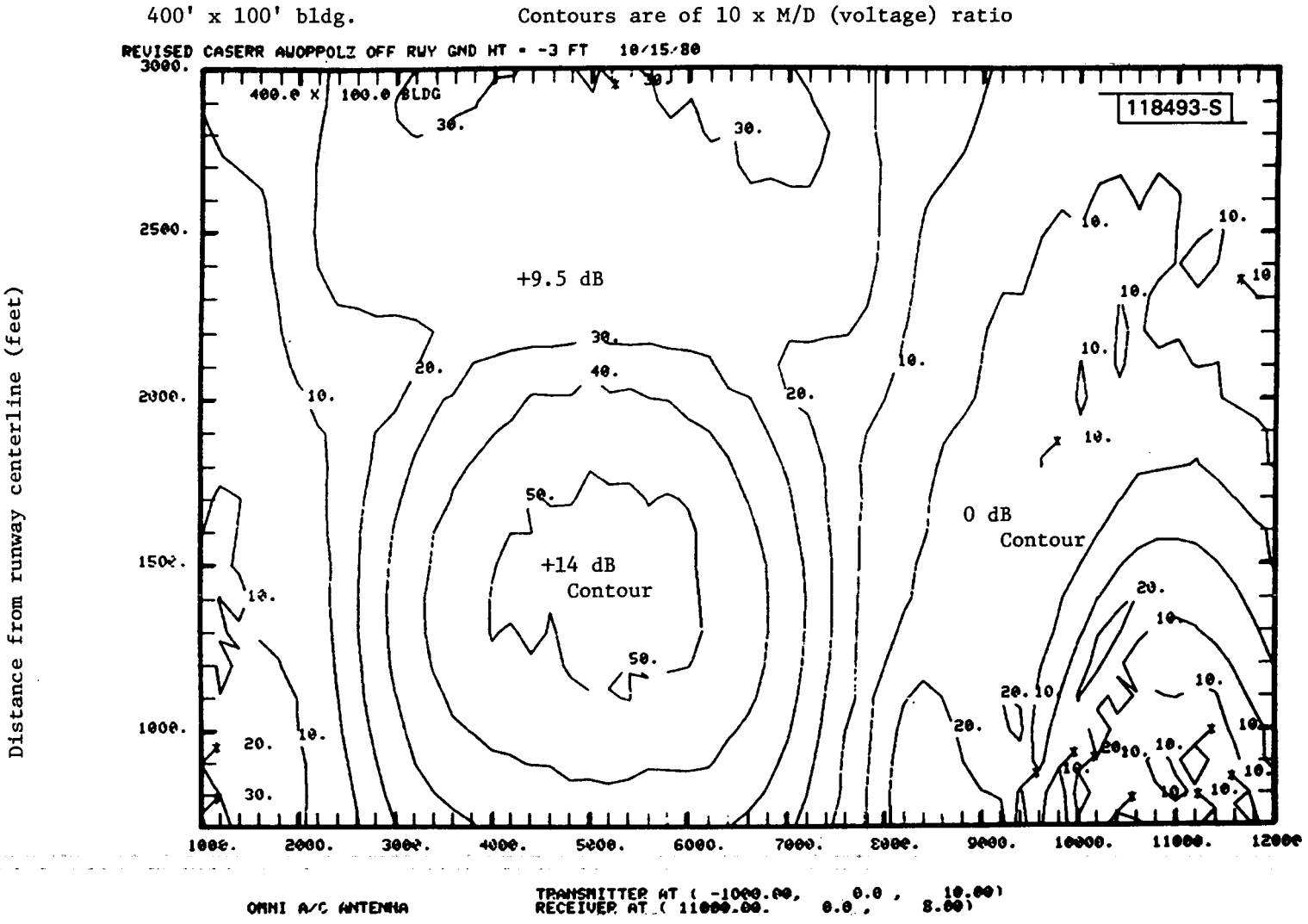


Fig.4-17. Effective M/D levels from large building with off runway terrain 3 feet below runway level when receiver is near touchdown.

wide building model, assuming flat terrain on and off the runway. In several cases, more than one contour plot is presented so as to show different plot features. We see that effective M/D values in excess of unity may occur at all the receiver heights considered, but that the worst likelihood is at low altitudes. This low altitude increase arises from the direct signal nulling and the greater likelihood of the building being high enough to generate specular reflections (as was discussed in Chapter III).

Comparing Figs. 4-11 to 4-12, we see that the use of a higher transponder antenna phase center height is advantageous in reducing the M/D levels. This is because 1) the direct signal lobing is reduced, and 2) various building reflection terms become smaller due to the change in $z_s$.

Another factor which influences the effective level is the height of the off runway terrain corresponding to the paths bg and cg in Fig. 3-2. If this terrain height is lower than that of the runway (e.g., to provide rain runoff), the effective transmitter and receiver heights are increased for the building reflection. This [recall Eq. (3-5)] results in a reduction in the ground reflection nulling of the building reflection such that the M/D levels are increased significantly . Figure 4-17 shows the effective levels for a 3-foot ground level difference when the receiver is near touchdown. Comparing Fig. 4-12 with Fig. 4-17, we see that the M/D levels have increased by 3-5 dB over much of the region, as might be expected from Eq. (3-5).

Figures 4-18 to 4-23 show the computed levels at various receiver heights for the 50 foot high, 100 foot wide building model. Comparing these plots to those in Fig. 4-11 to 4-17, we see that the levels are generally much lower, especially when the receiver altitude is above 100 feet. This arises because the building is no longer high enough to yield a specular reflection over much of the region. However, multipath levels in excess of unity (i.e., 0 dB) can arise over a sizable region at lower heights and/or when the off runway terrain is lower than the runway surface.

In interpreting these plots, several factors should be kept in mind:

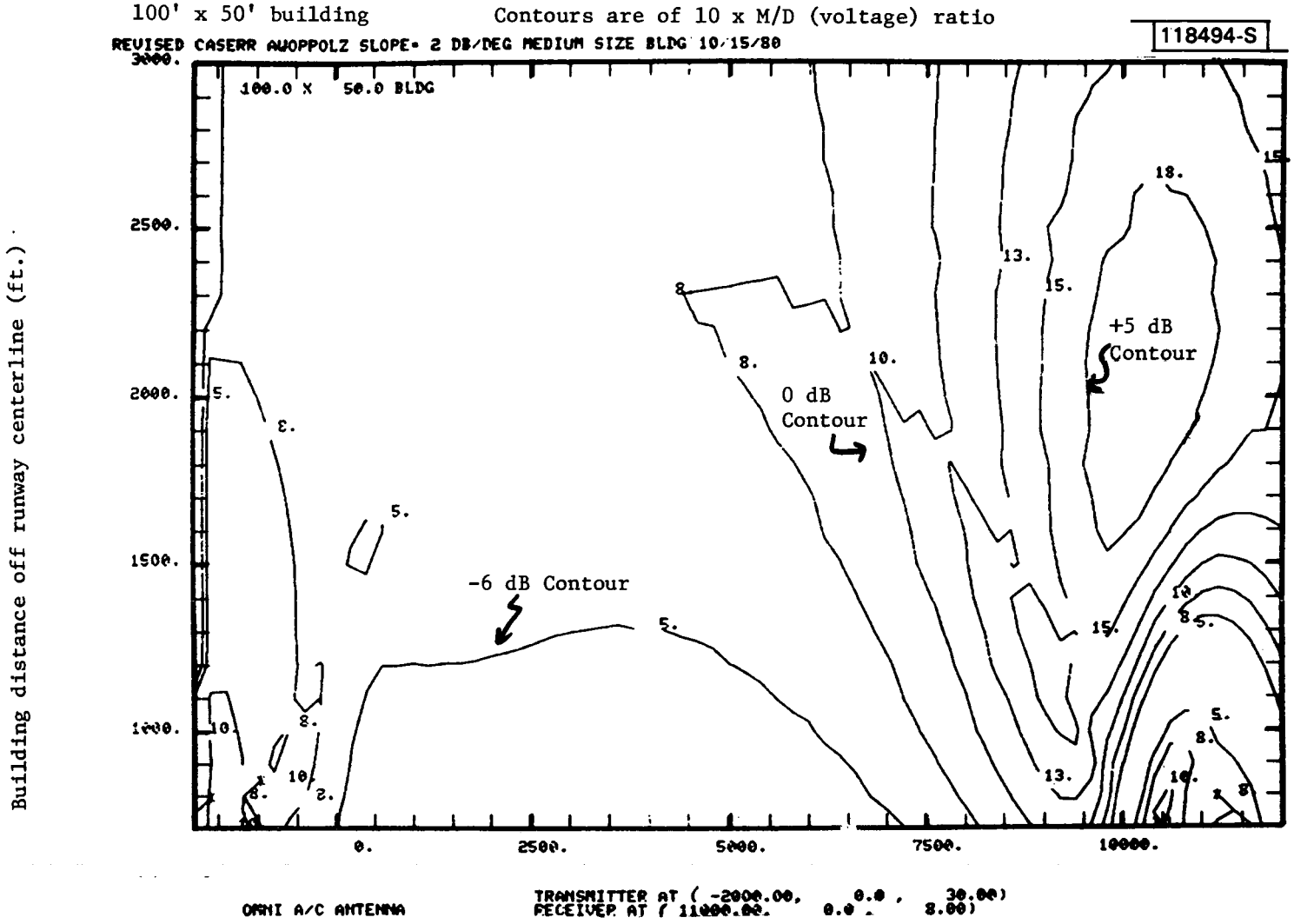


Fig.4-18. Effective M/D levels from medium size building with receiver near touchdown.

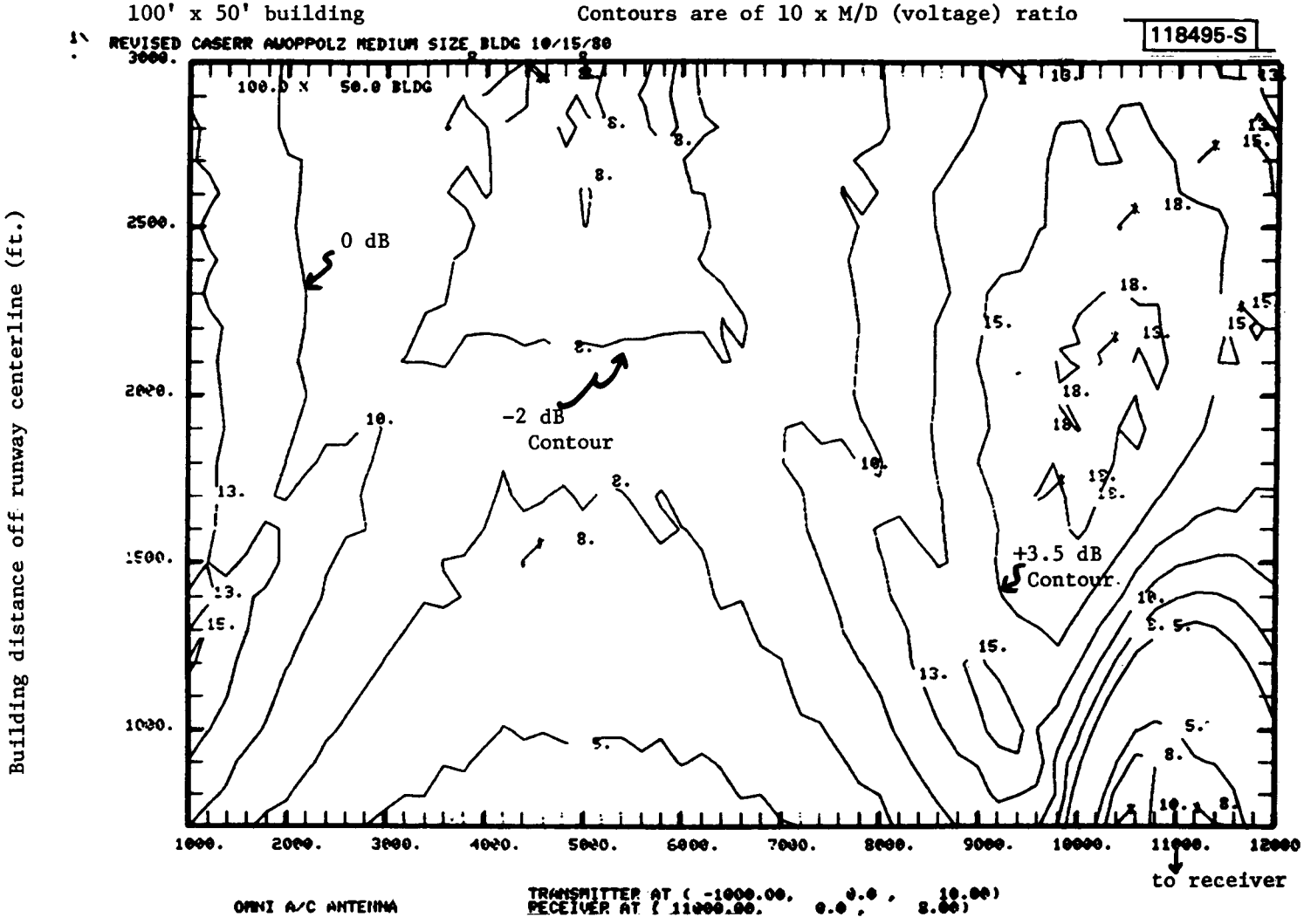


Fig.4-19. Effective M/D levels from medium size building with receiver near touchdown.

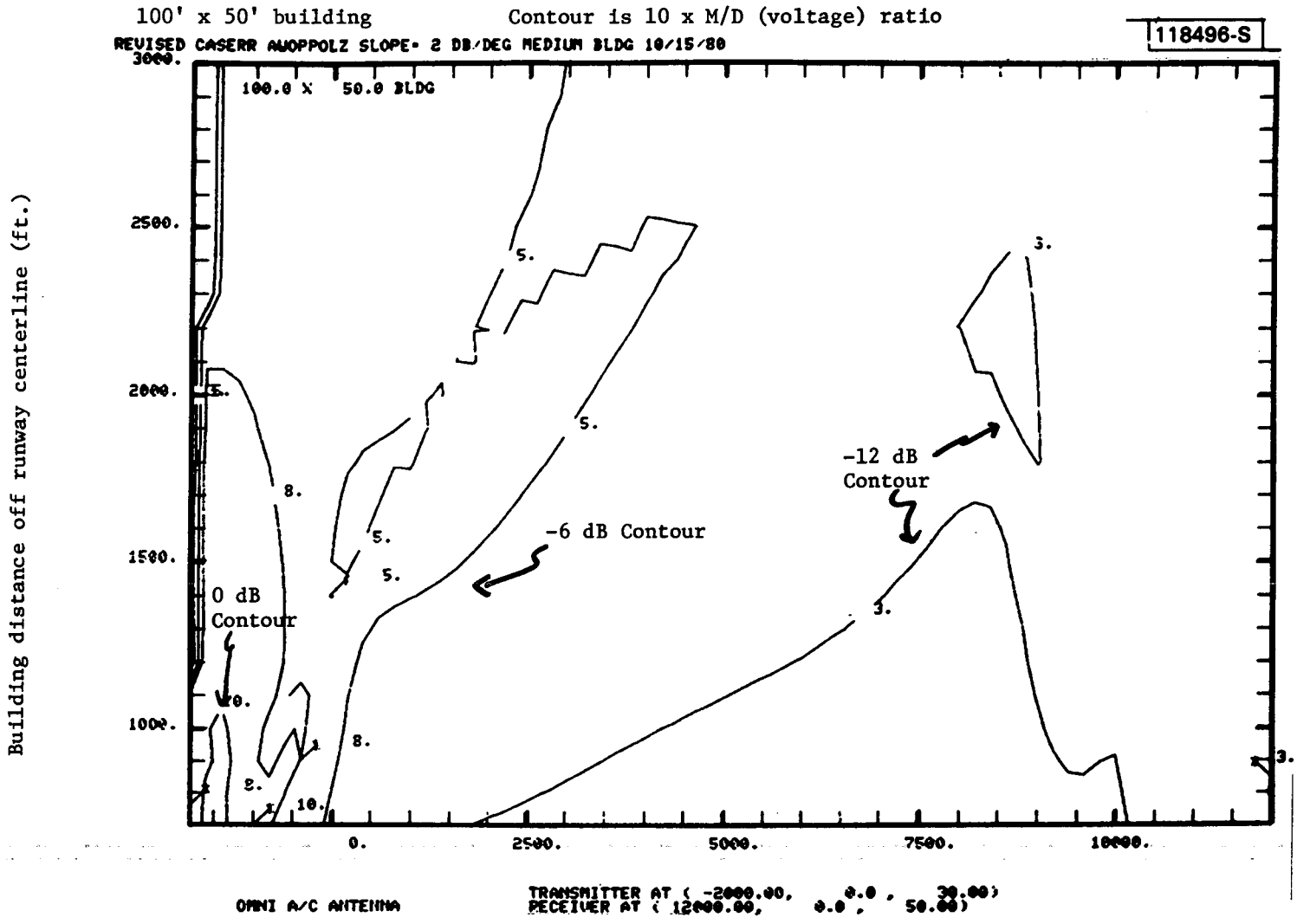


Fig.4-20(a). Effective M/D levels from medium size building with receiver at threshold.

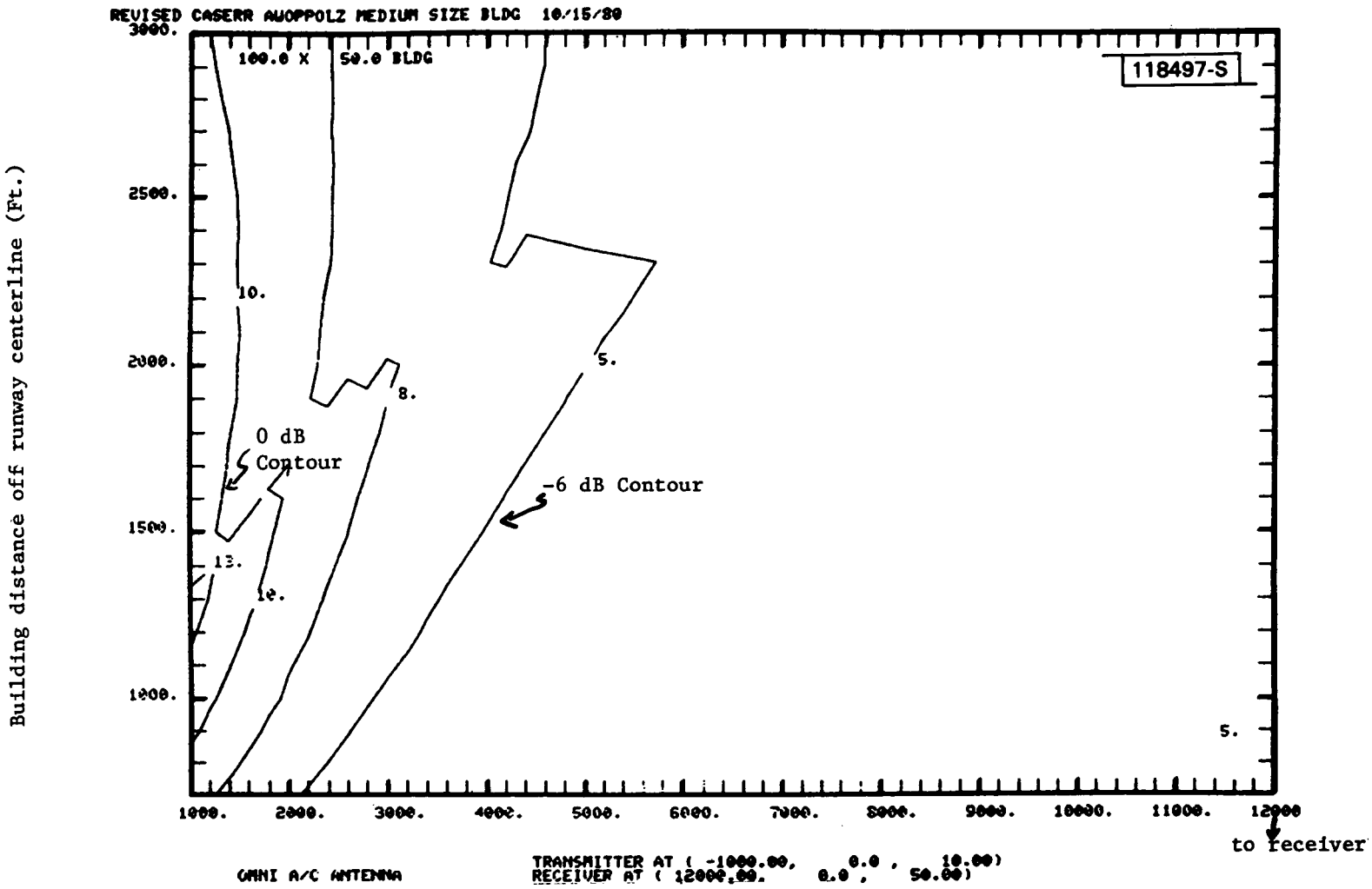


Fig.4-20(b). Effective M/D levels from medium size building with receiver at threshold.

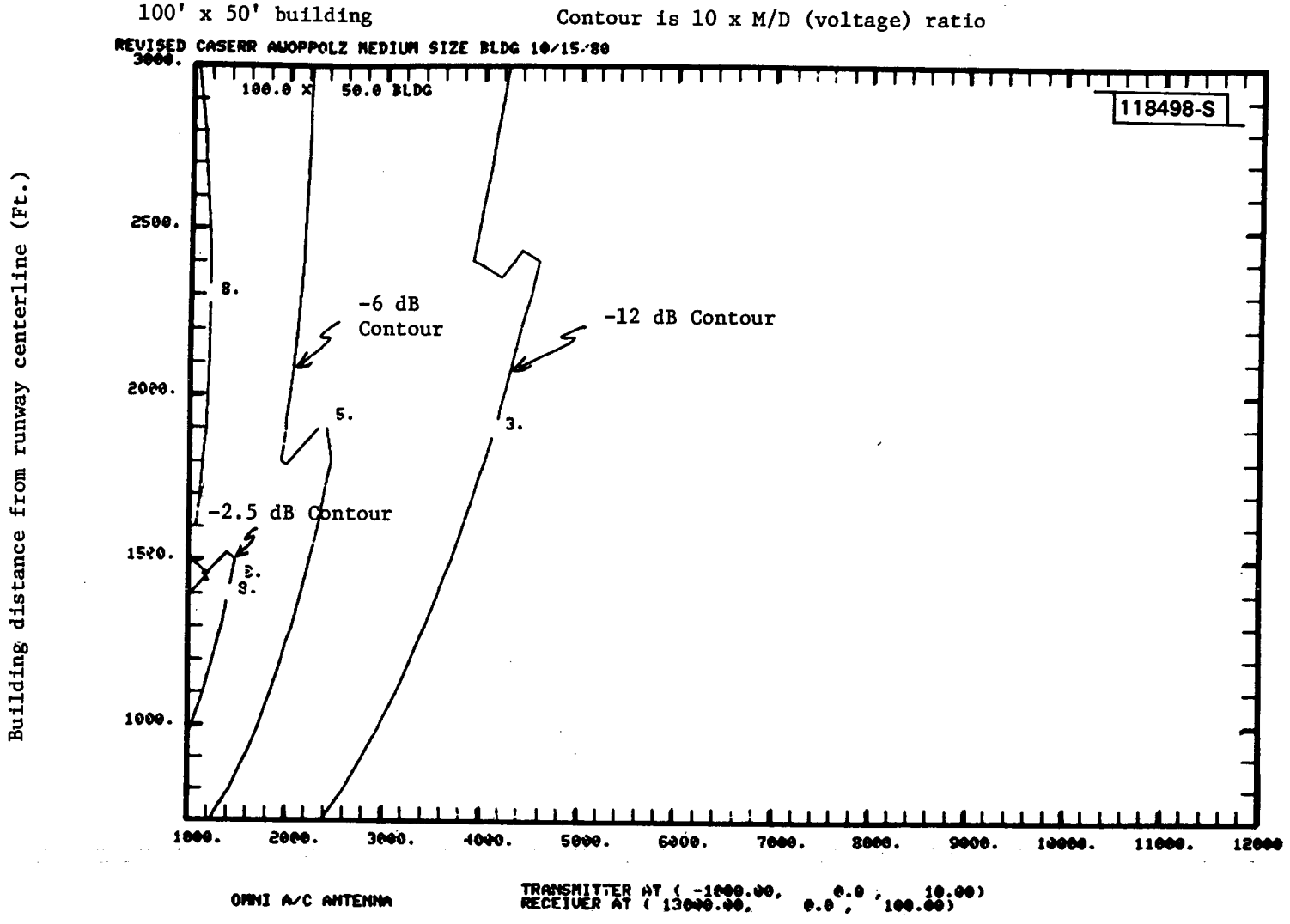


Fig.4-21. Effective M/D levels from medium size building with receiver at Cat II decision height.

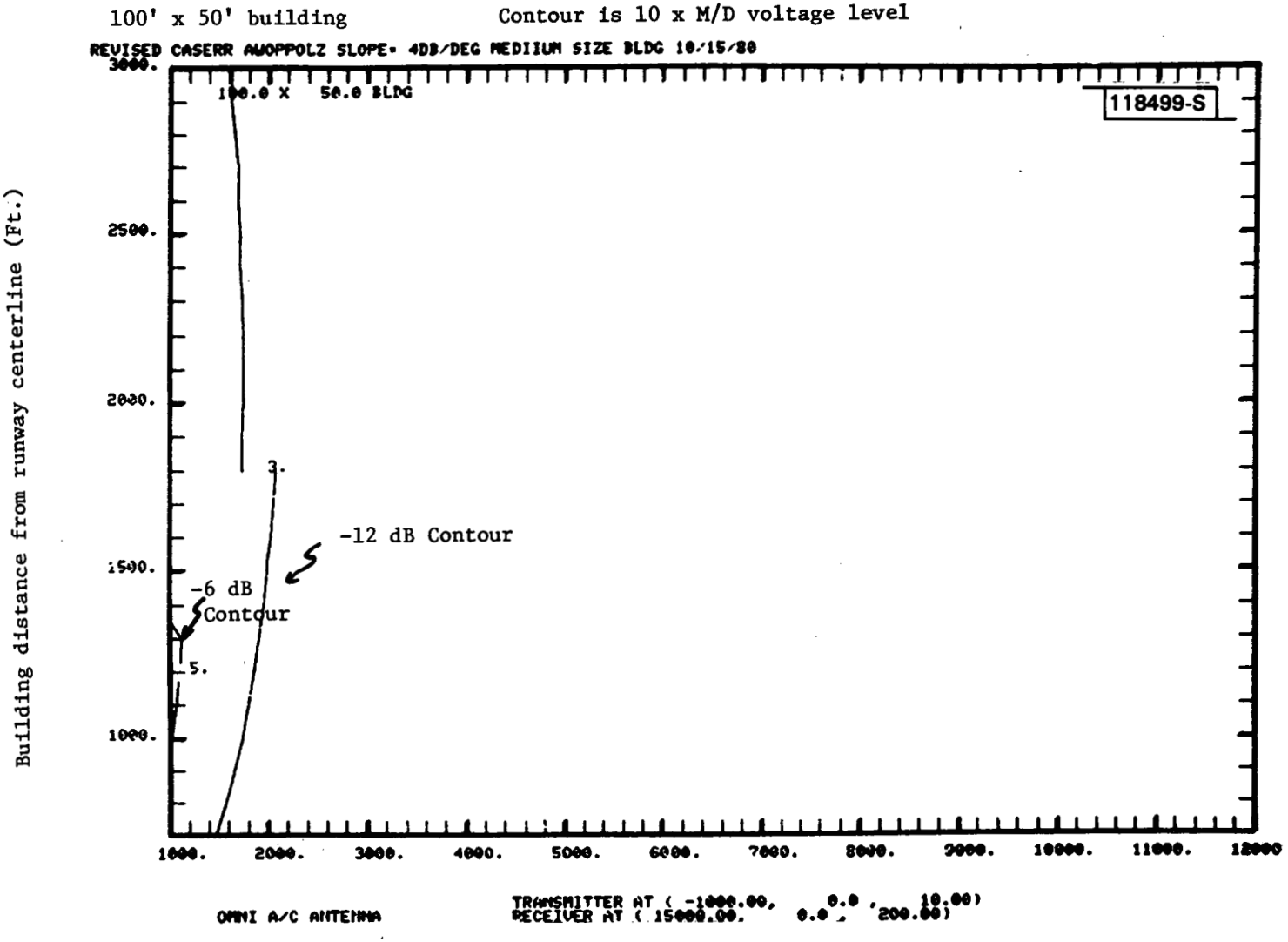


Fig.4-22. Effective M/D ratio from medium size building with receiver at Cat I decision height.

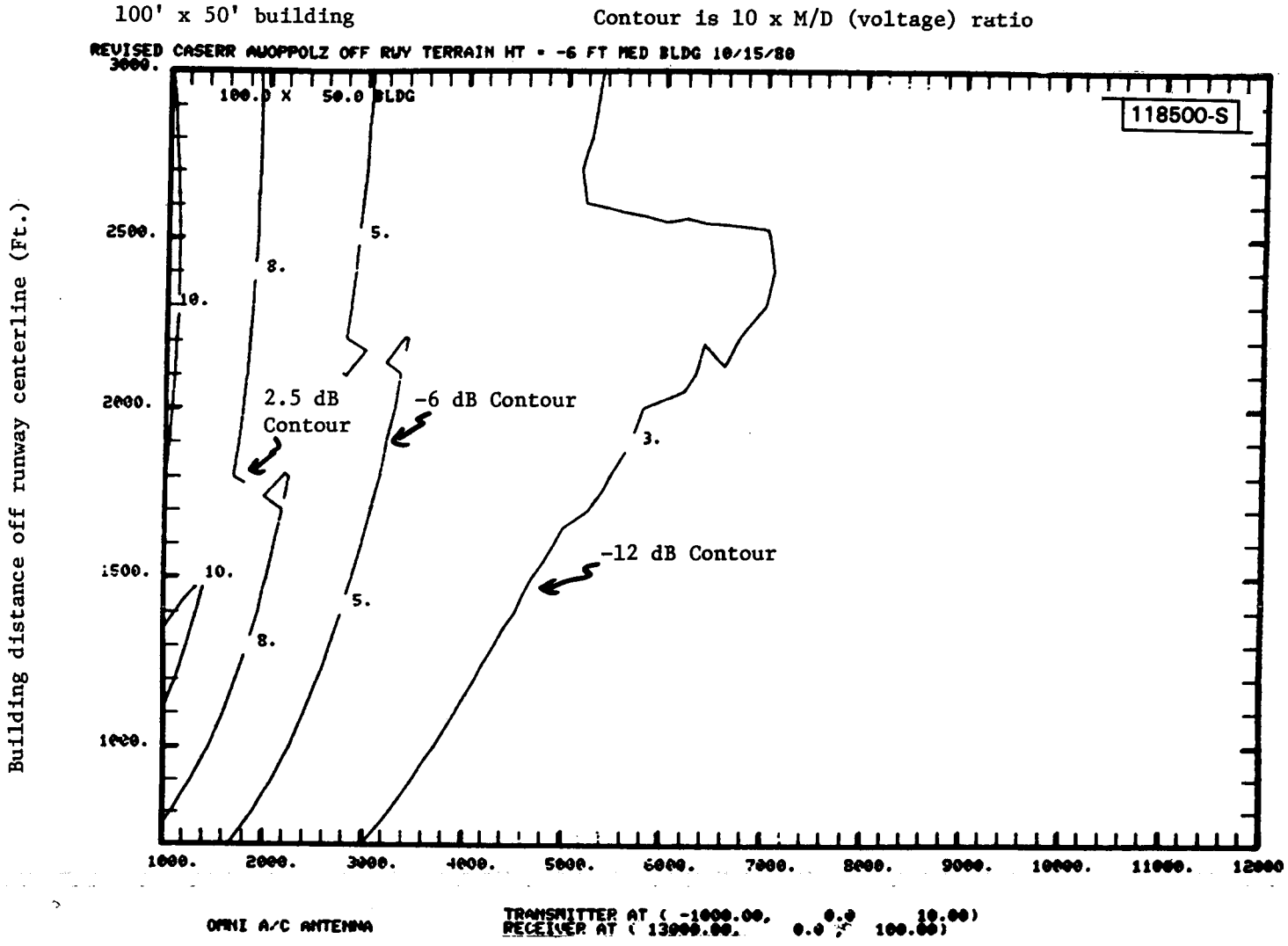


Fig.4-23. Effective M/D ratio from medium size building with receiver at Cat II decision height and off runway terrain 6.0 feet below runway level.

1. simplified, and, in some cases, exaggerated assumptions have been made regarding the terrain and building features [21]. In particular, the reflection signal levels at low receiver altitudes could be reduced significantly by blockage from intervening objects such as vehicles parked in front of the buildings, jet ways, etc. On the other hand, the reflected signal effective level reduction due to terrain reflections bg and cg in Fig. 3-2 would be significantly reduced if the terrain vegetation were quite high and thick.

2. omnidirectional aircraft and ground antenna azimuthal patterns have been assumed. Use of "centerline emphasis" in the DME ground antenna would yield lower M/D levels than shown here. On the other hand, L-band beacon antenna patterns [18-20] for the usual bottom side mounting show less gain in the forward direction than to the sides (see Fig. 4-24) which would serve to increase the M/D ratios.

3. dynamic effects such as motion averaging and time duration of the multipath region must also be considered in assessing overall performance.

C. DME/P Multipath Scenarios

A number of comparative MLS scenarios were developed by AWOP WG-A and used in its assessment of the various MLS proposals [45]. Unfortunately, the majority (5 of 8) of these scenarios are not relevant to DME/P assessment because they were intended as elevation multipath scenarios. One of the three azimuth multipath scenarios is concerned with guidance in the initial approach as opposed to final approach. Thus, only two of the WG-A scenarios warranted consideration as PDME scenarios.

Scenario 2 shown in Fig. 4-25 was based on the geometry at Los Angeles International Airport (LAX). This scenario is principally a test of MLS azimuth performance rather than DME performance, because the principal building reflections have fairly large differential delays as shown in Fig. 4-26. Since optimized DME/P designs [3, 12, 34] are typically unaffected by

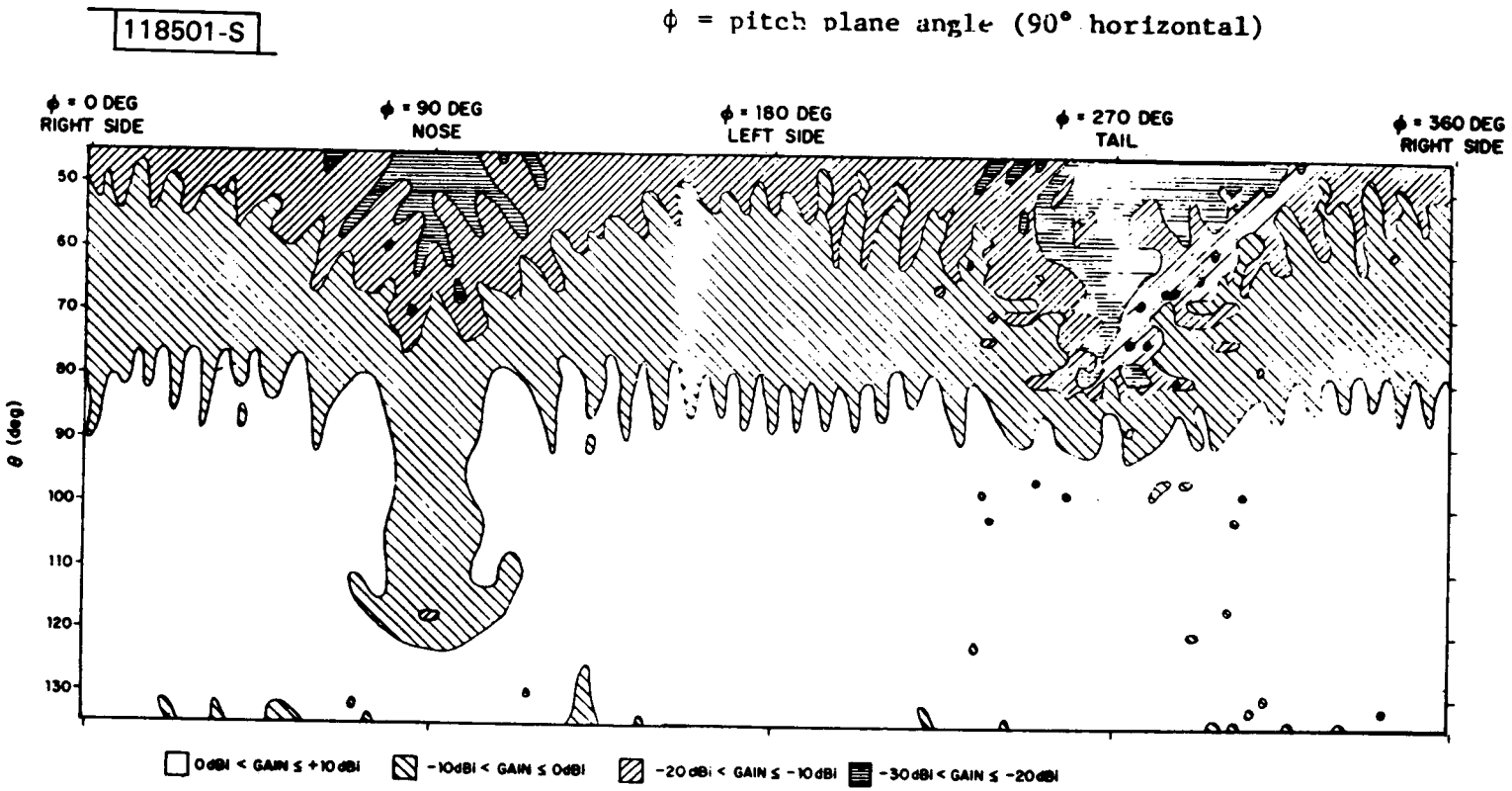


Fig.4-24(a). Gain contours for Boeing 727 over θ, ϕ (antenna 2; gear down) (from [19]).

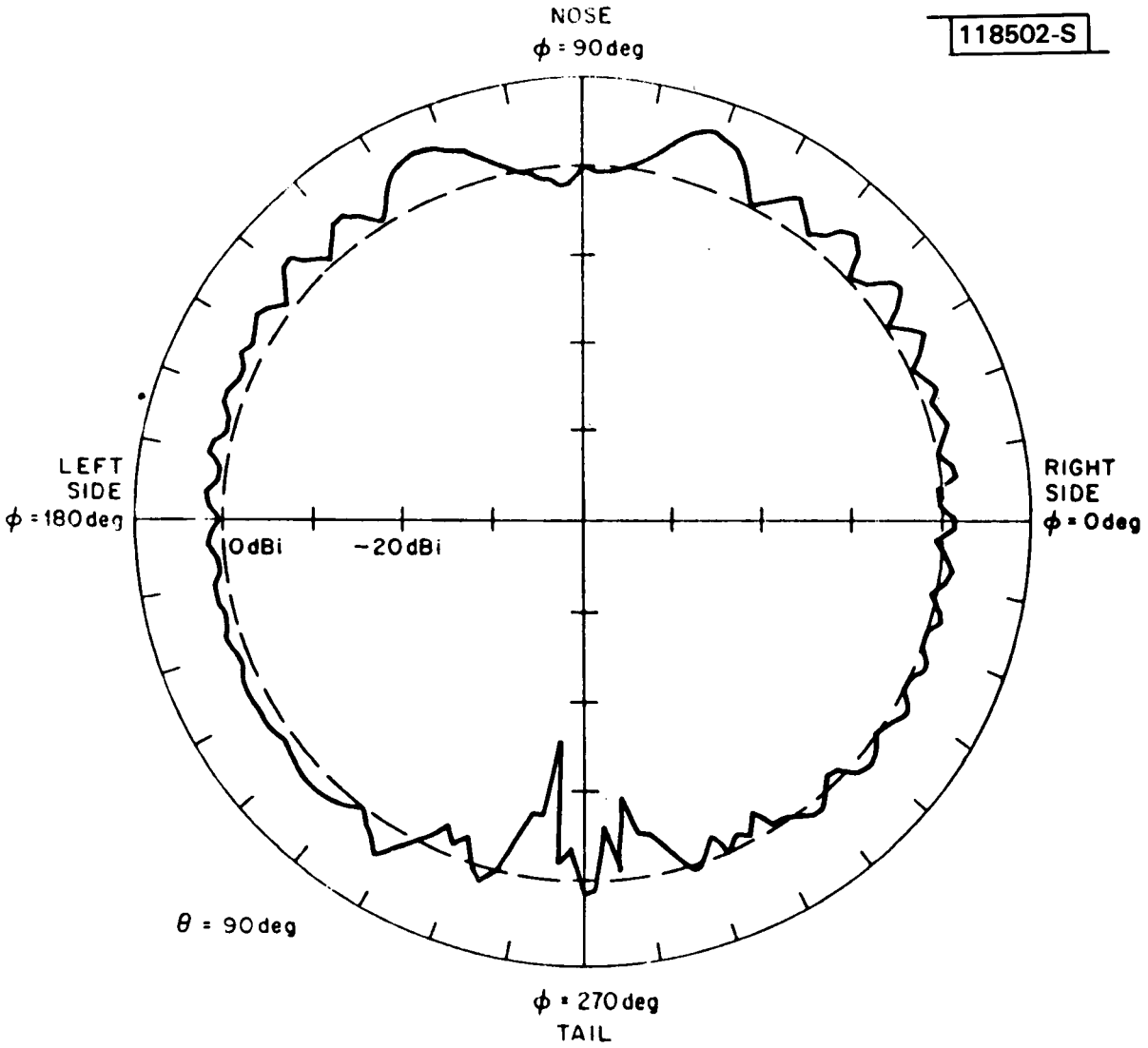


Fig.4-24(b). Boeing 727 antenna pattern in XY-plane (antenna 2; gear down) (from [19]).

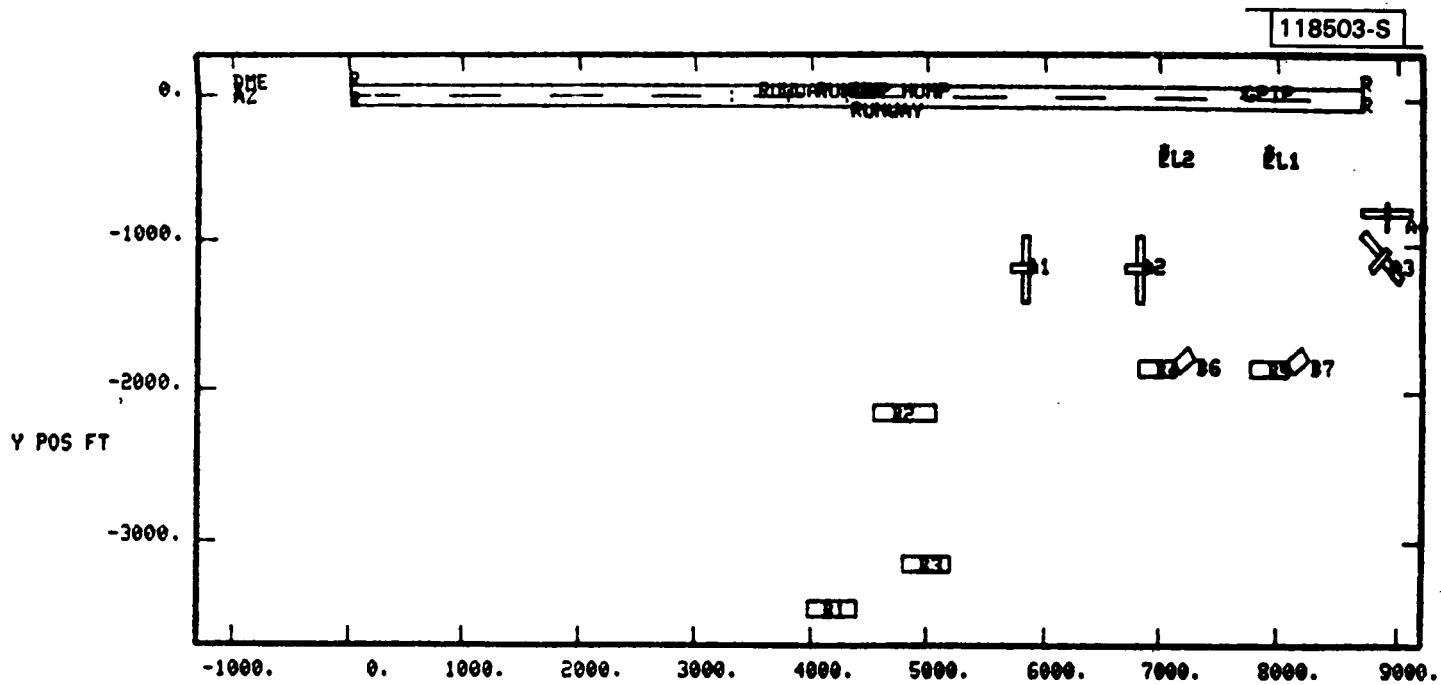


FLT PTH A

AZ SYSTEM

| OBST | RANK | AMP | DIST | RDOP |
|---|---|---|---|---|
| G | 12 | 80 | 0.0 | 0. |
| B1 | 1 | 0 | 8079.1 | -35. |
| B2 | 2 | 2 | 7376.6 | -14. |
| B3 | 4 | 5 | 6542.4 | -24. |
| B4 | 6 | 25 | 2766.3 | -5. |
| B5 | 7 | 26 | 790.4 | -4. |
| B6 | 10 | 39 | 9747.5 | -135. |
| B7 | 3 | 2 | 9352.4 | -193. |
| A1 | 9 | 29 | 4961.7 | -3. |
| A2 | 8 | 27 | 9132.8 | -32. |
| A3 | 5 | 19 | 9045.0 | -240. |
| A4 | 11 | 61 | 9001.1 | -275. |
| D | 0 | 80 | 0.0 | 0. |

EL SYSTEM

| OBST | RANK | AMP | DIST | RDOP |
|---|---|---|---|---|
| G | 1 | 0 | 10012.5 | 0. |
| B1 | 11 | 60 | 7420.5 | -27. |
| B2 | 7 | 56 | 6981.4 | -12. |
| B3 | 9 | 58 | 7376.6 | -29. |
| B4 | 4 | 41 | 9176.7 | -77. |
| B5 | 3 | 26 | 9045.0 | -116. |
| B6 | 6 | 50 | 9396.3 | -94. |
| B7 | 5 | 42 | 9220.7 | -176. |
| A1 | 10 | 59 | 0.0 | -1. |
| A2 | 8 | 58 | 0.0 | -1. |
| A3 | 2 | 22 | 9045.0 | -235. |
| A4 | 12 | 62 | 9001.1 | -253. |
| D | 0 | 80 | 0.0 | 0. |

RANK = multipath ranking

AMP = maximum -M/D ratio (dB)

DIST = distance along flight path (ft) at which maximum M/D occurred = 17700 - x pos (ft)

RDOP = relative Doppler (Hz) at point of maximum M/D

Fig.4-25. Airport map for WG-A scenario 2 for L-band carrier.

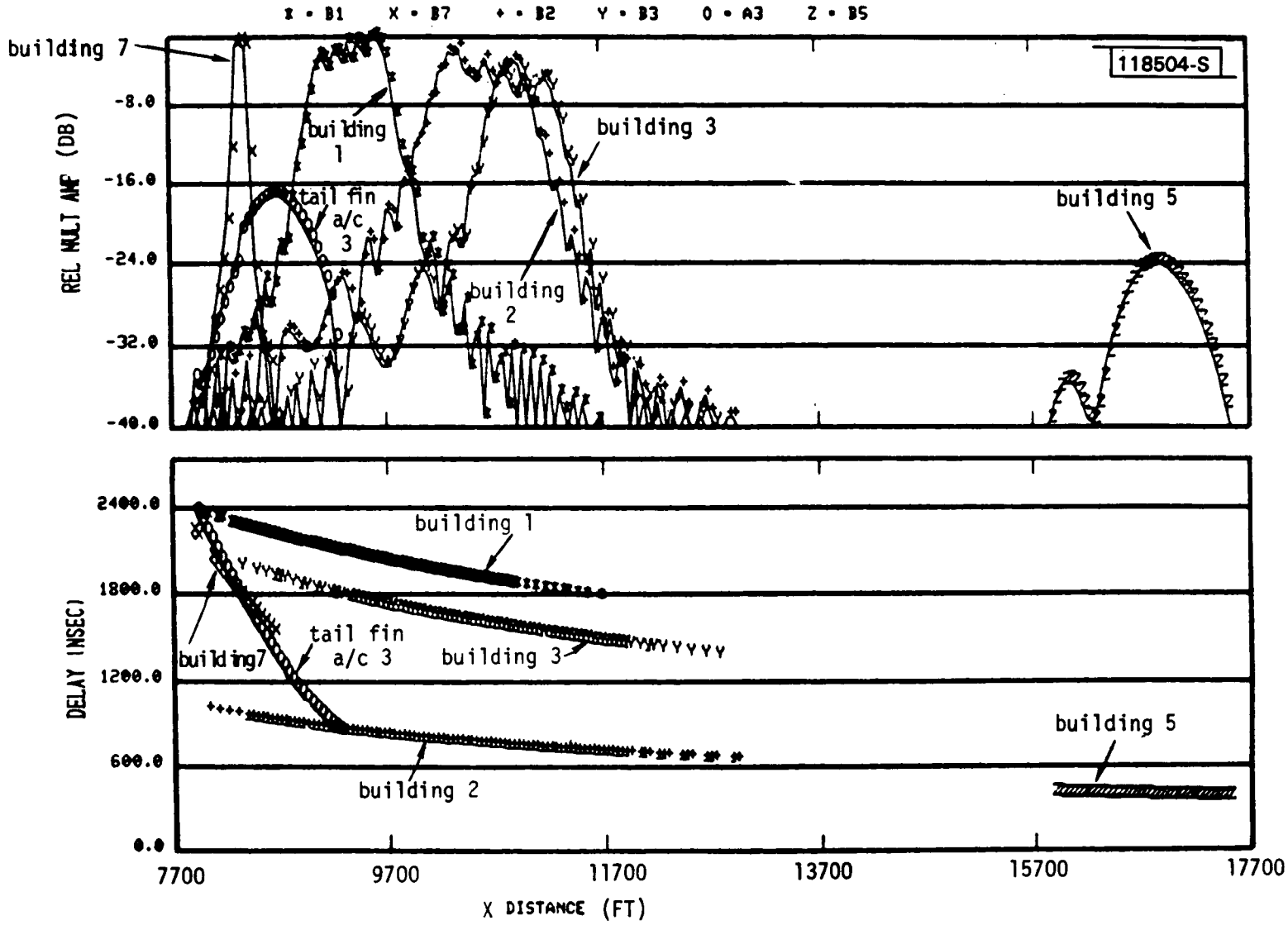


Fig.4-26. DME multipath levels and relative time delays for AWOP scenario 2.

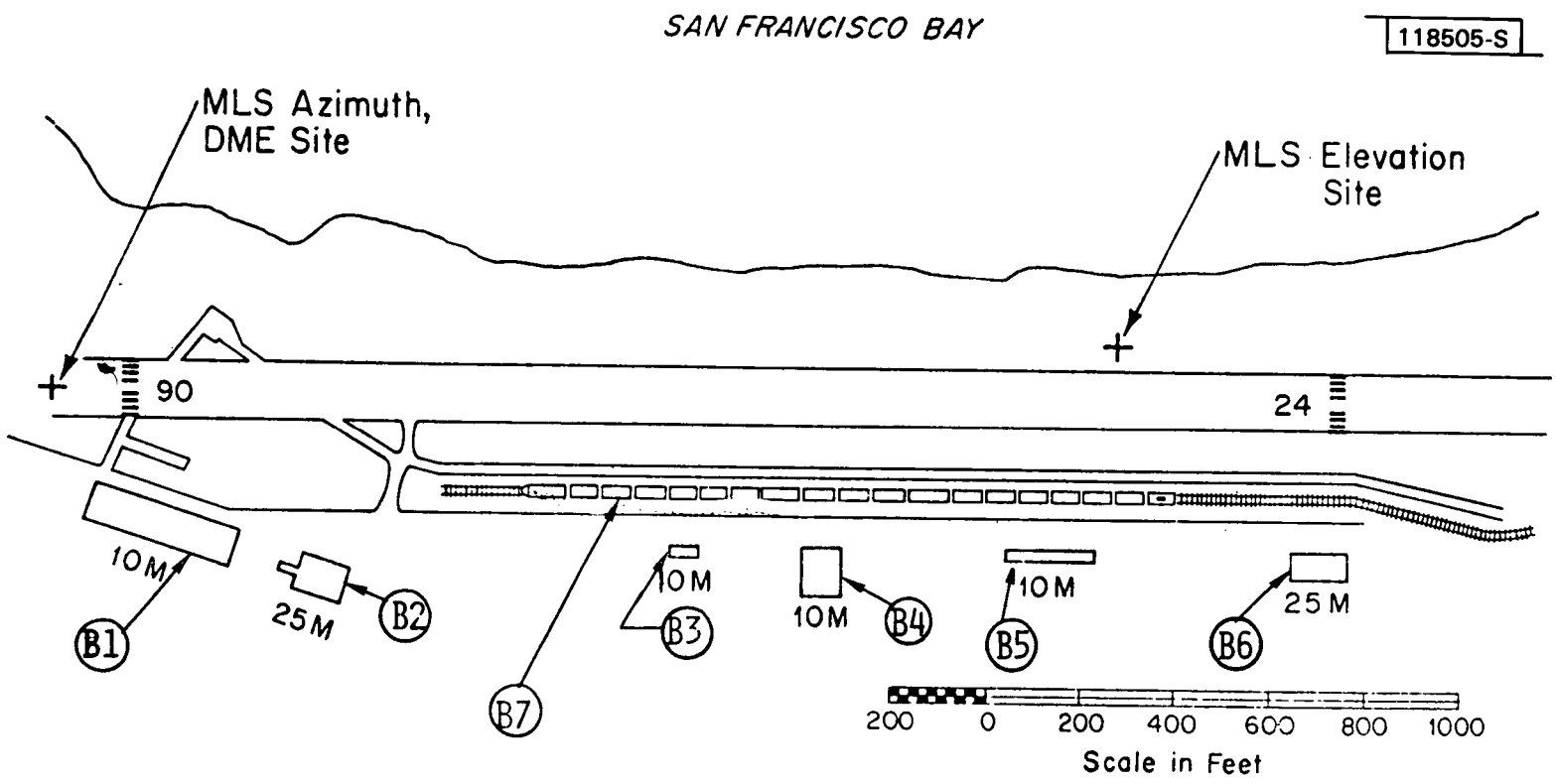


Fig.4-27. AWOP scenario 3 based on Crissey Army Airfield in San Francisco.

multipath with relative delays greater than 400 nsec, we see that scenario 2 would not be a stringent test of the optimized design.

Scenario 3 shown in Fig. 4-27 was based on the geometry at Crissey Army Base near San Francisco. This STOL scenario has high level building multipath with short relative delays (see Fig. 4-28) as well as low scalloping rates. This combination of multipath characteristics is such that multipath errors can be expected for even an optimized DME/P design.

Figure 4-29 shows the computed errors computed by DFVLR[42] for this scenario with the following DME/P system implementation:

| | |
|---|---|
| pulse: | $\cos - \cos^2$ with 10% - 90% risetime of 800 ns |
| thresholding: | delay-and-compare with gain of 2 and 100 ns delay |
| ground antenna: | 4 ft. vertical aperture with a pattern rolloff of approximately 3 dB/deg at the horizon [9] |
| height: | 6 feet. |

A comparison of the error trace with the multipath diagnostic plot shows that the peak error occurs where the B1 multipath is largest (M/D = 0 dB, $\tau$ = 110 nsec). Equation (A-35) predicts a maximum error of about 40 feet at this point; the error trace indicates a 50 foot error. Motion averaging here was effective only in the vicinity of runway threshold.

Figure 4-30 shows a DME/P multipath scenario which was developed by translating the locations of several buildings at Heathrow Airport down the runway and increasing the building heights*. Table 4-1 shows the building locations and heights assumed for this scenario. Figure 4-31 shows the effective M/D ratio and time delays while Fig. 4-32 shows the errors computed by DFVLR[42]. The errors here are low due to the relatively long time delays.

---

* DME/P multipath levels from these actual buildings will be quite low due to their location and low heights.

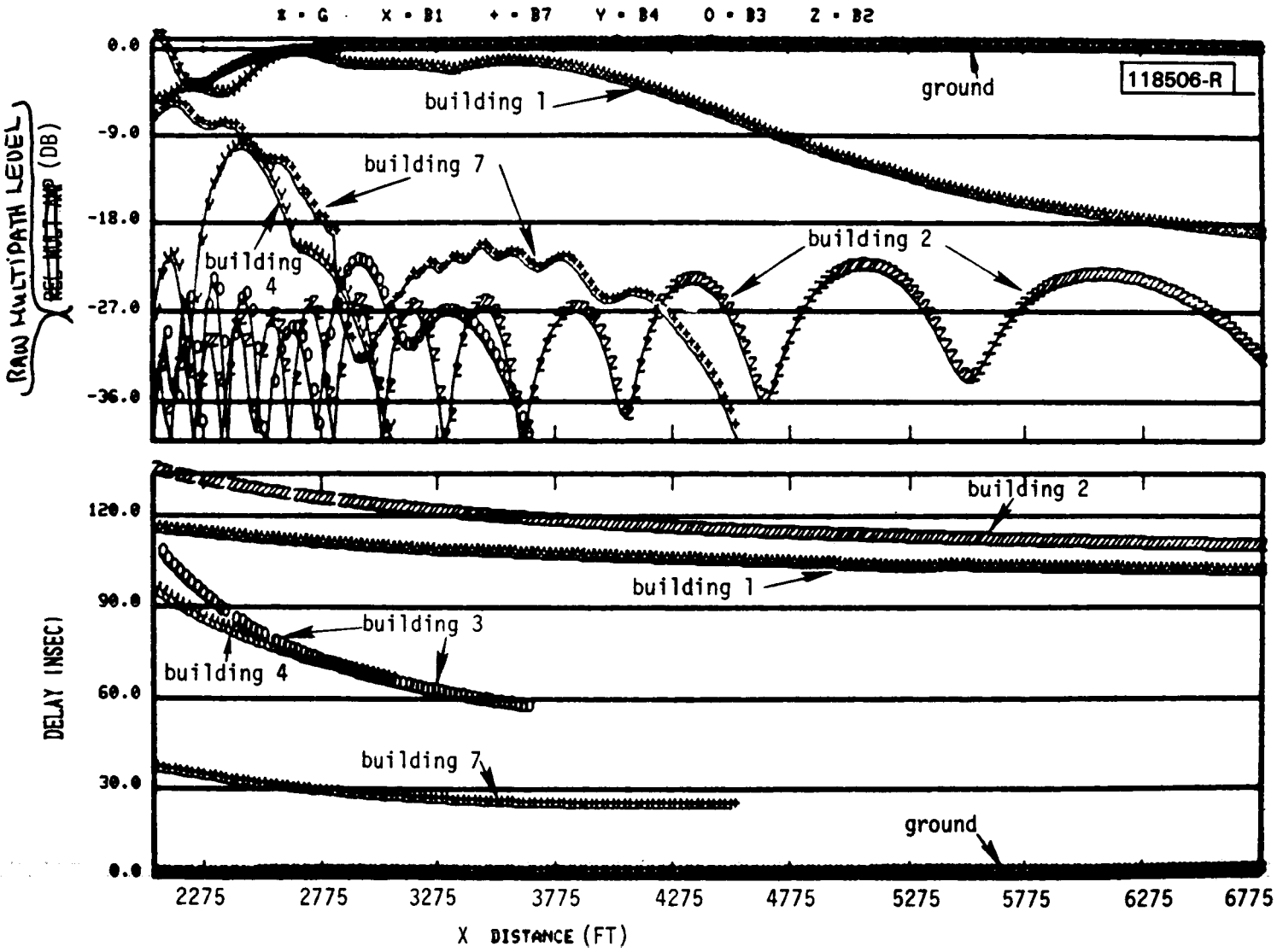


Fig.4-28(a). DME multipath levels and relative time delays for AWOP scenario 3.

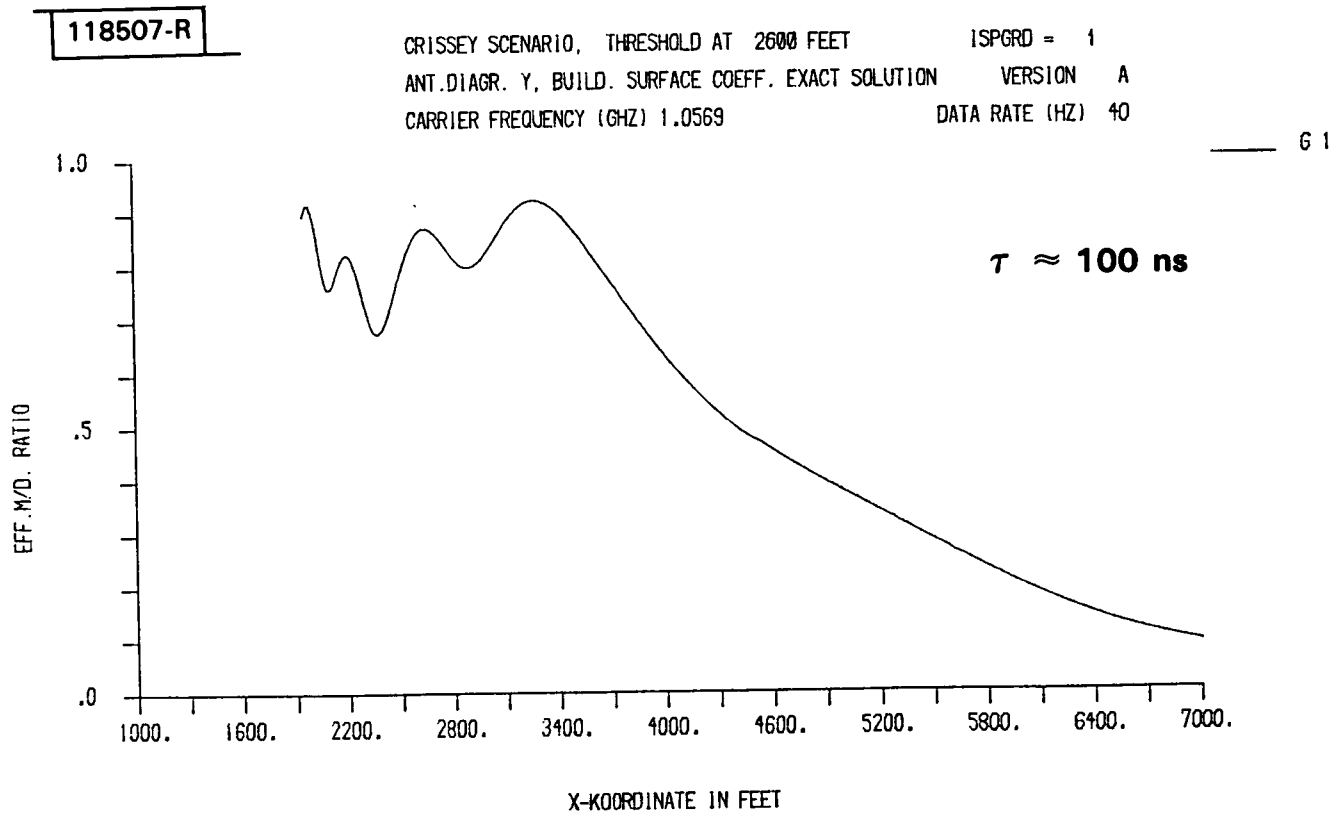


Fig.4-28(b). Effective M/D ratio for Building #1 in AWOP scenario 3 (from [42]).

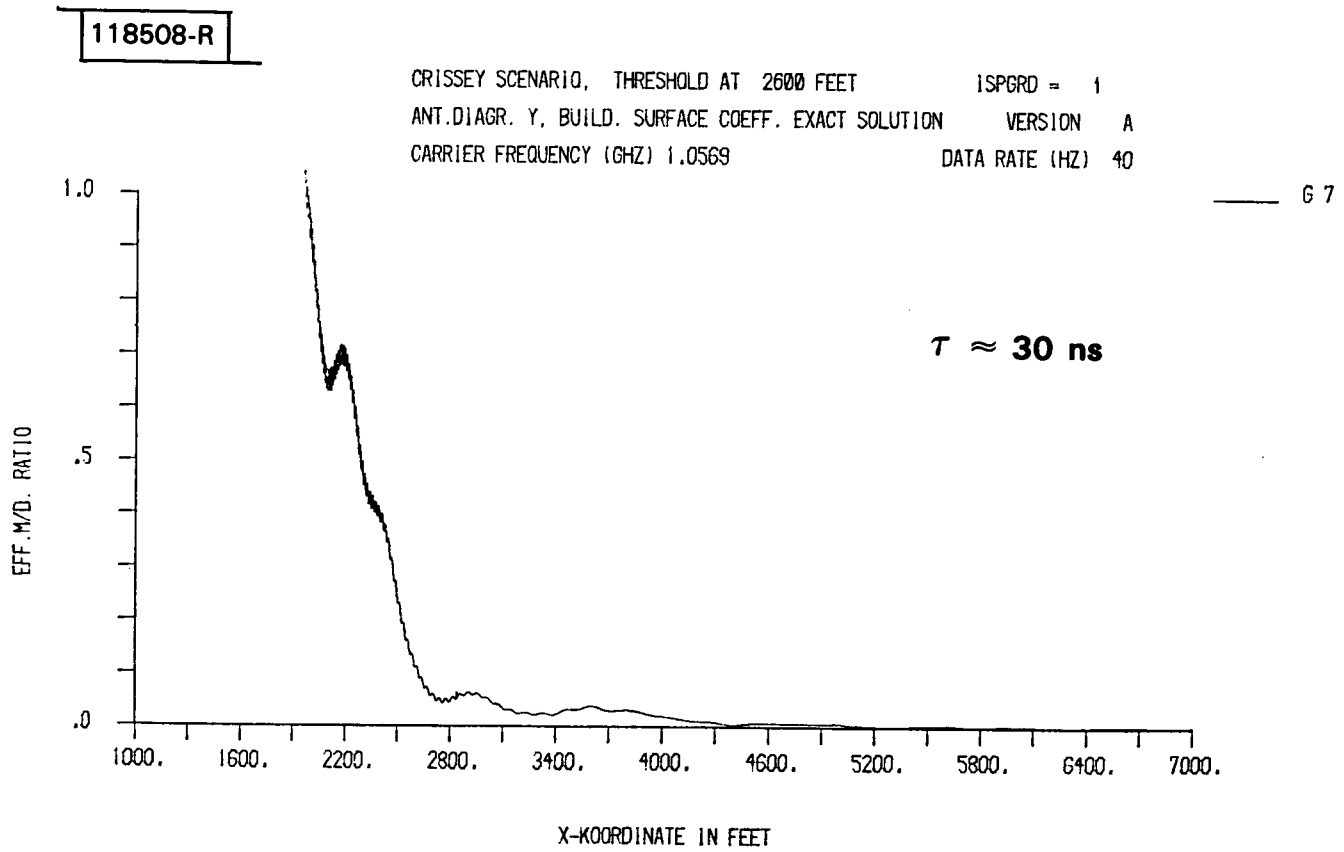


Fig.4-28(c). Effective M/D ratio for Building #7 in AWOP scenario 3 (from [42]).

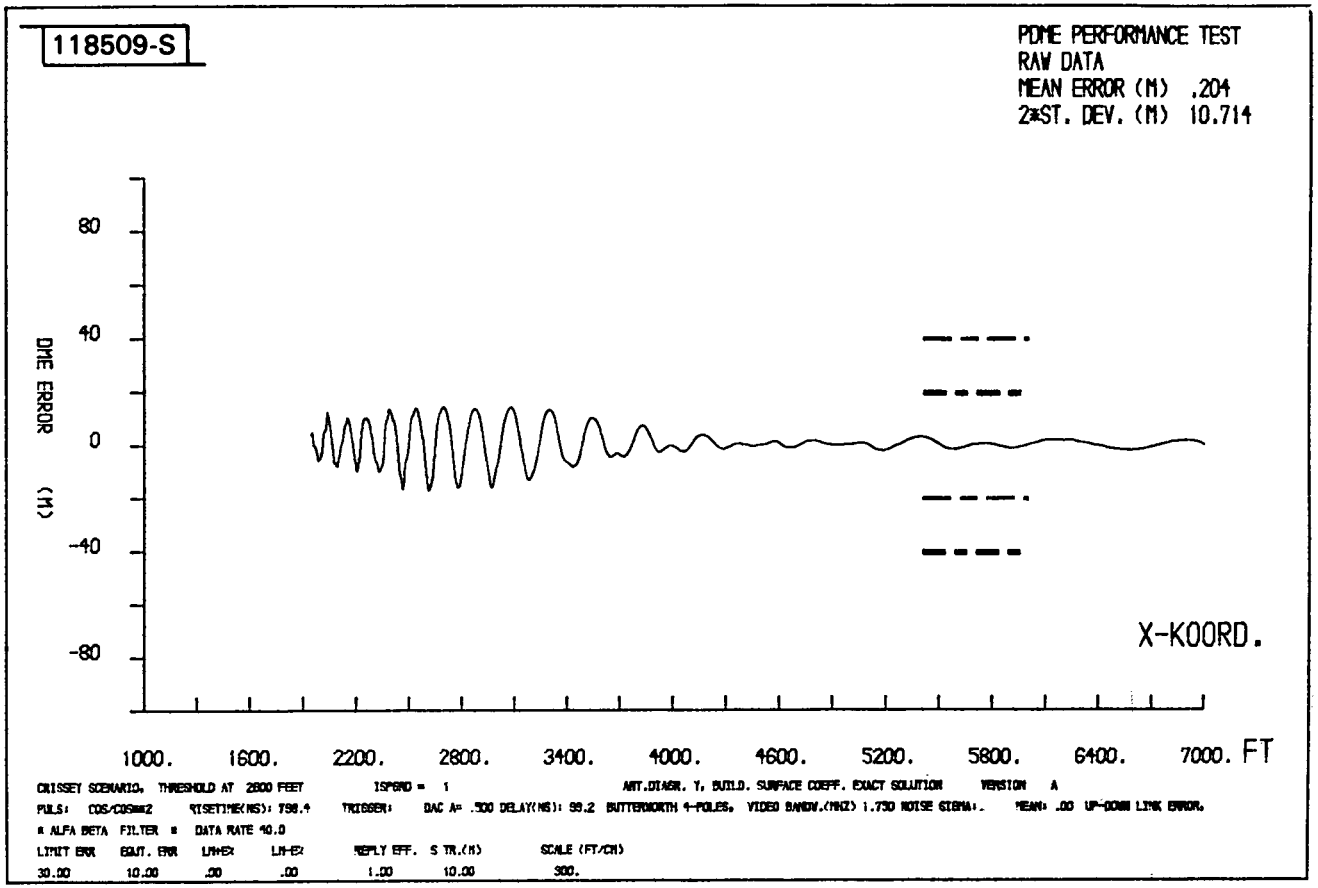


Fig.4-29(a). Raw DME/P error for AWOP scenario 3.

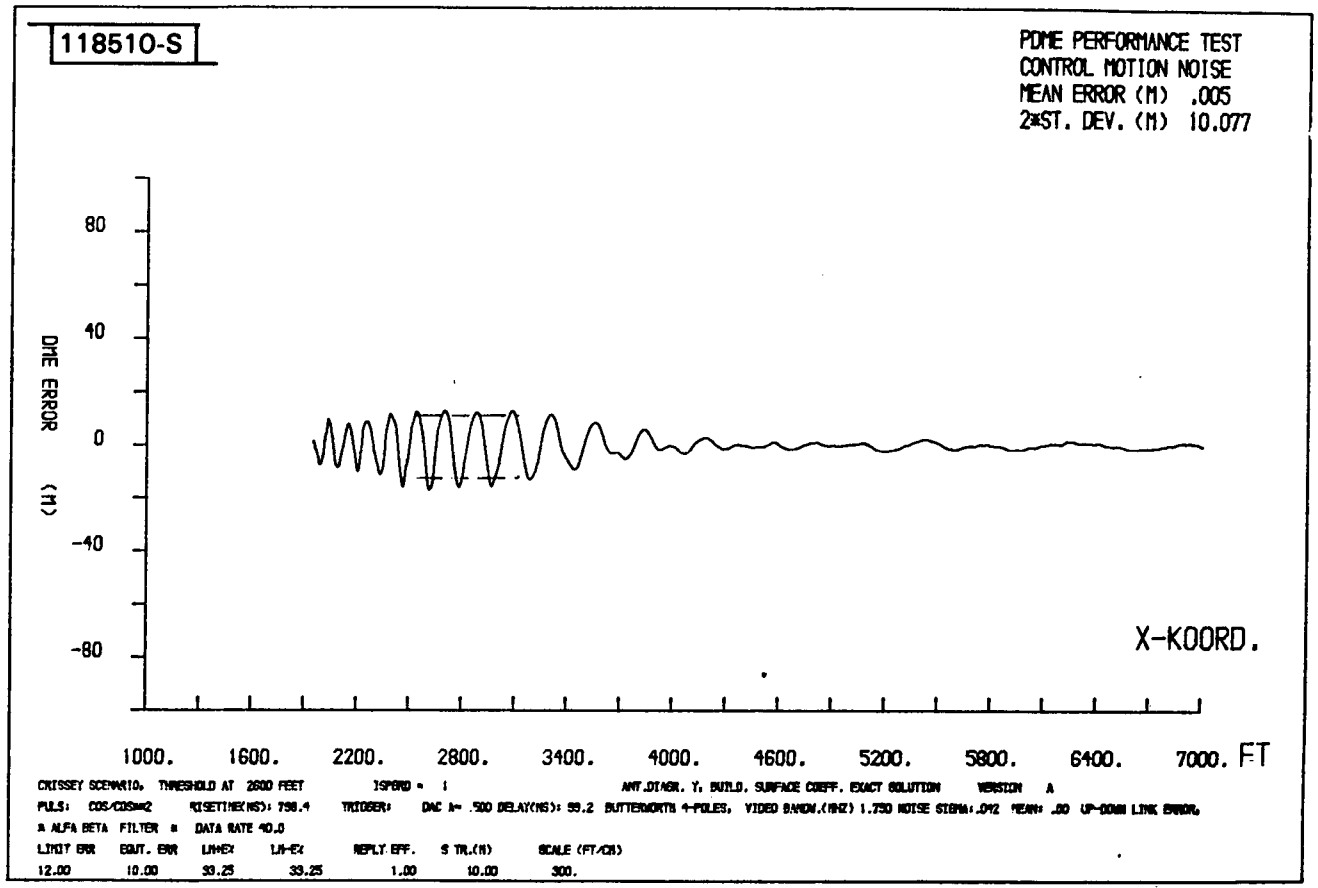


Fig.4-29(b). CMN error filter output for AWOP scenario 3.

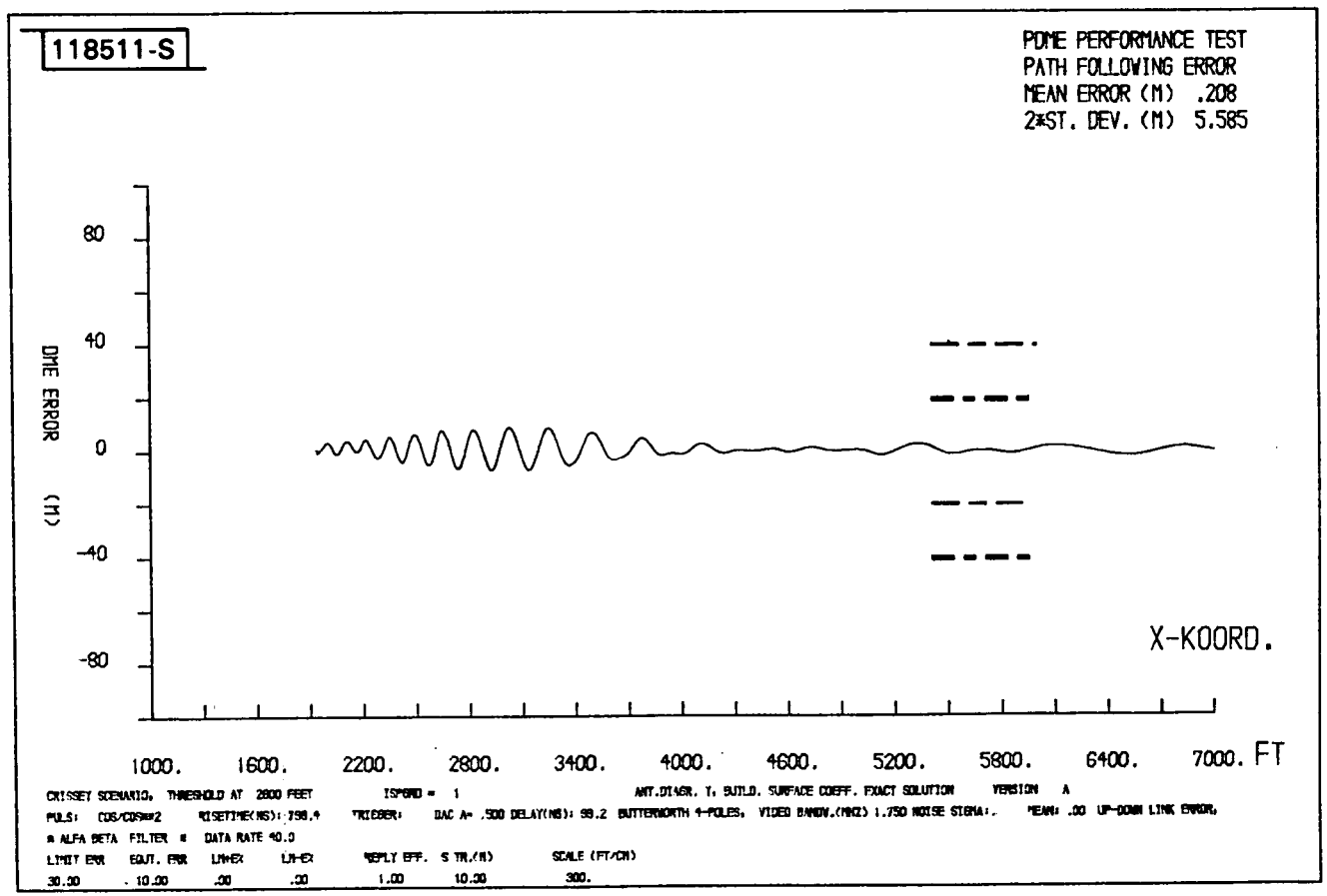


Fig.4-29(c). PFE error filter output for AWOP scenario 3.

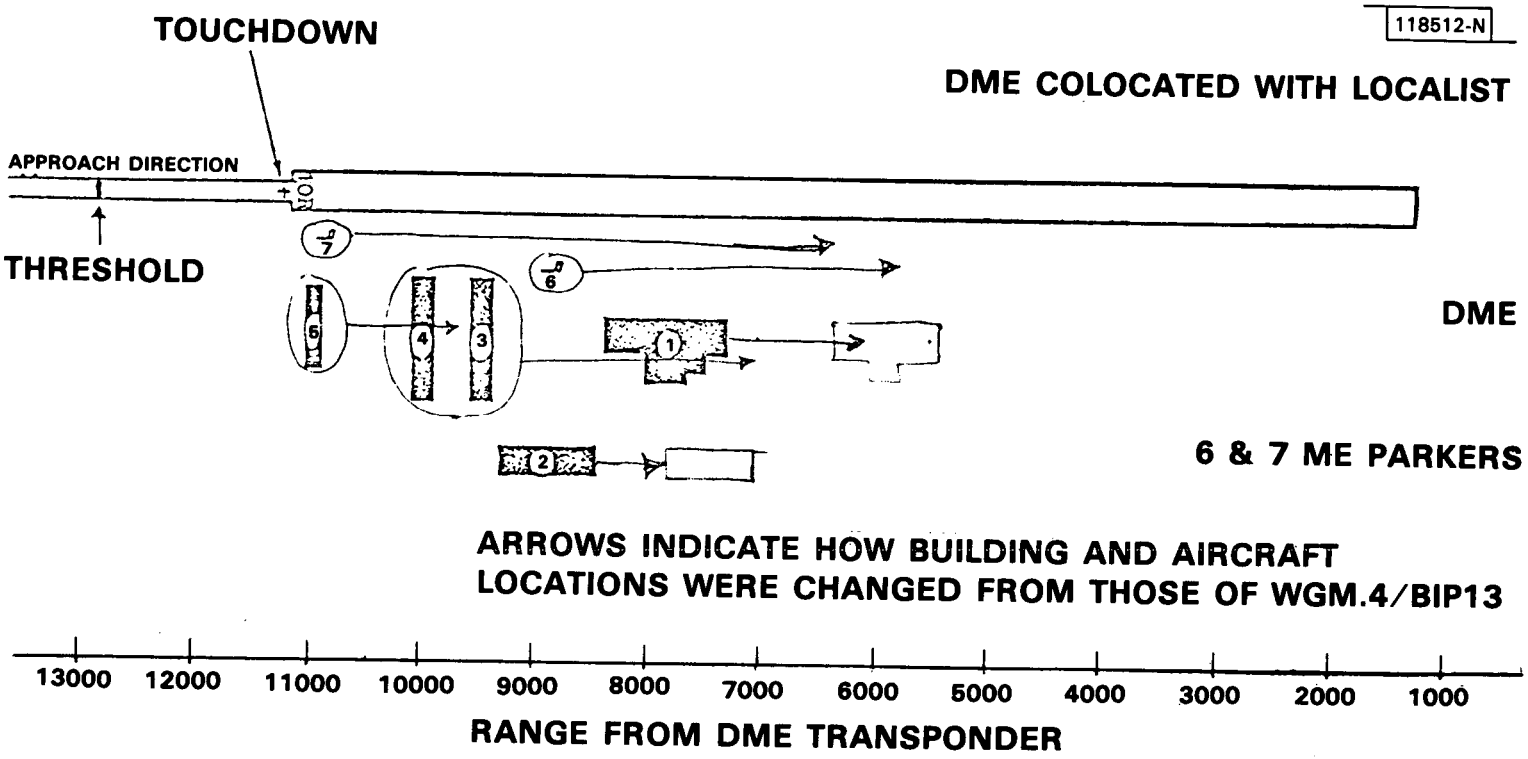


Fig.4-30. Precision pulse CTOL scenario.

TABLE 4-1
BUILDING AND AIRCRAFT LOCATIONS FOR
PRECISION PULSE CTOL SCENARIO

| Building | Center of Specular Region x Coordinate (ft) | Building Locations | | Height (ft) |
|---|---|---|---|---|
| 1 | 12000 | (5500,1082) | (6550,1082) | 83 |
| 2 | 14600 | (7000,2180) | (7750,2180) | 100 |
| 3 | 15100 | (7550,738) | (7763,738) | 50 |
| 4 | 16100 | (8050,738) | (8263,738) | 50 |
| 5 | 19000 | (9639,836) | (9803,836) | 40 |

Aircraft Locations

| | Nose Location | Orientation |
|---|---|---|
| 6 | (5500,492) | Parallel to Runway |
| 5 | (6400,410) | Parallel to Runway |

Origin of Azimuth Transmitter is at (0,0,5)

DME is colocated with Azimuth Transmitter and is at (0,0,30)

DME Height (Phase Centre) is 30 ft.

Aircraft "Touchdown" is at 11,000 ft.

Flight Path: Linear from (21000,0,410) to (12800,0,50)
Linear from (12800,0,50) to (11000,0,8)

Flat Terrain: $(e/e_o = 3)$

Building Surface Reflection Coefficient as in AWOP WG-A
(-1 dB for cases shown)

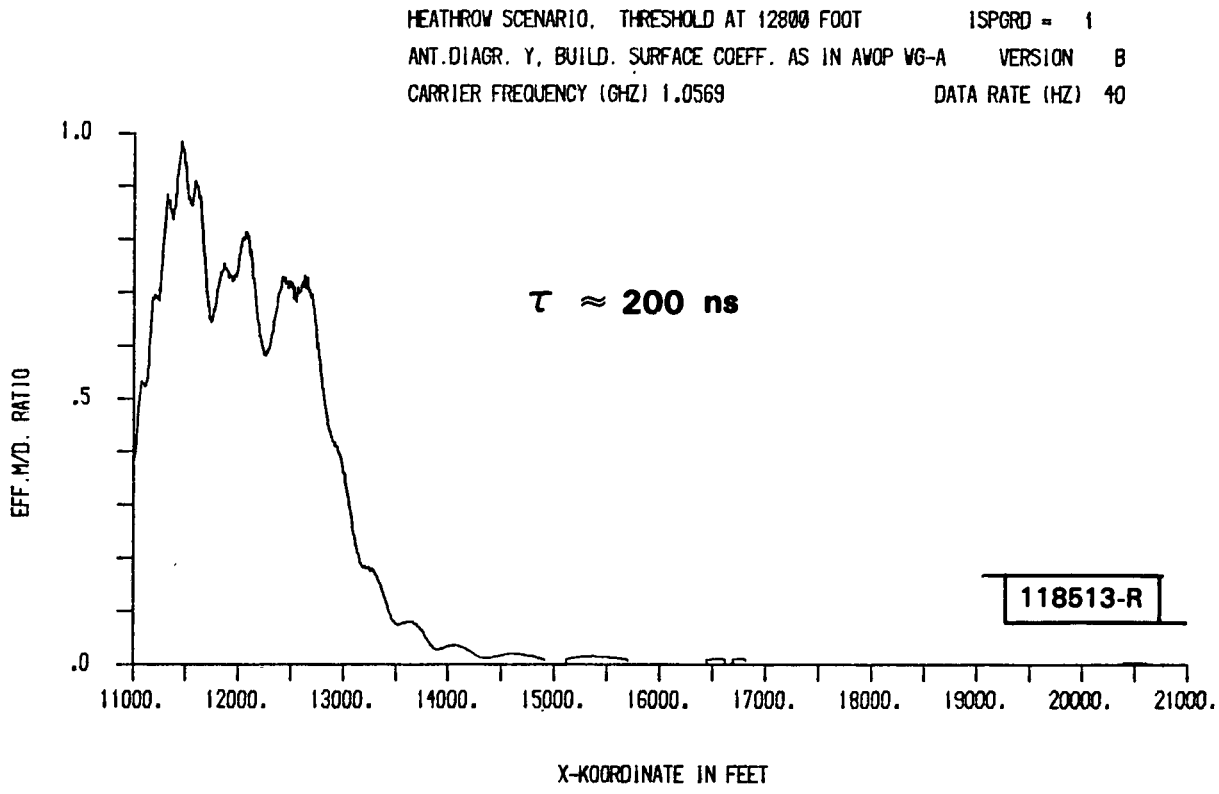


Fig.4-31(a). Effective M/D ratio for Building #1 in DME/P CTOL scenario.

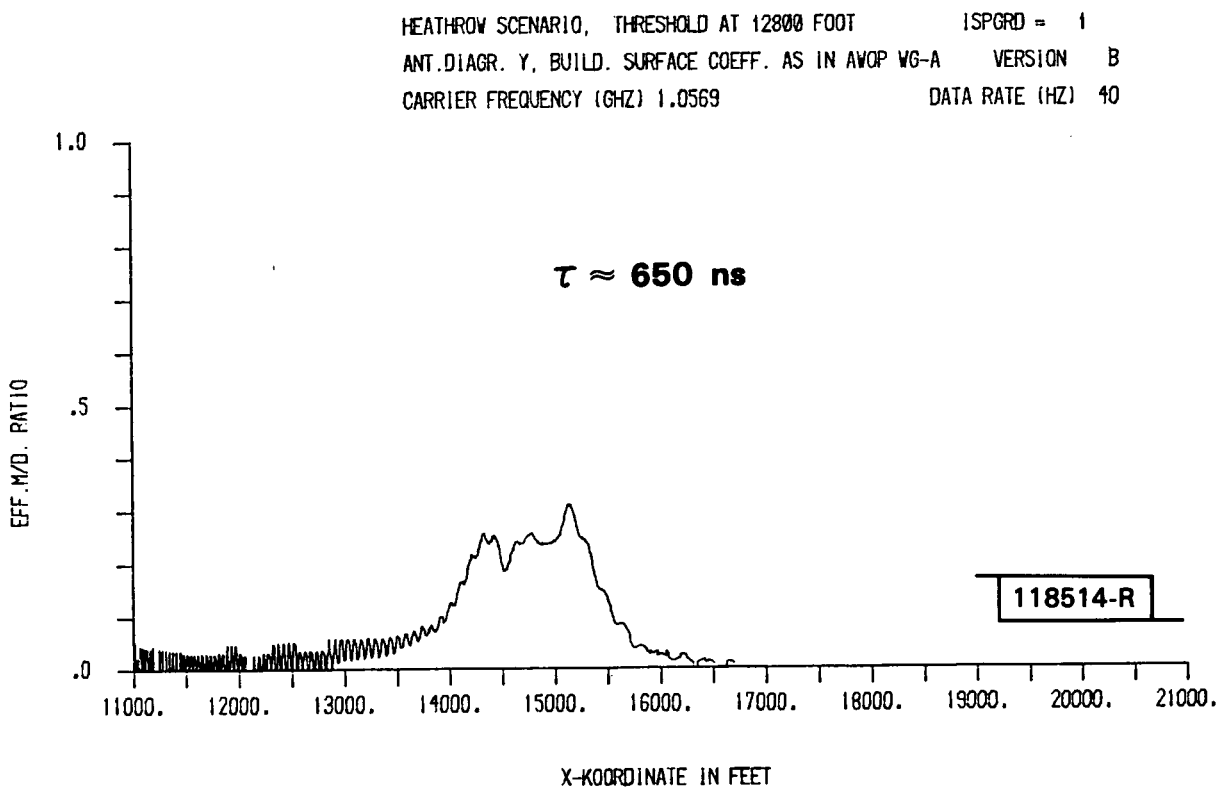


Fig.4-31(b). Effective M/D ratio for Building #2.

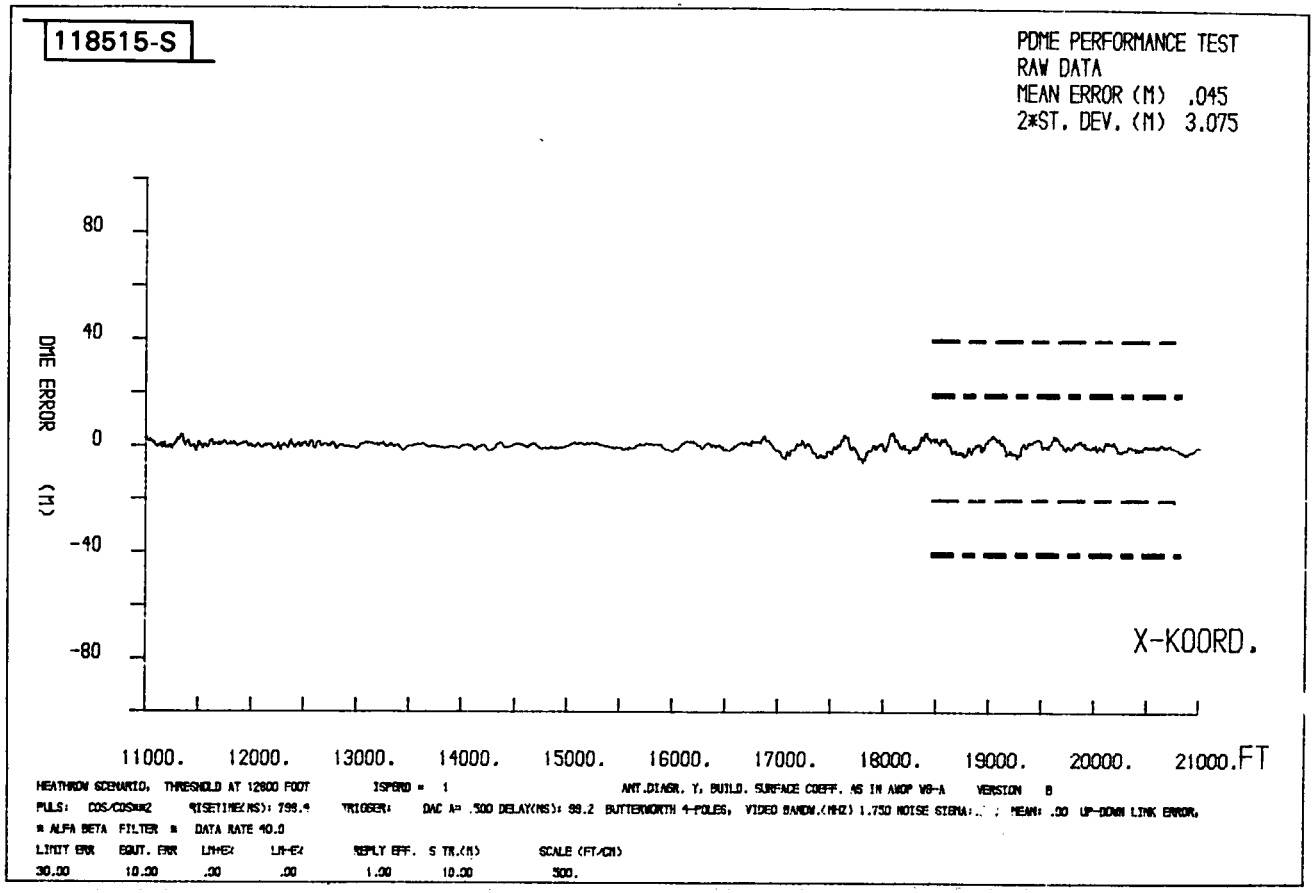


Fig.4-32(a). Raw DME/P errors for DME/P CTOL scenario.

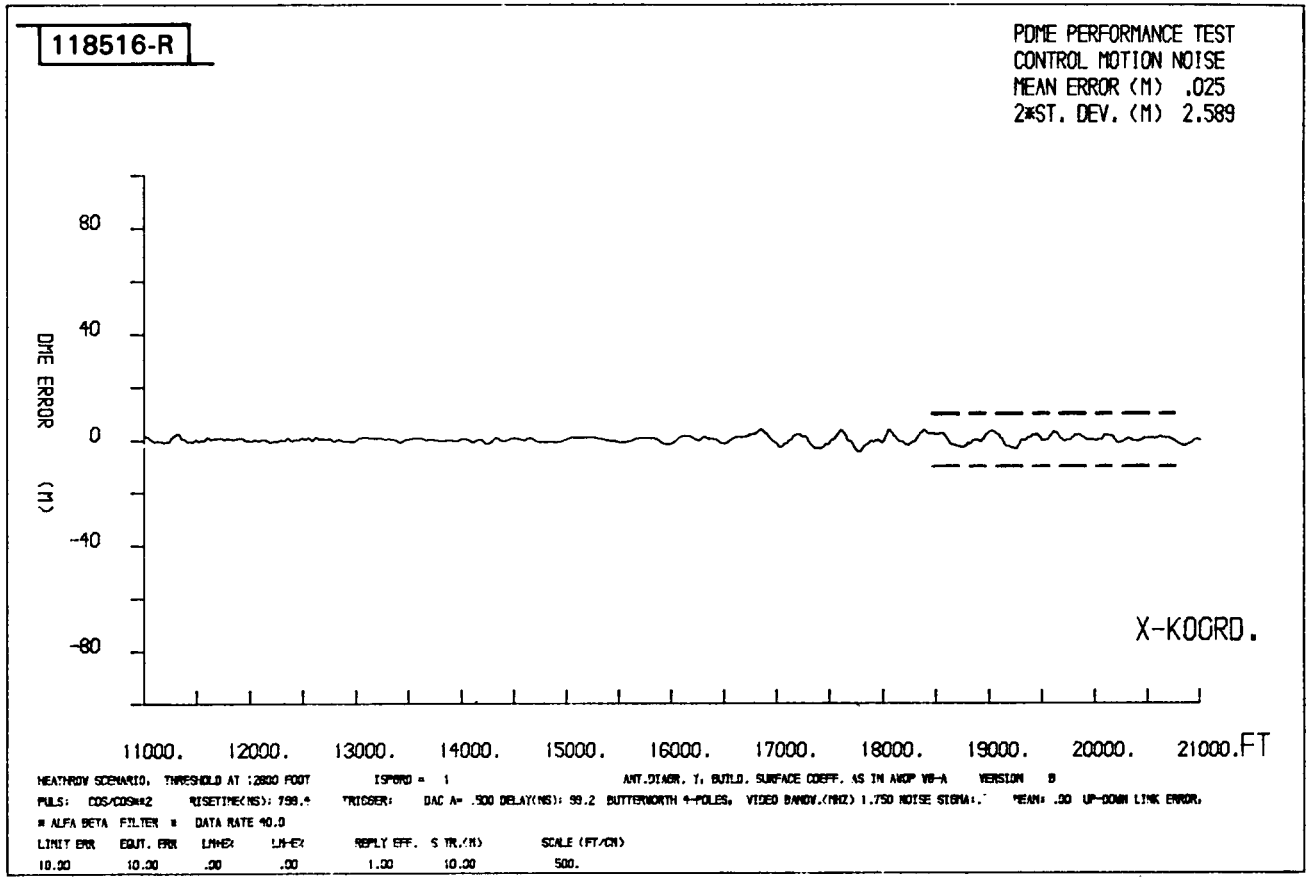


Fig.4-32(b). CMN error filter output for DME/P CTOL scenario.

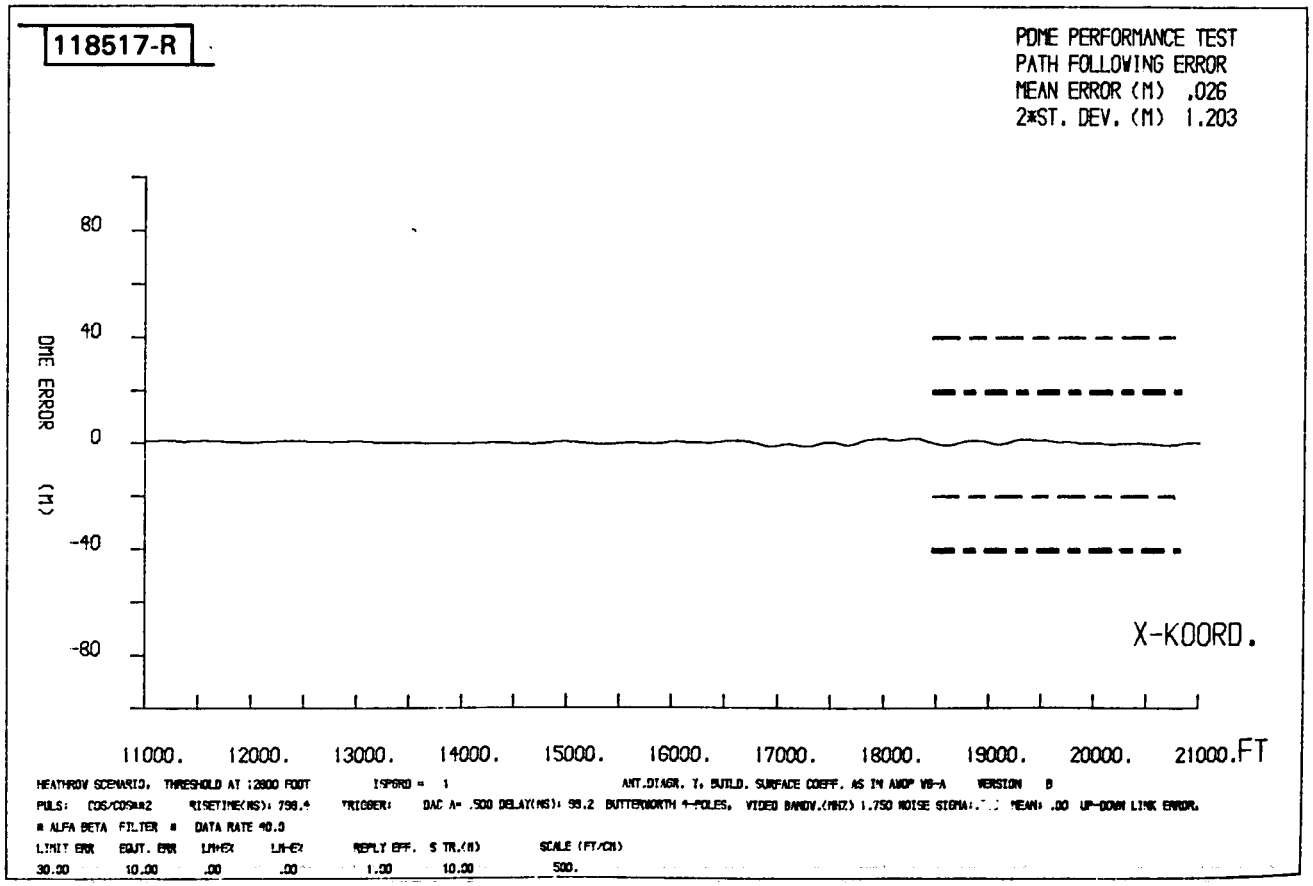


Fig.4-32(c). PFE error filter for DME/P CTOL scenario.

It should be emphasized that both of these scenarios were contrived to be quite stressful to DME/P. However, the fact that fairly good performance was obtained in both cases with the "nominal" DME/P design is encouraging.

## V. EXPERIMENTAL STUDIES BY LINCOLN LABORATORY

The analysis in Chapter III and simulation studies of Chapter IV indicate that specular reflections from buildings are an important challenge to successful DME/P operation, and, that there is some uncertainty regarding the reflection levels from irregular terrain and/or small scatterers at the airport. In this section, we summarize experimental work at Lincoln Laboratory* which substantiates the principal factors identified in the preceding chapters. The first of the factors concerns the lobing in the direct level as the interrogator nears the threshold. Quantitative L-band data related to this issue was obtained in the context of airport surface traffic control (ASTC) studies and is reported in Section A. Section B describes the results of building reflection measurements made at some six US airports to (partially) validate the computer simulations. Section C discusses the results of S-band (3 GHz) high time resolution measurements at L. G. Hanscom airfield to assess the reflection levels from a nominally flat airport runway environment while section D considers multipath from irregular terrain.

### A. ASTC Measurements of Direct Signal Lobing

The classical flat earth propagation model presented in Chapter III has been used for the power budget calculation in the bulk of the PDME proposals (e.g., [3, 12, 14]) to date. Nevertheless, most airport runways have various undulations which potentially could yield a received signal level vs. interrogator height which is rather different from the $h^2 R^{-4}$ dependence indicated in Chapter III. As an outgrowth of studies at Lincoln Laboratory on

---

*It had originally been hoped that a more substantive quantitative multipath data base would be available given the wide spread use of DME. However, it appears that the current DME has not been used for precision approach and landing guidance, and (as noted earlier) the DME/P tests to date have not been conducted at sites with substantial building multipath. Appendix B discusses related experimental work by others.

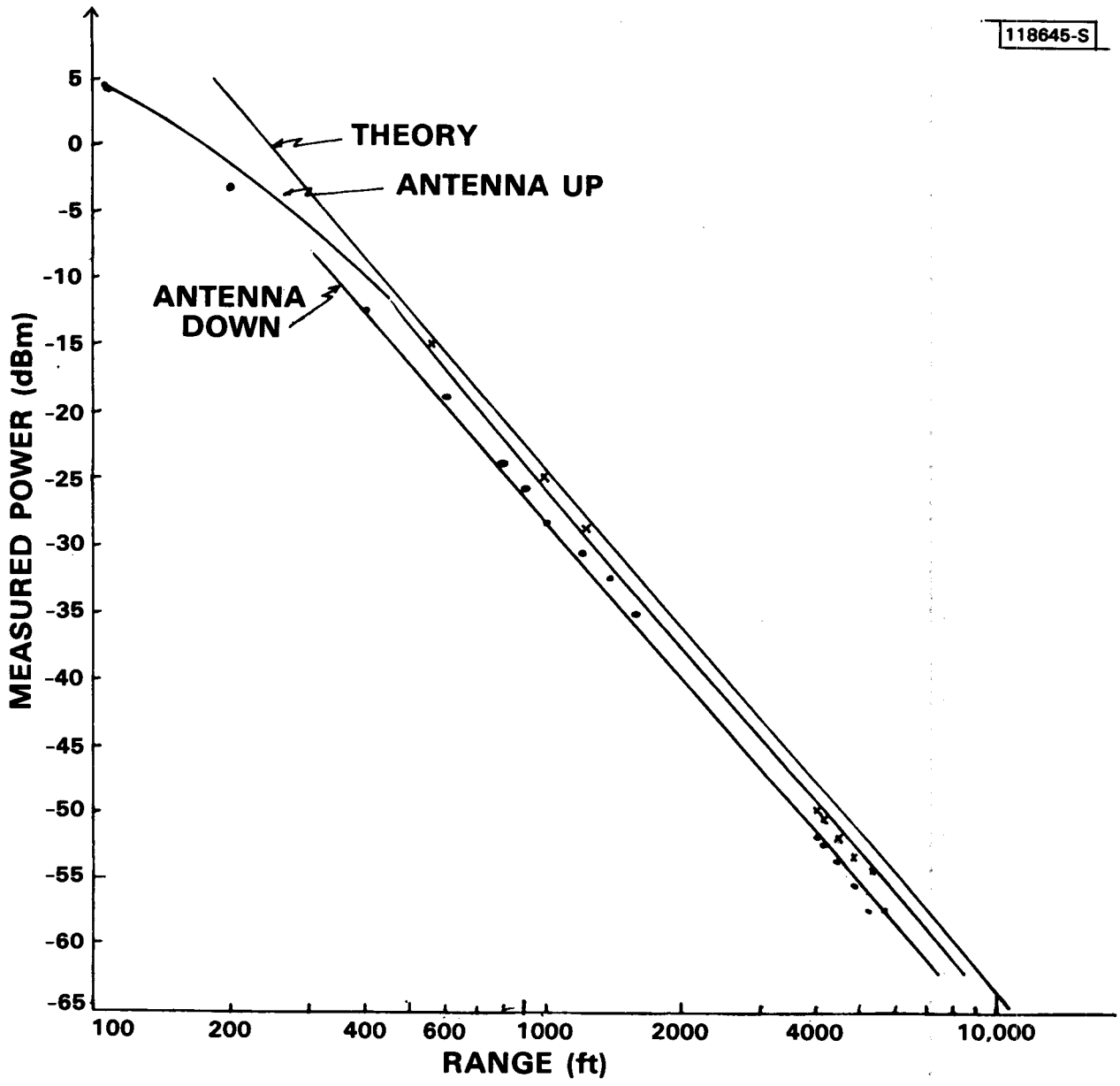


Fig.5-1. Measured signal level along Hanscom taxiway with both antennas at 5 feet, dipole pointed down (from McGarty [22]).

the feasibility of achieving airport surface traffic control with an ATCRBS/DABS based system, measurements of the received signal power were made along several taxiways at the L.G. Hanscom Airport (Bedford, MA) at various transmitter-receiver geometries [22]. Figure 5-1 shows the results of one such measurement. We see that the measured levels at two different heights fit the $R^{-4}$ law quite well over a distance range of several octaves. Measurements at various receiver heights for fixed ranges showed similar good agreement.

## B. Summary Results of L-Band Airport Measurements

In this section, we summarize the principal results of measurements accomplished at a number of US airports to quantify the L-band multipath environment. The program objectives were:

1) measurement of the principal multipath parameters (amplitude and time delay) with realistic aircraft/ground site locations at runways which had the major DME/P multipath sources (large buildings) identified in previous analytical (simulation) studies.

2) determination of whether significant DME/P multipath sources exist which had not been considered to date in the DME/P studies to date, and

3) comparison of the measured results with computer simulation results obtained with simplified airport models (such as have been used for DME/P system design to date).

The measurements placed particular emphasis on the final approach region including the flare and rollout regions since these areas correspond to the most stringent DME/P accuracy requirements and, have not been utilized operationally with the current L band DME.

Measurements were made at five major operational US airports (Philadelphia, Washington National, Wright Patterson AFB, St. Louis, and Tulsa) as well as a preliminary test at Quonset Point, RI. Since these

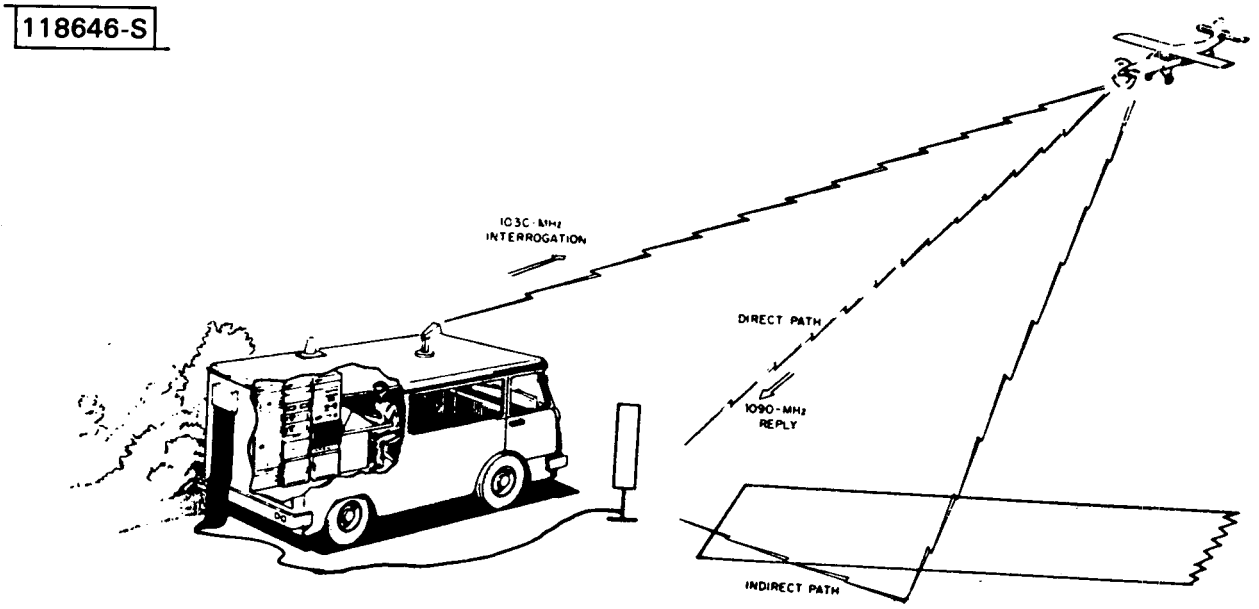


Reply pulse width ~ 100 nsec

Received amplitude digitized (8 bits) every 50 nsec

Aircraft range also recorded

Fig.5-2. DME/P multipath measurement system.

measurements are described in depth in a companion report [46], the discussion here attempts to provide an example of the results obtained at each airport and then summarizes the remaining data.

A highly mobile equipment was desired which could measure the multipath parameters of greatest interest. This was accomplished by transmitting a narrow (100 nsec - 200 nsec wide) L-band pulse from an aircraft and (digitally) recording the received signal envelope at a ground antenna as a function of time as shown in Figs. 5-2 and 5-3. By examination of the digitized envelope, it was then possible to determine the pertinent multipath characteristics (amplitude and time delay relative to the direct signal level) on a given signal reception. The aircraft transmitted signals at a 10 Hz rate, corresponding to approximately 18 feet of aircraft displacement between successive measurements. This relatively dense spatial sampling of the multipath environment allowed us to use correlation between adjacent measurements to reject erroneous data due to cochannel interference and/or low signal to noise ratio (SNR).

Aircraft range information was obtained by having the narrow pulse transmission times controlled by a standard Air Traffic Control Radar Beacon (ATCRBS) transponder which was being interrogated by the ground measurement system. In this way, the delay time between the interrogation and received ATCRBS reply yielded the aircraft range. The flight profiles were such (e.g., centerline approaches using an ILS localizer to furnish vertical position) that knowledge of the range generally would permit one to determine the aircraft position.

Each (digitized) received waveform was examined to locate discrete pulses according to criteria based on pulse width and magnitude. Cochannel interference due to asynchronous replies from other ATCRBS transponders was rejected by measurement of the pulse width. The reduced pulse parameter data were then displayed in plots of multipath level and time delay versus distance along the flight path. By considering the nature of adjacent multipath environment estimates and repeatability of the phenomena between successive

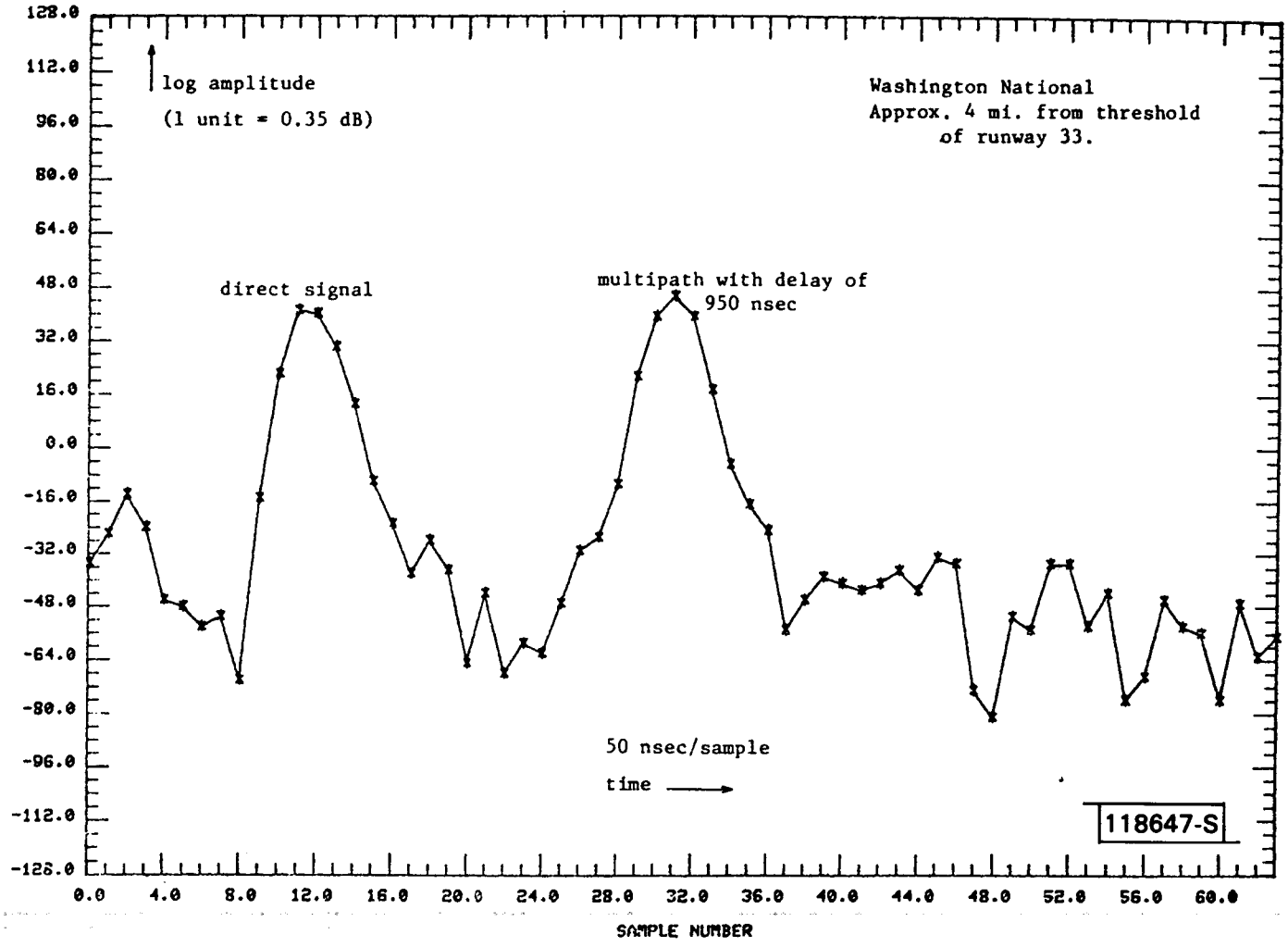


Fig.5-3. Example of digitized waveform.

(nominally) identical runs, it was possible to identify questionable data which required hand analysis of the waveforms.

1. Washington National Airport (DCA)

Figure 5-4 shows the airport geometry at DCA. Measurements were made on 3° and 6° approaches to runway 15 since the runway is to be used for STOL operations with a small community MLS. The principal multipath identified in the preliminary airport survey was the row of hangars (hangars 9-12) across the runway from the measurement van. The hangar fronts were largely smooth metal with a height of 20 m (60 feet).

Figures 5-5 and 5-6 show results of analyzing* the received waveforms

---

*The principal focus for the automated analysis was specular reflections which are manifested by large pulses which are well separated from the direct signal as shown in Fig. 5-3. The criteria used to identify the pulses were:

2. the peak amplitude should correspond to an SNR of at least +10 dB or, the minimum M/D ratio of concern (typically -20 dB)

3. the pulse width between -6 dB points should lie in the interval (W -50 μsec, W +100 μsec) where W = expected pulse width in μsec. (W = 150μs for the narrowest pulses used)

The first pulse encountered in the digitized time interval which meets the above criteria was assumed to be the direct signal. The peak level of the pulse is taken to be the direct signal amplitude and the direct signal amplitude and the point midway between the first leading and trailing edge digitized amplitudes which are at least 6 dB down from the peak level is taken to be the centroid.

If no pulses meeting the above criteria were encountered in the digitized waveform, an "M" is placed on the M/D summary plot at the -25 dB M/D level and no symbol is placed in the corresponding time delay ($\tau$) plot. If only a "direct" pulse is encountered, an "X" is plotted at -20 dB on the M/D plot with no corresponding symbol on the $\tau$ plot.

Any additional pulses meeting criteria (1) and (2) are assumed to be multipath. Their peak amplitude and centroid are computed as for the direct signal. The displayed M/D ratio represents the ratio of peak amplitudes while (con't.)

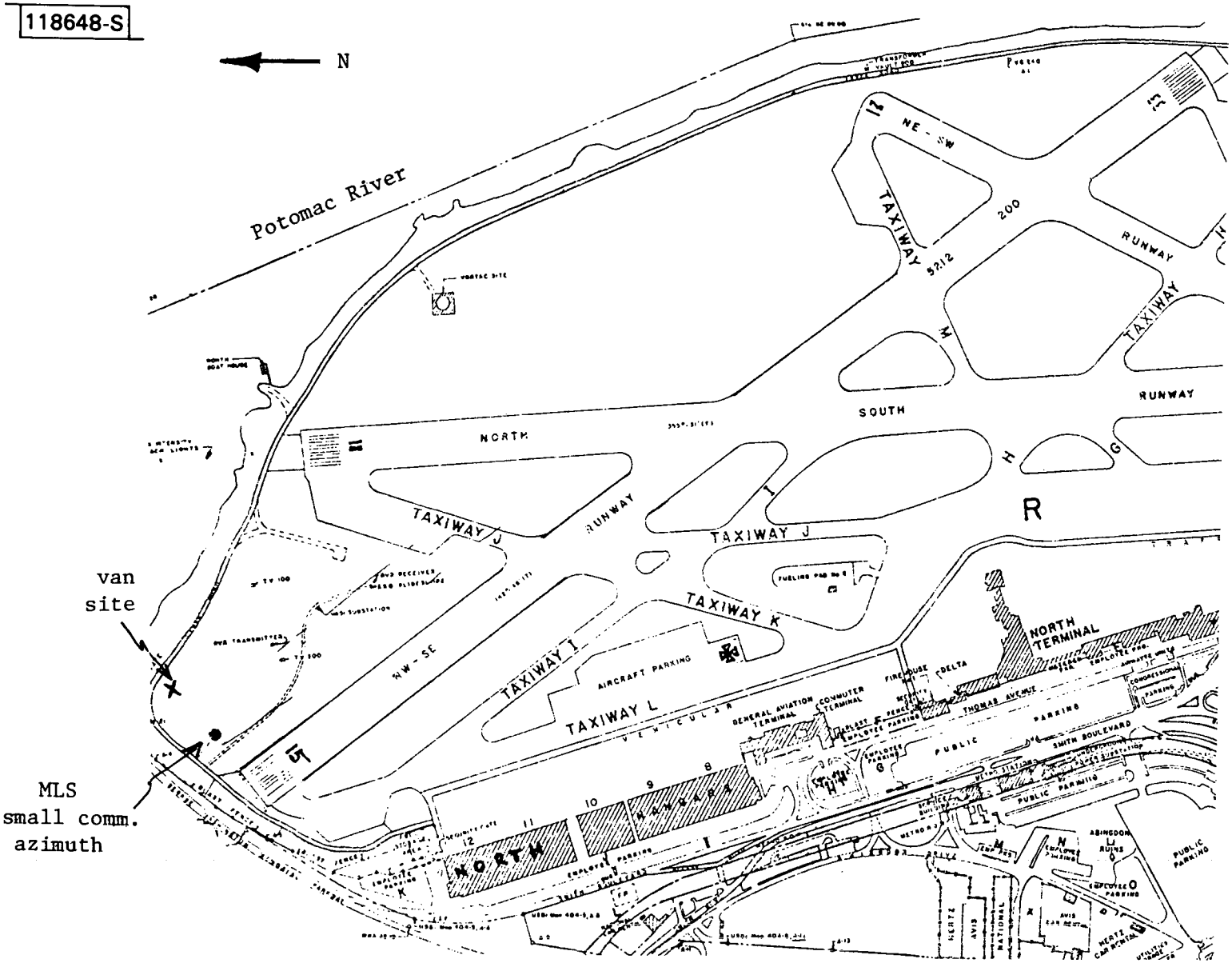


Fig.5-4. Washington National Airport DME multipath measurement site.

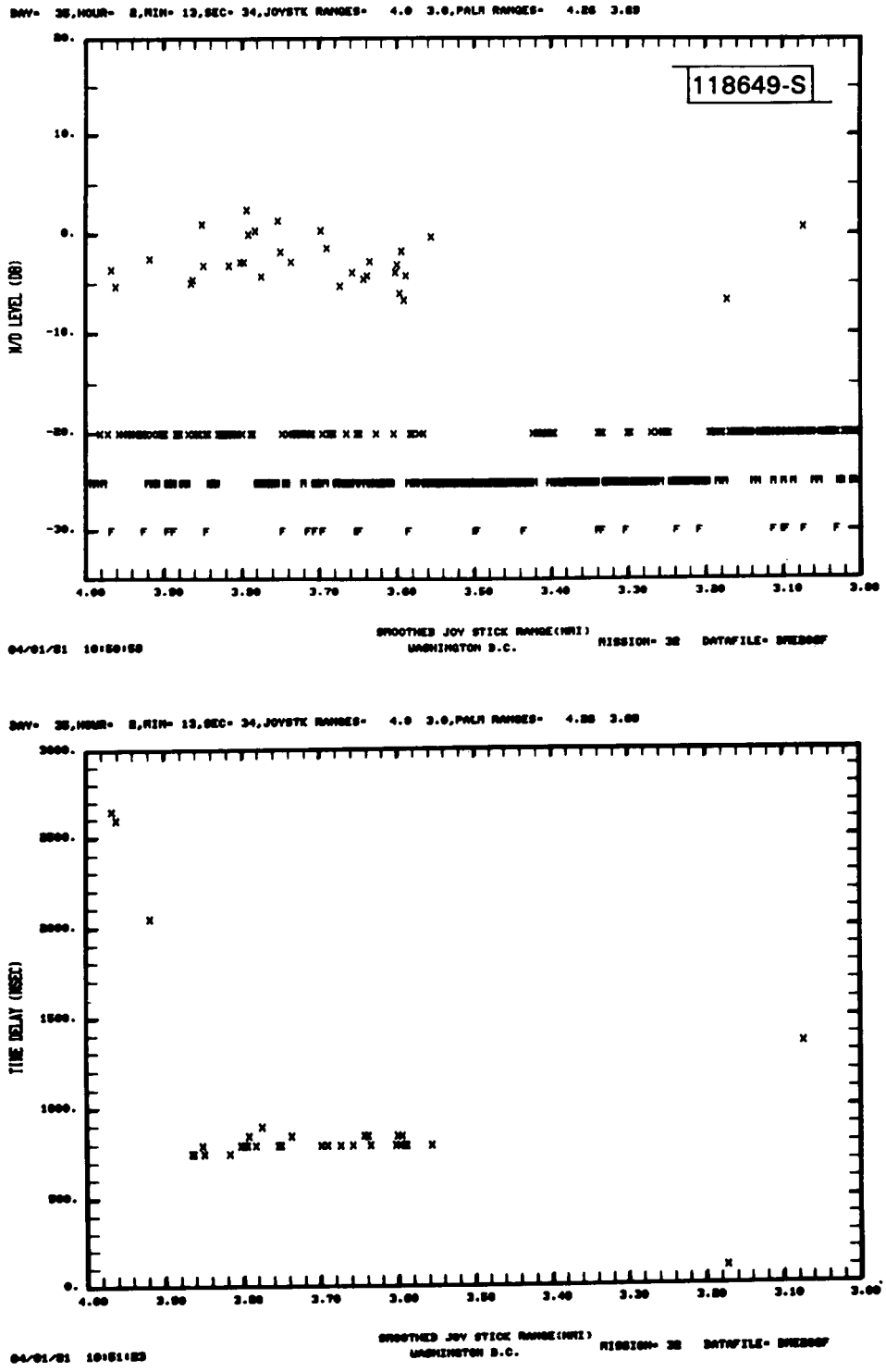


Fig.5-5(a). Summary results for 3° approach to DCA before threshold.

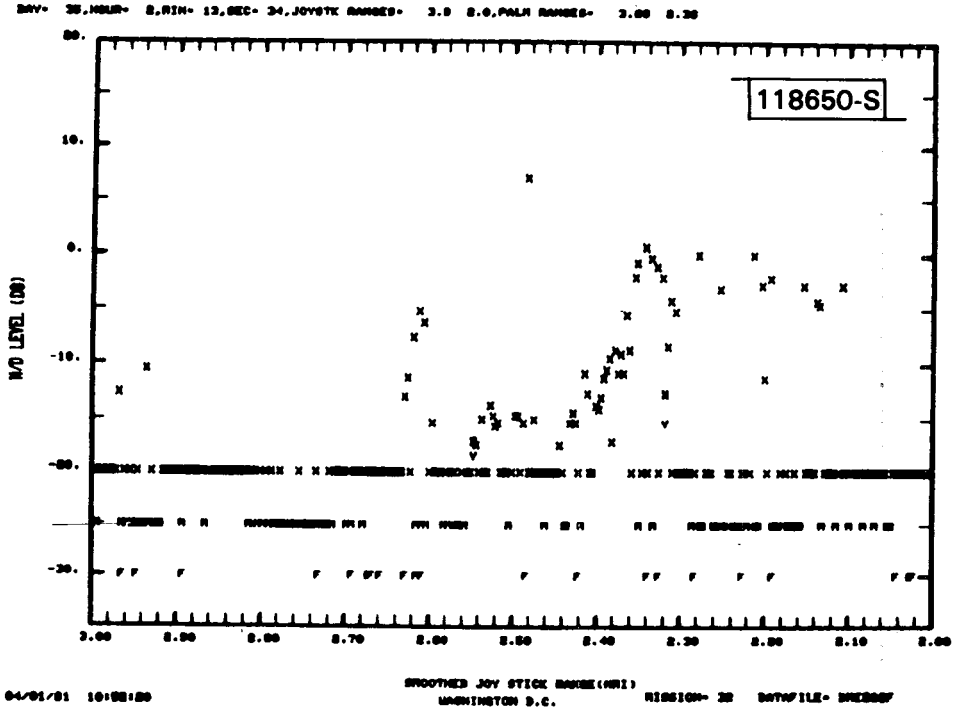


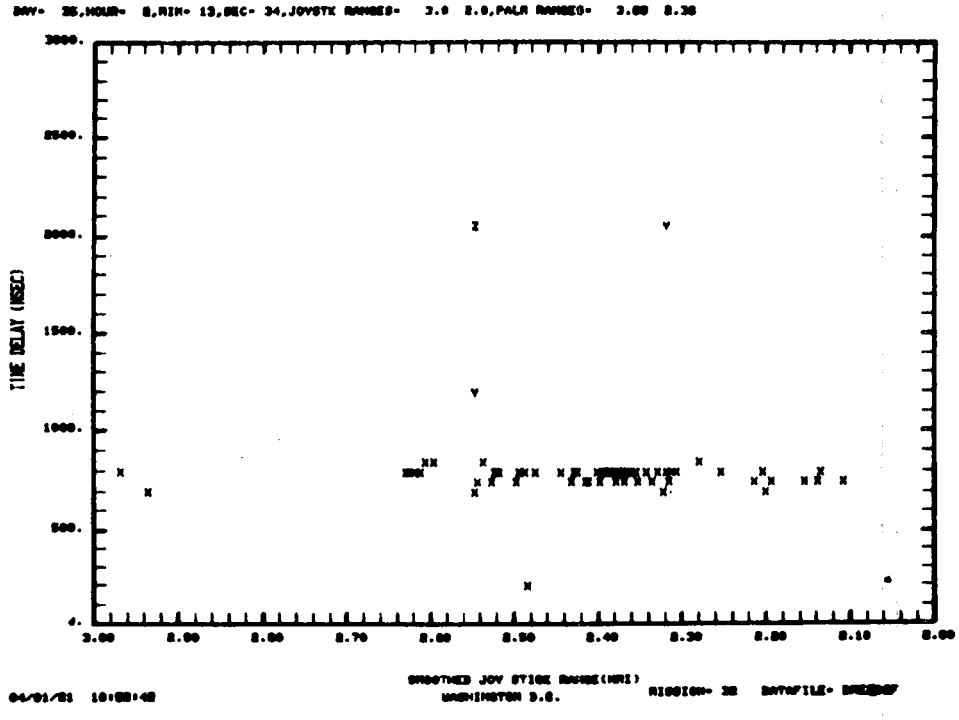


Fig.5-5(b). Summary results for 3° approach to DCA before threshold.

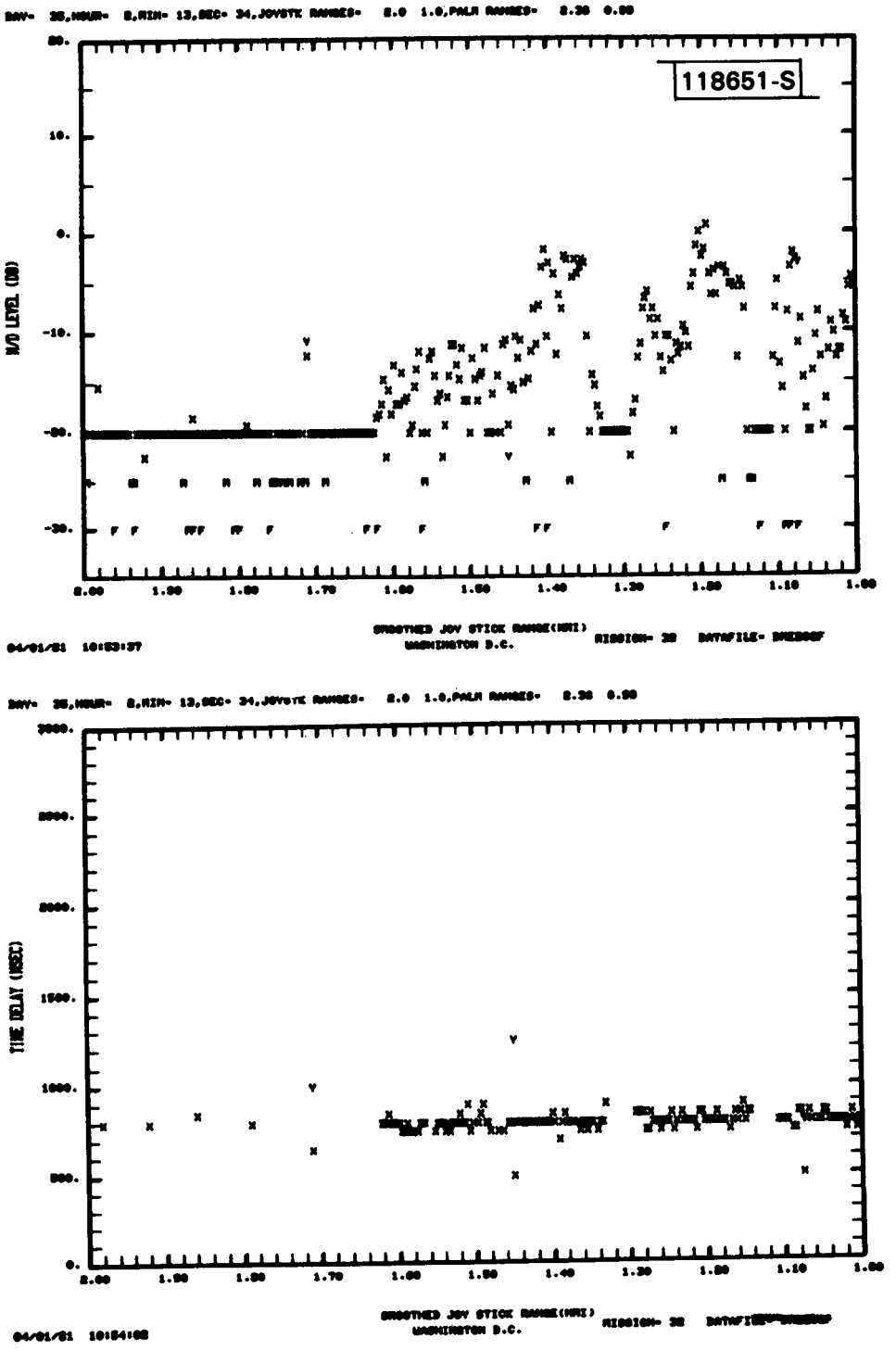


Fig.5-5(c). Summary results for 3° approach to DCA near threshold.

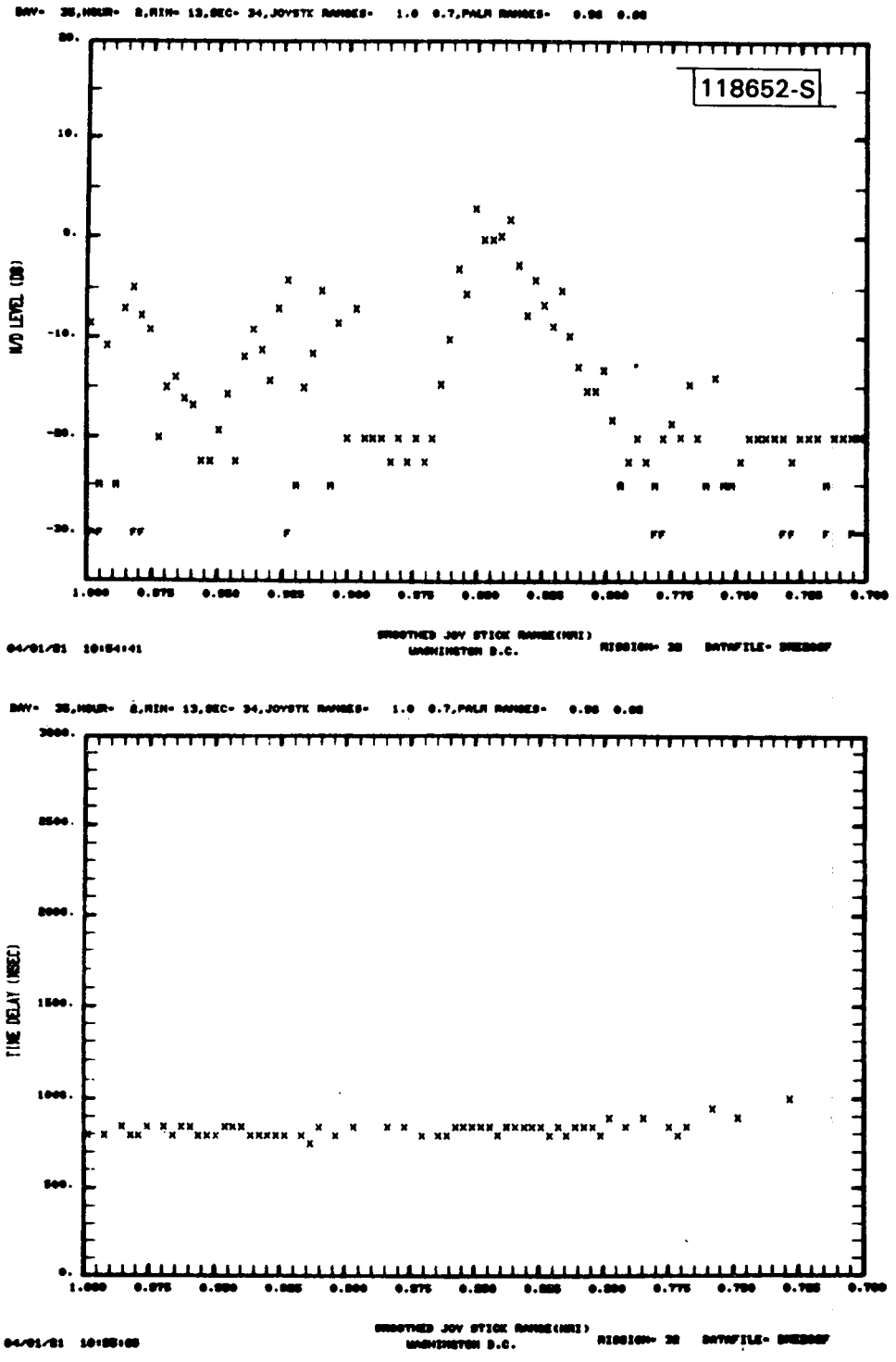


Fig.5-6. Summary results for DCA over runway.

(such as shown in Fig. 5-3) to determine the relative multipath levels and time delays. Figure 5-7 shows a representative simulation which took into account the nonverticality of the hangar wall above the doors.

The measured and simulation levels increase rapidly near 1.5 nmi from threshold; however, the measured M/D ratio values range from -10 dB to 0 dB, whereas the simulation levels are closer to -27 dB. Both levels decrease sharply and then increase to near 0 dB near threshold. Sizable oscillations in the M/D levels are evident on either side of threshold (joystick range = 0.83 nmi). This reflects the influence of multipath from different buildings as well as oscillations in the multipath level from individual scatterers as will be discussed in the section on simulation results. For the most part, the multipath delays in this region are tightly grouped in the 700 nsec - 1100 nsec region predicted by ray tracing considerations.

The fairly high level (-8 dB to 0 dB M/D ratio) 800 ns delay multipath measured near 3.0 nmi from threshold cannot be explained by the simple airport model. The aircraft x-y location here is at the edge of the specular region for the North Hangar complex, but the elevation angle of the aircraft is far in excess of the angle subtended by the lower level buildings (e.g., general aviation terminal and North Terminal complex) which are south of hangar 8. Thus, if the hangar walls and doors were vertical, large specular reflections should not have been encountered in this region. Another possibility is that this multipath arose from the hillside between the public parking area and Thomas Avenue and/or the Washington Metro Station which borders Smith

---

the relative time delay is computed as the time between the respective pulse centroids. The first multipath signal encountered after the direct signal is denoted by an "X" in the M/D level and $\tau$ plots. Succeeding multipath signals, if any, are denoted by the letters Y, Z, A, and B, respectively, on both plots.

The replies of other ATCRBS transponders to other ATCRBS interrogators may lie within the data recording interval. These "fruit" pulses were readily identified since their pulse width is approximately 450 nsec. Measurements with fruit present are flagged in the summary plots with an "F" at an M/D level of -30 dB as a warning that the data on that individual reply may have been corrupted by the fruit.

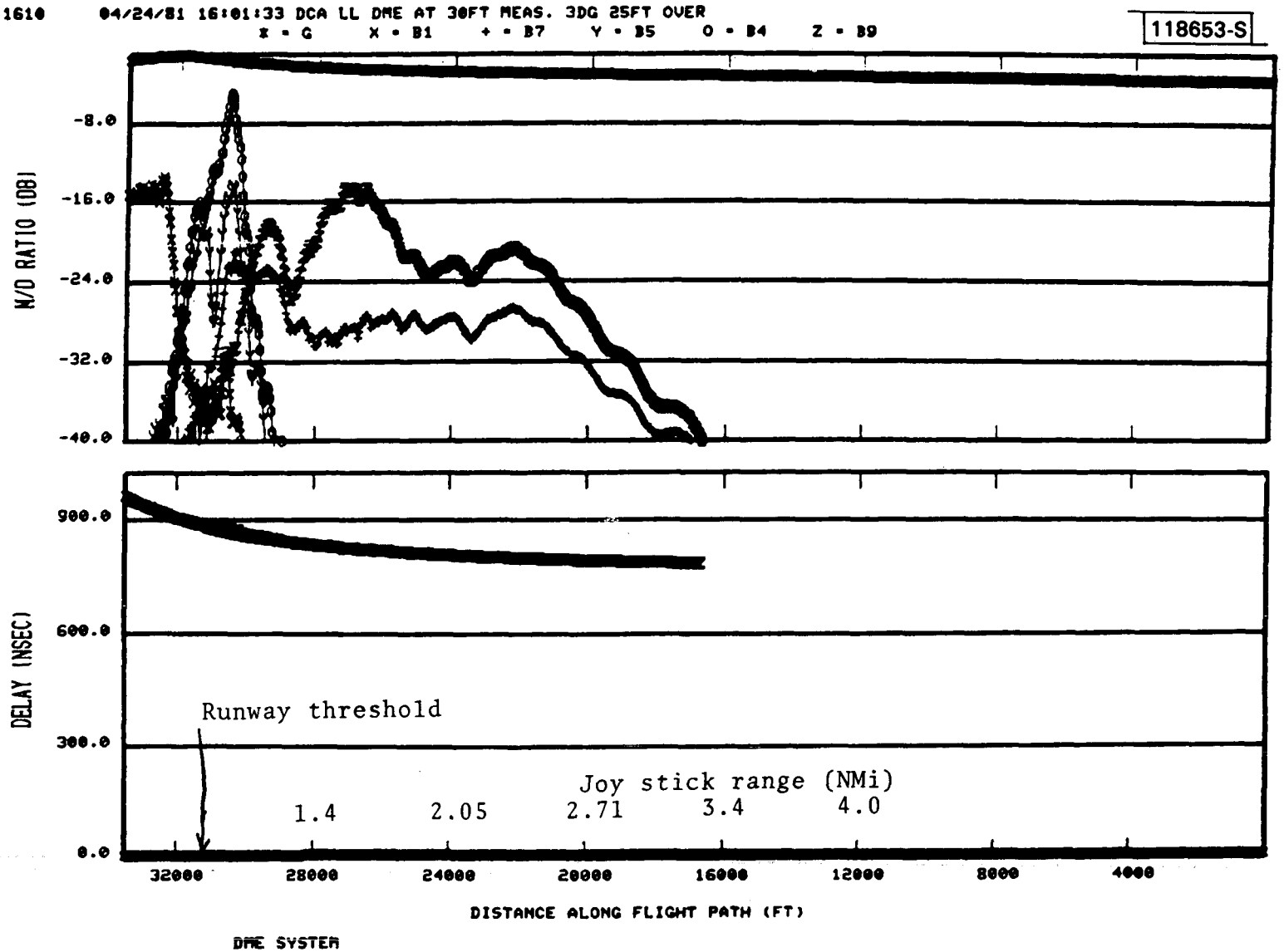


Fig.5-7. Computed multipath characteristics for DCA 3° approach scenario.

Boulevard, since the 800 nsec delay is slightly greater than that associated with the hangar complex at this range.

In general, the multipath regions near the threshold of DCA runway 15-33 correlated fairly well with the specular regions associated with a row of hangars bordering the runway. The time delays of the multipath near threshold agreed quite well quantitatively with the predictions using a simple airport model, but the experimental M/D levels were in several cases substantially larger than were predicted. Also, strong multipath was encountered at longer ranges on the approach (e.g., 3 - 5 nmi from threshold) which could not be explained by reflections from vertical walls of the hangars which border the runway.

### 2. Wright Patterson Air Force Base (WPAFB)

Figure 5-8 shows the airport geometry at WPAFB runway 5-23. This airport had been shown to have high level multipath in the flare and rollout region in earlier tests at C-band [27]. The principal multipath threat here is hangar 206 which is over 25 m high and some 133 m long. The runway is approximately level for the first 1500 m (4500 ft) and then slopes upward toward the threshold.

Figures 5-9 and 5-10 show representative received waveforms and summary results at WPAFB on a 3° approach to runway 23. Only fragmentary results were obtained in the region past threshold due to low SNR. This low SNR arose from extreme ground lobing due to the runway length and contour.

Figure 5-11 shows the corresponding simulation results. The simulation predicts low level (-12 dB M/D) reflections from building 152 at threshold with a delay of approximately 1.6 μs and high level (-3 dB M/D) reflections from hangar 206 with a time delay of 2 μs. The multipath regions and time delays correlate reasonably well with the field measurements, but the predicted M/D levels are, in some cases, considerably lower (e.g., 10 - 15 dB) than the measured values. This difference could arise from several factors:

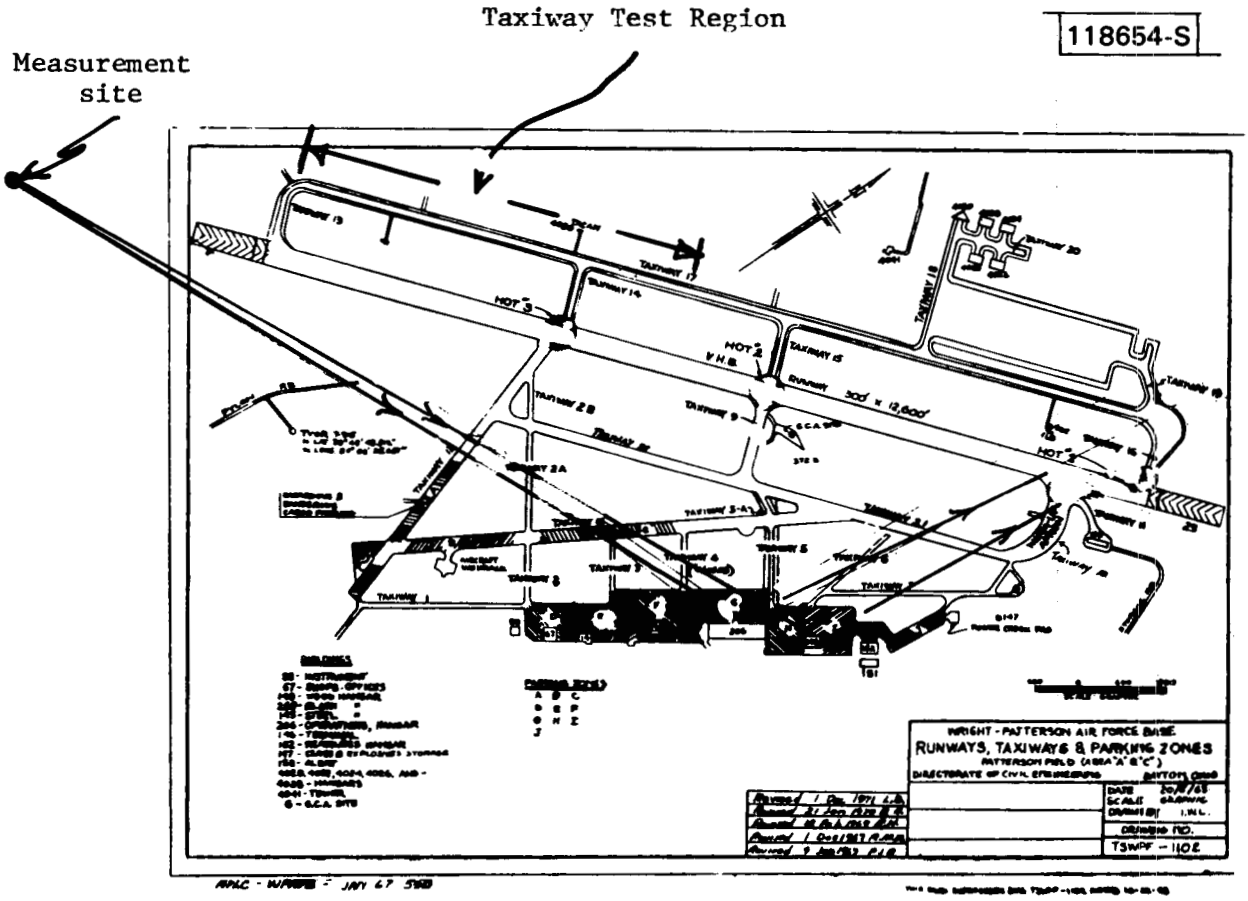


Fig.5-8. Airport geometry at Wright Patterson AFB.

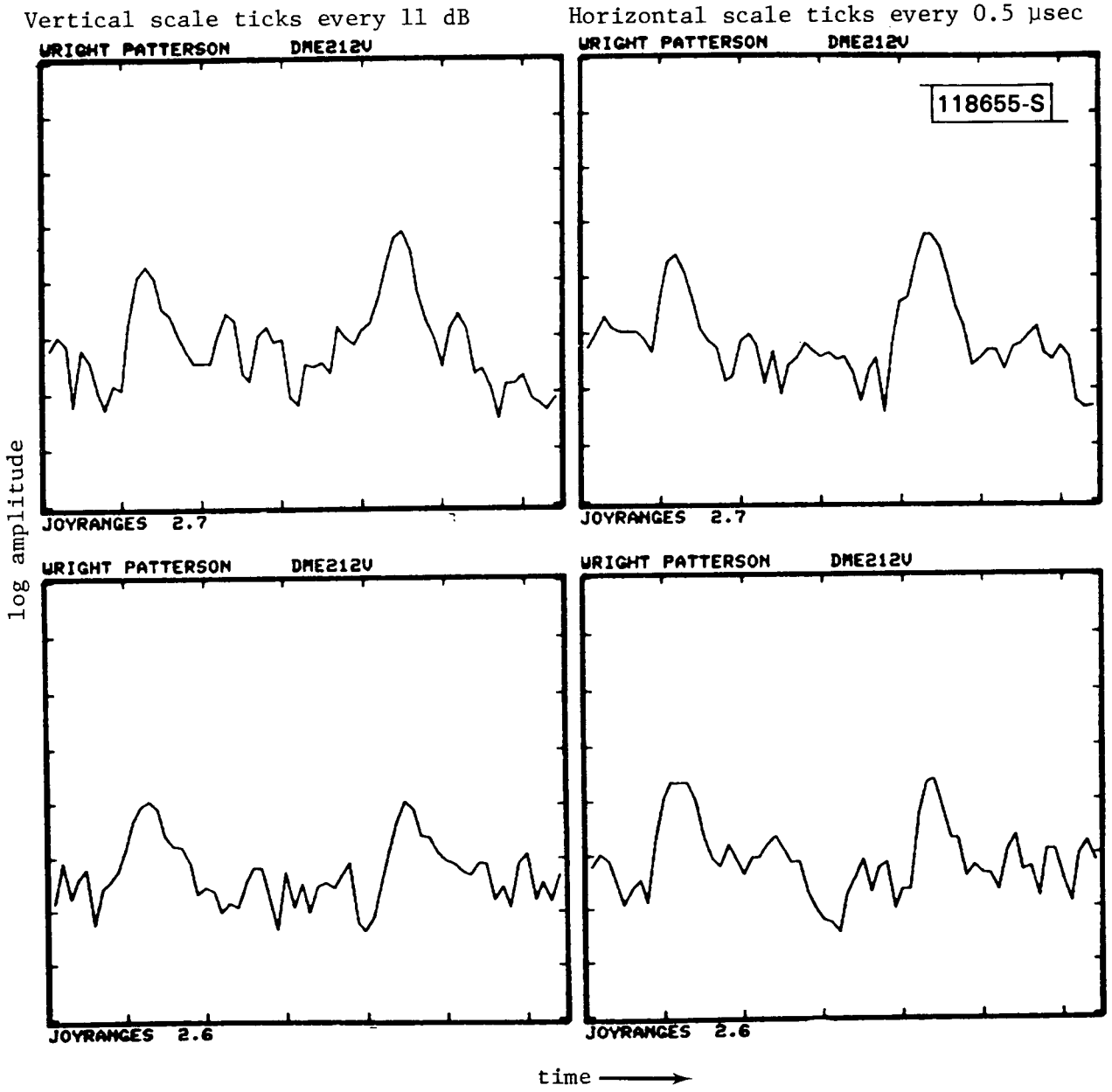


Fig.5-9. WPAFB waveforms near threshold.

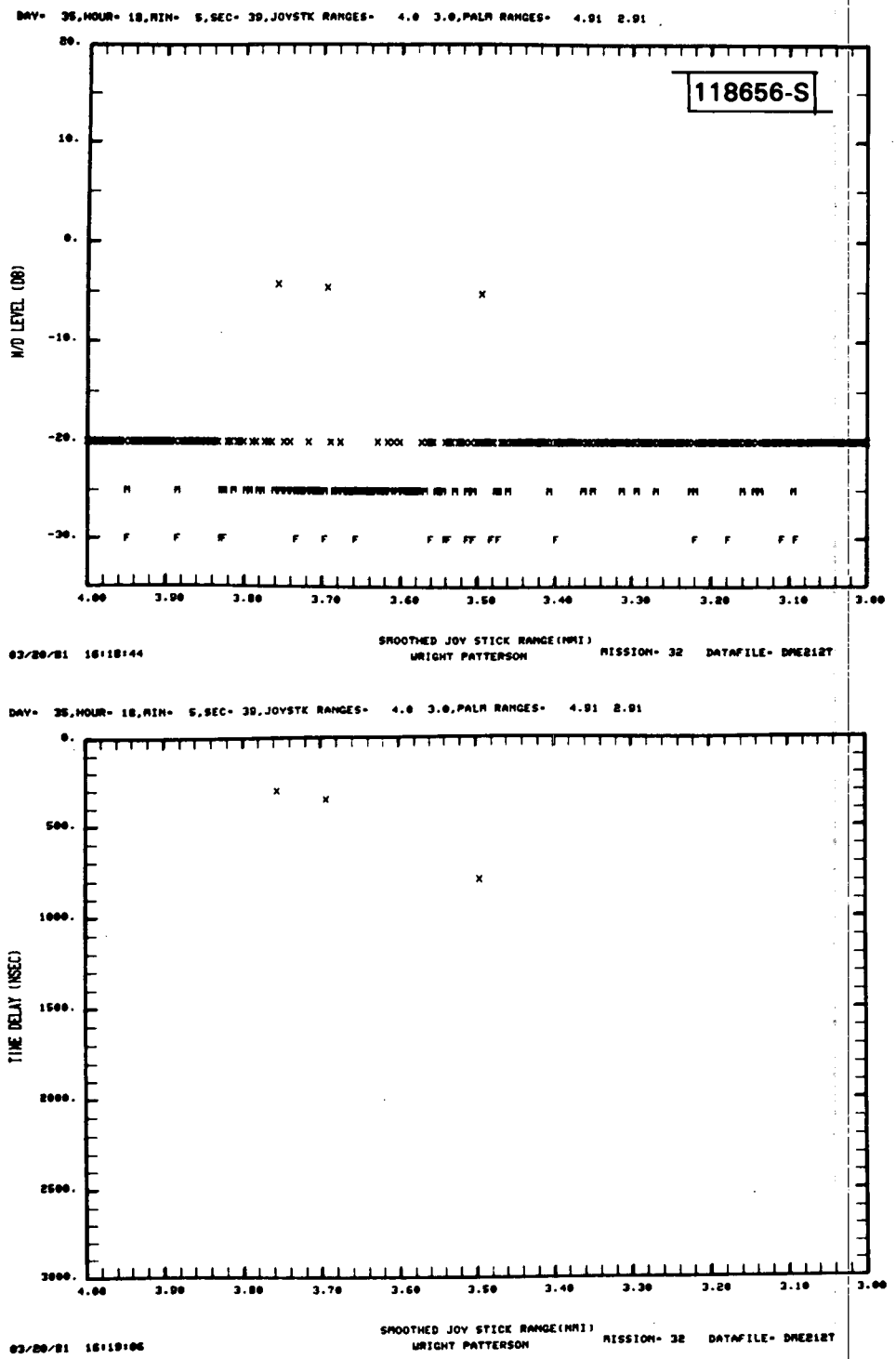


Fig.5-10(a). Summary results for flight profile 1 at WPAFB.

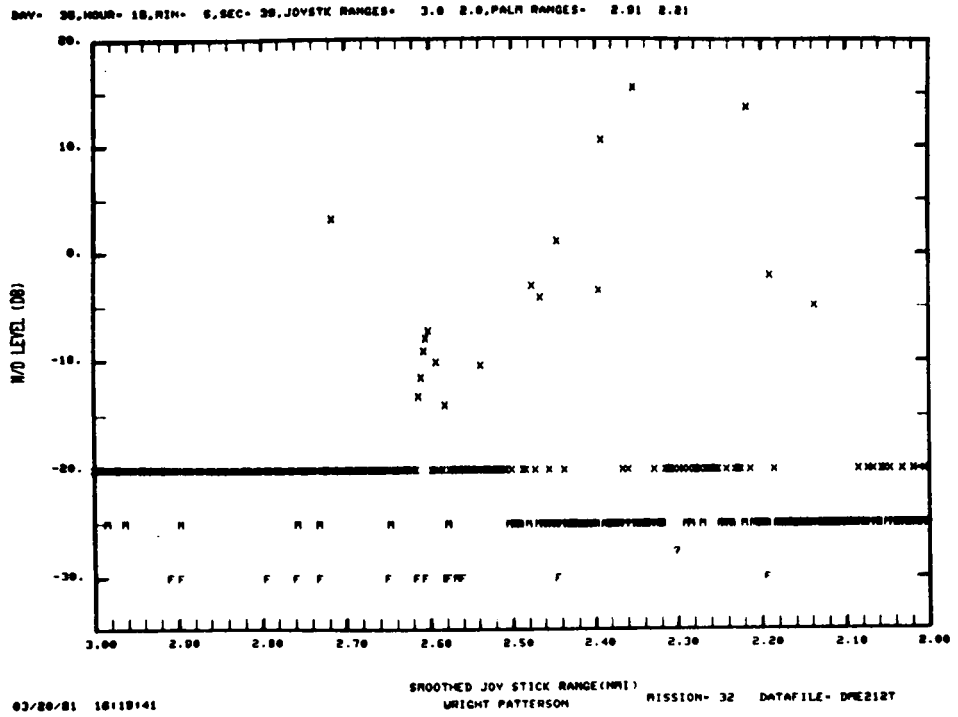


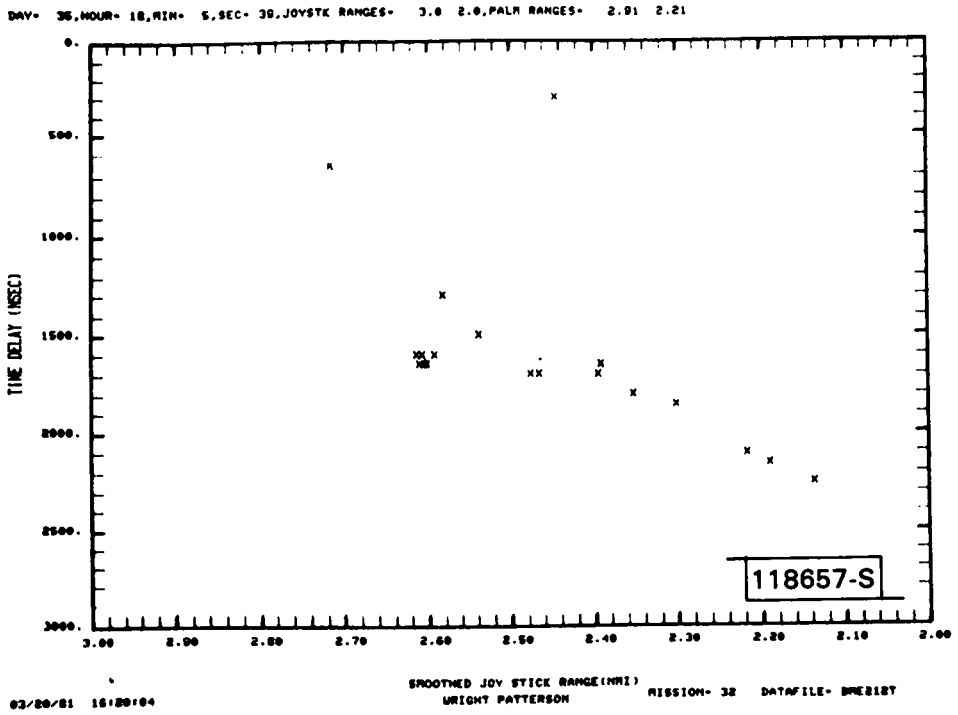


Fig.5-10(b). Summary results for flight profile 1 at WPAFB.

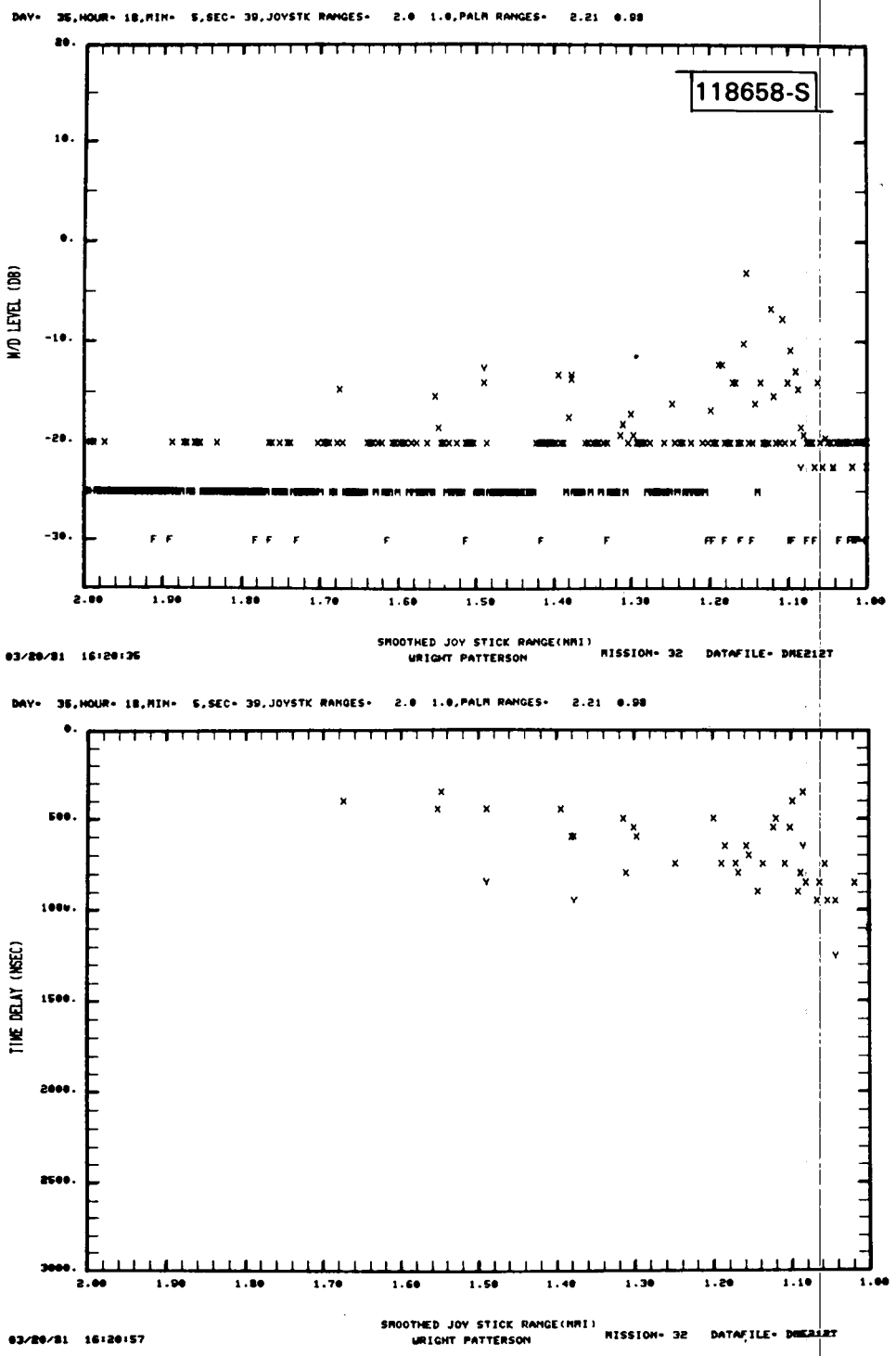


Fig.5-10(c). Summary results for flight profile 1 at WPAFB.

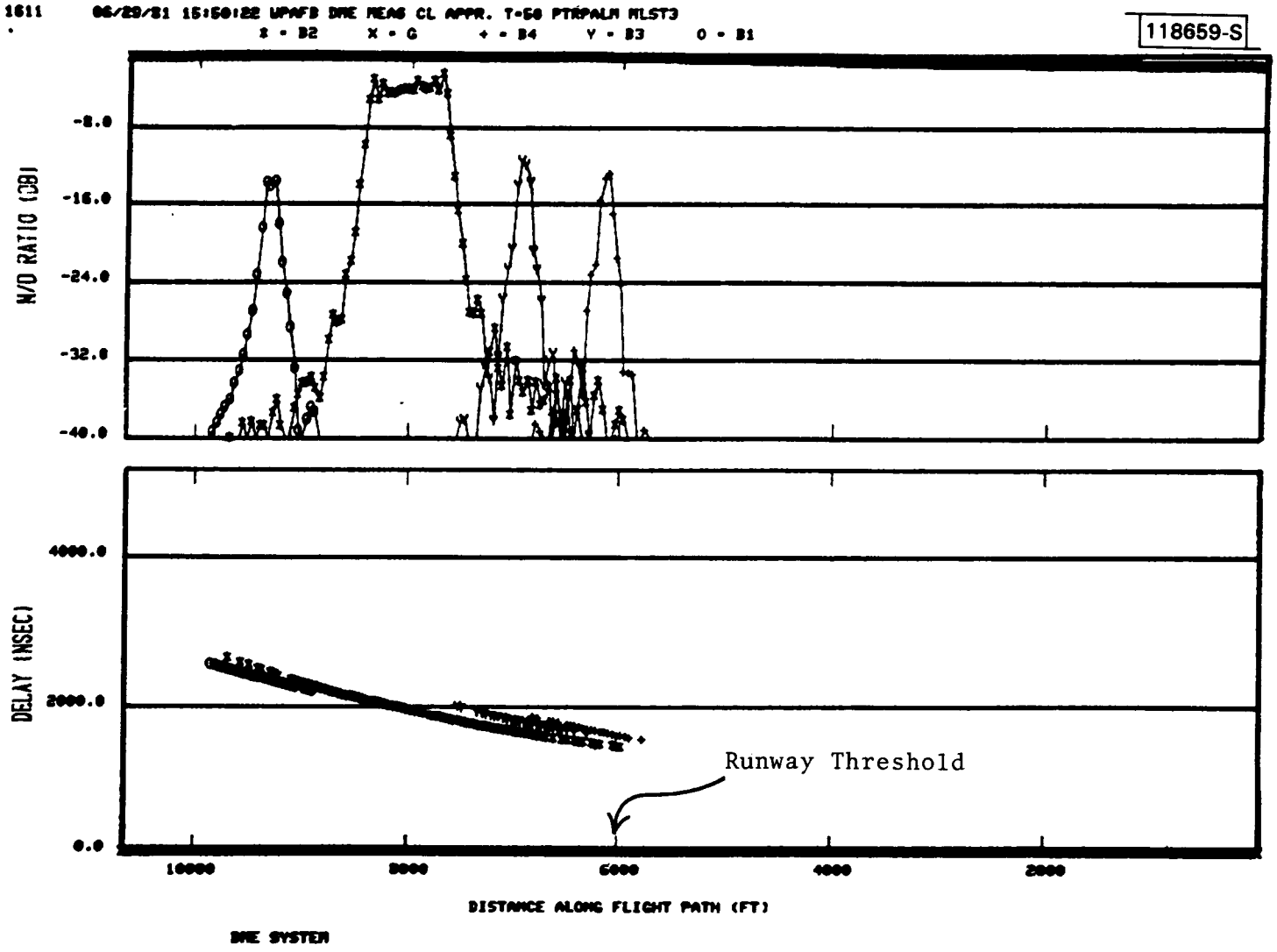


Fig.5-11. Computed DME multipath characteristics for WPAFB scenario.

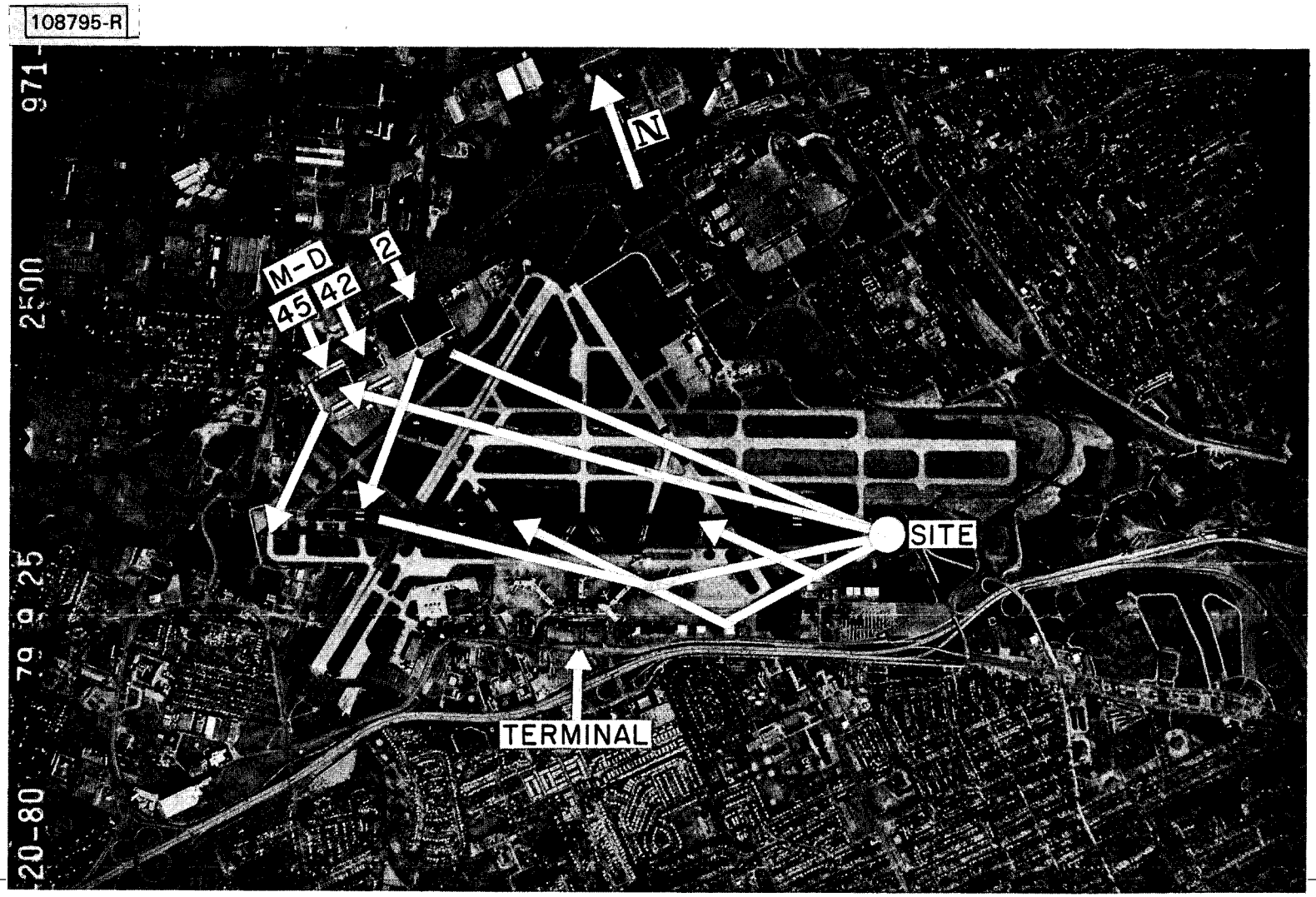


Fig.5-12. Lambert-St. Louis International, St. Louis, Missouri, showing azimuth reflection paths.

1. the terrain contour along the runway and building reflection paths was assumed to be flat in the simulation. This may have understated the amount of differential direct signal lobing due to the ground since the off runway terrain is lower than the along runway terrain, and

2. the staggering of the doors on building 206 was ignored. In studies of C band reflection behavior along this runway, it was found that the reflected signal levels could oscillate very rapidly in the specular region due to reinforcement and cancellation of signals from adjacent doors [27].

In general, the measured data at WPAFB correlated reasonably well with the multipath regions and time delays expected from ray tracing and computer simulations. Unfortunately, the severe reflection environment (terrain lobing and/or building reflections) was such that only fragmentary data were available in the flare region where the highest M/D levels were anticipated. The measured data available in that region suggest that the actual M/D levels were comparable to and, in many cases in excess of, the simulation results using a simple airport model.

### 3. St. Louis (Lambert) International (STL)

Figure 5-12 shows the airport geometry for measurements at STL. The principal multipath sources were the McDonnell Douglas aircraft factory buildings (labeled M-D in Fig. 5-12) and the terminal building/hangar complex to the south of runway 12R. These structures were typically 20m (60 feet) high. The runway sloped downward from the measurement site to the runway threshold.

Figures 5-13 and 5-14 show representative waveforms and summary measurement results for a 3° glideslope approach to runway 12R. Figure 5-15 shows the corresponding simulation results for a simple airport model. We see that the multipath from the M-D building 42 with a level of approximately -8 dB is expected near threshold with a time delay of approximately 1.4 μs to

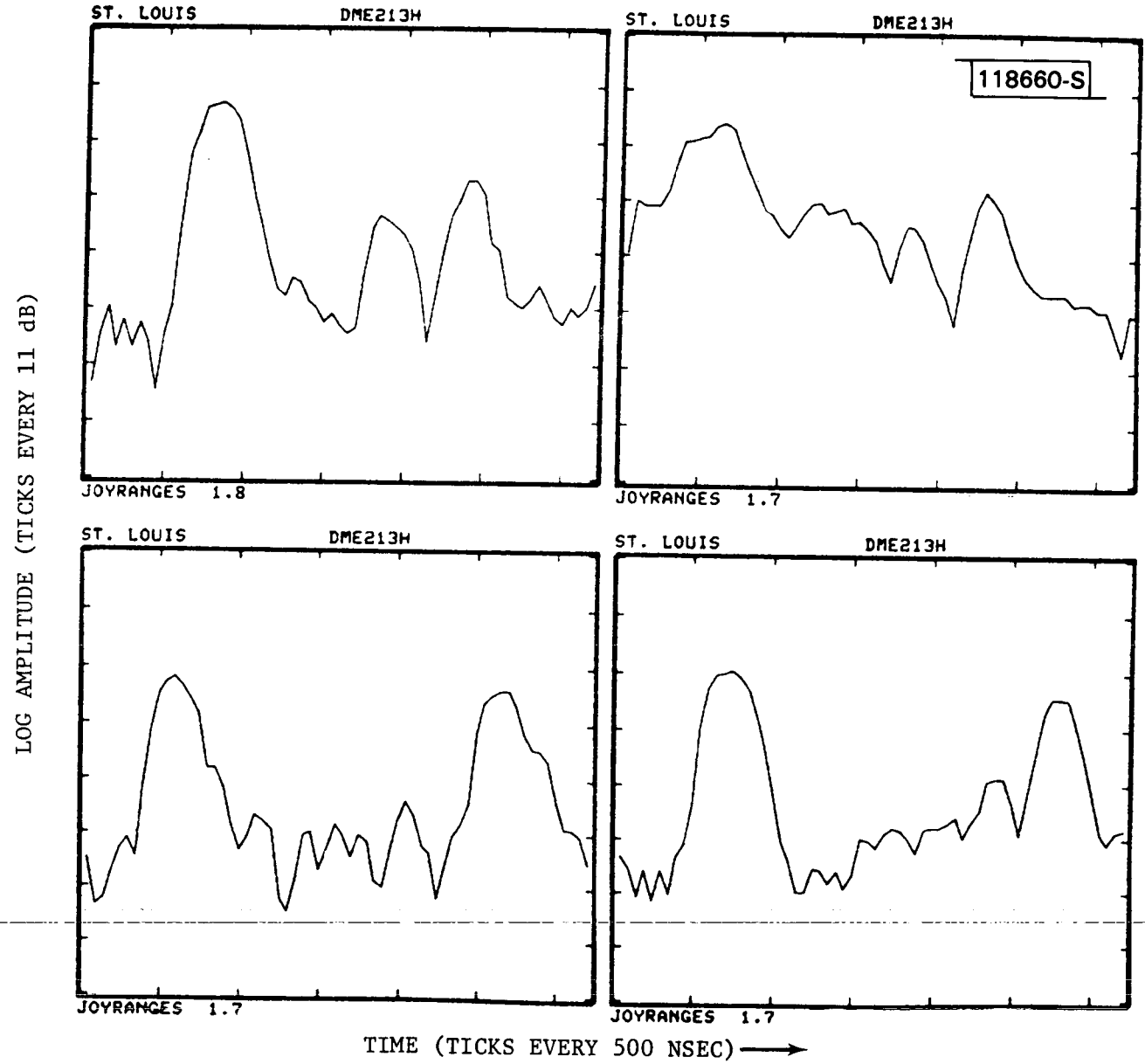


Fig.5-13. St. Louis waveforms at threshold (50 ft. AGL).

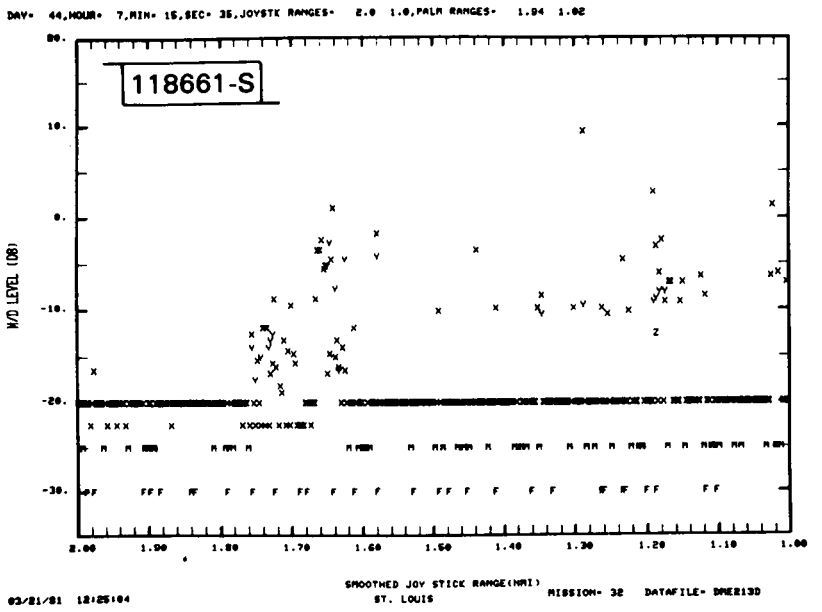


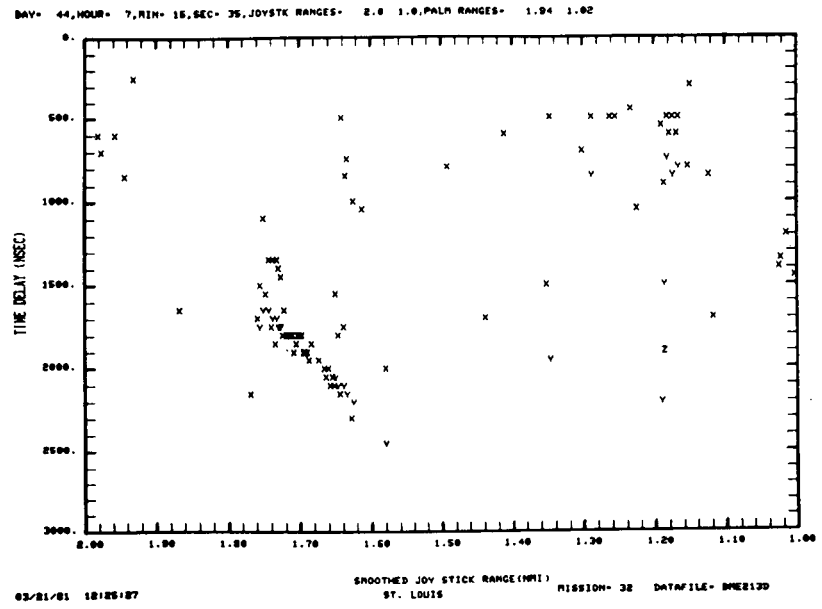


Fig.5-14(a). Data summary for St. Louis's approach with 50 ft. threshold height.

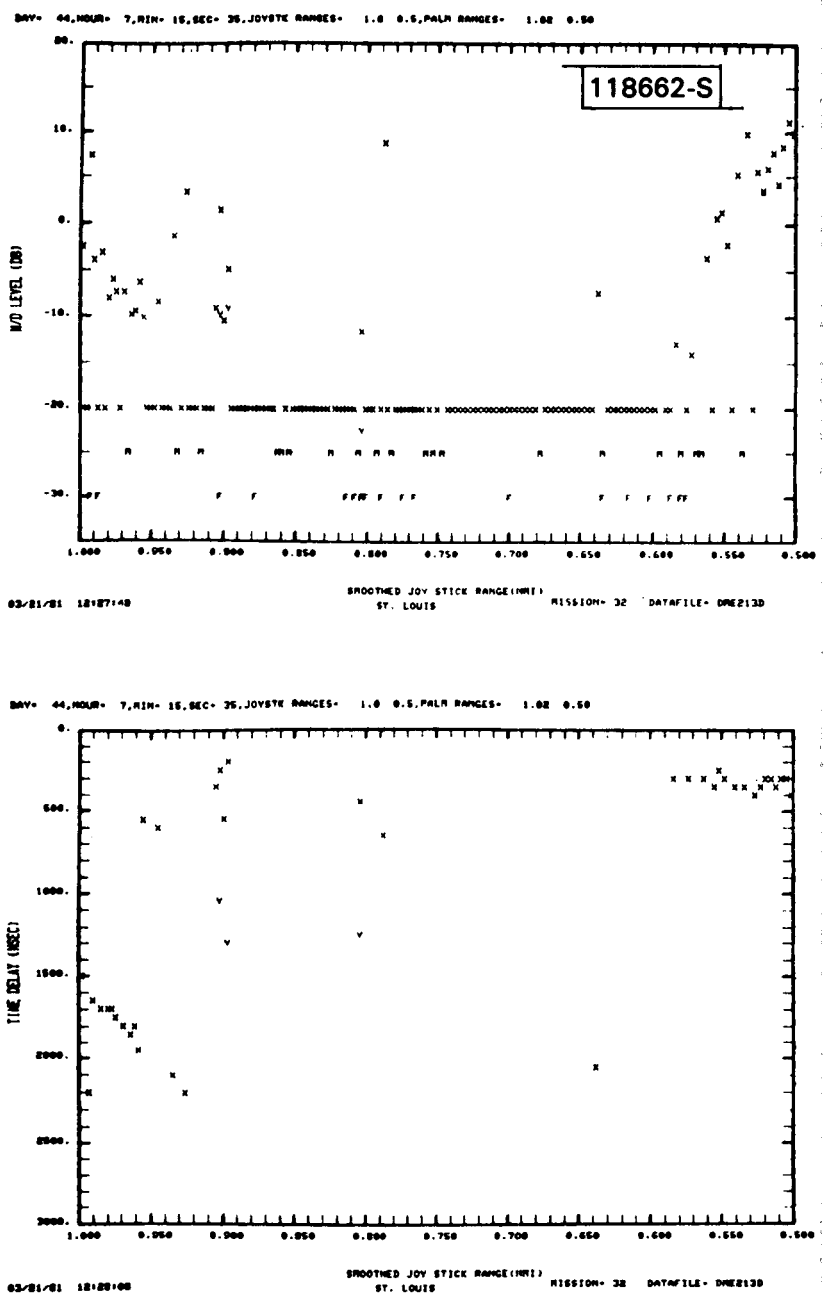


Fig.5-14(b). Data summary for St. Louis's approach with 50 ft. threshold height.

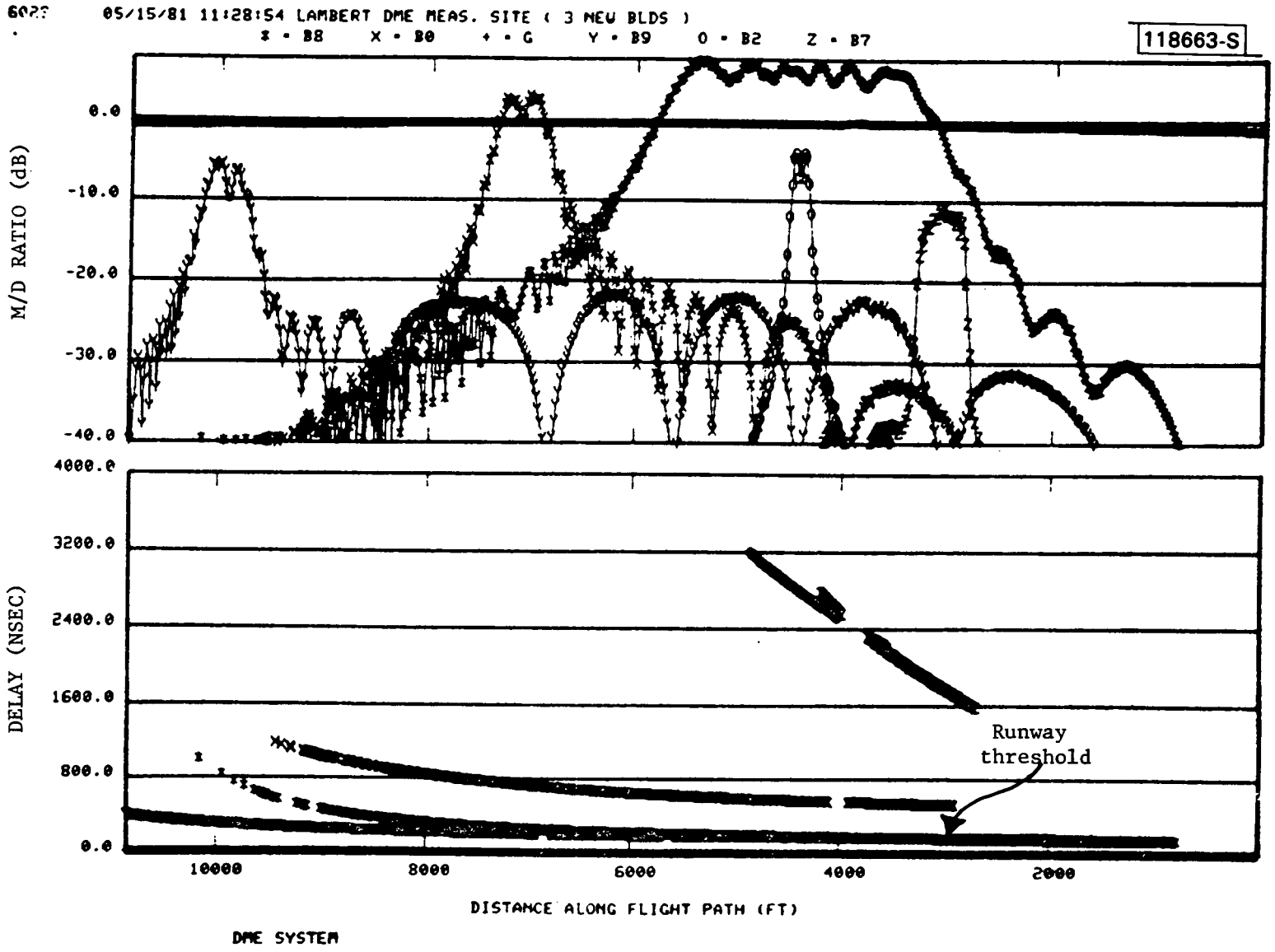


Fig.5-15. Computed multipath characteristics for Lambert-St. Louis scenario.

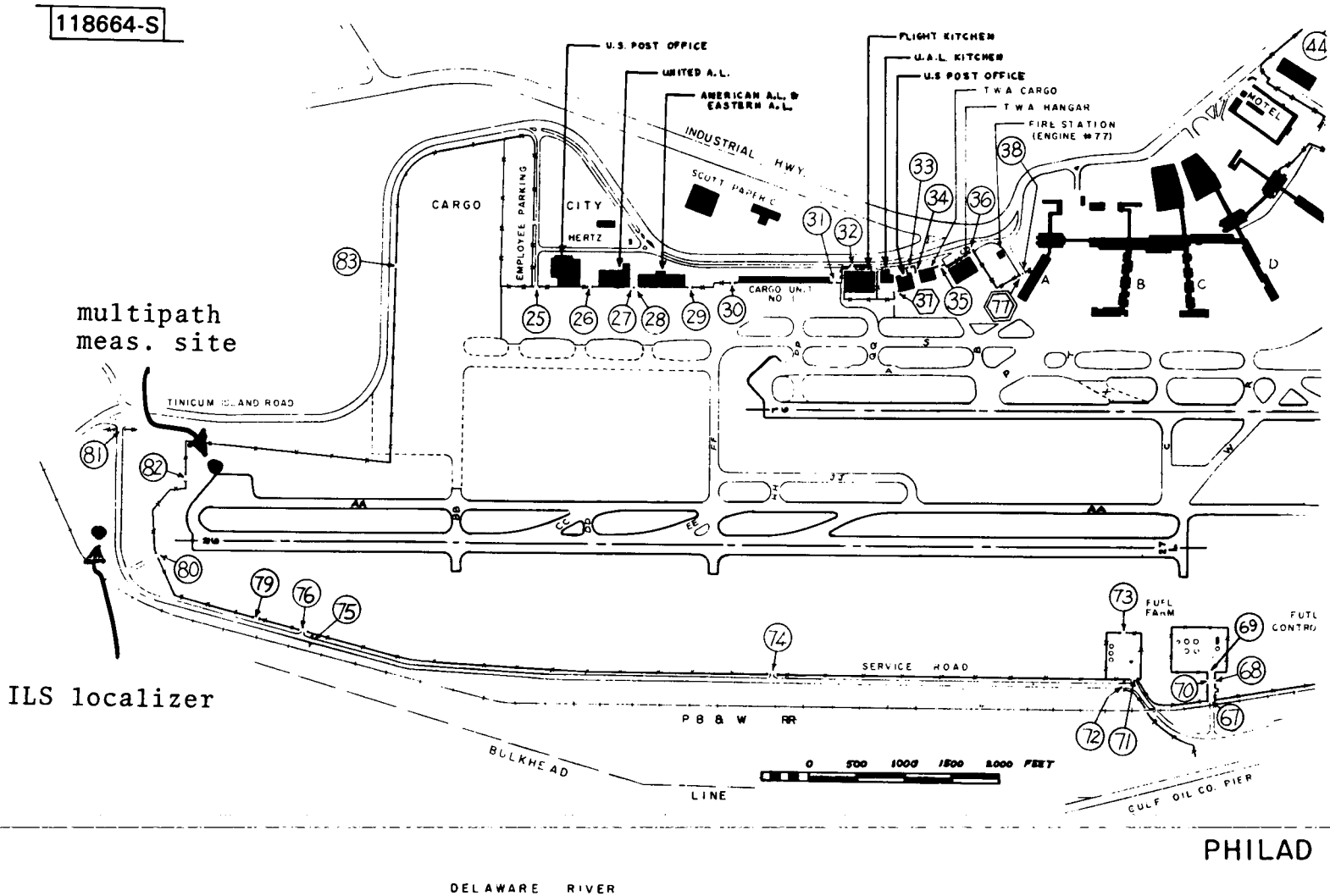


Fig.5-16. Philadelphia International Airport in vicinity of runway 9R-27L.

2.0 μs. This level agrees reasonably well with the measured results in Fig. 5-14. Similar levels/time delays are predicted from the other M-D buildings in a 1200 foot region (0.2 nmi) starting 1200 feet (0.2 nmi) after threshold and, in fact, this appears to be the case although several very high level M/D experimental points occur which are not suggested by the simulation model. These undoubtedly arise from the complicated fine structure of the M-D building surfaces which was not considered in developing the simulation airport model.

The experimental data multipath after threshold has delays comparable to those predicted for the terminal building east concourse; however, the levels and spatial duration are significantly less than suggested by the simulation result. This dramatic difference arises because the loading gates and parked aircraft block most of the multipath from the building surface. The experimental short duration multipath at 1.0 nmi joystick range correlates with the region predicted for the TWA hangar multipath.

In general, the multipath regions at St. Louis in the approach and flare regions correlated fairly well with the specular regions associated with the large buildings which face the runway. The M/D levels and time delays predicted using the MLS propagation model and a very simple airport model agree fairly well for the M-D buildings modeled, although some isolated measurements suggested M/D levels much higher than predicted.

The measured M/D levels for the terminal concourse wing were substantially lower than suggested by the simple airport model. The low terminal concourse levels are attributed to blockage of the reflection paths by the parked aircraft and jetways. Similar phenomena were noted in C-band multipath measurements at Logan Airport [8].

### 4. Philadelphia International Airport (PHL)

Figure 5-16 shows the airport geometry at PHL. The principal multipath sources here were the various hangars to the north of the runway. The runway

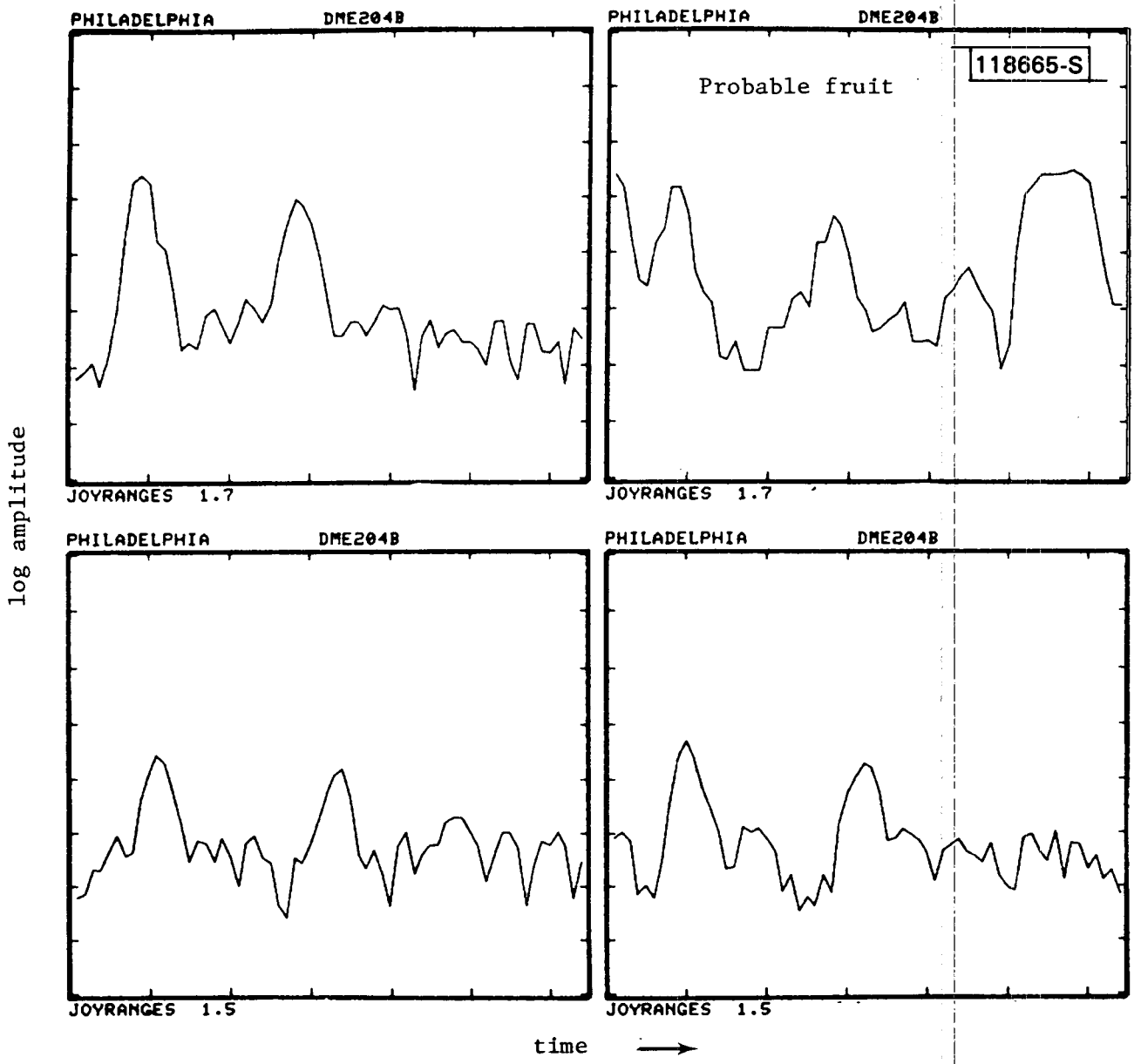


Fig.5-17. Philadelphia waveform at and past threshold.

sloped downward approximately 12 feet from the measurement site to the runway midpoint and was flat thereafter.

Figures 5-17 and 5-18 show representative signal waveforms and summary results for a 3° approach to runway 27L. Most of the measurements were missed at or just after threshold due to low SNR. This low SNR probably arose from the runway contour causing excessive lobing and/or excess signal losses due to mismatch in the receiver cables.

Figure 5-19 shows the computed multipath characteristics using a simple airport model. The predicted M/D level of -8 dB for the UA cargo unit correlates reasonably well with Fig. 5-18. It should be noted, however, that no multipath within -20 dB of the direct signal was detected on any of the other approaches. The predicted peak M/D levels of -18 dB and -28 dB for the AA/EA cargo building and cargo unit #1 are not inconsistent with Fig. 5-18, although here again the experimental data show large variations which are not suggested by the computer simulation.

In general, the Philadelphia measured results correlated reasonably well with the predictions from ray tracing analysis and computer simulations using a simple airport model. The measured M/D ratios and $\tau$ values were quantitatively in reasonable agreement on the approaches with adequate SNR; however, in most cases, the SNR was so low as to cause significant problems in data interpretation.

### 5. Tulsa Internationl Airport (TUL)

Figure 5-20 shows the airport geometry at TUL where 3° approaches were conducted to both ends of runway 17L-35R. A distinctive feature of the TUL environment was the sizable hump (see Fig. 5-21) which is approximately 1000 m (3300 ft.) from the threshold of runway 35R. The principal multipath threat here were the American Airlines hangar (approximately 30 m high) and the McDonnell Douglas aircraft factory (approximately 20 m high).

Figures 5-22 and 5-23 show representative waveforms and summary results

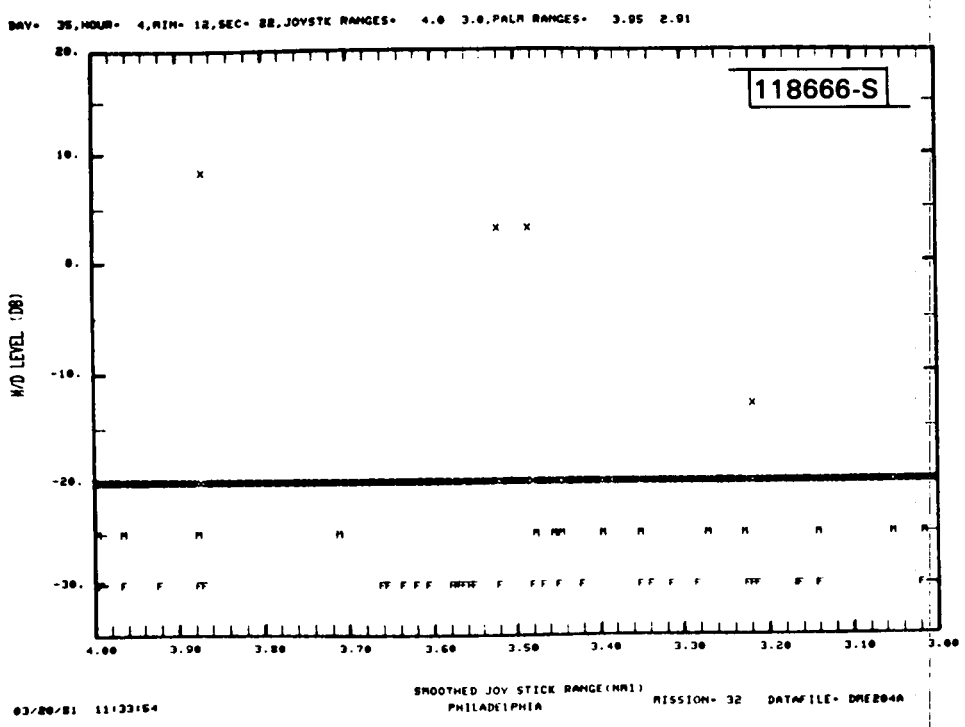


Fig.5-18(a). Summary results for flight profile 1 at Philadelphia.

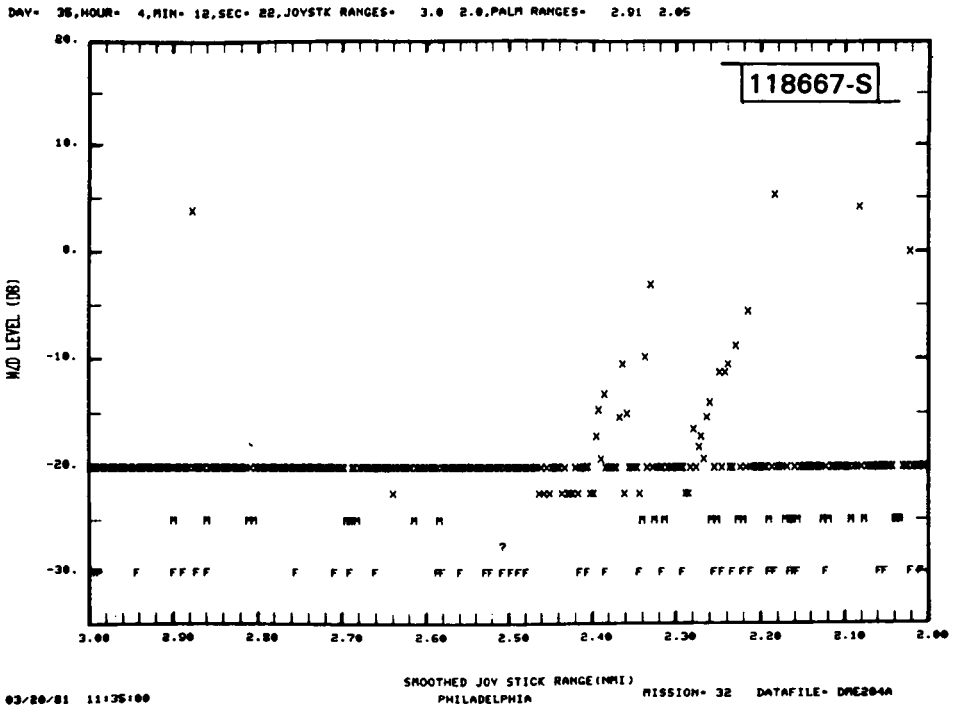


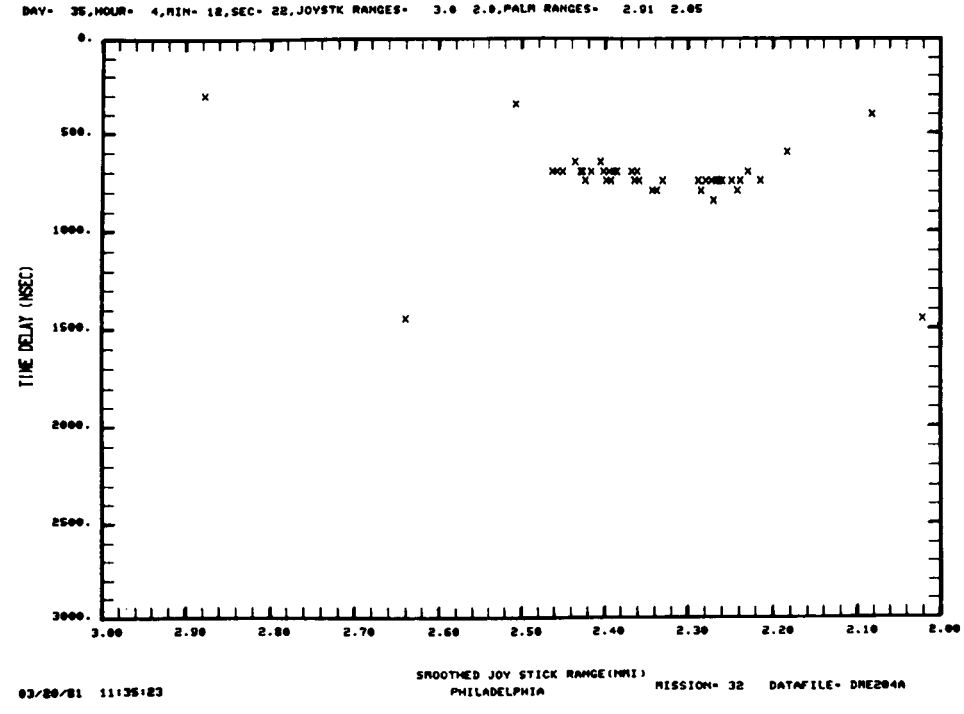


Fig.5-18(b). Summary results for flight profile 1 at Philadelphia.

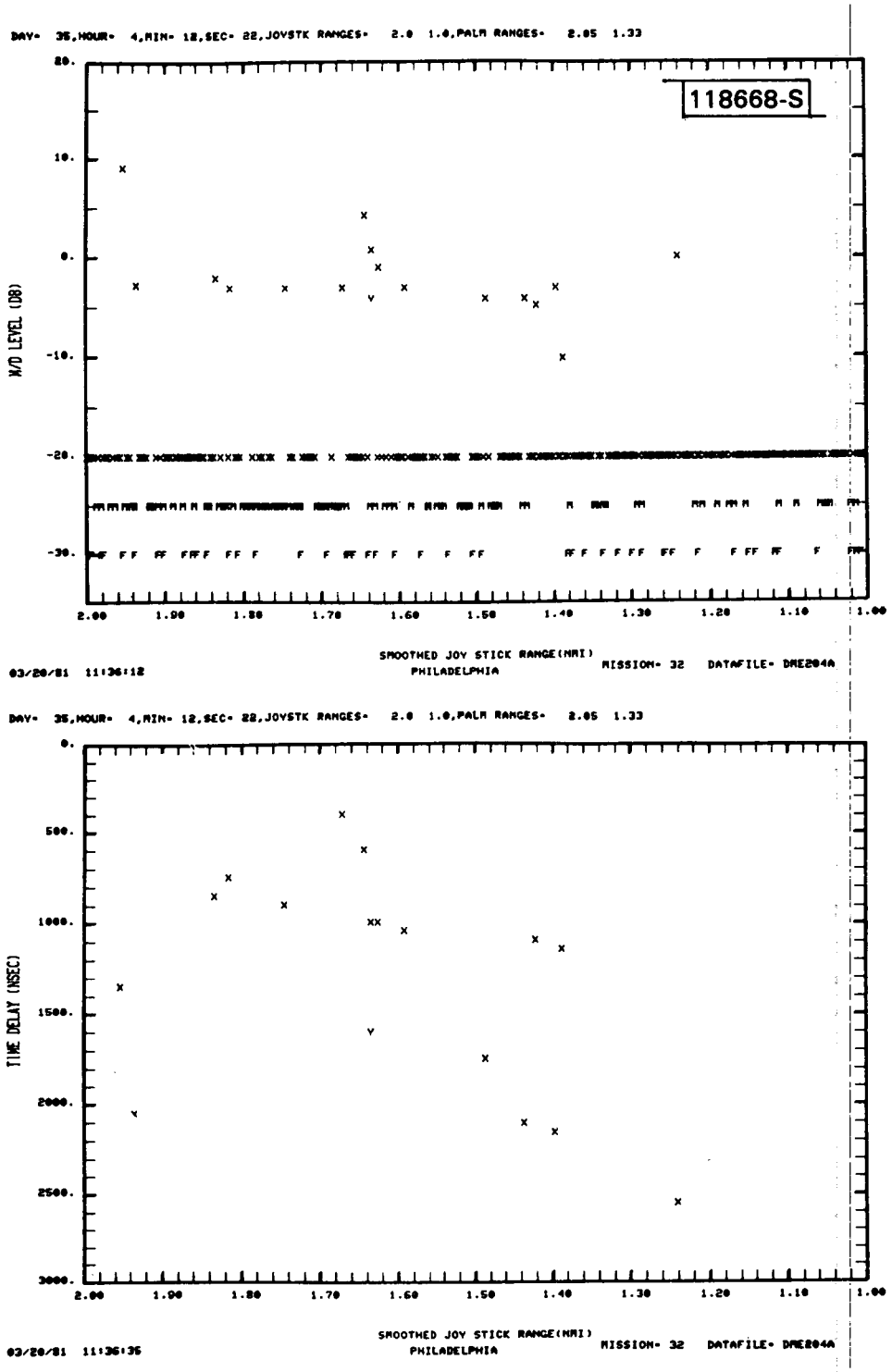


Fig.5-18(c). Summary results for flight profile 1 at Philadelphia.

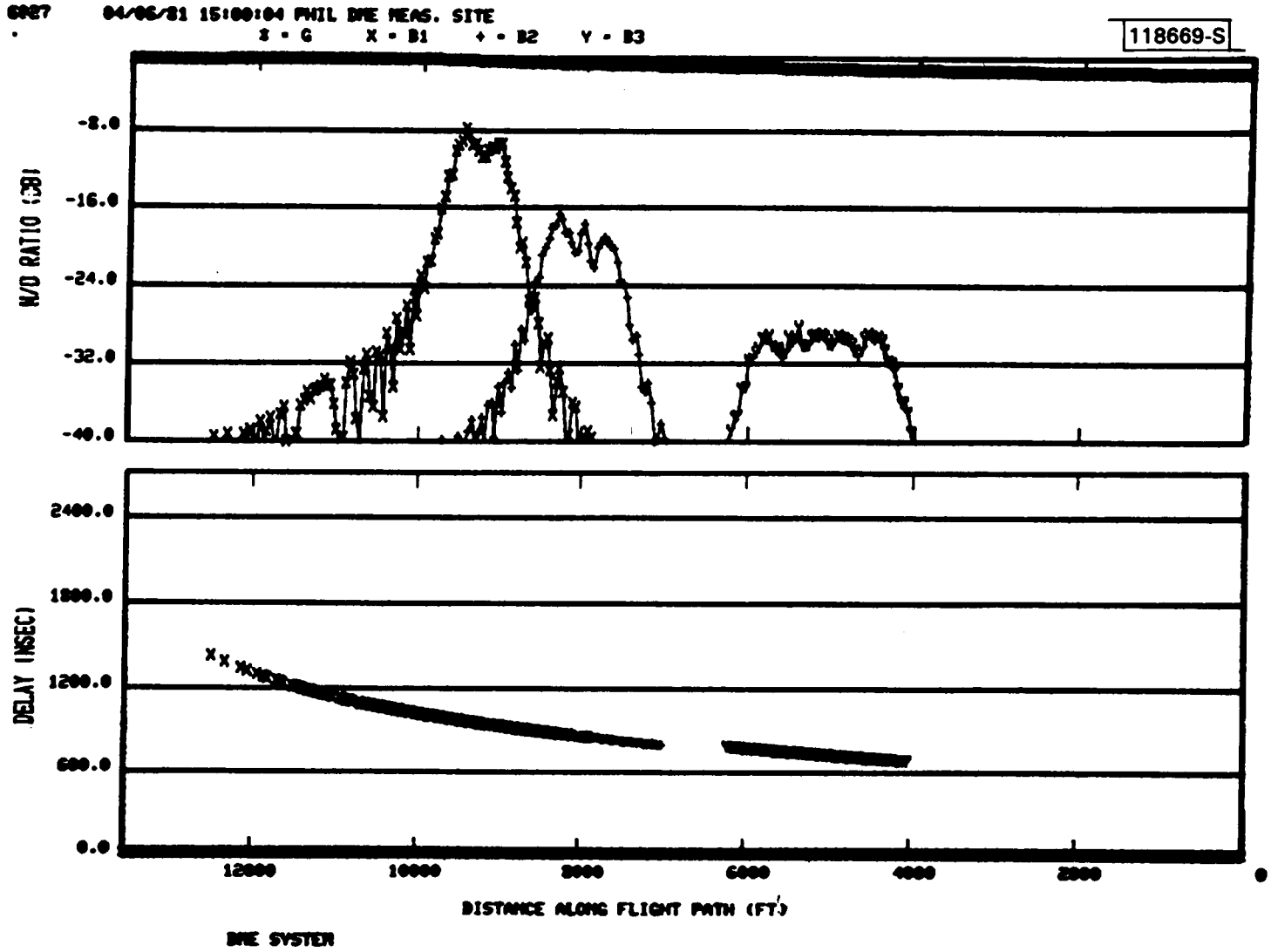


Fig.5-19. Computed multipath characteristics for PHL measurement scenario.

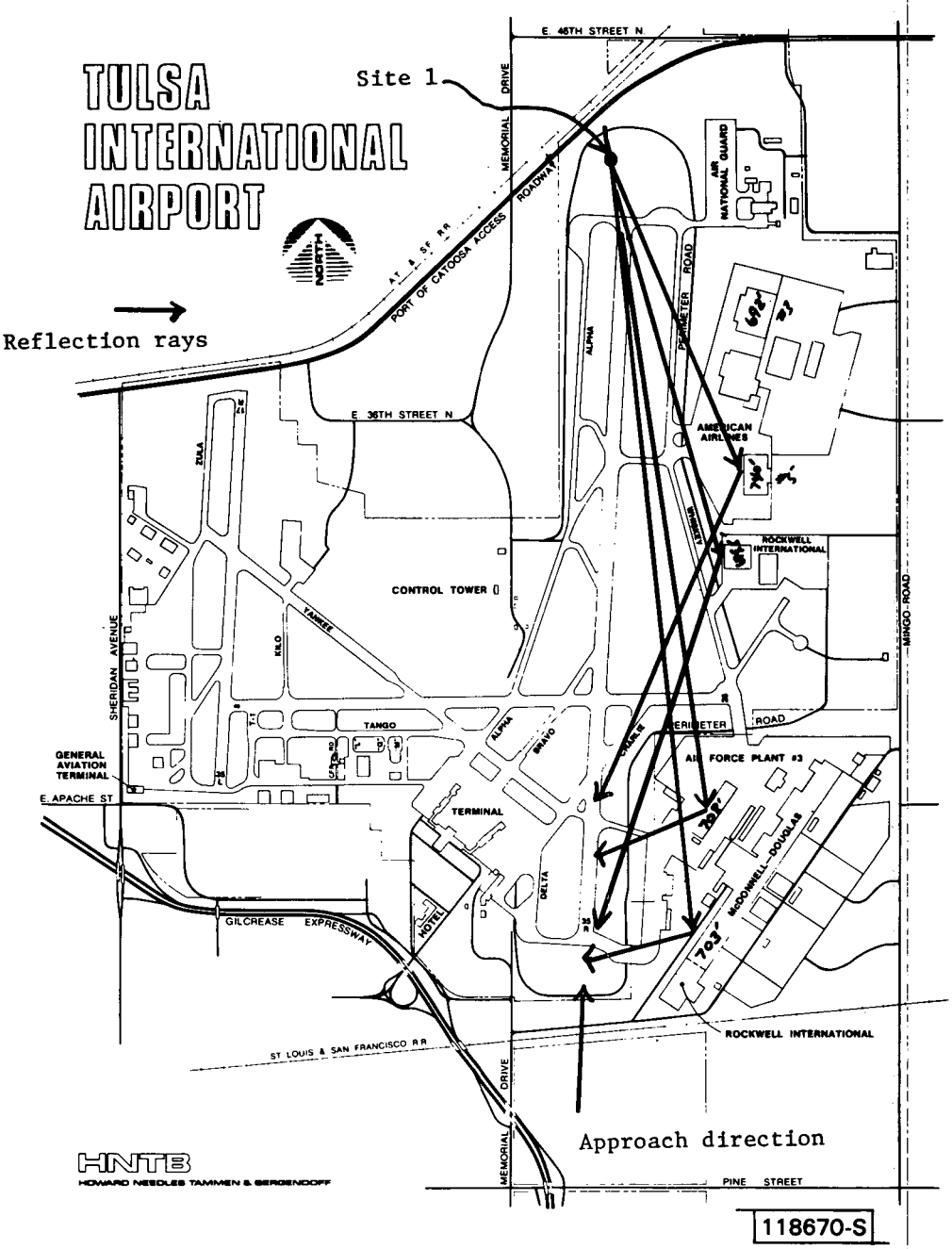


Fig.5-20. Tulsa site 1 measurement geometry and reflection rays.

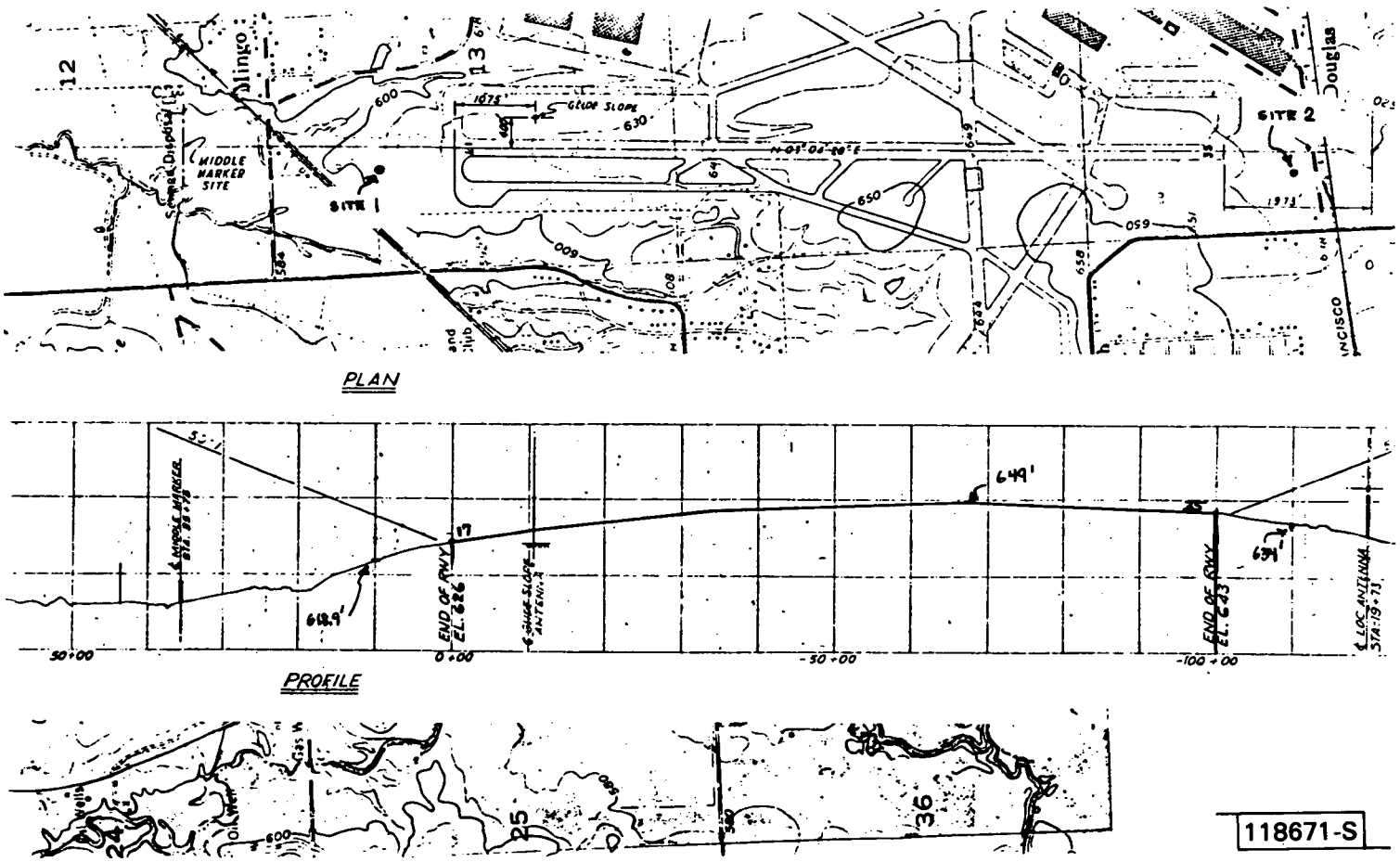


Fig.5-21. Terrain contour along Tulsa runway 17-35.

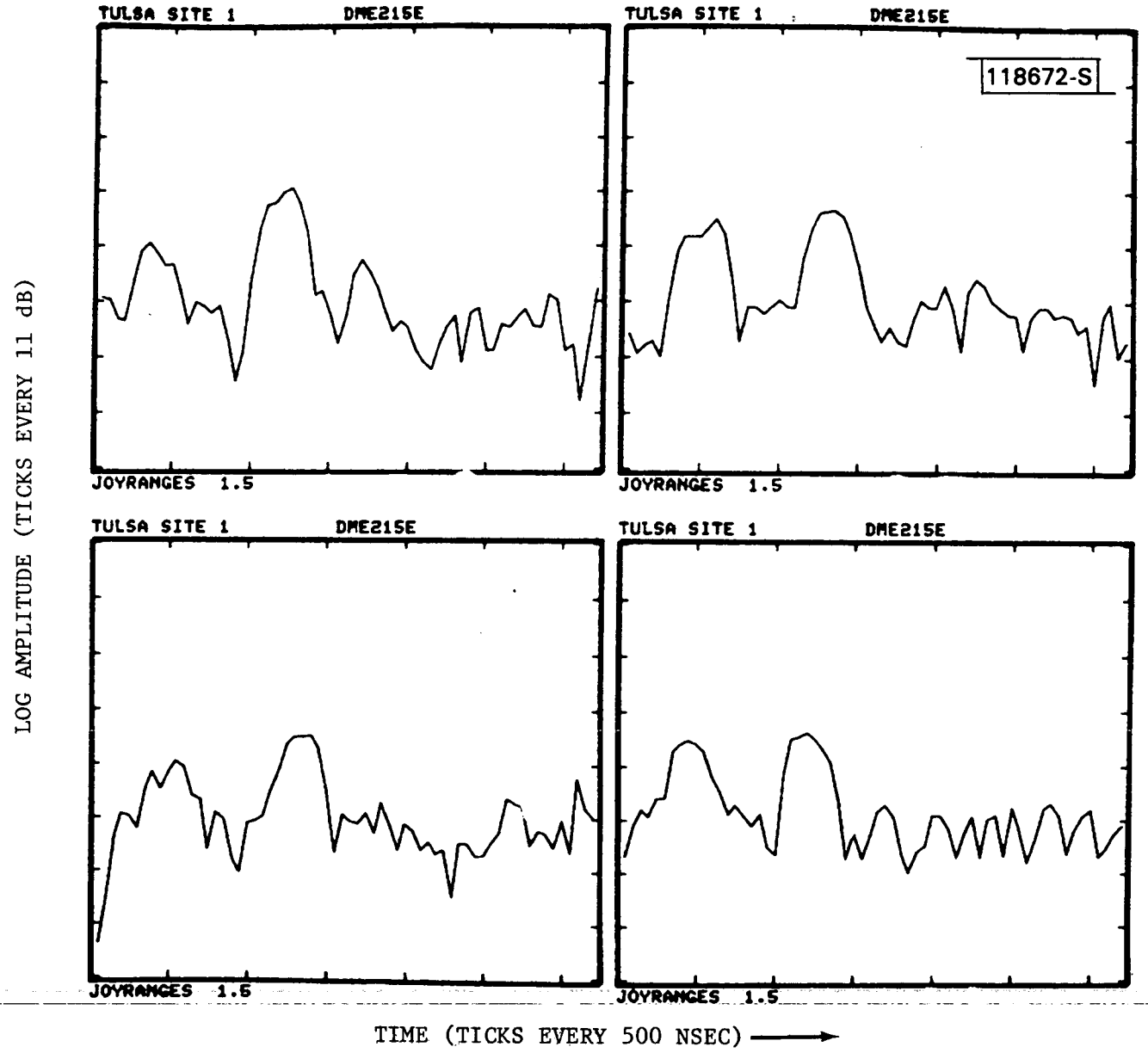


Fig.5-22. Tulsa site 1 waveforms over runway on flight profile 1.

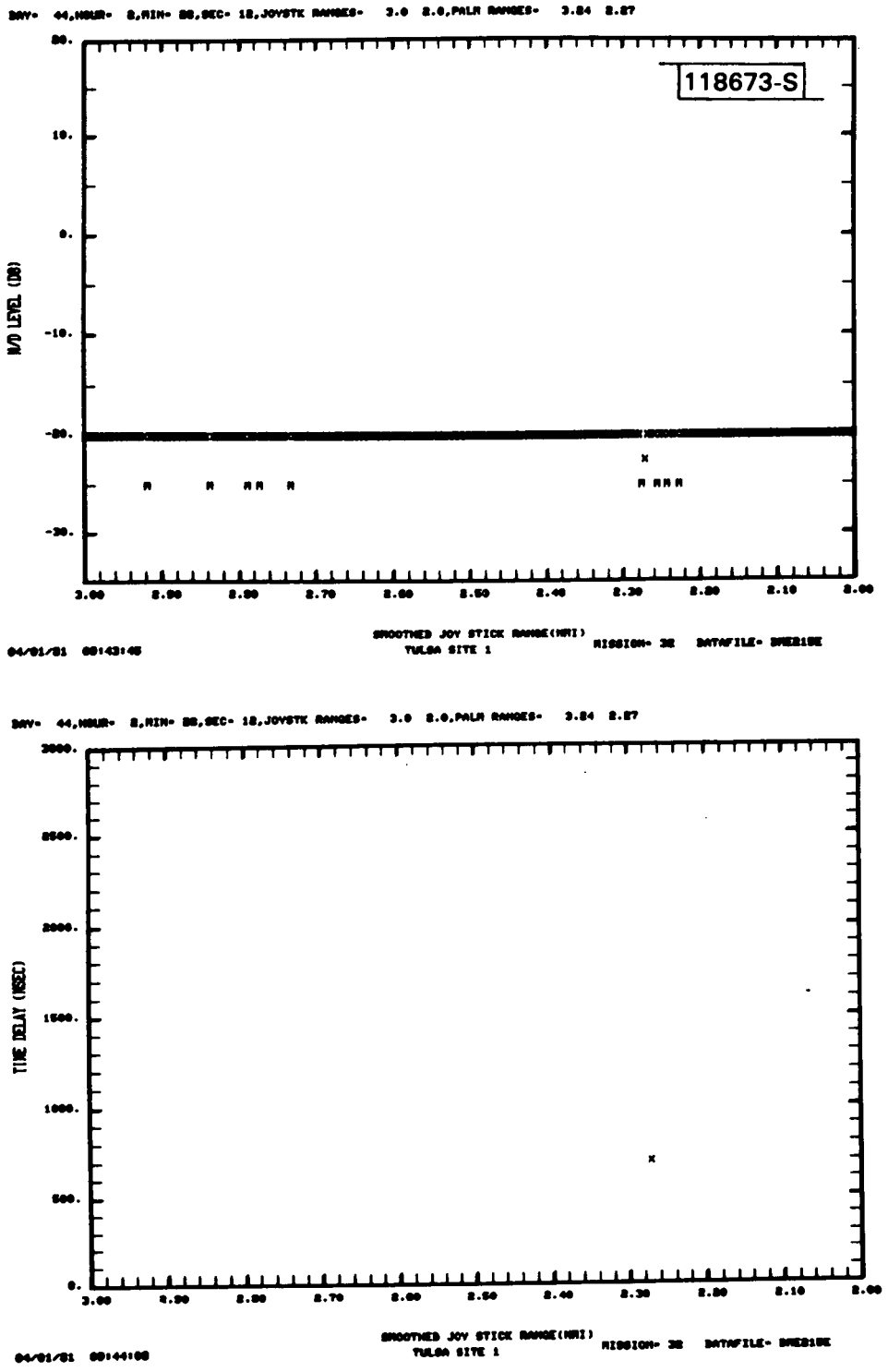


Fig.5-23(a). Tulsa site 1 data summary for 25 ft. threshold crossing height.

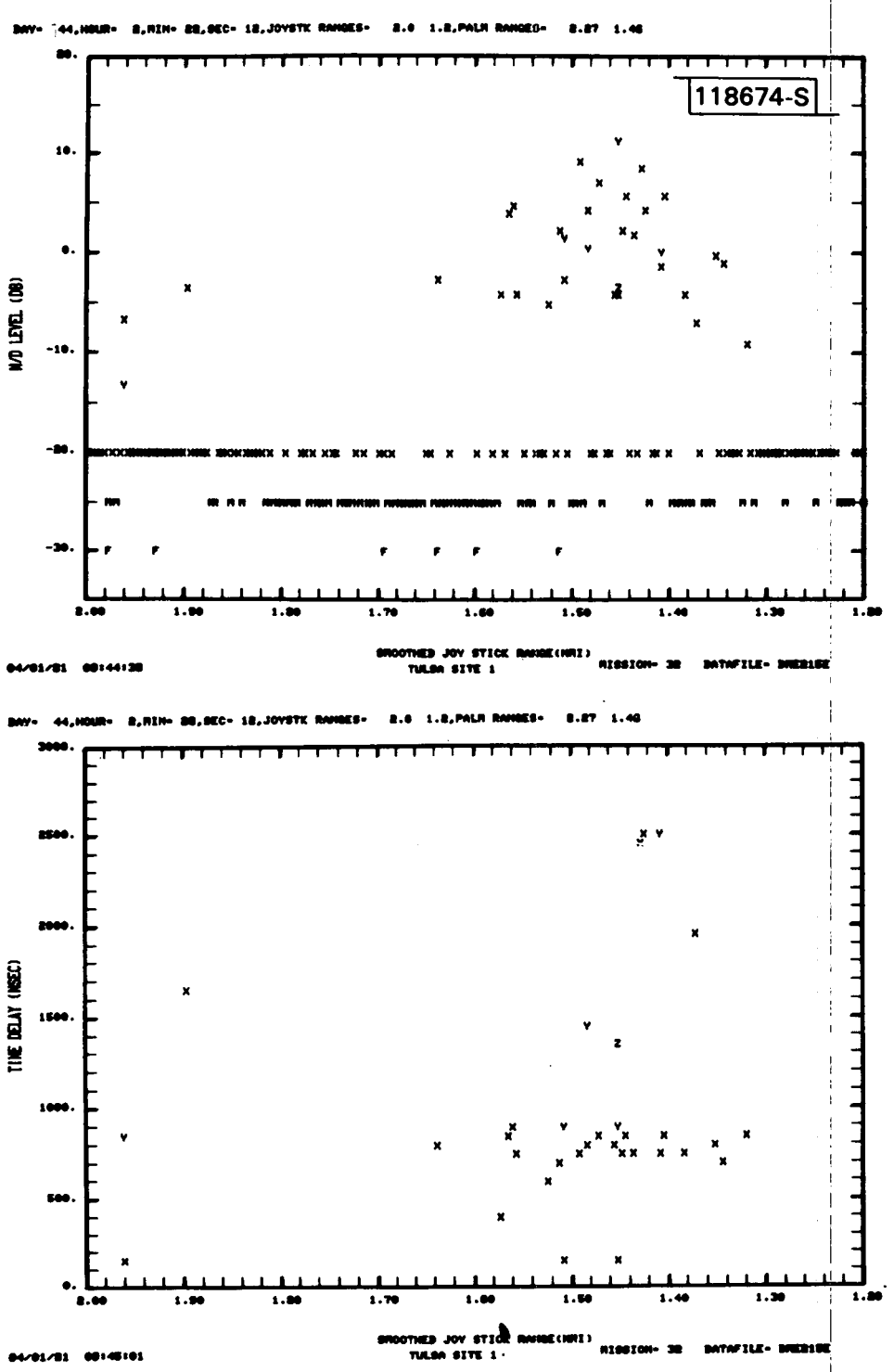


Fig.5-23(b). Tulsa site 1 data summary for 25 ft. threshold crossing height.

for a 3° approach to runway 35R. Much of the data in the expected multipath region after threshold were missed due to a combination of signal attenuation by the runway hump and/or suppression of the ATCRBS transponder by high level multipath from the M-D hangar (with a time delay of approximately 2 $\mu$s).

Figure 5-24 shows the simulation results for an approach to runway 35R with a 50-foot threshold crossing height and a 25-foot height along the runway. We see that low level ( $\geq$ -5 dB ) multipath with a $\tau$ of 700 -1100 ns is anticipated in a region approximately 2000 feet prior to the threshold from the McDonnell Douglas factory building. This correlates reasonably well with -15 dB multipath at 2.0 nmi joystick range in Fig. 5-23.

High level multipath is expected in the flare region (approximately 800 feet past threshold to 2000 feet past threshold) from both the AA hangar (800 ns delay) and McDonnell Douglas factory building (1000 to 3000 ns delays). These multipath levels and delay values do correlate with the few data points that were obtained in this region.

Figures 5-25 and 5-26 show representative waveforms and summary results for a 3° approach to runway 17L. The very high level multipath (+5 dB to as high as +15 dB M/D ratios) at threshold with relative time delays in the 400 - 600 ns range correlates quite well with the expected time delays and multipath region for the AA hangar. Farther down the runway, high to very high level multipath is encountered with a variety of multipath delays corresponding to reflections from several of the buildings.

Figure 5-27 shows the simulation results for an approach to runway 17L with a 50-foot threshold crossing height and a 25-foot height along the runway. High level (> 0 dB) multipath with a $\tau$ of 550 - 650 ns is predicted in a 600 foot region approximately 1000 feet prior to threshold (corresponding to a joystick range of approximately 2 nmi). This prediction of multipath region and delay correlates quite well with the measured results in Fig. 5-26; however, the peak measured M/D levels are considerably higher (6 dB to 12 dB) than the simulation results. This discrepancy probably reflects terrain contour features not considered in the simulation.

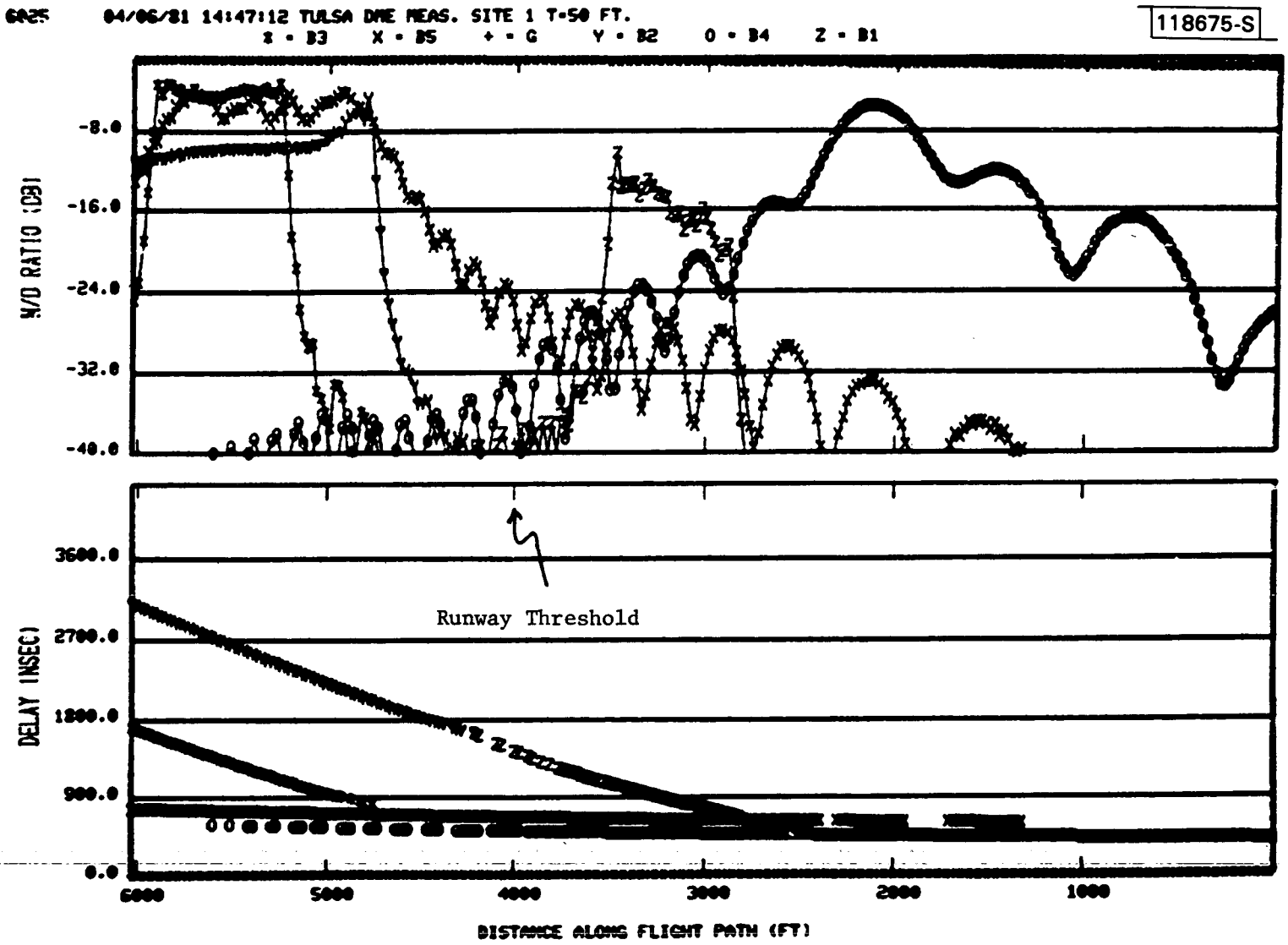


Fig.5-24. Computed multipath characteristics for simulation of Tulsa site 1 measurements.

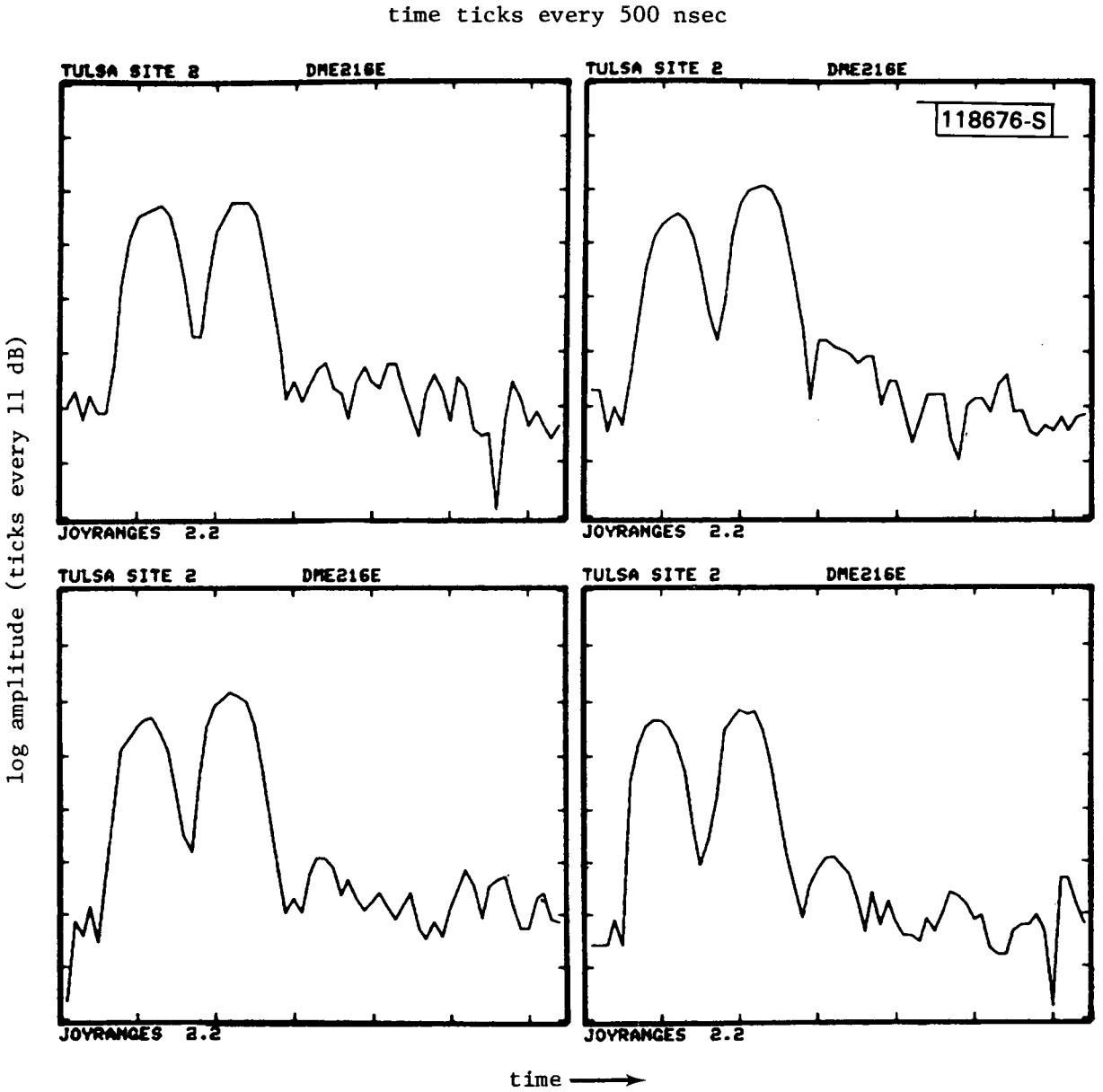


Fig.5-25. Tulsa site 2 waveforms near threshold.

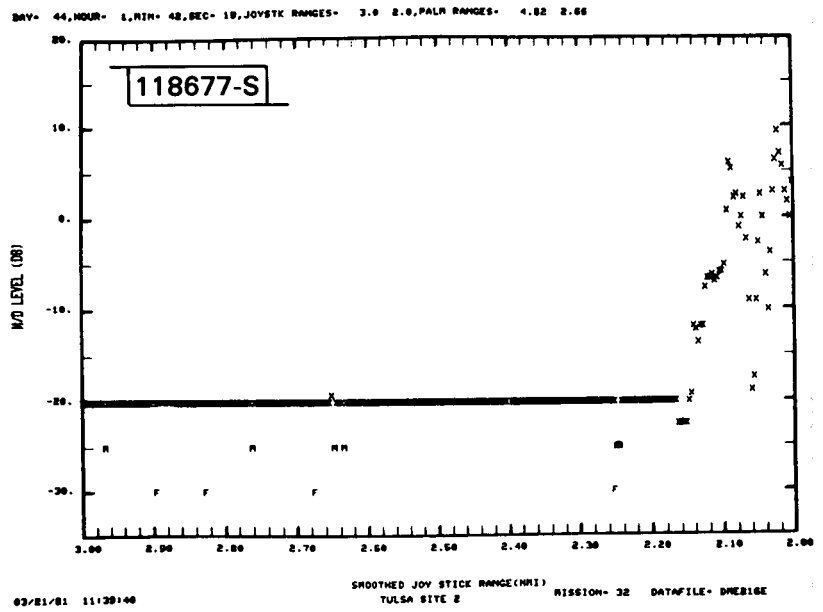


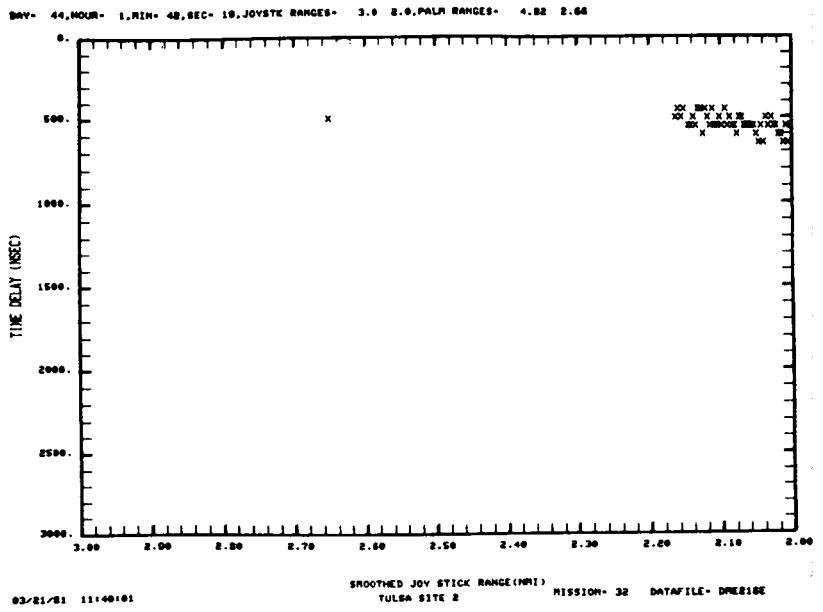


Fig.5-26(a). Tulsa site 2 data summary for 50 ft. threshold crossing height.

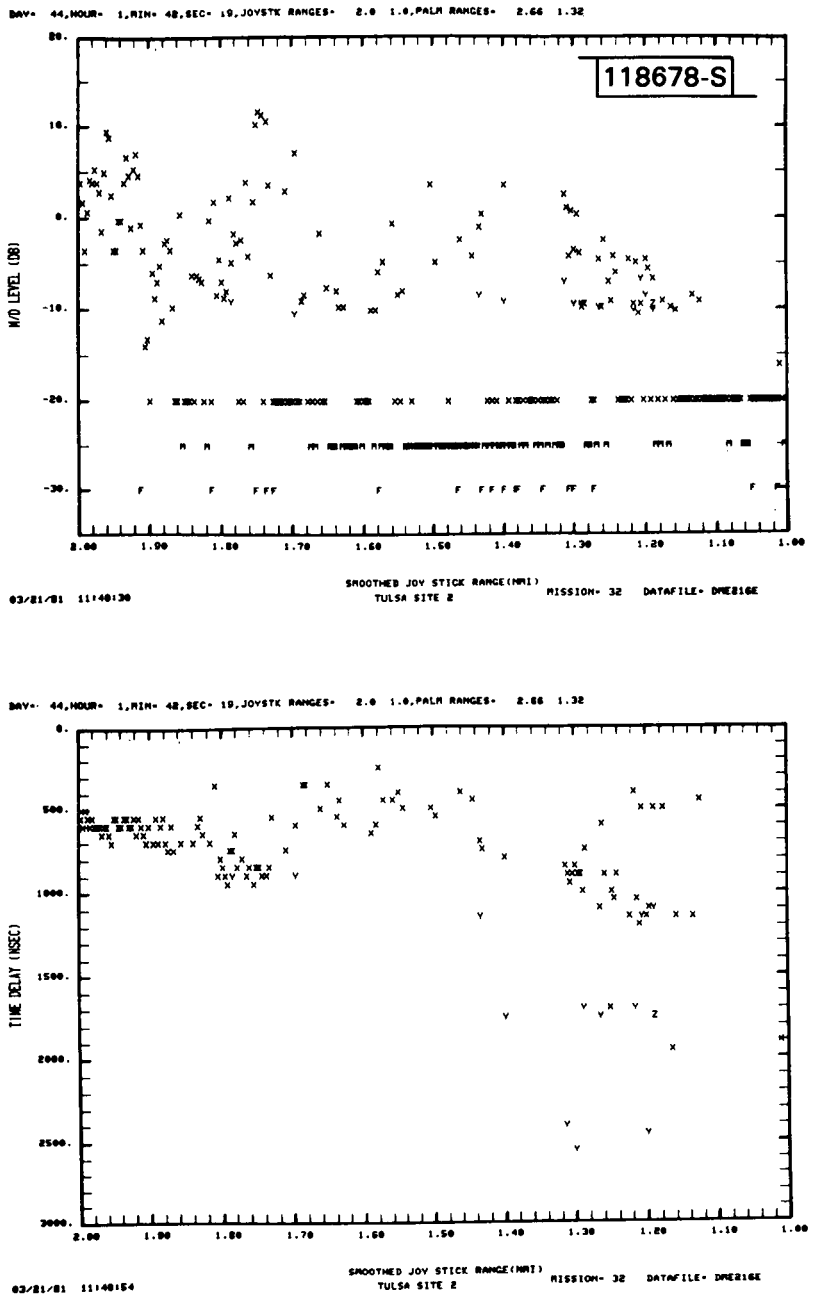


Fig.5-26(b). Tulsa site 2 data summary for 50 ft. threshold crossing height.

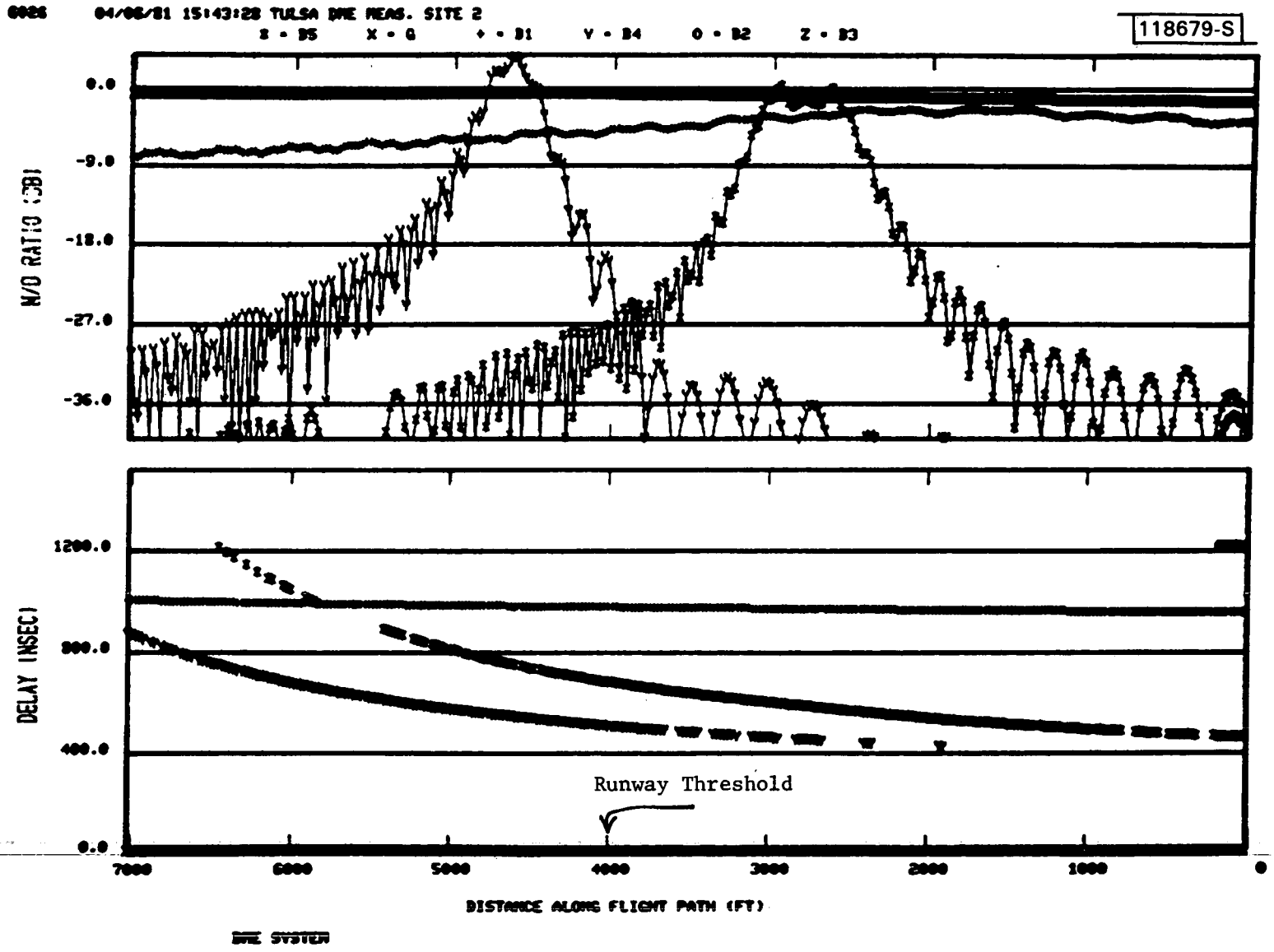


Fig.5-27. Computed DME multipath characteristics for simulation of Tulsa DME measurement site 2.

In general, the measured multipath regions and time delays at Tulsa International agreed quite well with the predicted characteristics using simple ray tracing. The measured M/D levels agreed reasonably well with the predicted levels at one site (although a detailed comparison in the flare region was not possible due to the many missed measurements), while at the other, the observed M/D levels were considerably larger (e.g., 6 to 12 dB) than those predicted. The large differences are felt to arise from the (sizable) differences in terrain contour features along runway centerline and along the path to the buildings which were not considered in the simple airport model.

### 6. Quonset State Airport, Rhode Island

Figure 5-28 shows the measurement geometry for van tests at Quonset State airport which is a former military field now being used for general aviation aircraft. Four sizable hangars (approximately 20 m high) were expected to be the principal threats. This airport is very flat and much of the surface is paved so that the ground lobing here should agree fairly well with the classic models.

The measurements here were accomplished before the digital system was available. Thus, the M/D ratios determined by analysis of slope photographs taken at selected points inside and outside the expected multipath region. Figure 5-29 shows representative scope photographs while Fig. 5-30 shows that the measured M/D levels agreed fairly well with those predicted using a simple airport model.

In general, at Quonset State:

1. The peak levels of M/D as measured agreed with the model predictions, and

2. the variation of peak M/D levels with transmitter height was also successfully predicted.

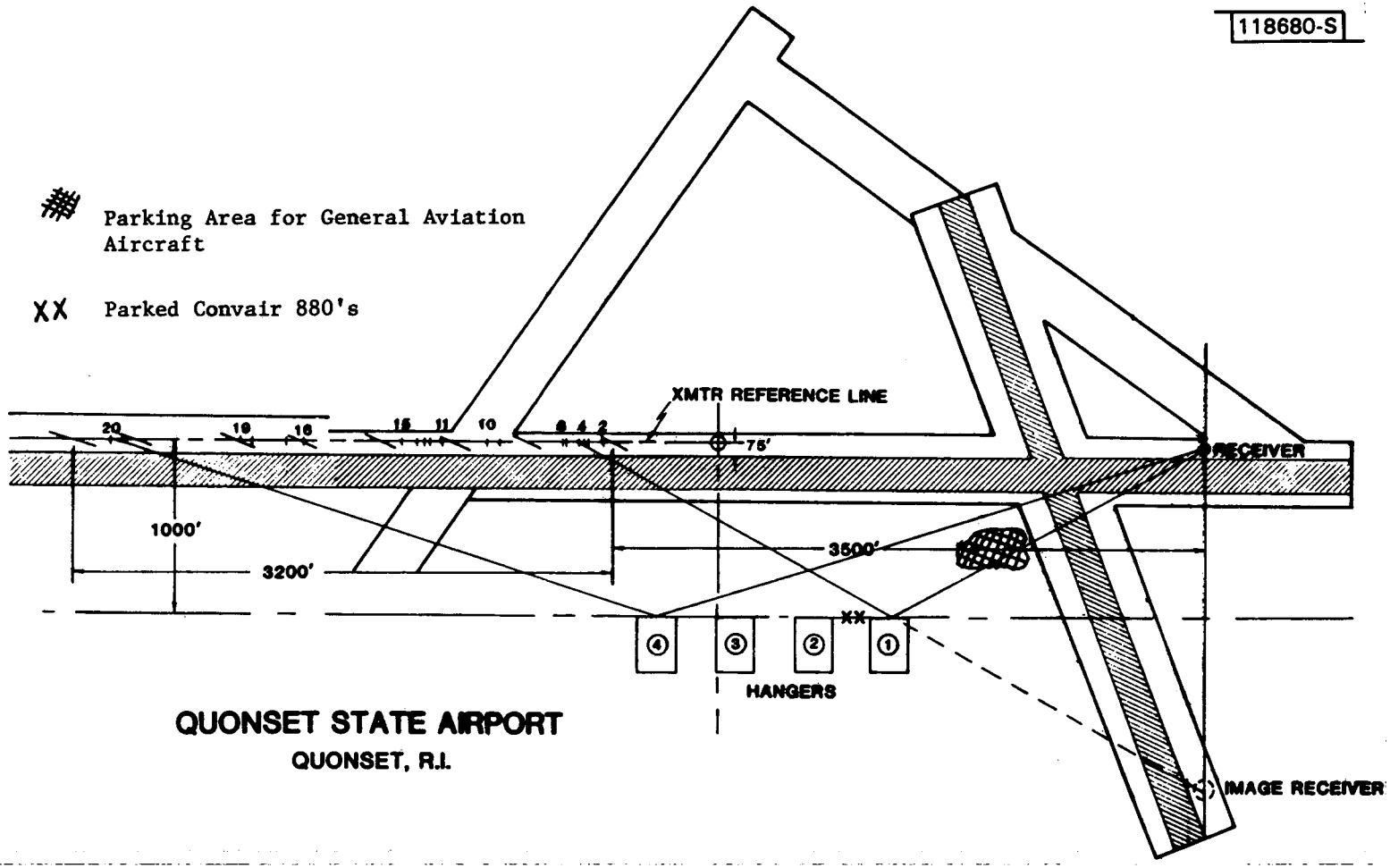


Fig.5-28. Quonset State Airport measurement geometry.

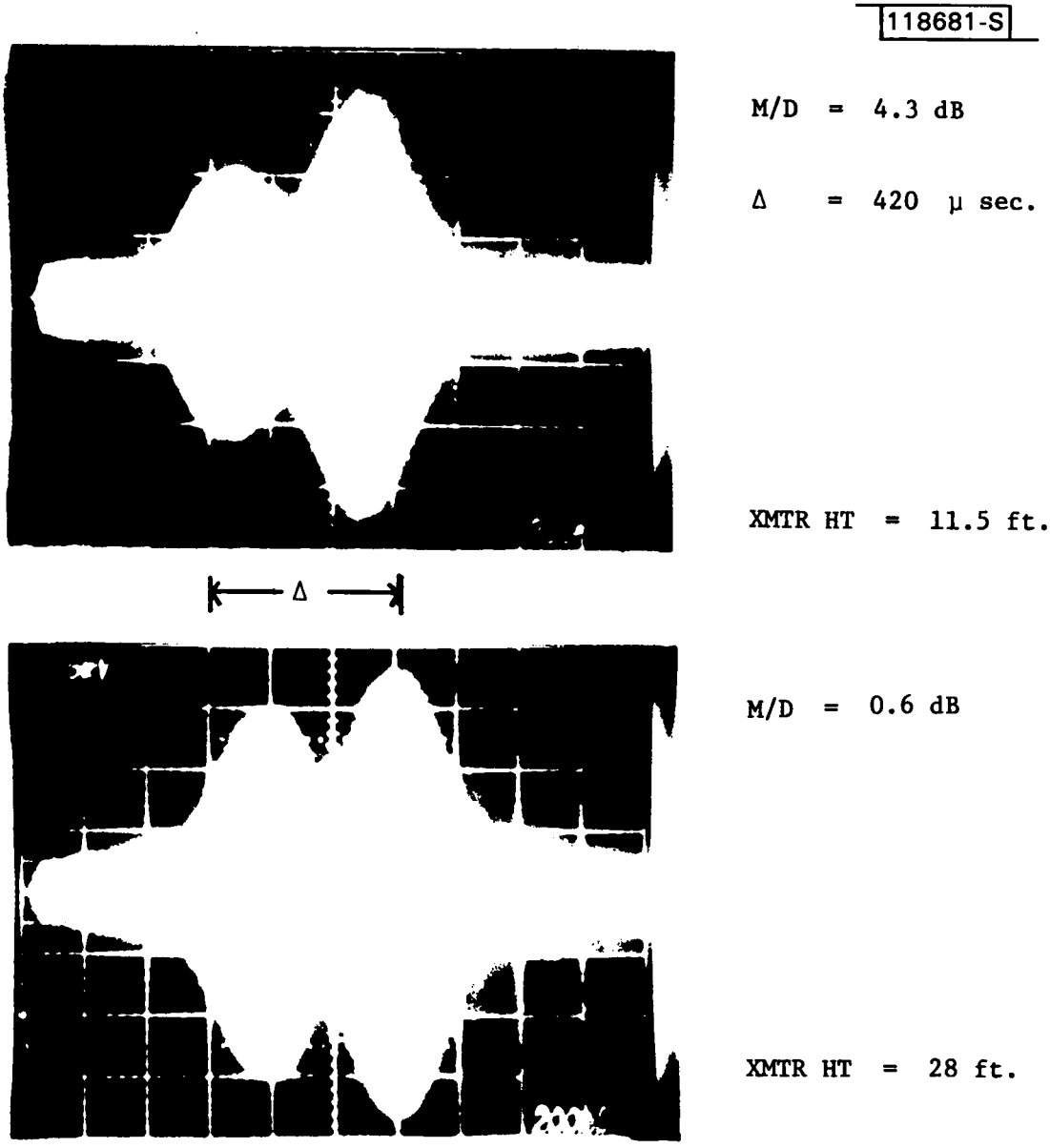


Fig.5-29. Measurement station #14 data.

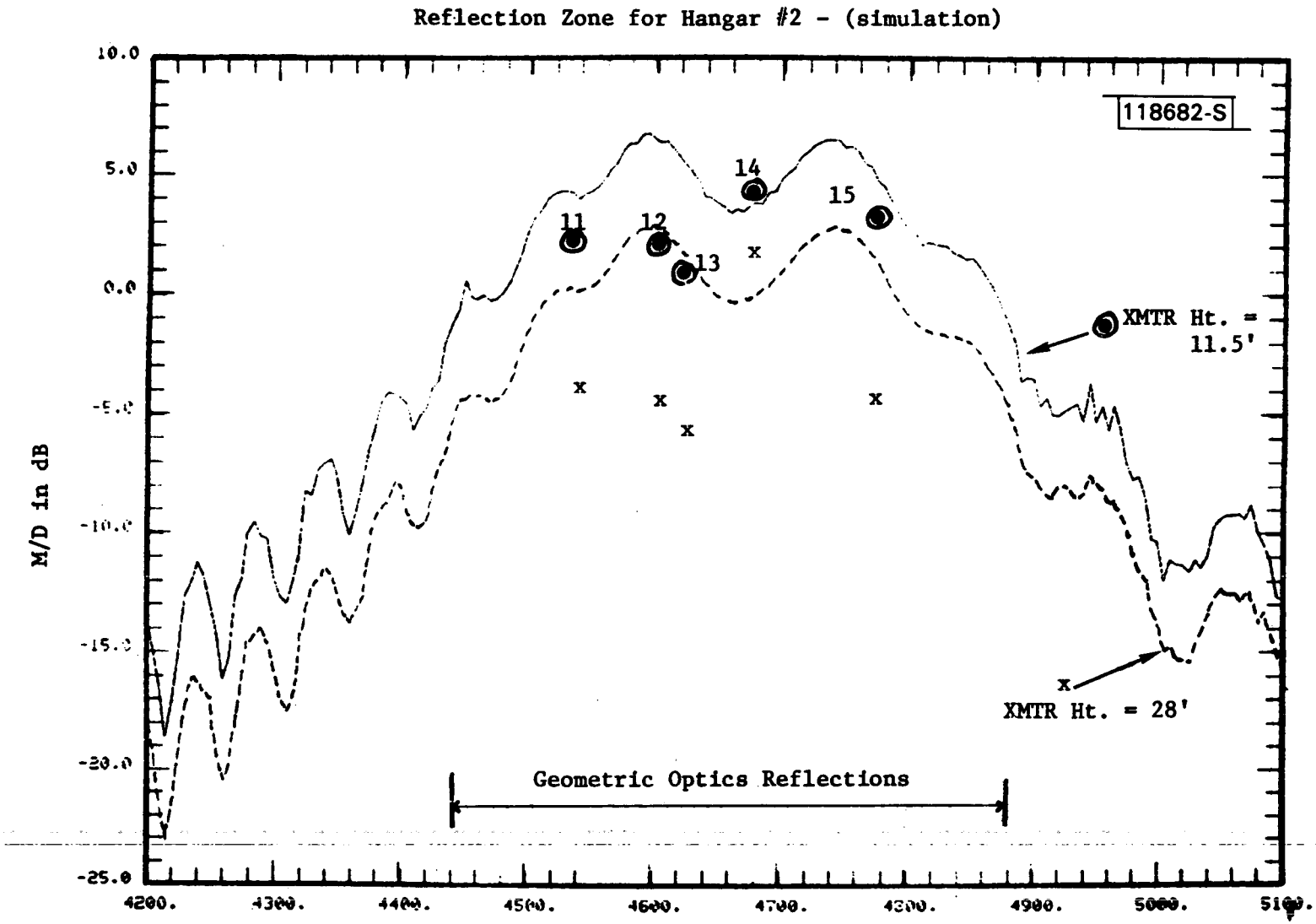


Fig.5-30. Comparison of Quonset State measured and simulated M/D levels.

The agreement here was quite good considering that a very crude building model used and that blockage by intervening aircraft was ignored.

### 7. Summary of L-Band Results

All of the L-band measurement program objectives were achieved although in some cases [especially, WPAFB, PHL, and Tulsa site #1] the experimental data in the flare/rollout region was of poor quality due to low signal to noise ratio. The spatial region and time deal of specular multipath generally correlated well with expectations based on simple ray tracing for these cases in which adequate airport maps were available. With the exception of Washington National (DCA), no significant (M/D ratio > -10 dB) specular multipath was encountered which was not predicted. In the case of DCA, there is some question as to whether the multipath encountered at 2-3 nmi from threshold arose from the identified buildings as opposed to other airport features.

The absence of significant specular multipath* from other than readily identified structures at aircraft altitudes above 100 feet is viewed as particularly important for the initial implementation of MLS since the vast majority of the installations will provide category I/II service only.

When the aircraft antenna was at low altitudes (e.g., 10-20 feet) over runways and/or taxiways, a variety of multipath signals were encountered which generally correlated with the principal identified structures. On the other hand, the large number of potential multipath sources in this region precluded a detailed quantitative analysis for each of the various sites.

The airport models used for DME/P analyses to date have typically made a number of simplifying assumptions such as:

---

*The possible existence of numerous low level (e.g., diffuse) specular reflections in this region is discussed below.

1. buildings are represented by single flat vertical rectangular plates with a constant reflection coefficient

2. the terrain is assumed to be flat both along and off the runway centerline, and

3. blockage of reflection paths by intervening objects is ignored.

The physical features of actual airports differ considerably from each of these assumptions, but arguments can be advanced to support either higher or lower levels than predicted by the simplified models. Thus, we sought to determine to what extent simplified airport models could predict the measured data. The quantitative predictions of the simple airport models generally agreed with the experimental data, although in some cases (especially near threshold at WPAFB, DCA, and Tulsa), the measured M/D values were considerably higher than predictions. We attribute the WPAFB and Tulsa high levels to terrain contour features. In this context, it should be noted that 4 of the 6 airports had runway contours which differed considerably from the nominally flat model used for DME/P power budget computations.

Although the M/D levels encountered at several of these airports were above the -3 to -6 dB levels assumed in some DME/P "worst case" analyses (see, e.g., [3]), the relative time delay were in all cases considerably larger than the 300 ns value which is the upper limit of the "sensitive region" for the proposed DAC designs. Thus, building reflection multipath at these airports should not pose a threat to the DME/P precision mode. On the other hand, a conventional DME (e.g., slow rise time Gaussian pulse and -6 dB RTT receiver) would clearly have multipath problems at several of these sites.

## C. Results of High Time Resolution S-Band Multipath Measurements at an Operational Airport

The multipath measurements summarized in the preceding section utilized pulses with relatively large widths (e.g., 100 - 200 ns). Consequently, it

was not possible to resolve multipath returns whose time delay relative to the direct signal fell within the 0 - 200 ns range which is of greatest concern to the precision mode of DME/P. It had been suggested that there may be diffuse multipath from small scatterers near the runway which could (by virtue of its short relative time delays) significantly degrade the performance of DME/P [37].

To quantify the magnitude of such diffuse multipath, a set of measurements were carried out using a wideband (100 MHz bandwidth) channel probing system developed at M.I.T. Lincoln Laboratory. Frequency allocation constraints necessitated operation at S-band (3 GHz). However, in view of the general similarity between terrain reflections at C- and L-bands in earlier measurement programs [17, 27], it is anticipated that the S-band results are applicable to L-band.

1. Measurement System

The high time resolution multipath measurement ground van is shown in Fig. 5-31. S-band (3.0 GHz) signals are transmitted from a helicopter through a blade antenna (Fig. 5-32) to the receiving horn antenna* (27° beamwidth). The IF signal is correlated with an internal replica of the transmitted waveform and the correlator output envelope displayed on an oscilloscope. For the experiments described here, the oscilloscope display was recorded on a standard (Sony) TV video recorder for subsequent playback. At the same time, a call out of helicopter position and other data was placed on the audio track so that the measured multipath characteristics could be correlated with airport features.

The transmitted waveform is obtained by modulating a CW carrier with a biphase pseudonoise waveform. The pseudonoise waveform is generated by a 10 stage, maximal length shift register generator with 1023 code elements and a

*The horn antenna is at the top of the ladder on the measurement van side in Fig. 5-32.

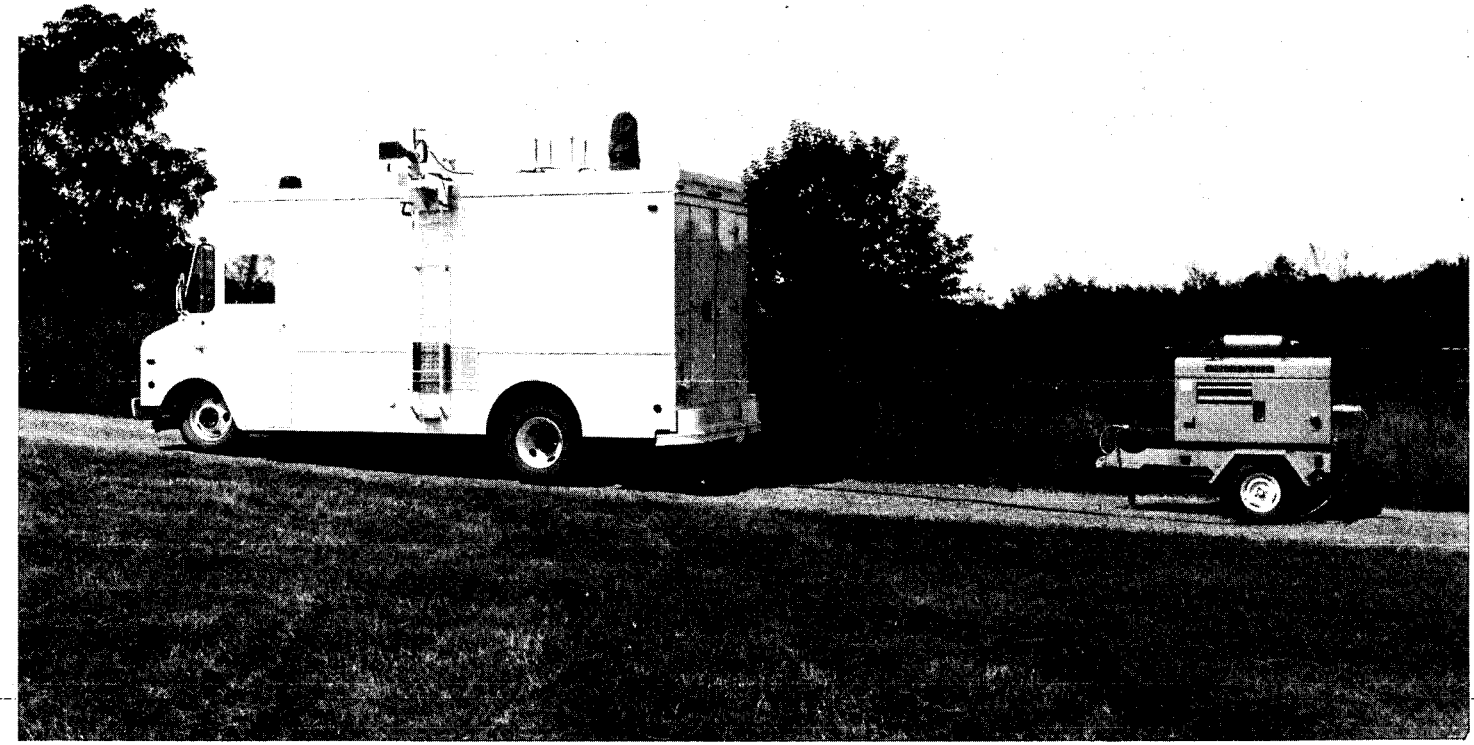


Fig.5-31. Measurement van and diesel generator.

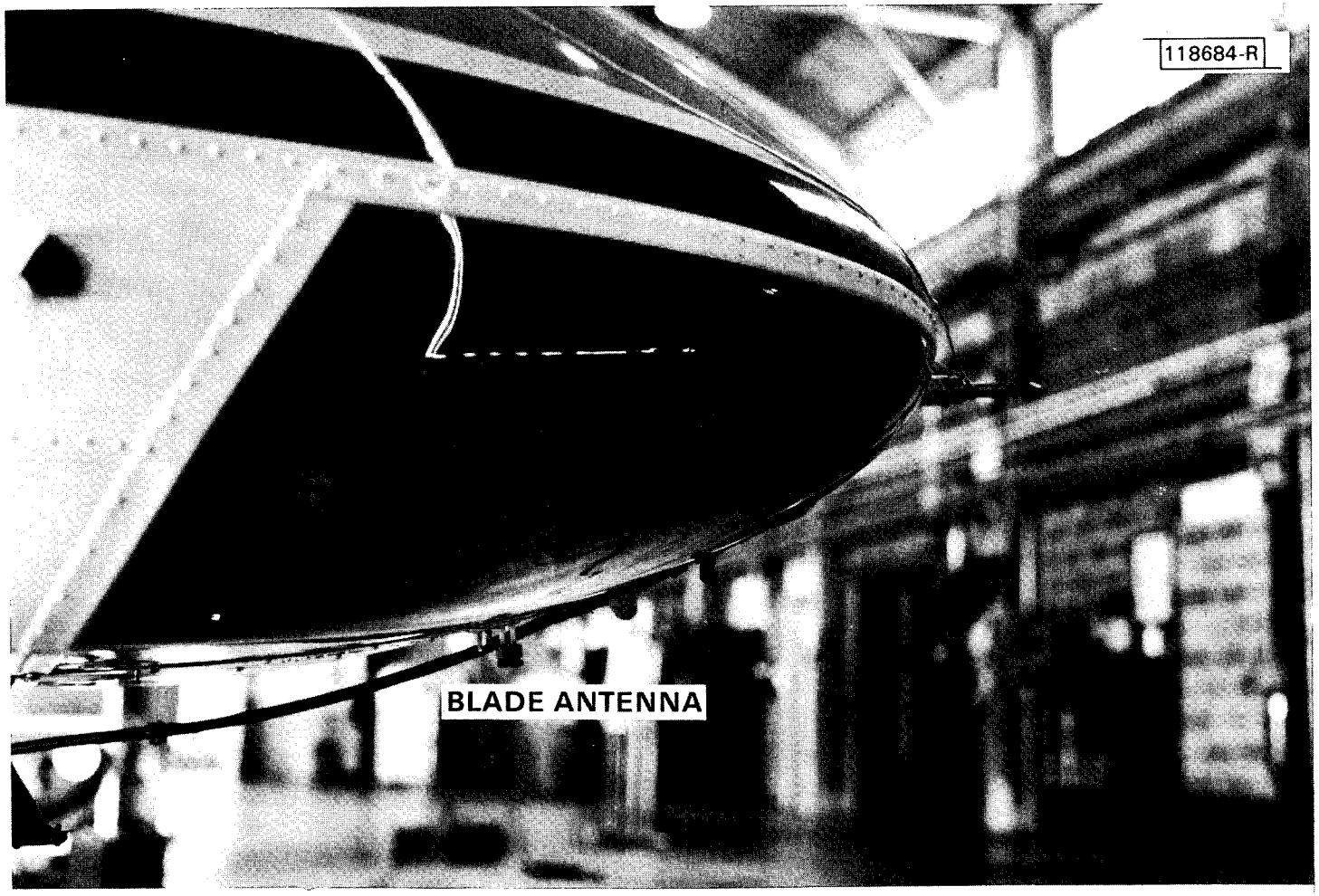


Fig.5-32. Closeup of blade antenna on helicopter.

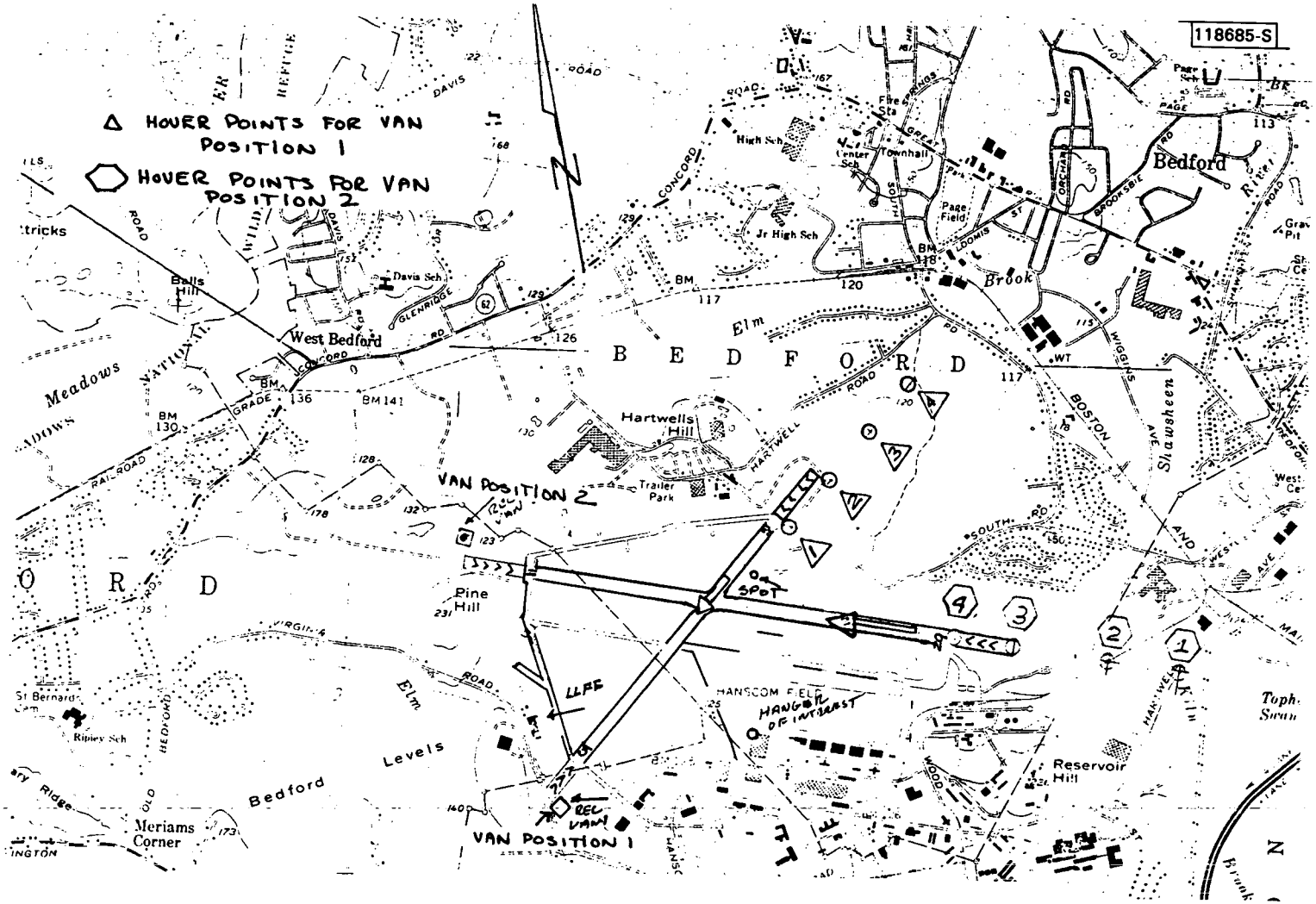


Fig.5-33. High time resolution multipath experiment geometry at L.G. Hanscom Airport (Bedford, MA).

bit rate which can be as high as 200 MHz. The correlation peak width is approximately 10 ns at the 200 MHz bit rate and the peak to sidelobe ratio is approximately 30 dB ( = 10 log 1023).

The correlator produces an output for each component of the received signal which is in phase with the waveform generated at the receiver. Thus, by varying the relative delay between the receiver and transmitter waveforms, received signals with relative time delays differing by more than 10 ns can be resolved as long as the relative amplitudes do not differ by more than (approximately) 25 dB.

The matched filter output envelope is linearly proportional to input amplitude, thus it was difficult to quantify multipath with M/D levels of less than -20 dB when the direct signal peak was also displayed. Consequently each flight profile was repeated with a variety of known receiver gains so as to display lower level multipath. However, the minimum discernable M/D level is approximately -27 dB due to the -30 dB pseudonoise sequence signal sidelobes.

Figure 5-33 shows the measurement locations for the measurements on two runways at L. G. Hanscom airport (Bedford, MA). Hanscom airport is a former military airport which is now actively used by general aviation aircraft (including jets) as well as some large military transport aircraft. The measurements were made at locations corresponding to key points on a 3° approach (e.g., cat I, II decision height and threshold) since the receiving system required a nearly stationary helicopter position to avoid Doppler artifacts.

The receiving antenna heights were chosen to be approximately the same number of wavelengths above the ground as would be a DME/P antenna at the same height. This choice is appropriate because the effective direct signal level near the threshold is:

$$D = \left[ 1 - \rho \, e^{j 4\pi (h_t/d)\,(h_r/\lambda)} \right] D_{fs}$$

where

$D_{fs}$ = free space direct signal level at range d

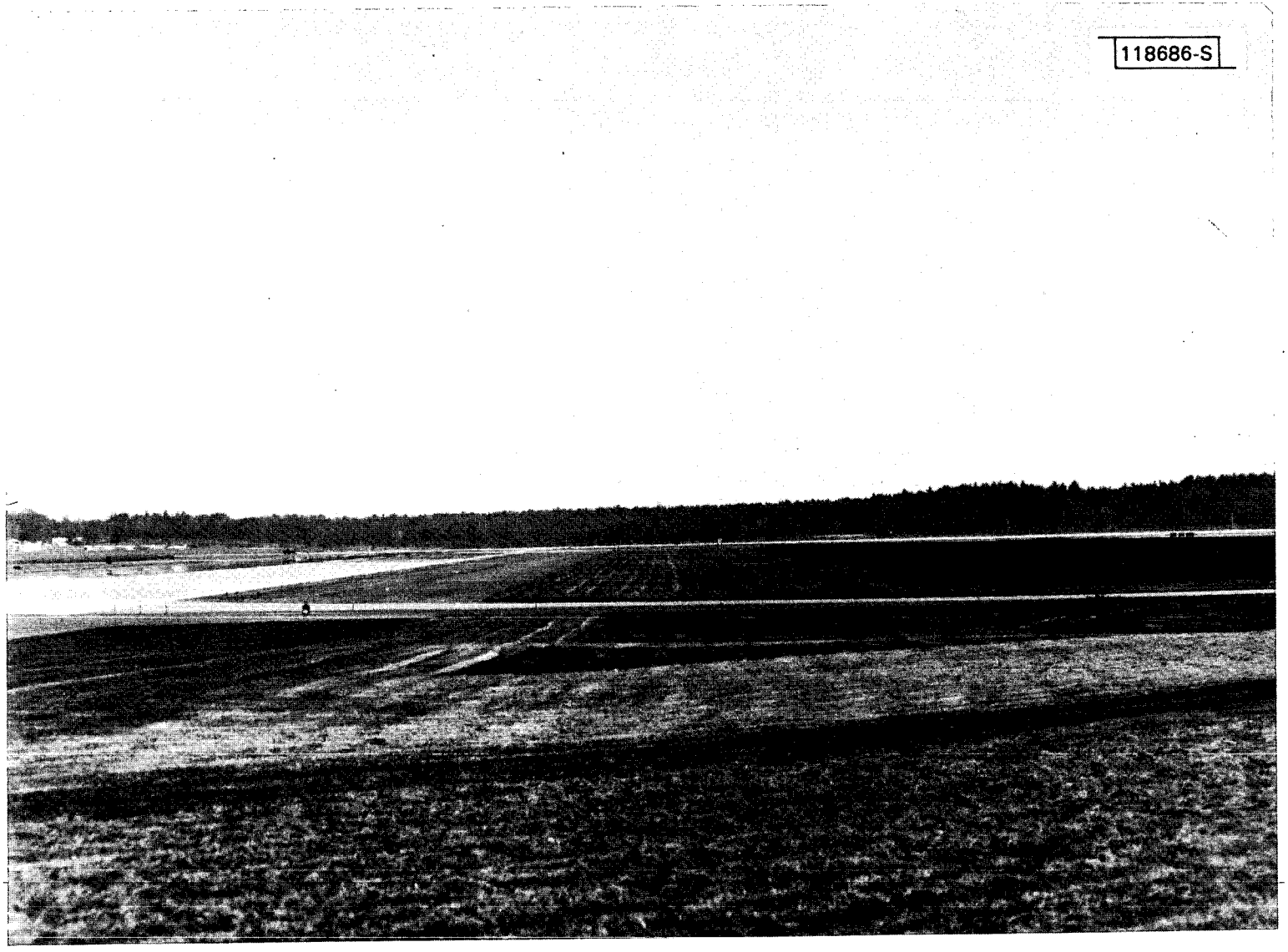


Fig.5-34. View from van site for runway 5-23 measurements.

$h_t$ = transmitter (i.e., aircraft) height

$h_r/\lambda$ = receiver (i.e., ground antenna) height in wavelengths

$\rho$ = ground reflection coefficient (approximately 1.0 for the elevation angles in these experiments).

Thus, by keeping $h_r/\lambda$ constant, one has roughly the same degree of ground lobing at S-band as would be the case at L-band.

The first set of measurements on runway 5-23 were conducted 30 July 1981. Figure 5-34 shows the view from measurement van site while Fig. 5-35 shows the runway as seen from the 23 threshold. The van to threshold distance was approximately 5880 feet and the receiving antenna height approximately 7 feet. The environment near the runway is seen to be quite flat and devoid of sizable objects near the runway. However, there is a sizable (30m high) hill with trees and a variety of buildings aproximately 1000 feet to the side of the runway threshold.

Figure 5-36 shows the nominal envelope and, the envelope with 10 db additional gain (so as to show low level multipath) at 150 feet altitude. Figures 5-37 and 5-38 show corresponding results at 100 feet altitude and threshold, respectively. In all cases, the multipath levels in the 0-400 ns relative time delay region are at least 25 dB below the direct signal level.

Figure 5-39 shows the output envelope at an altitude of 15 feet when the helicopter was at the intersection of runways 5-23 and 11-29. Again, no discernable multipath with relative delays in the 0 - 400 ns region is evident in the correlator output envelope.

Figure 5-40 shows runway 11-29 from van site 2 while Fig. 5-41 shows the view from the 29 threshold. In this case, a greater number of potential scatterers border the runway. These include the ILS glideslope and transmitter building (left hand side of Fig. 5-40) as well as a small hill (left hand side of Fig. 5-41), trees and shrubs near the threshold as well as a number of hangars and parked aircraft approximately 1000 feet off the runway. Figures 5-42 and 5-43 show the hangar and parked aircraft area to the

118687-S

Fig.5-35. View from threshold of runway 22.

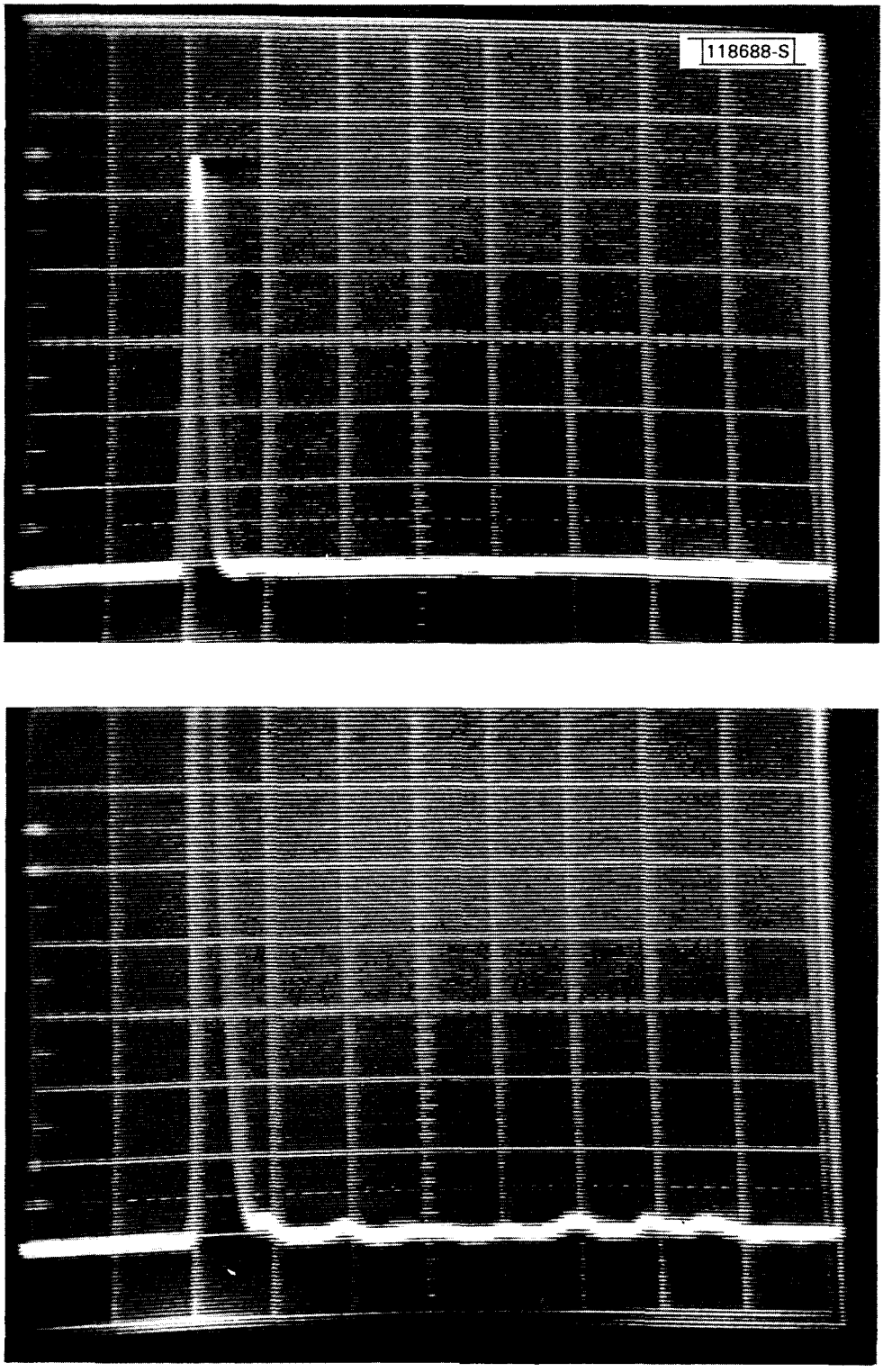


Fig.5-36. Received envelope 150 ft. above ground.

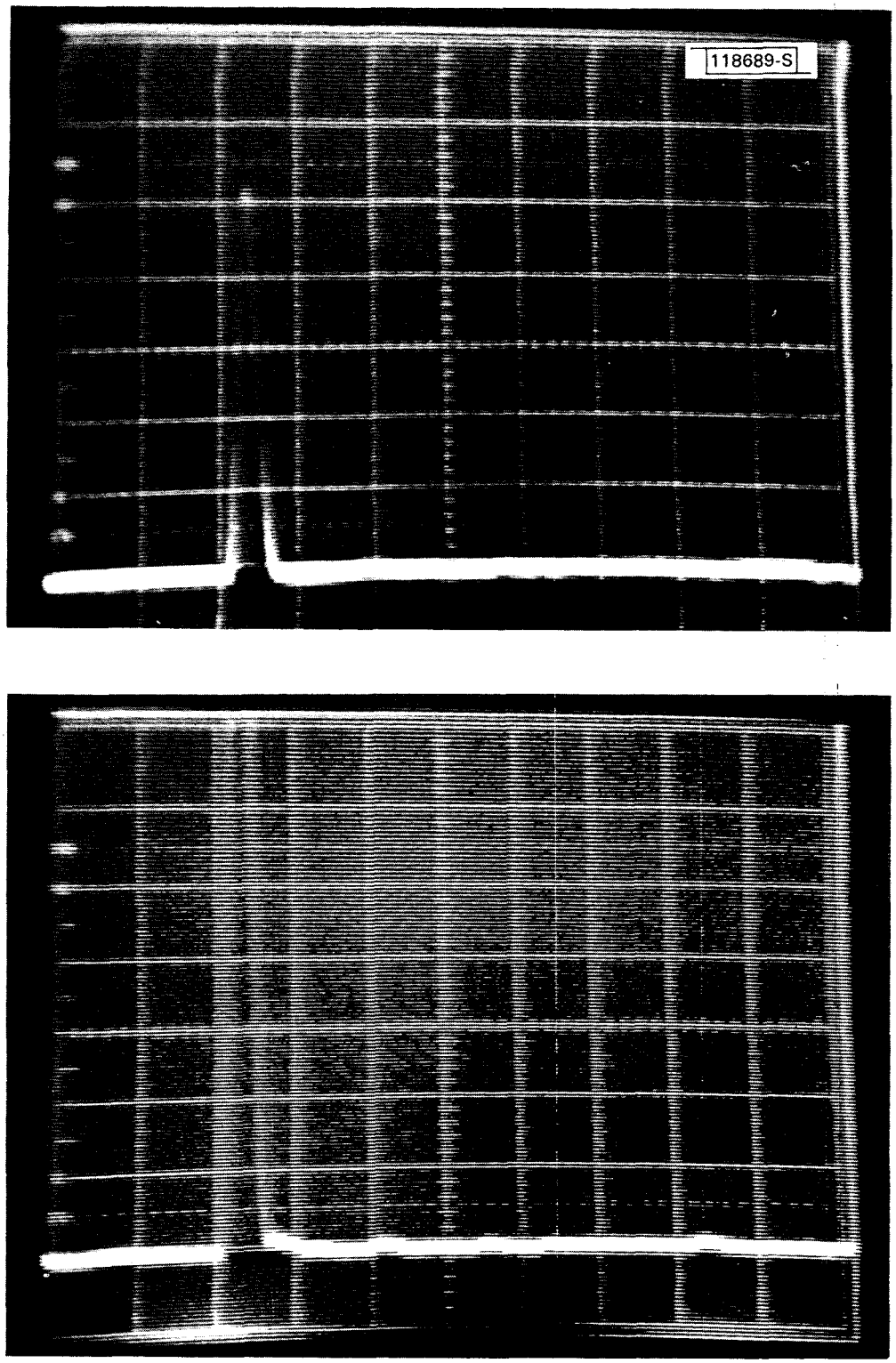


Fig.5-37. Received envelope at runway 22 threshold.

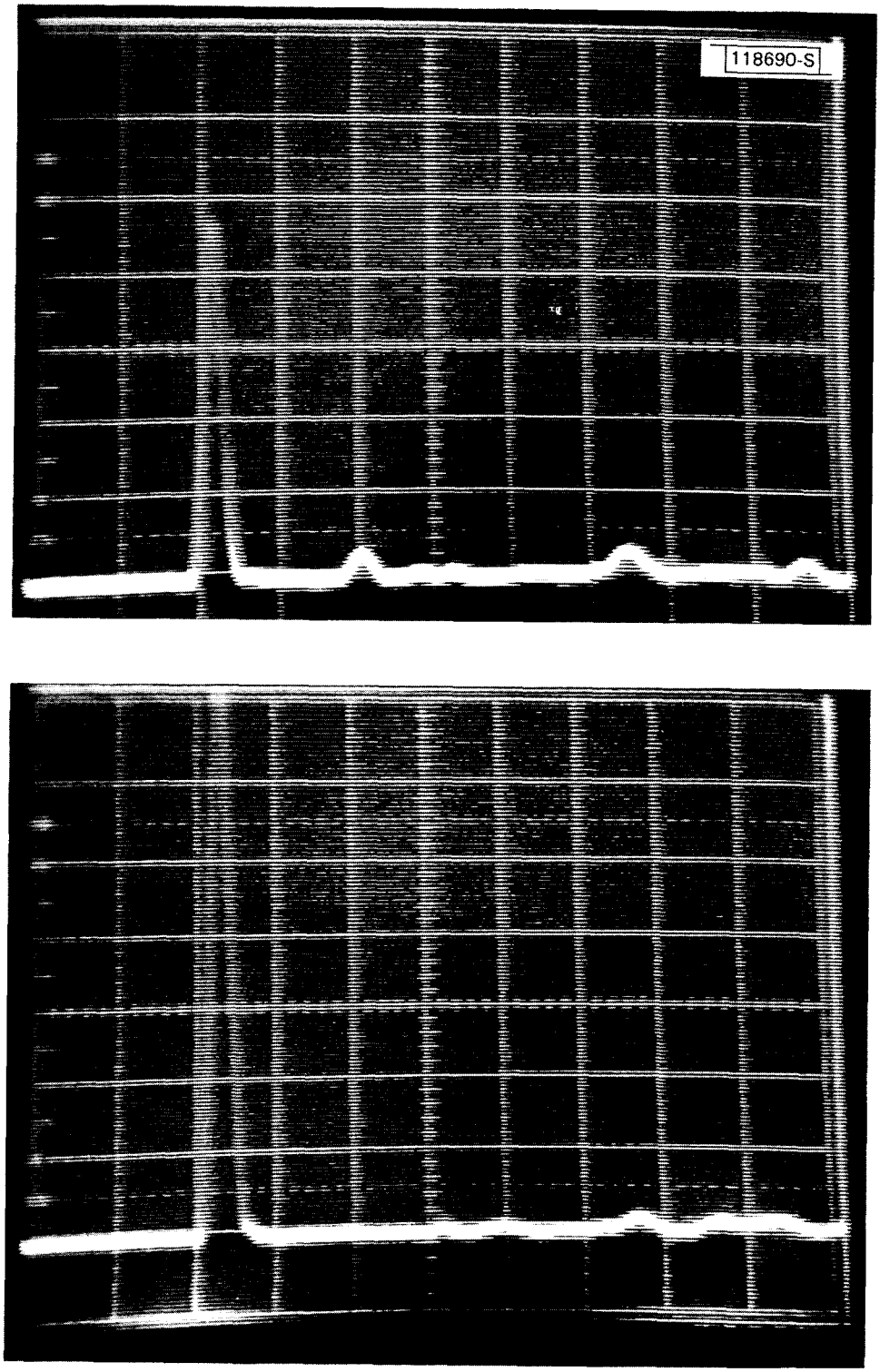


Fig.5-38. Received envelope 100 ft. above ground.

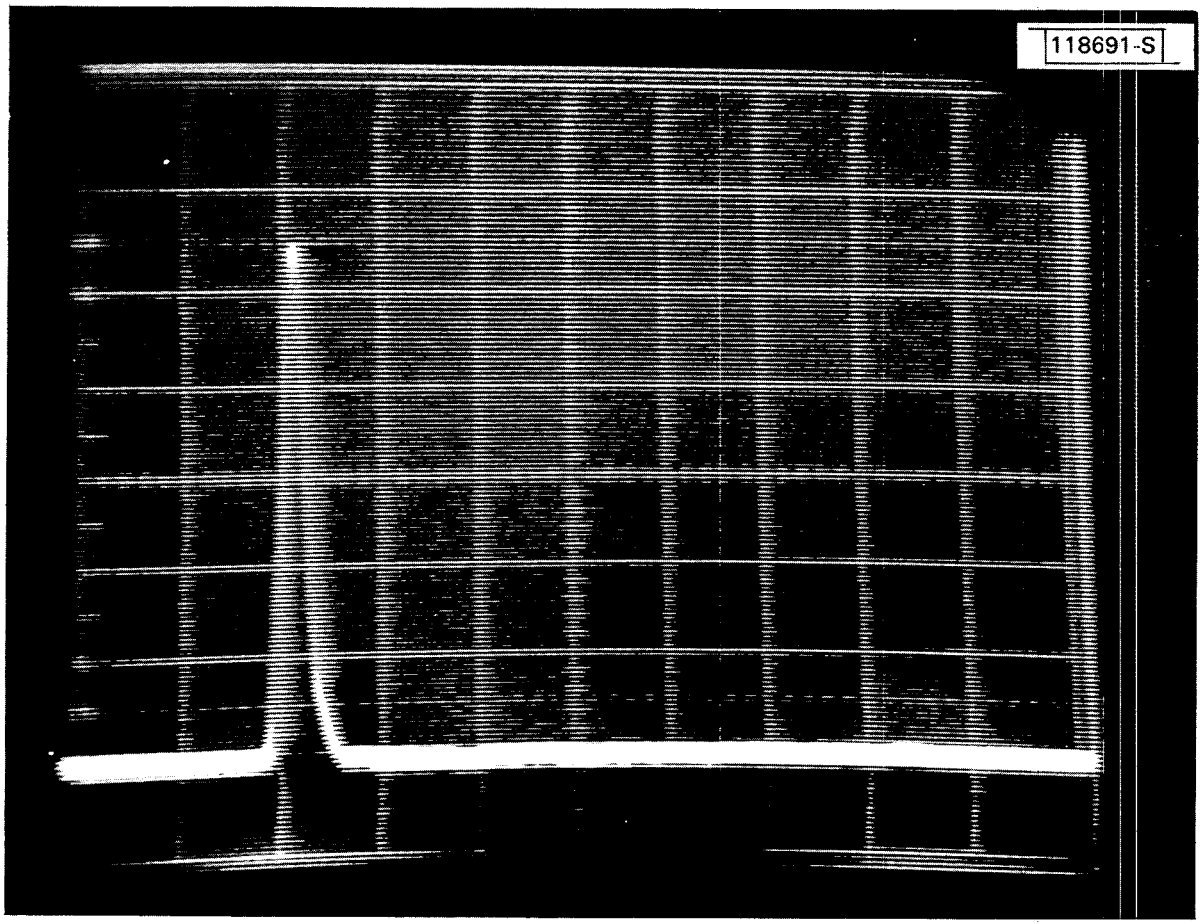


Fig.5-39. Received envelope 15 ft. above runway.

118692-S

Fig.5-40. View from van site for runway 11-29 measurements.

118693-S

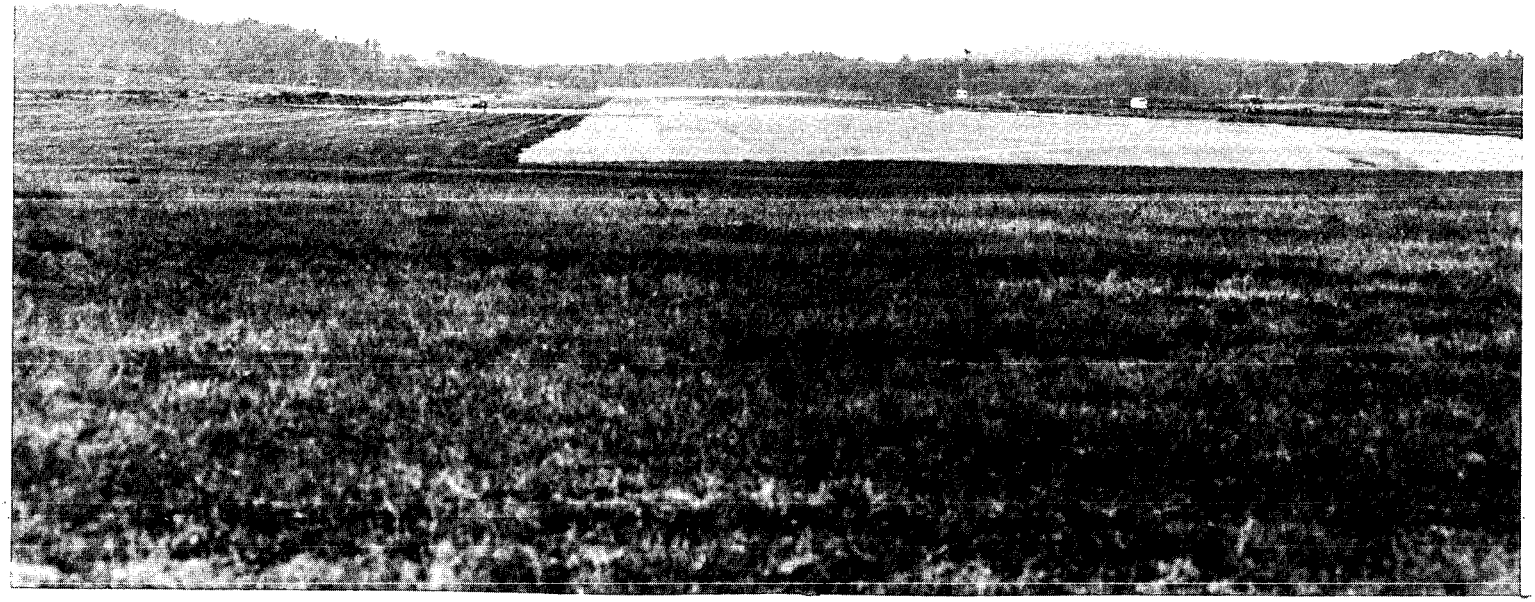

Fig.5-41. View from threshold of runway 29.

118694-S

Fig.5-42. Hangars and parked aircraft near runway 29 threshold.

118695-S

Fig.5-43. Hangars and parked aircraft near runway 11-29 midpoint.

south of runway 11-29.

Figures 5-44 to 5-47 show the received envelopes at the four principal measurement points for an approach to runway 29 with the direct signal peak displayed (upper photo) and, with the receiver gain increased by 10 dB to show low level multipath (lower photo). For these measurements, the receiving horn was aimed down the runway with phase center height of approximately 10 feet above the nominal runway level.

On a second series of approaches, the horn was directed to a point midway between the runway and the large hangar so that longer delay multipath from the hangar/parked aircraft complex would be displayed. Figures 5-48 to 5-51 show the received envelopes at the four receiver locations corresponding to Figs. 5-44 to 5-47. For both receiving antenna orientations, little or no multipath was observed with short delays ($\tau$ < 300 ns).

However, when the helicopter was between measurement points 2 and 3, specular reflections were encountered from the large hangar which borders the runway as well as several adjacent hangars. Figures 5-52 to 5-54 show representative correlator envelopes in this region. The high level (occasionally greater than +0 dB M/D ratio) multipath with a relative delay of approximately 800 ns correlates with the large hangar to the south of the runway midpoint. This S-band building multipath level is consistent with the earlier L-band analysis and measurements.

07-31-81
Run #3
MK-1
MAN-2dB

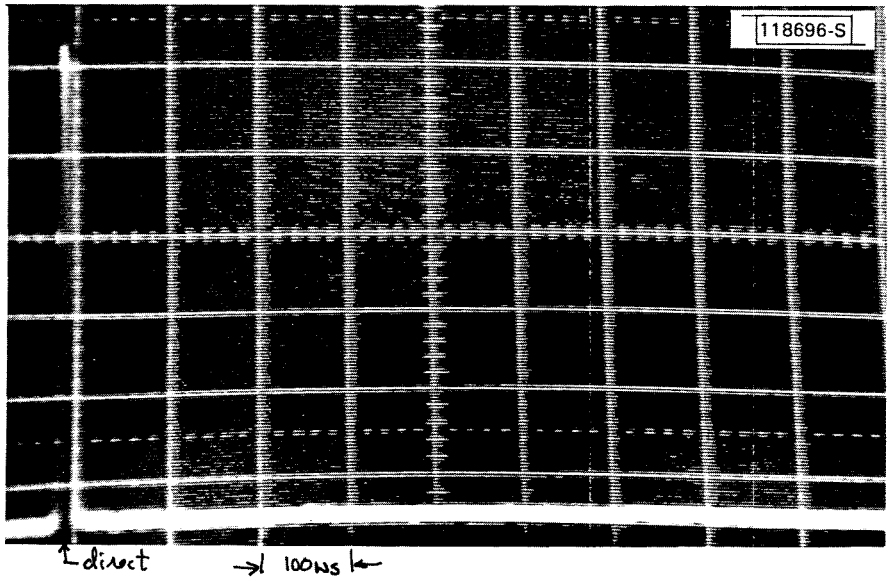


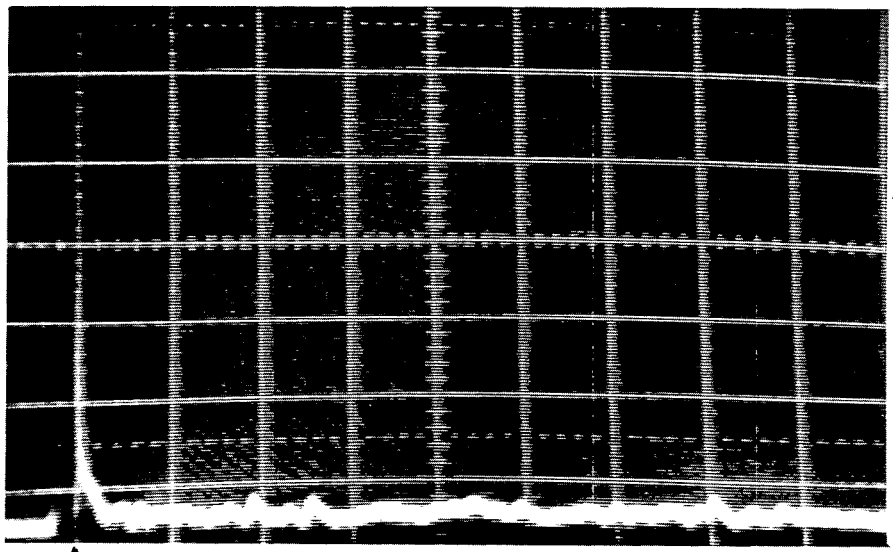


Run #2
MAN-16dB
MIC-1
07-31-81

Fig.5-44. Site 2 multipath at 200 ft. altitude.

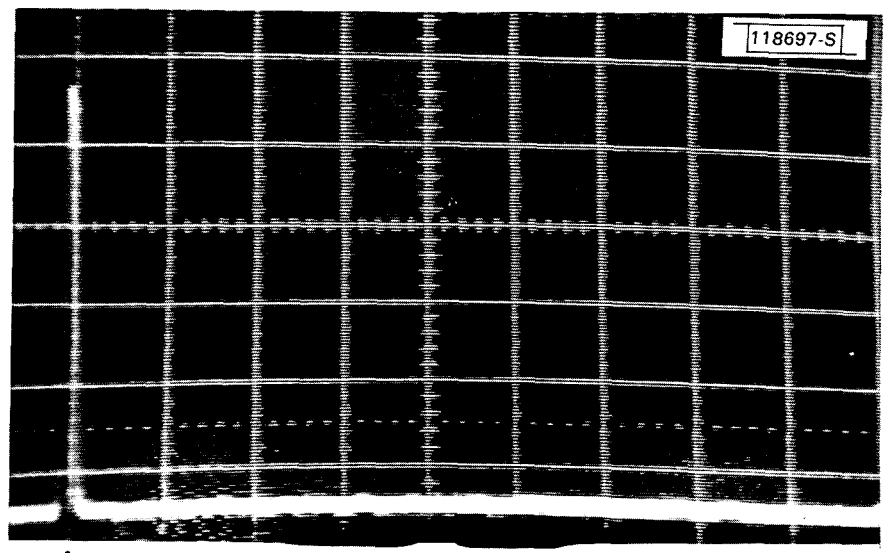


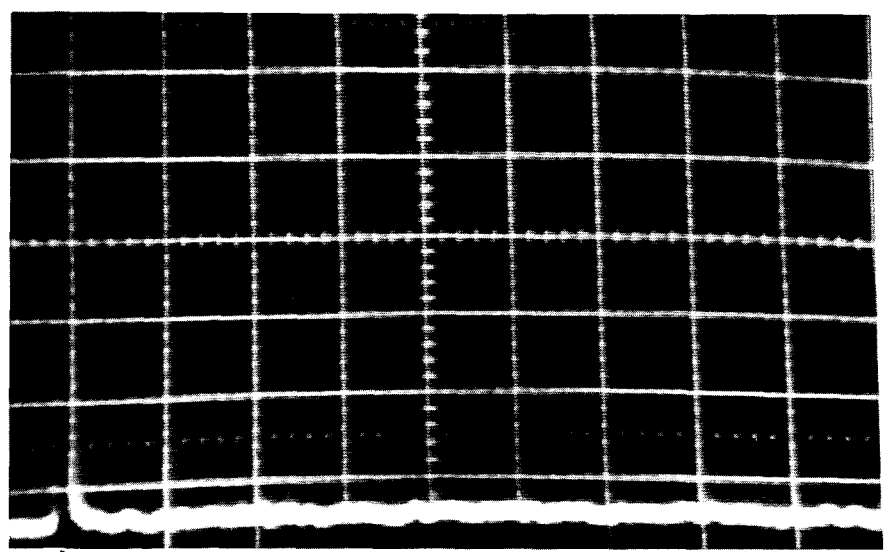


Fig.5-45. Site 2 multipath at 150 ft. altitude.

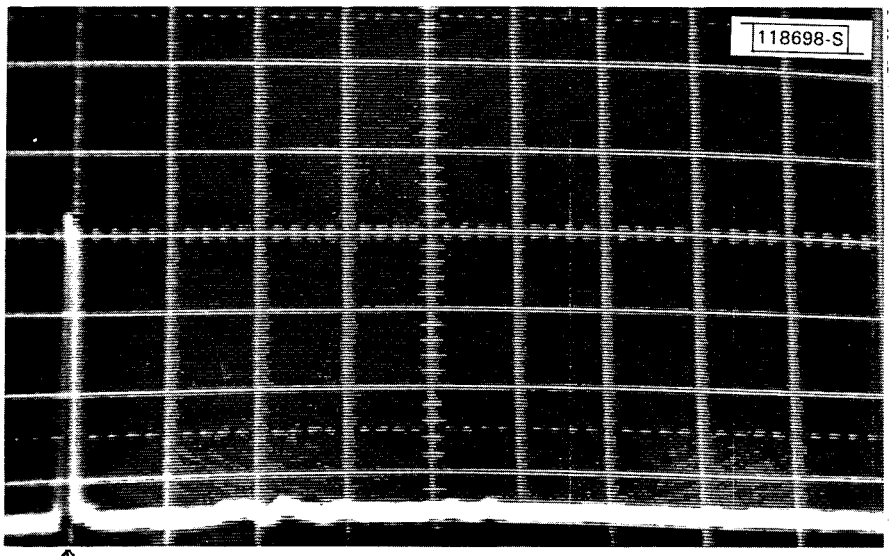


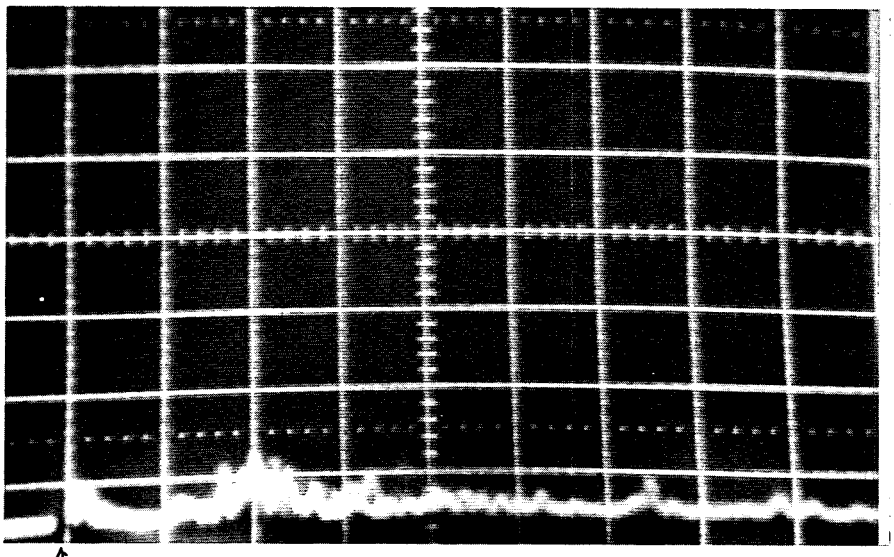


Fig.5-46. Site 2 multipath at 100 ft. altitude.

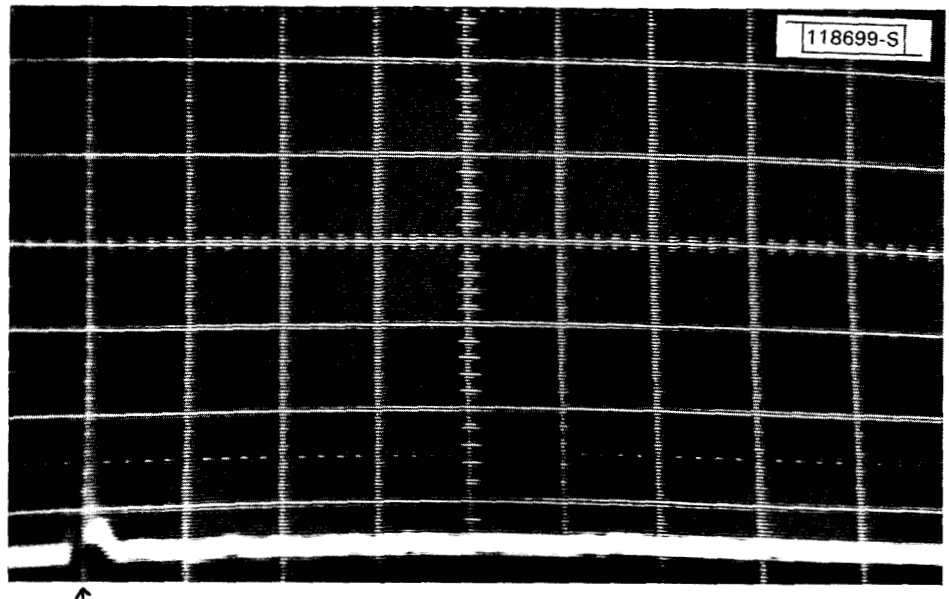


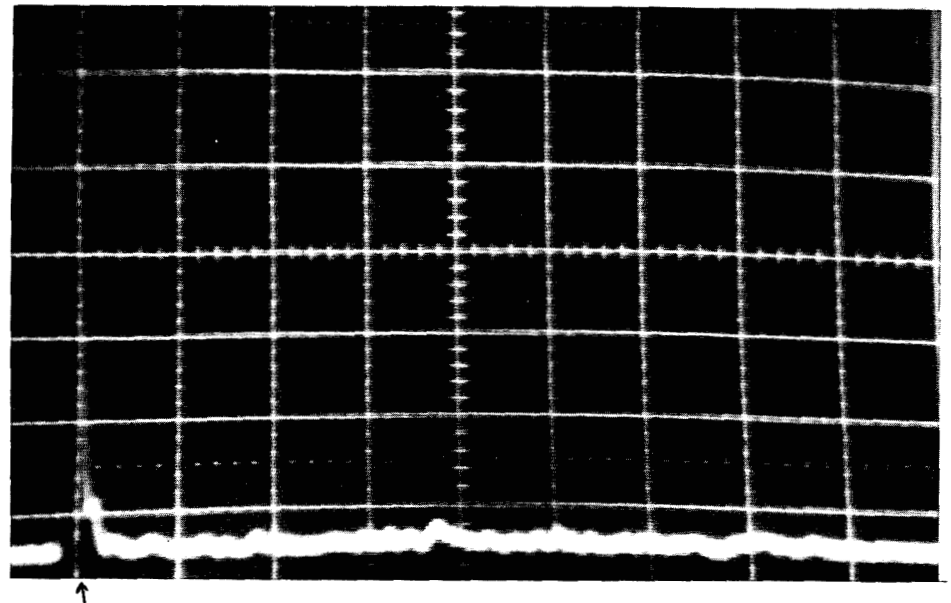


Fig.5-47. Site 2 multipath at threshold.

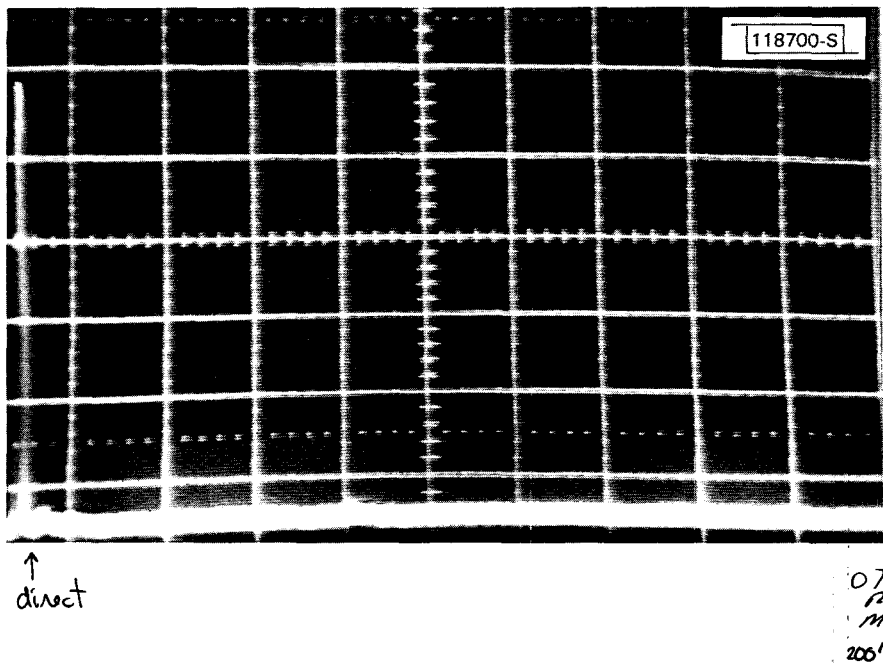


Fig.5-48. Site 2 multipath at 200 ft. altitude.

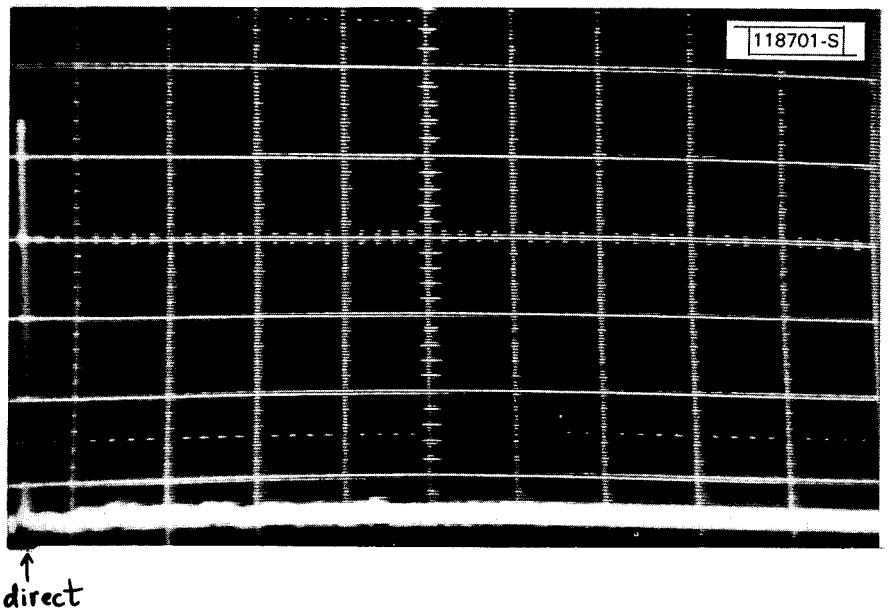


Fig.5-49. Site 2 multipath at 150 ft. altitude.

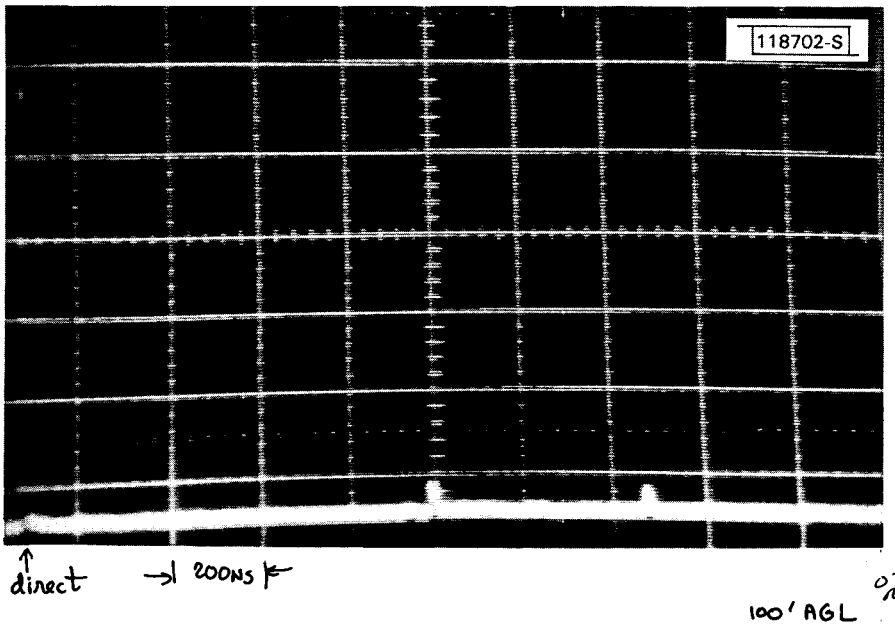


Fig.5-50. Site 2 multipath at 100 ft. altitude.

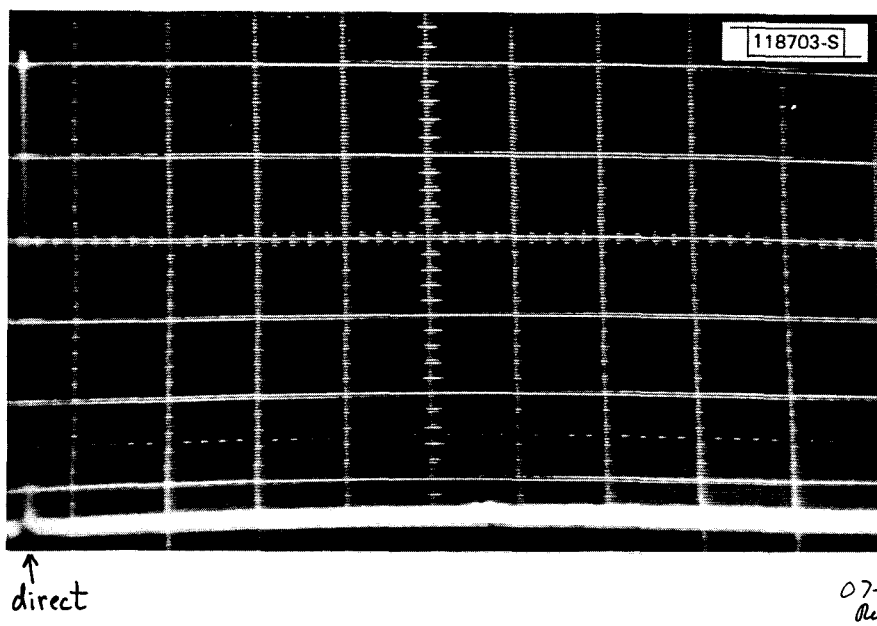


Fig.5-51. Site 2 multipath at threshold.

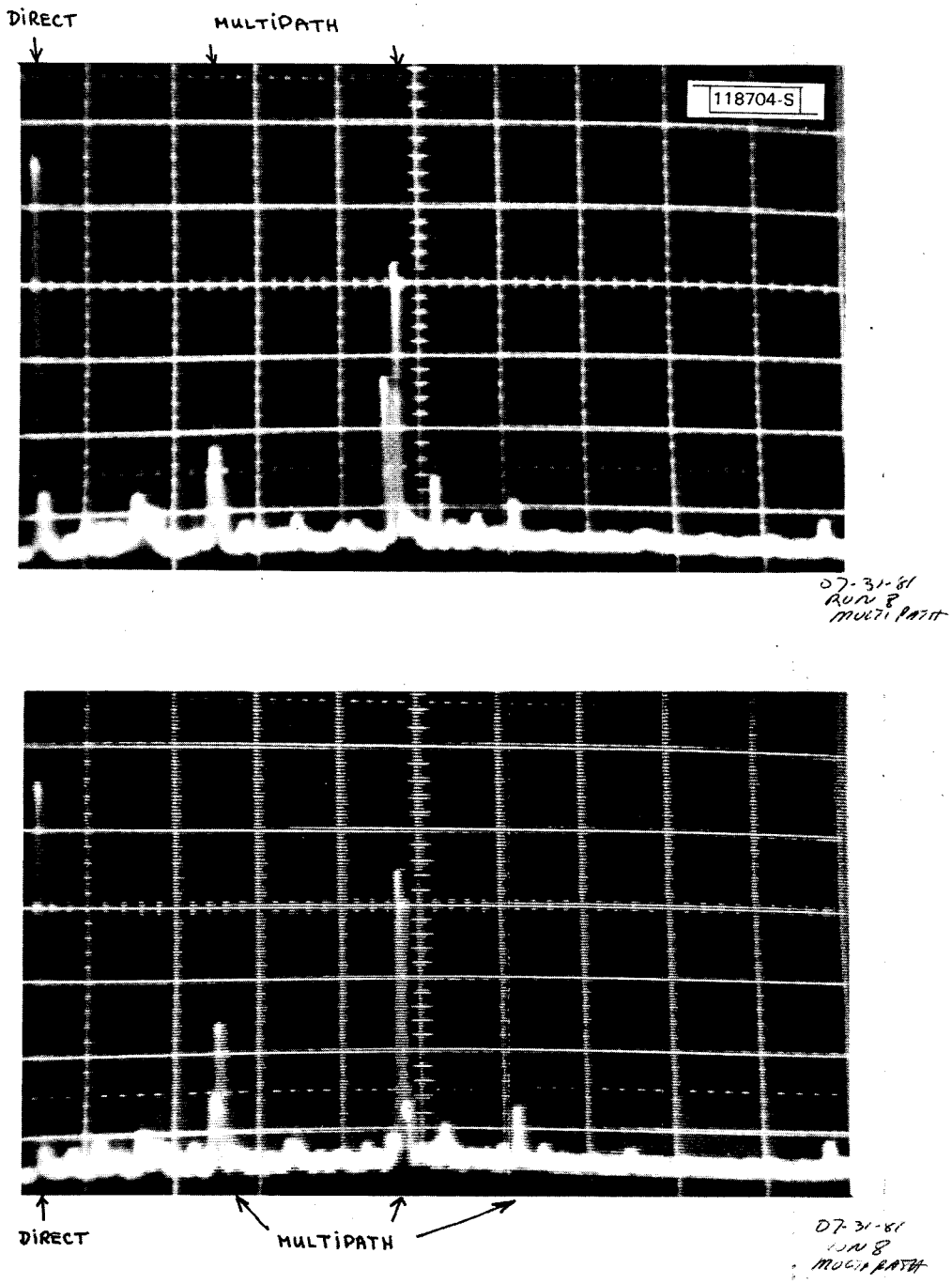


Fig.5-52. Site 2 multipath near 125 ft. altitude.

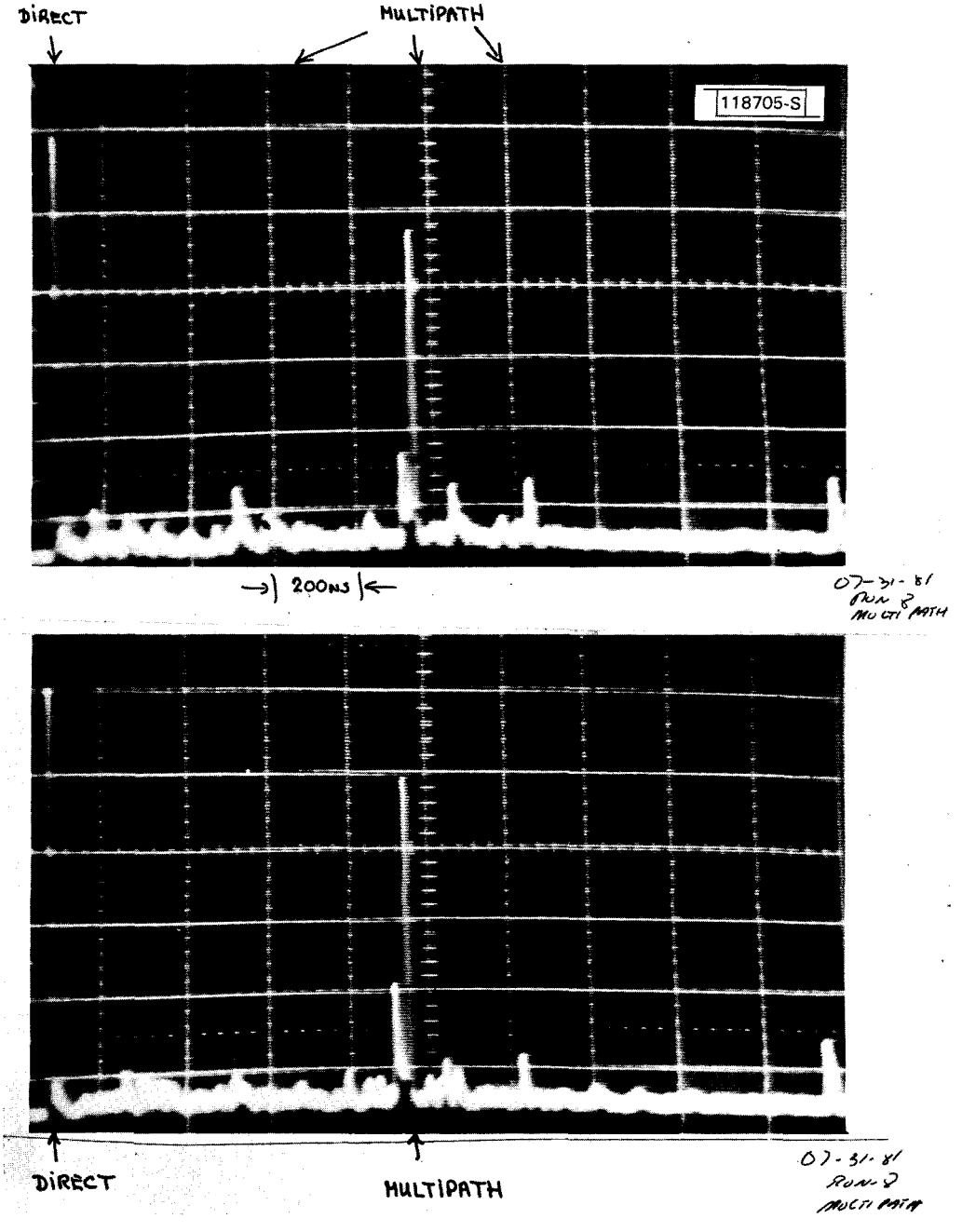


Fig.5-53. Site 2 multipath near 125 ft. altitude.

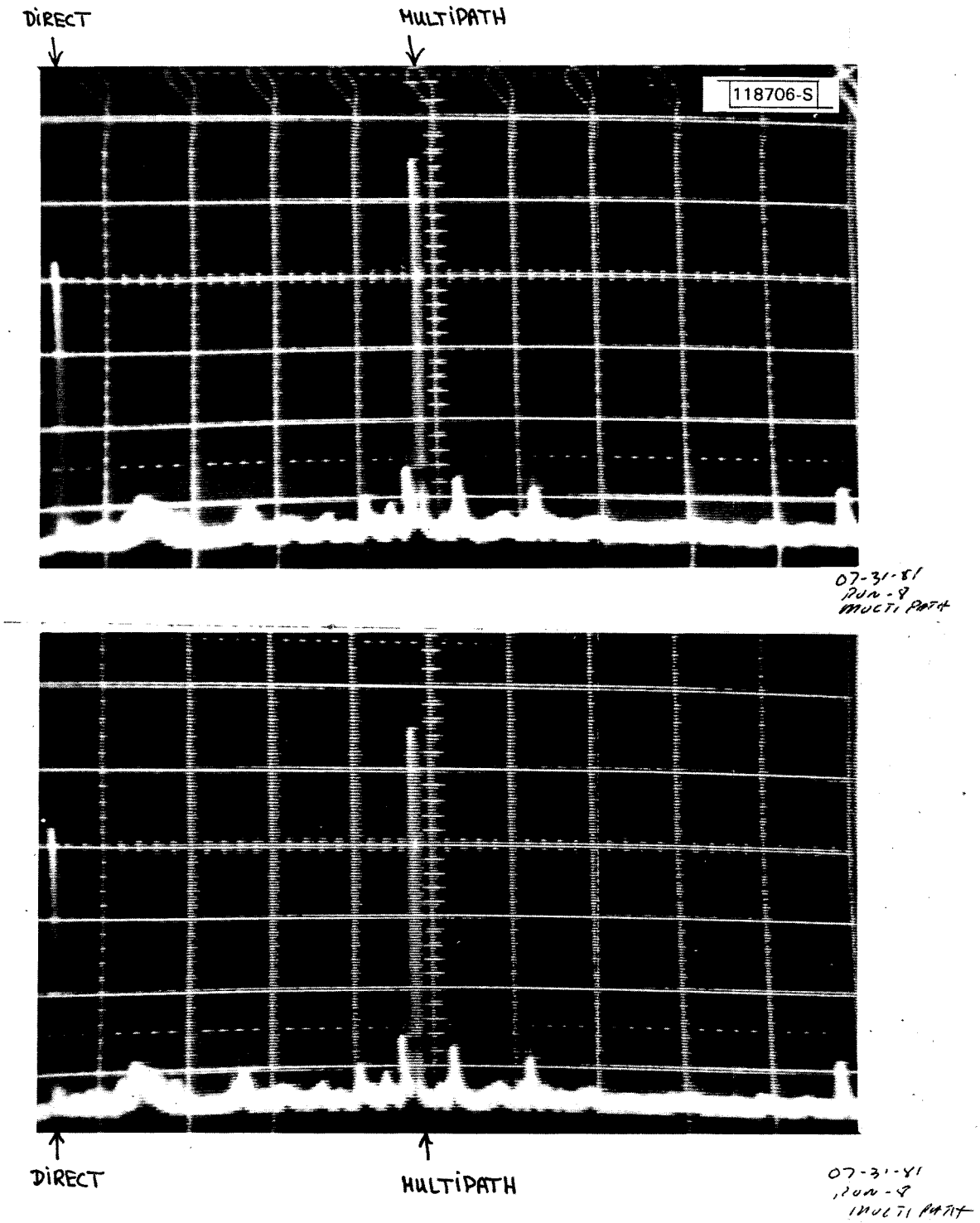


Fig.5-54. Site 2 multipath near 125 ft. altitude.

# VI. LIKELIHOOD OF ENCOUNTERING DME/P REFLECTIONS FROM BUILDINGS ON FINAL APPROACH

We have seen from the preceding sections that specular reflections from buildings represent a major challenge to successful PDME operation. In this section, we consider how likely it is that one would encounter such multipath in the final approach and landing region based on maps of some 24 airports from a number of countries. In particular, we have focused on

(1) distribution of time delays

(2) specular reflection regions, and

(3) the distribution of scalloping frequencies

as representing computable* relevant parameters for system design/analysis.

The method used to obtain these distributions was as follows:

1. the specular reflection region is obtained by assuming classical geometric optics reflection applies and then determining the points $(x_n, x_f)$ where the reflections from the ends of the walls pass through the (extended) runway centerline as shown in Fig. 6-1.

2. the vertical regions of the reflections is considered by comparing the receiver elevation angle at the points $x_n$, $x_f$ with the elevation angle subtended by the corresponding building walls. If the building elevation angle is at least as large as the aircraft elevation angle at either point, it is assumed that a specular reflection occurs.

Prevention of building wall illumination by objects not on the airport maps is

---

*Another key parameter - relative multipath amplitude - is not readily computable unless we were to consider many airport environment details (e.g., building surface composition, terrain contours, blockage by intervening obstacles) as well as implementation dependent factors (e.g., transponder and interrogator antenna characteristics).

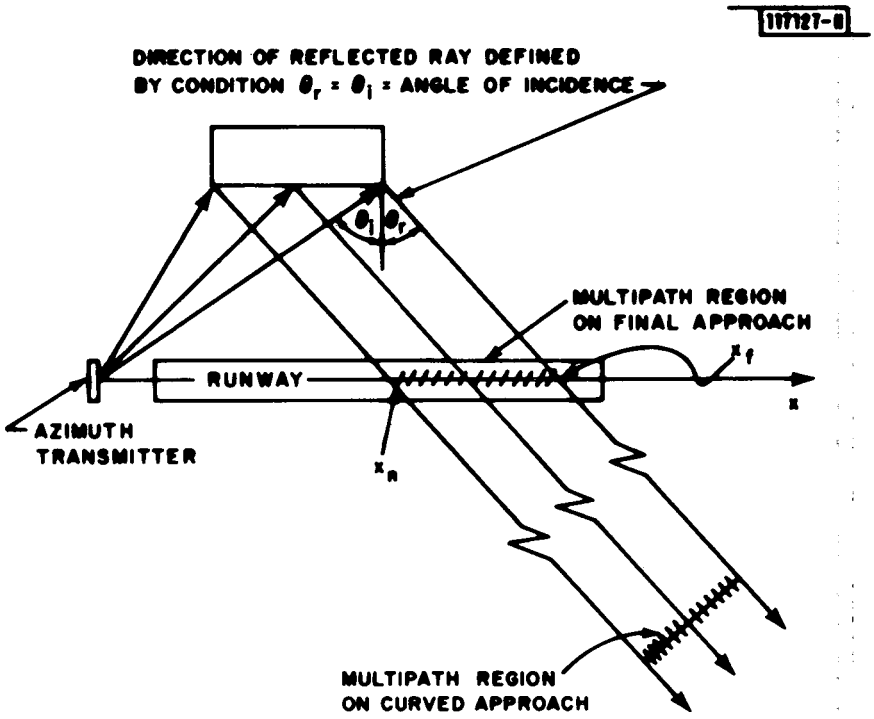


Fig.6-1. Determination of MLS multipath by ray tracing.

not considered nor is blockage of the reflected rays by objects. Similarly, periodic surface corrugations are ignored since the associated $d/\lambda$ values are less than unity at L-band.

Table 6-1 shows the airports considered in the data base. The corresponding airport maps are available in Appendix B.

Several MLS PDME sites were considered:

(1) cosited with the azimuth array on the extended runway centerline 1000 feet beyond the stop end of the runway.

(2) sited ±200 feet (66 meters) to either side of the azimuth site (e.g., as with the MLS azimuth transmitter building) so as to permit a higher phase center height.

(3) sited with the elevation antenna some 820 feet from runway threshold and ±400 feet off the runway centerline.

The building data base had been originally accumulated for azimuth clearance and out of coverage function studies in which case only buildings within 6000 feet of the azimuth site were considered. However, for the current assessment, many other buildings are also of concern. To permit maximum use of the earlier data base, the buildings were assessed in two groups:

a. those near the runway stop end

b. those near the runway threshold

The various statistics for the various DME/P sites are shown in Figs. 6-2 to 6-10. The probabilities shown are obtained by summing up all the occurrences of a given multipath parameter (e.g., $\tau$, $f_s$ or specular reflection region value) and dividing by the number of runways. Thus,

1. a single building will yield $\tau$, $f_s$ and region contributions to the abscissa at a number of values of the ordinate in each case, and

TABLE 6-1

AIRPORTS CONSIDERED IN DATA BASE
FOR MULTIPATH STATISTICS

| Airport | Runway Approaches | Runway Approaches With Bldgs. | Actual Heights | Actual Surface Known |
|---|---|---|---|---|
| JFK | 8 | 5 | YES | YES |
| LOS ANGELES | 8 | 8 | YES | YES |
| MIAMI | 6 | 6 | YES | YES |
| MINNEAPOLIS | 6 | 6 | YES | YES |
| O'HARE | 12 | 10 | YES | YES |
| PHILADELPHIA | 6 | 6 | YES | YES |
| TULSA | 6 | 3 | YES | YES |
| SAN FRANCISCO | 8 | 4 | YES | YES |
| HEATHROW | 6 | 5 | YES | YES |
| MELBOURNE | 4 | 4 | NO | NO |
| ORLY | 4 | 2 | NO | NO |
| SANTOS DUMONT | 4 | 4 | YES | NO |
| OLD TOKYO | 4 | 4 | YES | NO |
| NEW TOKYO | 2 | 2 | YES | NO |
| LENINGRAD (Pulkova) | 4 | 0 | NO | NO |
| MOSCOW (Sheremetyevo) | 2 | 0 | NO | NO |
| (Vnukovo) | 4 | 0 | NO | NO |
| WASHINGTON (National) | 6 | 2 | YES | YES |
| FRANKFURT | 4 | 4 | YES | YES |
| HAMBURG | 6 | 6 | YES | YES |
| SYDNEY | 4 | 2 | YES | YES |
| GATWICK | 2 | 2 | NO | NO |
| MONTREAL | 2 | 2 | YES | NO |
| WRIGHT PATTERSON (Ohio) | 2 | 2 | YES | YES |
| TOTAL | 122 | 92 | | |

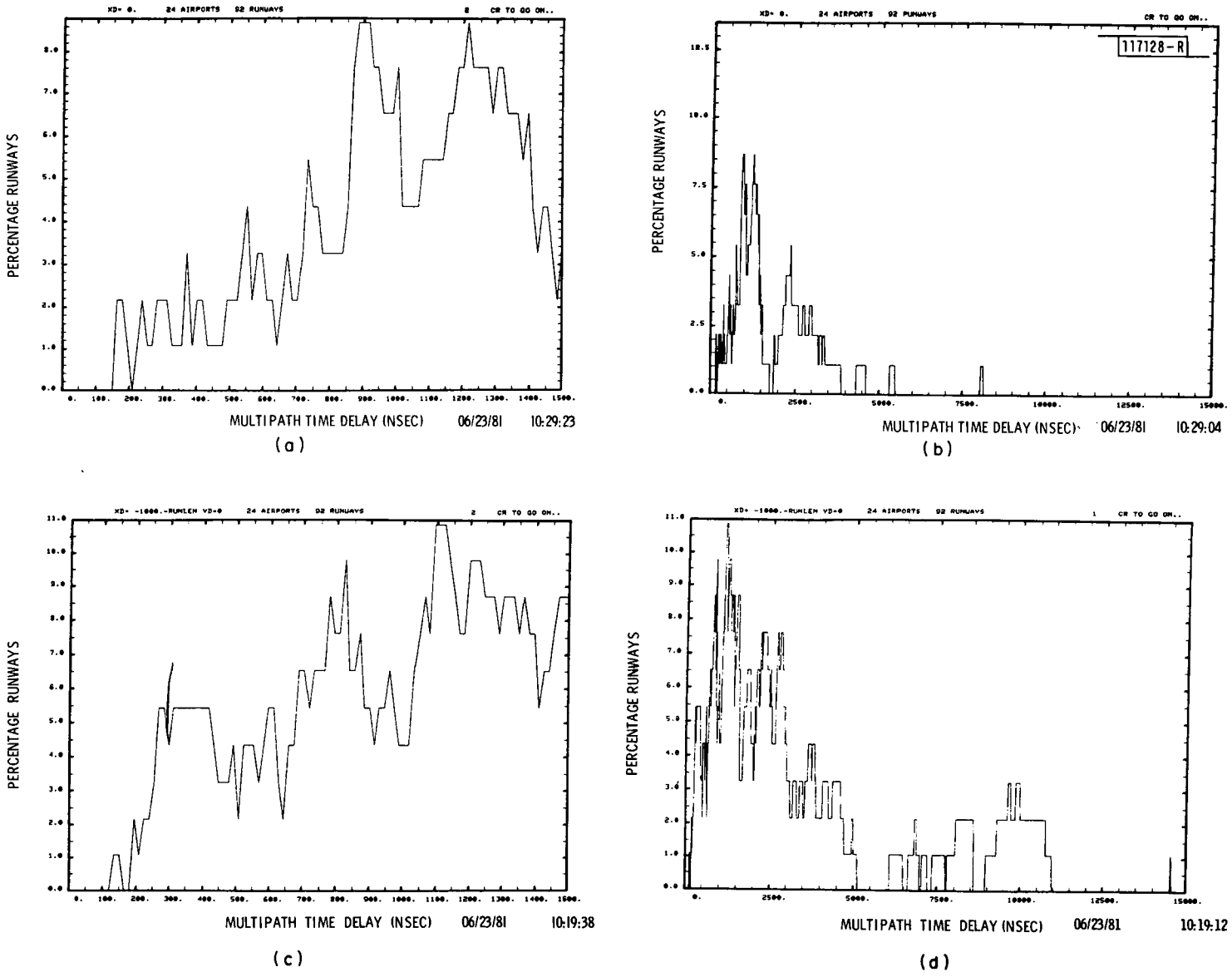


Fig.6-2. Time delay distribution for DME/P sited with azimuth array: (a-b) buildings near runway threshold and (c-d) buildings near runway stop end.

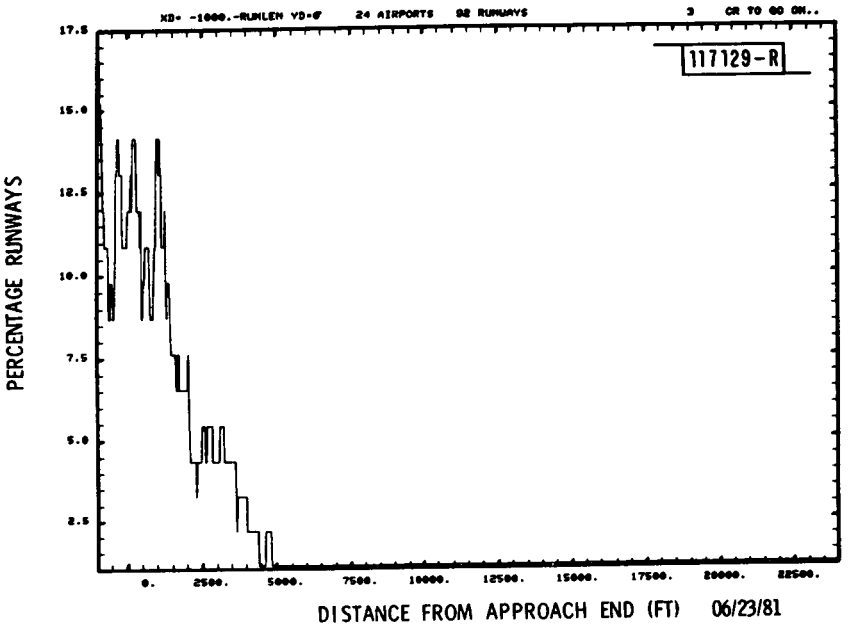


(a)

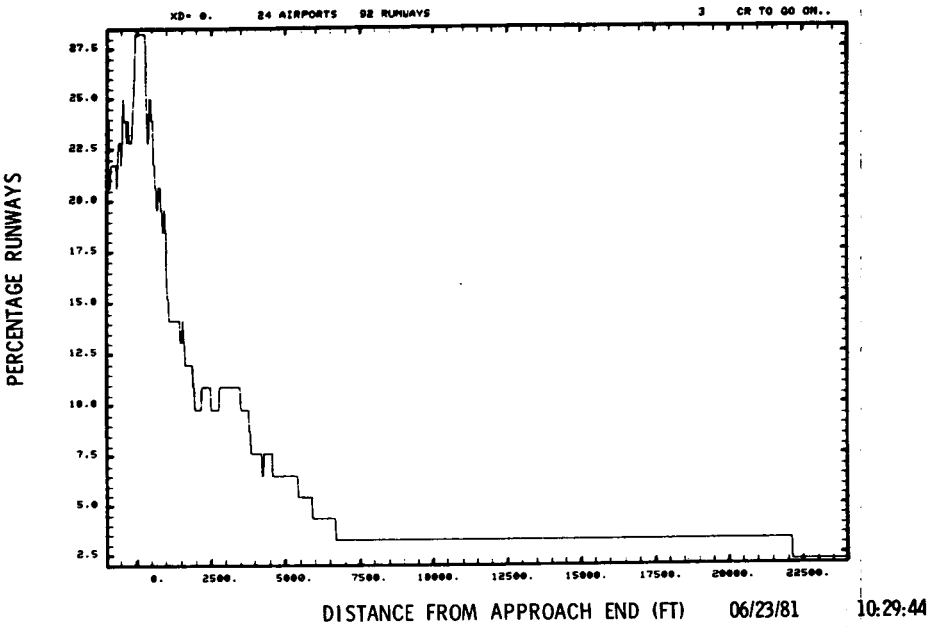


(b)

Fig.6-3. Multipath region distribution for DME/P sited with azimuth array: (a) buildings near threshold and (b) buildings near runway stop end.

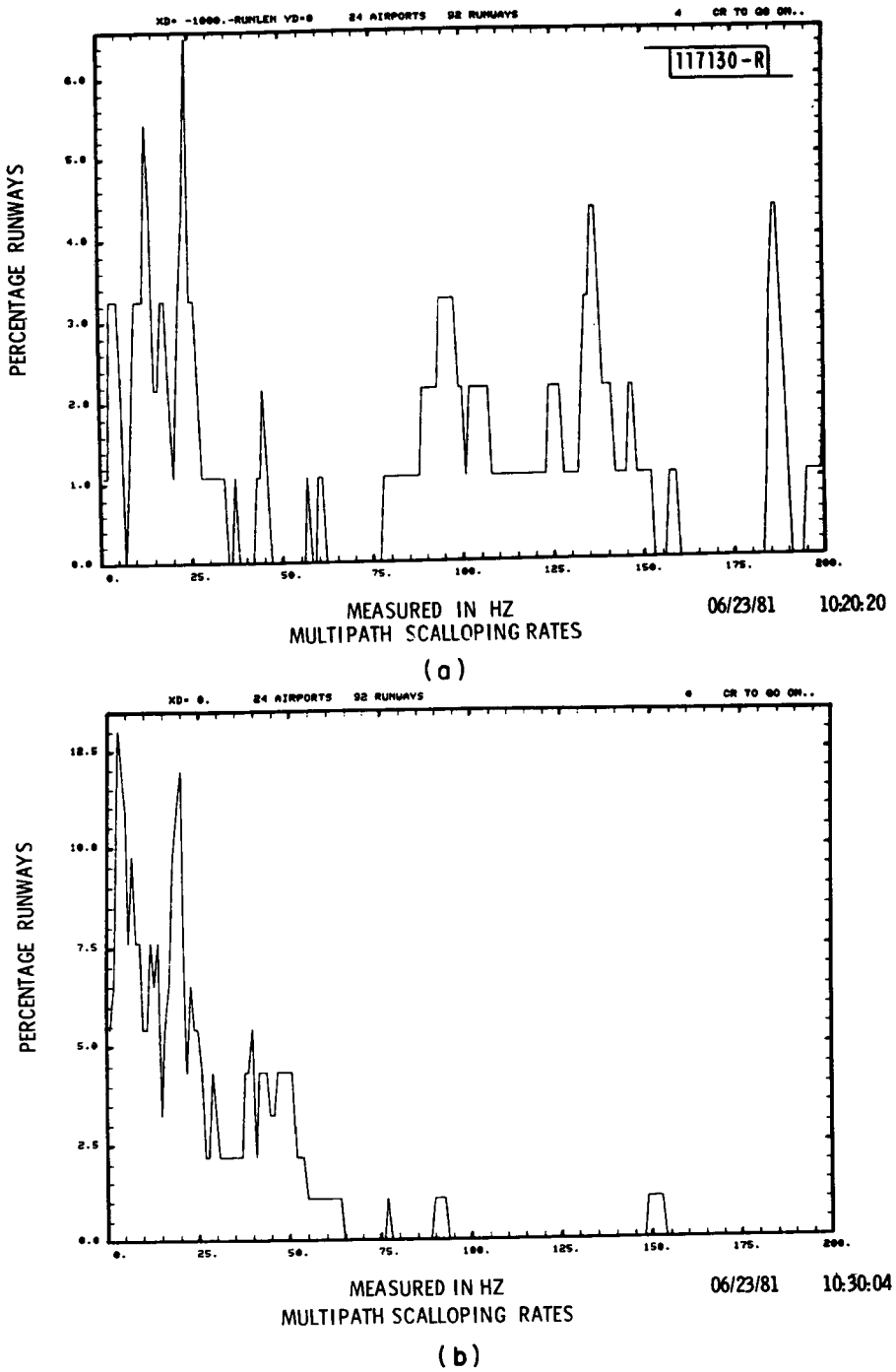


Fig.6-4. Distribution of scalloping rates for DME/P sited with azimuth array: (a) buildings near threshold and (b) buildings near runway stop end.

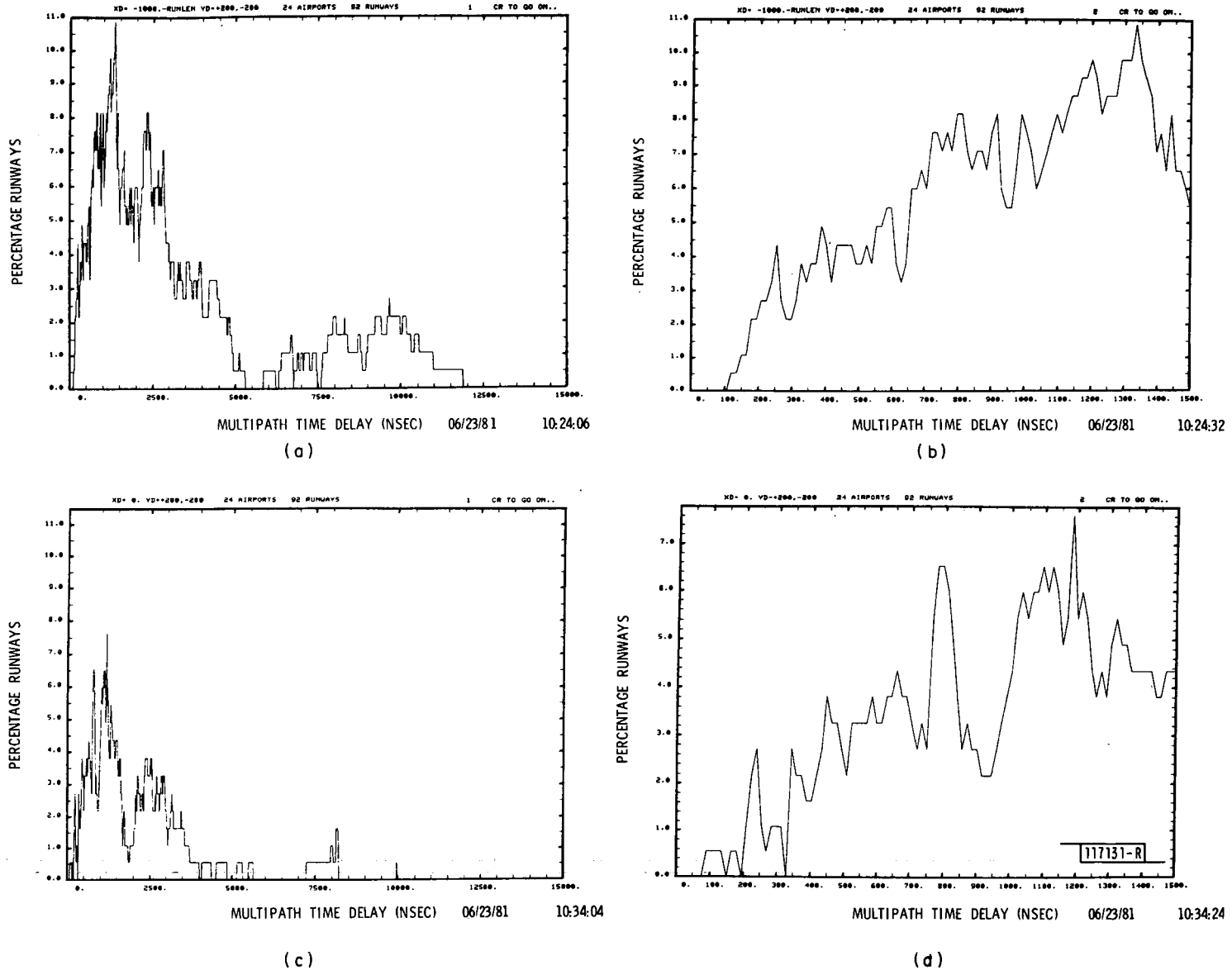


Fig.6-5. Distribution of relative time delay for DME/P sited with azimuth transmitter building: (a-b) buildings near runway threshold and (c-d) buildings near runway stop end.

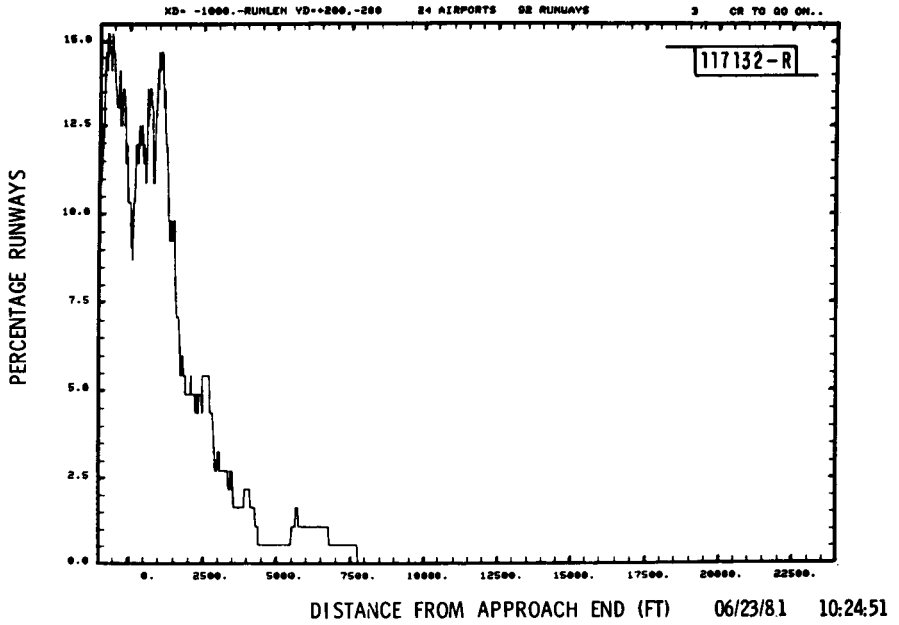


(a)

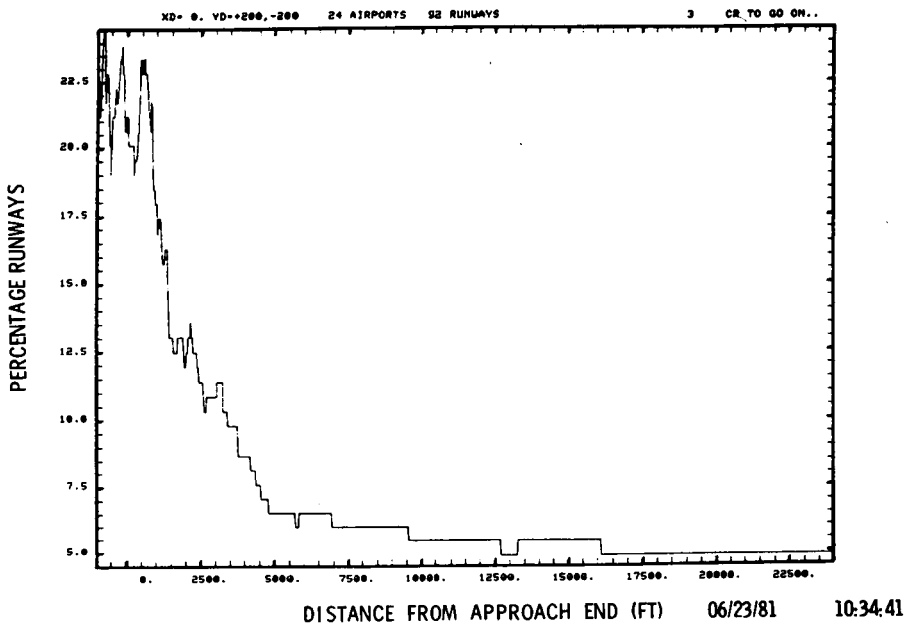


(b)

Fig.6-6. Multipath region when DME/P is sited with azimuth transmitter building: (a) buildings near threshold and (b) buildings near runway stop end.

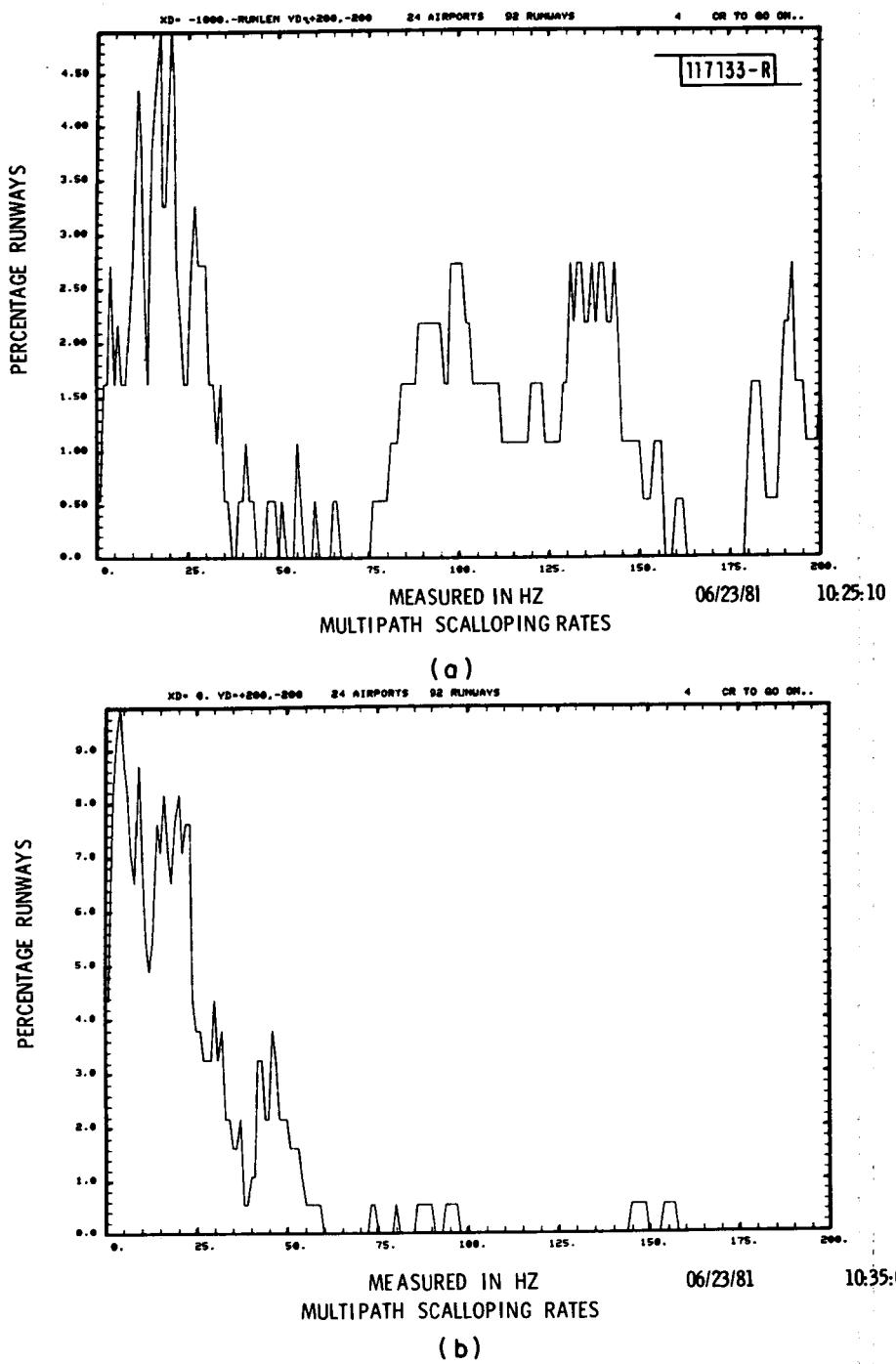


Fig.6-7. Distribution of scalloping frequencies when DME/P is sited with azimuth transmitter building: (a) buildings near threshold and (b) buildings near runway stop end.

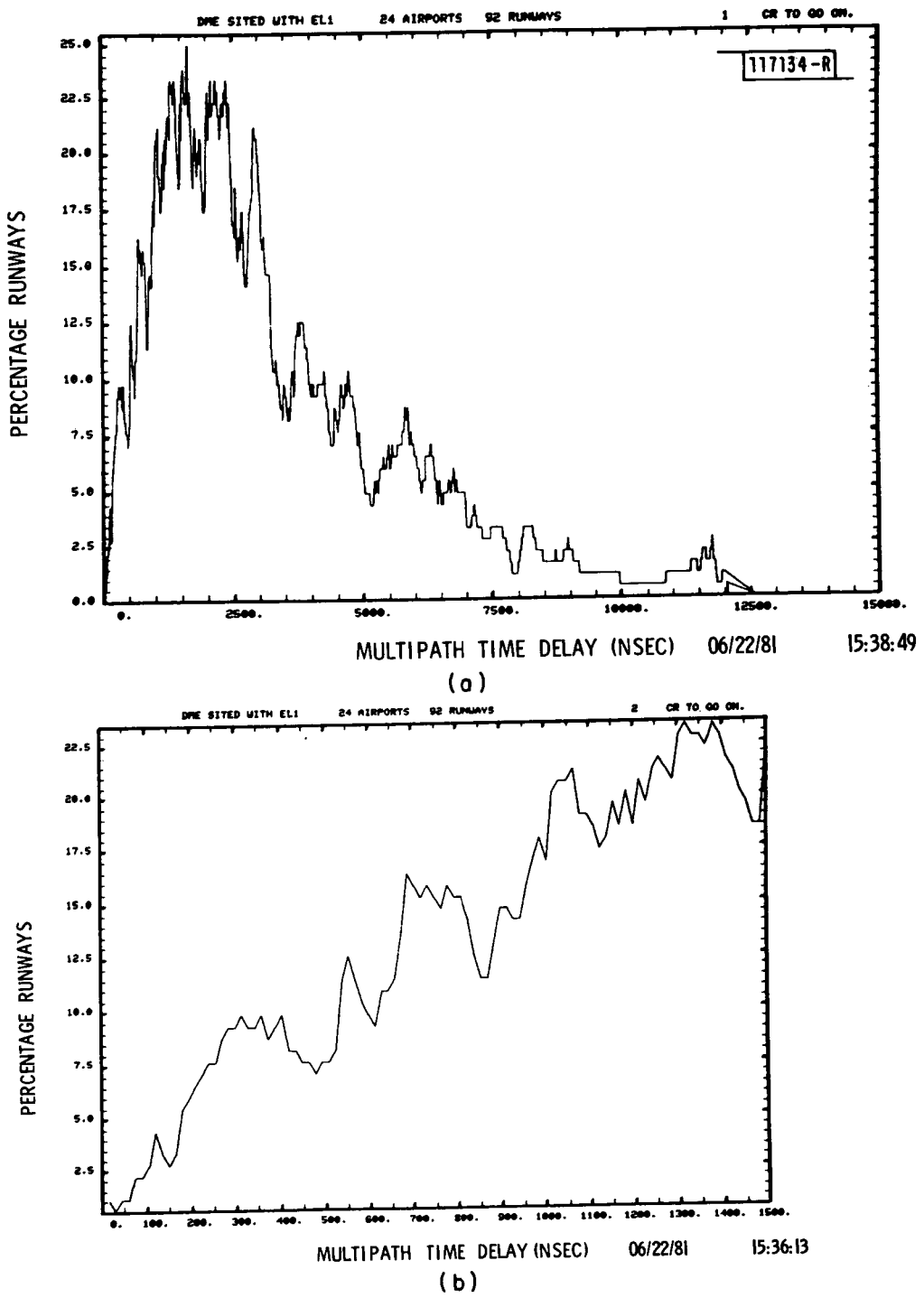


Fig.6-8. Multipath time delay distributions when DME/P is sited with MLS elevation antenna. Only buildings near runway threshold.

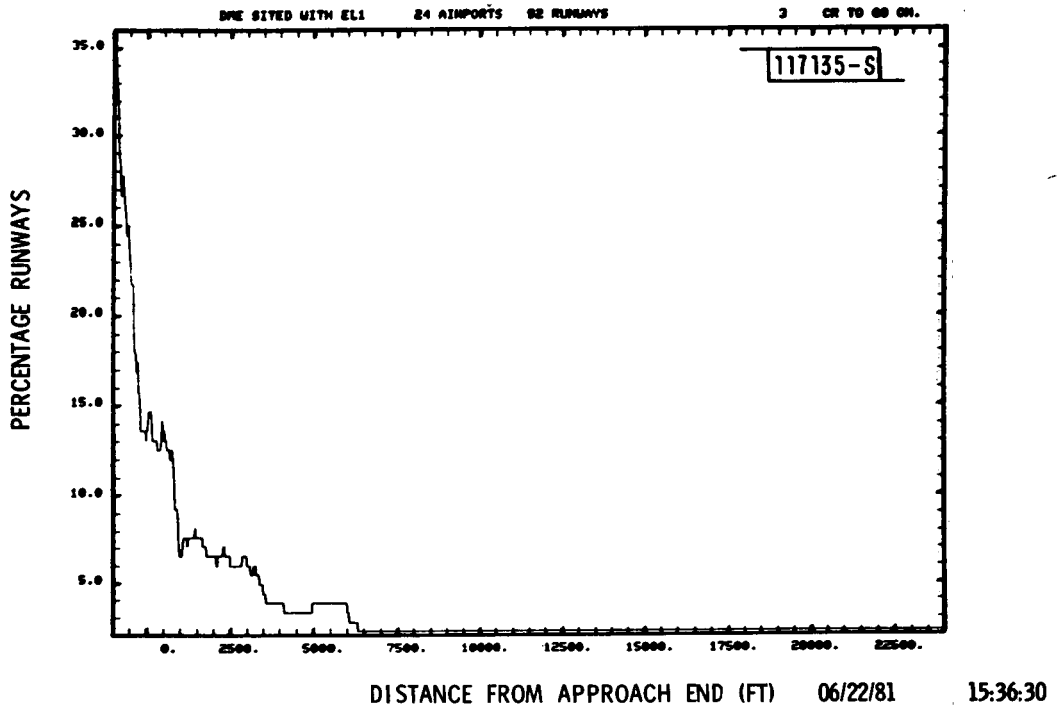


Fig.6-9. Multipath region distribution when DME/P is sited with elevation array.

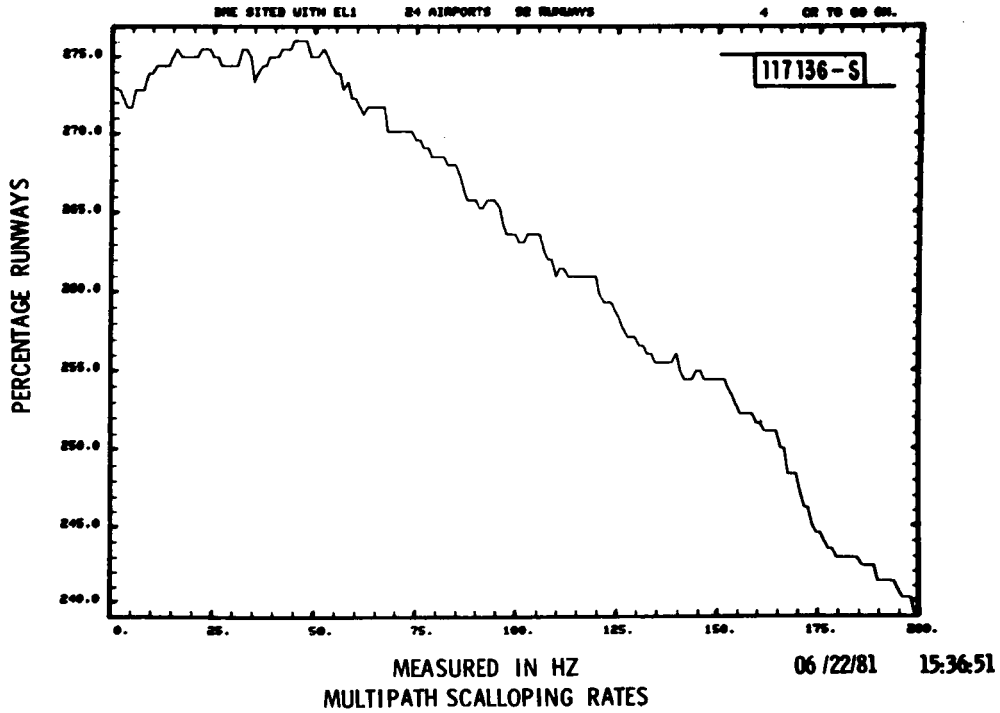


Fig.6-10. Scalloping frequency distribution when DME/P is sited with MLS elevation.

2. a single runway will yield contributions to the graphs for each building.

Consequently, the area under each of the probability curves is not equal to the probability of encountering some DME/P multipath at a given runway.

We see that the likelihood of DME/P multipath from the data base buildings with delays less than 200 ns is quite low for the DME/P sites located near the azimuth site. It might be thought that DME/P cosited with the elevation system would have a low incidence of multipath due to the high elevation angle of the aircraft and the (relatively) short DME/P to aircraft distance. However the considerable offset from centerline places the DME/P near to sizable buildings and thus increases the probability of short duration multipath.

# VII. CONCLUSIONS AND RECOMMENDATIONS FOR FURTHER STUDY

## A. Conclusions

In this report, we have reviewed the knowledge to date on the DME/P multipath in the landing region with the aim of identifying the principal challenges to successful operation. This analysis necessarily considered the major DME/P multipath rejection mechanisms (e.g., pulse shape, processing techniques, and antenna design) in order to assess the likely impact of a given threat as well as reviewing the available relevant L-band propagation data.

A number of studies and experimental measurements related to the DME/P multipath environment have been carried out over the past two years. Table 7-1 summarizes the principal multipath challenges and the current status of knowledge regarding them.

The results indicate that reflections from buildings which have been increased in relative level by specular reflections from the terrain could represent the major challenge to DME/P operation in the landing region if an appropriate pulse shape and signal processors are not utilized. In particular, simulations suggest that the relative M/D ratios could be considerably in excess of 0 dB, whereas the levels assumed in the bulk of the DME/P proposals to date (e.g., [2, 3, 12]) typically have been substantially less (e.g., 6 dB) than 0 dB.

However, the time delay discrimination available by the use of a sharper rise time pulse and improved signal processing (e.g., DAC) exclude the bulk of the building multipath. In Chapter II, we saw that the error using a representative DME/P receiver (3.5 MHz bandwidth IF filter with a delay and compare processor) with the proposed pulse shape is essentially immune to multipath with time delays greater than 300 ns.

Based on the results of Chapter VI, it can be concluded that the vast majority (at least 95%) of runway ends should not contain any high level building reflection multipath with a time delay of less than 300 ns. Since the precision mode of DME/P can successfully withstand lower level (e.g.,

TABLE 7-1 PRINCIPAL DME/P MULTIPATH CHALLENGES

| Challenge | Satisfactory Theory | Simulation Studies | Experimental Measurements | Comments |
|---|---|---|---|---|
| Specular building reflection | Yes | Yes<br>DFVLR [42] | Yes<br>Lincoln Lab. [46]<br><br>Tech Univ Braunschweig [33] | Levels cannot be bounded by a single number (e.g., -6dB M/D); and, aircraft antenna patterns may create even higher levels. However, relative time delays are nearly always greater than 300 ns |
| Specular aircraft reflections | Yes | Yes<br>DFVLR [42]<br>Lincoln Lab.* | Only at C-band | L-band levels should be lower than C-band. Simulations suggest minimal effects on DME/P precision pulse |
| Specular ground reflections from: | | | | |
| flat terrain | Yes | Yes | Yes | Direct signal lobing |
| rough terrain with well defined facets | Partially | No | Yes<br>Lincoln Lab [27,44]<br>Tech Univ Braunschweig [33,47] | May be problem at airports with rough, bare terrain in approach zone |
| Diffuse specular reflections | No | No | Yes<br>Tech Univ Braunschweig [33]<br>Lincoln Lab. * | Measured levels in S-band tests at Hanscom airfield (Bedford, MA) suggest very low levels in nominal (flat) environments |

*This report

-6 dB M/D ratio) multipath with delays between 0 ns and 300 ns, multipath from the smaller objects (e.g., aircraft, trucks, ASR radars) which often are inside the 300 ns time delay contours should not offer a significant challenge to DME/P.

The peak building reflections multipath levels which may occur with delays less than 300 ns are difficult to bound due to the strong sensitivity to terrain contour features and aircraft antenna patterns. In many cases, the M/D level should be less than the -3 dB level which can be readily tolerated by the current DME/P proposal.

However, as was shown in the measurements at U.S. airports and scenarios generated by the AWOP WG-M multipath subgroup [42], building reflections levels approaching and exceeding the direct signal level can arise in some cases. Several possible options exist for improving the performance of the "nominal" DME/P system to cope with these cases on an as needed basis:

a. Use of a "centerline emphasis" azimuth pattern on the ground antenna. This will probably necessitate a lower phase center-height, but the increased gain along centerline should offset much of the height/gain loss.

b. Siting the ground station so as to mitigate the multipath (e.g., atop the hump of a runway). If the DME/P transponder and MLS azimuth are not colocated, there is a possibility of ambiguous aircraft locations when the aircraft is close to the MLS azimuth (e.g., as during rollout or missed approach). The operational impact of such ambiguities (e.g., excluding the use of DME/P information within a certain minimum range) would have to be traded off against the improvement in DME/P multipath performance on a case by case basis.

c. Improved signal processing techniques at the transponder (e.g., "mismatched" IF filter), and

d. Lateral diversity transponder antennas.

For the AWOP WG-M scenario with excessive control motion errors, the use of a centerline emphasis transponder antenna would probably have reduced the errors to well within the current limits.

In summary, the experimental data base to date with precision DME systems (Crows Landing, California, and Wallops Island, Va) together with special DME multipath environment measurements at some seven airports (four of which were major civilian airports) suggest that the DME/P multipath performance and environment are sufficiently well understood to develop SARPS at this time. For the AWOP WG-M proposed system [49] there is a high degree of confidence that the "nominal" system should provide the desired performance at the vast majority of runways (e.g., over 95%); and there are several additional features which could be used to improve performance at those runways where the desired performance may not be met with the "nominal" system due to the local multipath environment.

Near term (e.g., within the next year) experimental measurements at additional airports should not substantially change the above conclusions regarding the multipath environment and the multipath performance of DME/P. If additional multipath performance data are needed for SARPS refinement, this might be accomplished by additional (limited) simulations. These simulations could involve additional scenarios and/or the inclusion of additional DME/P system possibilities for multipath rejection in the existing scenarios.

When significant operational experience has been obtained with DME/P, the FAA and AWOP should review the data base to determine whether additional multipath measurements and/or SARPS guidance material may be warranted. There are, of course, some second order issues which could be profitably investigated in the next few years. These are summarized below.

## B. Recommendations for Near Term Studies

### 1. Irregular Terrain Reflections

One uncertainty in the DME/P multipath environment is the nature of

reflections from rough and/or irregular terrain such as encountered in hilly or mountainous regions. Several of the U.S. interim MLS installations are located in mountainous regions (e.g., Aspen, Colorado) and it has been suggested [14] that three dimensional aircraft position information is particularly important in such regions. Limited L-band measurements were conducted by the FRG at Salzburg, Austria [15], but the pulse widths used (2μs) were too large to resolve the multipath of greatest concern to DME/P. Long delay (2μs to 20 μs) diffuse multipath was observed as well as some discrete specular multipath.

L-band measurements by Lincoln Laboratory using an aperture sampling technique have shown that high level specular reflections can arise from irregular terrain which is not heavily vegetated [8,44]. Figure 7-1 shows one such site at Camp Edwards, MA, while Fig. 7-2 shows the terrain profile. Figures 7-3 and 7-4 show the measured angular power spectrum as a function of elevation angle from the antenna phase center for two receiver angles. Multiple specular reflections from the terrain occurred in both cases as well as at several other sites.

However, the geometries used in the Lincoln measurements had a ground antenna much closer to the rough terrain than would be the case with the normal DME/P siting. Greater ground antenna to surface distances should reduce the number of terrain reflections (since the range of elevation angles to the ground antenna is much smaller) and may reduce the M/D levels (since the Fresnel zone size will be larger). Experimental measurements with more realistic geometries would be useful.

If the DME/P performance was substandard due to irregular terrain reflections, siting the transponder nearer the elevation antenna and utilizing a sharp cutoff elevation pattern on the transponder antenna appears to be the most attractive option for improving system performance. Due to the small differences between the direct and ground reflection signals in terms of time delay, doppler shift and azimuth, the options suggested above for building reflections will not be useful against ground reflections.

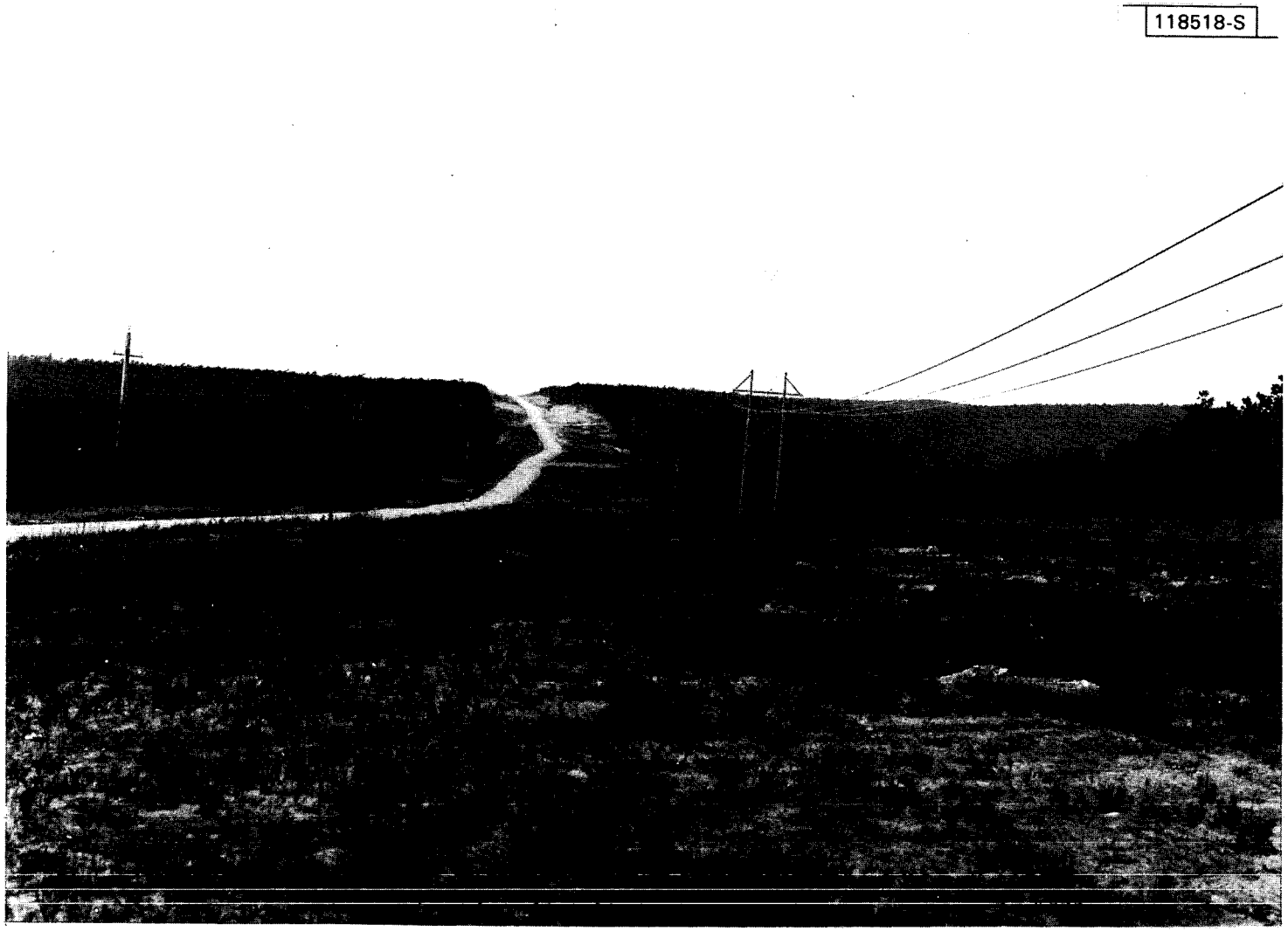


Fig.7-1. Terrain along road at Camp Edwards, Mass.

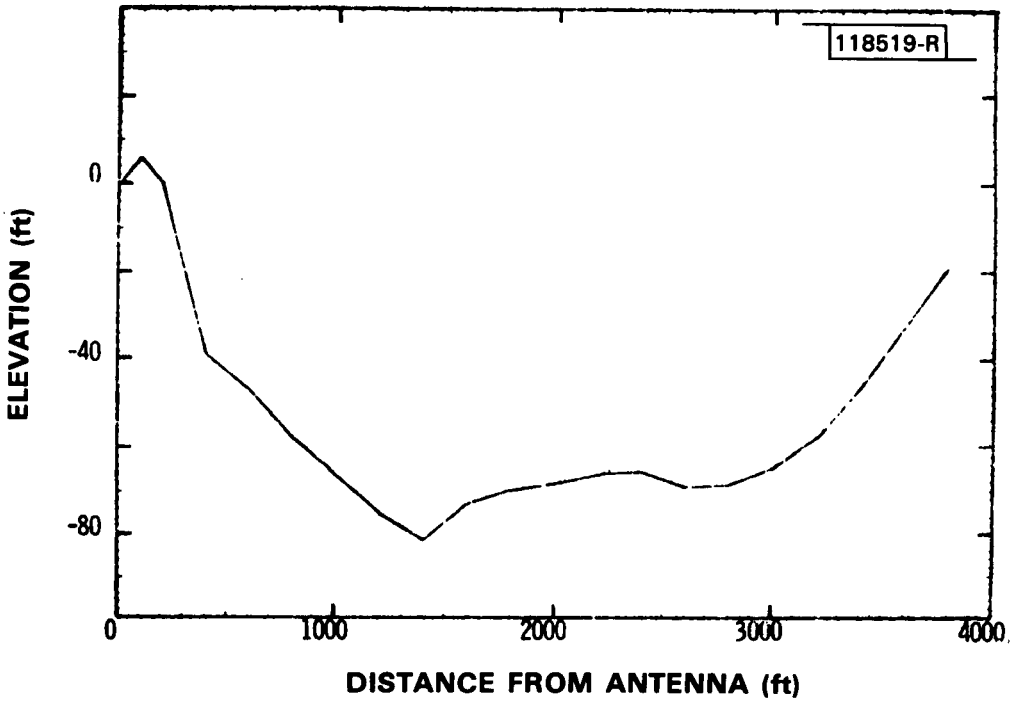


Fig.7-2. Terrain profile at Camp Edwards, Mass. site #2 (Gibbs Road).

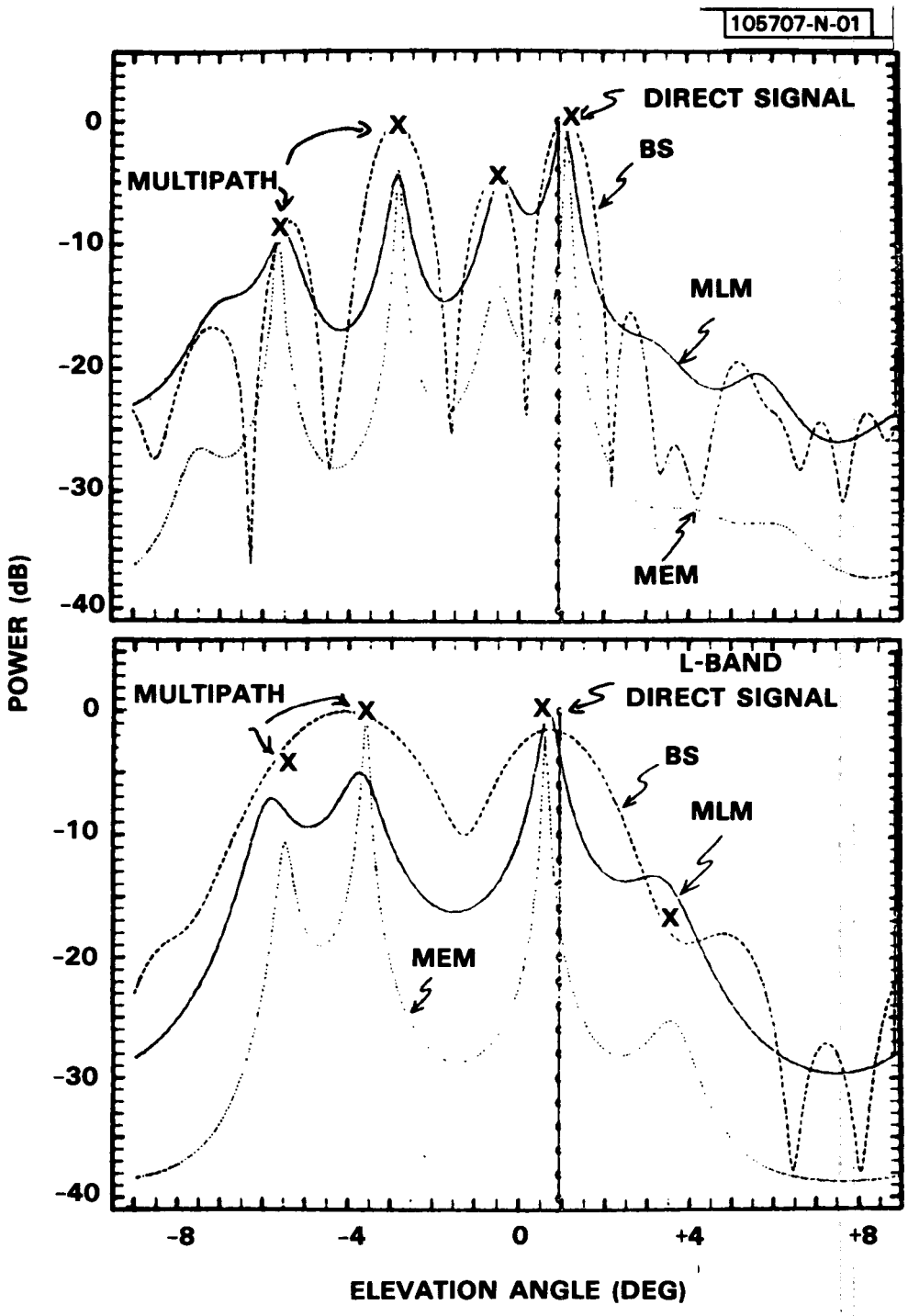


Fig.7-3. Received power vs. elevation angle at Camp Edwards site #2.

Field Measured

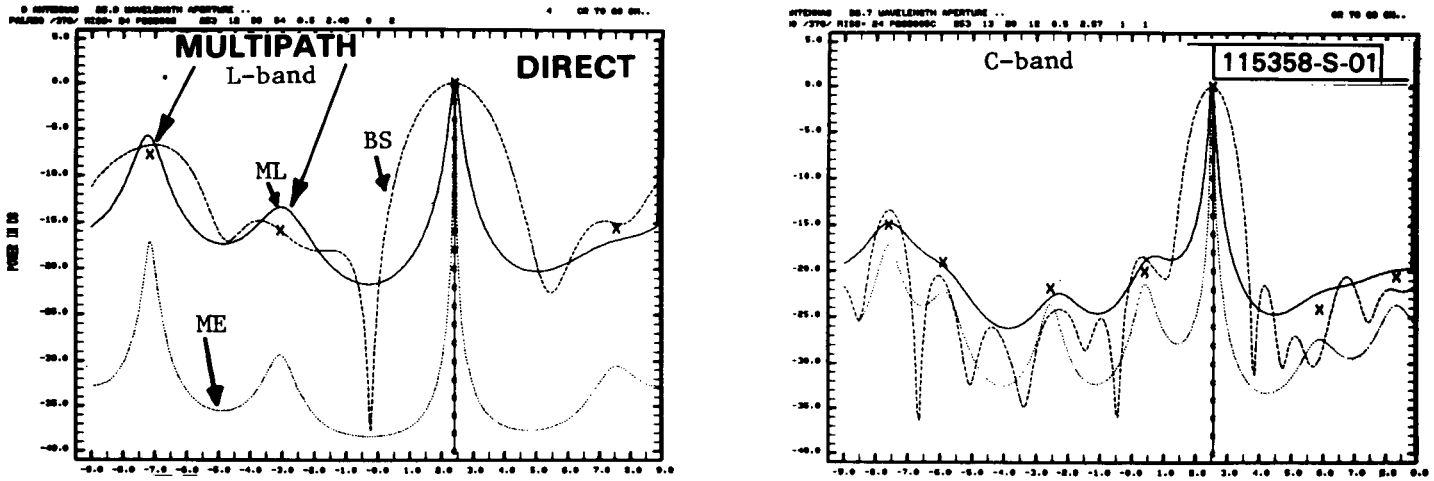


Simulation Predicted (ground reflection calculation/focusing ground)

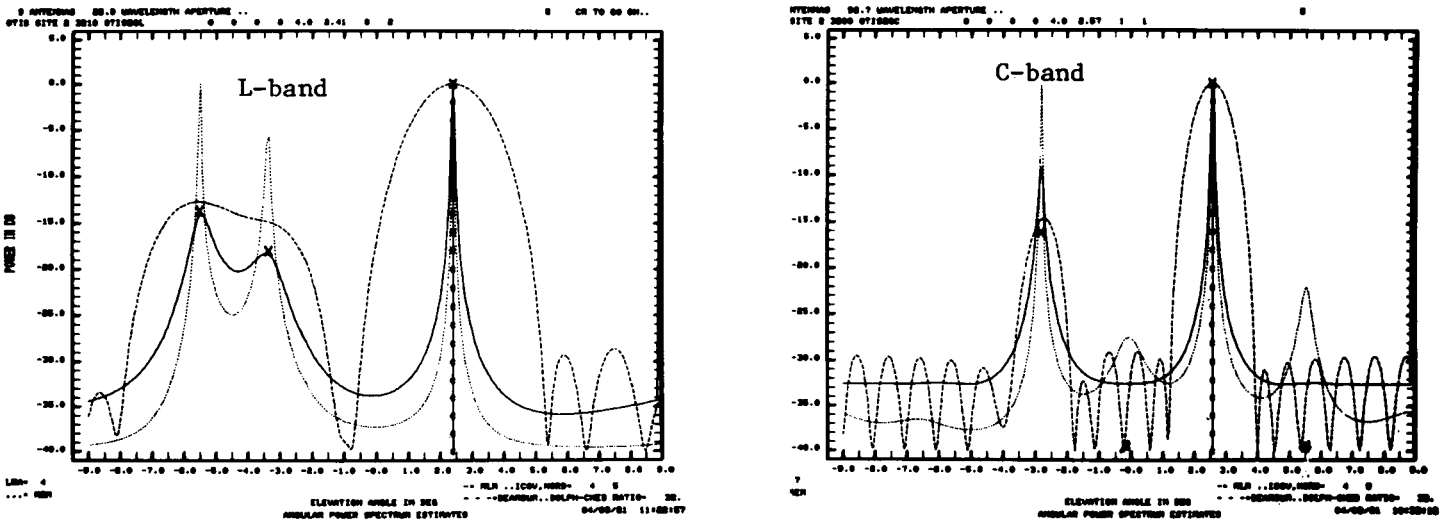


**ELEVATION ANGLE (DEG)**

Fig.7-4. Camp Edwards measurement: Gibbs Road, L-band and C-band elevation array, $\theta_{EL} \simeq 2.5^{o}$.

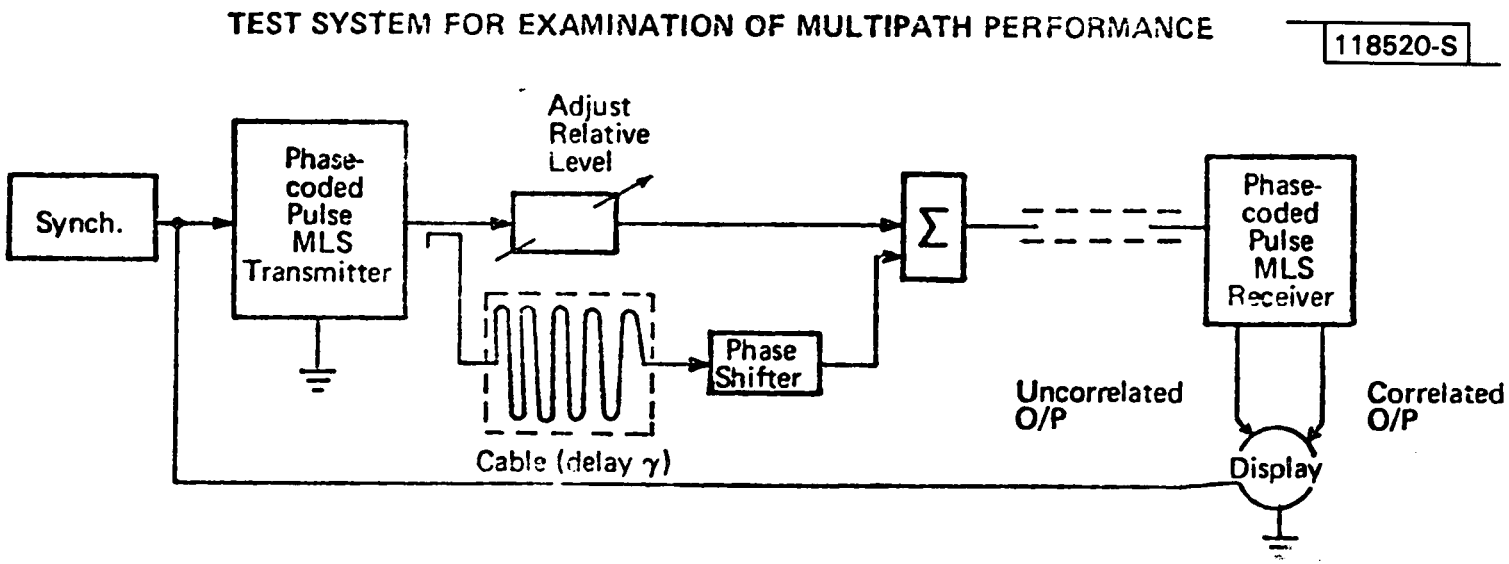


Fig.7-5. DME multipath bench test used in UK tests [38].

2. Bench Tests of Proposed Receivers

Bench tests of the proposed DME/P pulse shape and receivers in the presence of multipath will be invaluable for validating the computer simulations as well as confirming the analytical studies to date. Whereas with the MLS angle systems, the development of such a simulation is a nontrivial undertaking, the situation is much simpler for a PDME. Figure 7-5 shows the realization used in UK bench tests of a phase coded waveform [38].

It is suggested that errors be determined at a range of time delays for M/D ratios of -10 dB, -6 dB, -3 dB, +3 dB and +6 dB (levels in the ranges -1 dB to +1 dB are <u>not</u> recommended as the results in the antiphase condition will be very sensitive to precise level adjustment). A full range of relative rf phases should be explored for each ($\tau$, $\rho$) combination. Additionally, some measurements should be made at low SNR to ascertain whether multipath and front end noise effects can be root sum squared.

3. Investigation of STOL/VTOL Environments

The airport data set used to generate the empirical relative likelihood results in Chapter VI was heavily weighted toward CTOL operations. However, STOL/VTOL airports will be an important initial application of MLS (since ILS cannot be used in such cases). Thus, examination of representative STOL/VTOL airports geometries would be helpful in determining the appropriate DME/P hardware features.

## REFERENCES


1. International Standards and Recommended Practices, Aeronautical Telecommunications, Annex 10, ICAO, 3rd ed. (July 1972).

2. H. Ecklundt, "Technical Proposal for the PDME (FRG Proposal)," Presentation at the FAA/DMFT Experts Meeting (Dec. 12, 1979).

3. R. Kelly and E. LaBerge, "Guidance Accuracy Considerations for the Microwave Landing System L-Band Precision DME," Jour. of Navigation (May 1980).

4. C. Hirsch, "L-Band DME for the MLS," FAA Contract WI-71-3086-1, Final Report, (Feb. 1972).

5. C. Hirsch, "Experimentation for the use of L-Band DME with MLS," Final Report (April 1974).

6. C. Burrows, et al., "Microwave Landing System Requirements for STOL Operations," AIAA Paper 79-997, 6th Aircraft Design, Flight Test and Operation Meeting, Los Angeles (12-14 Aug. 1974).

7. "Final Report of Analytic Study of MLS Operations with L-Band DME," Bendix Flight Systems Division, Peterboro, NJ (Sept. 1975).

8. J. Evans, T. Burchsted, R. Orr, J. Capon, D. Shnidman and R. Sussman, "MLS Multipath Studies," Lincoln Laboratory, M.I.T. Project Report ATC-63, Volumes I and II (1976), FAA-RD-76-3, DDC AD-A023040/9 and A025108/2.

9. J.E. Evans, "Synthesis of Equiripple Sector Antenna Patterns," IEEE Trans. Antennas Propag. AP-24, pp. 347-353 (May 1976).

10. P. Beckmann and A. Spizzichino, The Scattering of Electromagnetic Waves from Rough Surfaces (Pergamon Press, The Macmillan Co., New York, 1963).

11. "Refined Microwave Landing System (MLS) Development Program Plan, Feasibility Demonstration Phase II," Report No. 11009, Vol. II Part 3 Section 30, Hazeltine Corp., Greenlawn, NY (15 May 1974).

12. S. Nakamura, "Some Considerations for the DME/M," ICAO AWOP Background Information Paper WGM/3-BPI/2 (March 1980).

13. "The DME-Based Landing System," Federal Republic of Germany, Vol. 2 (Sept. 1975).

14. M. Whitney, "DME(M) Trial Results," ICAO AWOP WG-S Background Information Paper AWOP-WG-S/BIP-6 (Sept. 1979).

15. R. Crow, Private Communications to R.S. Orr (May 1976).

16. "A New Guidance System for Approach and Landing," Document No. DO-148, Radio Technical Commission for Aeronautics, SC-117 (18 Dec. 1970).

17. J. Capon, "Multipath Parameter Computations for the MLS Simulation Computer Program," Lincoln Laboratory, M.I.T. ATC Project Report ATC-68 (8 April 1976), FAA-RD-76-55, DDC AD-A024350/1.

18. K.J. Keeping and J.C. Sureau, "Scale Model Measurements of Aircraft L-Band Beacon Antenna," Lincoln Laboratory, M.I.T. Project Report ATC-47 (4 March 1975), FAA-RD-75-23.

19. G.J. Schlieckert, "An Analysis of L-Band Beacon Antenna Patterns," Lincoln Laboratory, M.I.T. Project Report ATC-37 (15 January 1975), FAA-RD-74-144.

20. D.W. Mayweather, "Model Aircraft L-Band Beacon Antenna Pattern Gain Maps," Lincoln Laboratory, M.I.T. Project Report ATC-44 (16 May 1975), FAA-RD-75-75.

21. R. Butler (Rappoteur), "Report of Multipath Subgroup of WG-A Held Near Boston, Mass., USA, October 11-15, 1976." L.WP/3 in the report of AWOP Working Group A, Seventh Meeting, London (Nov 1-12, 1976).

22. T. McGarty, "Measurements of Beacon Propagation and Multipath on the Airport Surface," Lincoln Laboratory, M.I.T. ATC Working Paper 42WP-5038 (22 Nov. 1974).

23. H. Postel, "Precision L-Band DME Tests," FAA Technical Center Report No. FAA-CT-80-25, (August 1980), FAA-RD-80-74.

24. "Flight Trials of TRSB/Interscan Equipment at Sydney International Airport, Australia," Paper AWO/78-WP/88 presented by Australia at ICAO AWO Division Meeting (April 1978).

25. "Tracked Flight Trials of Doppler MLS at Manchester Airport," Paper AWO/78-WP/123 presented by United Kingdom at ICAO AWO Division Meeting (April 1978).

26. A. Lopez, "Scanning-Beam Microwave Landing System - Multipath Errors and Antenna Design Philosophy," IEEE Trans. Antennas Propag. AP-25, pp. 290-296 (May 1977).

27. J. Evans, D. Sun, S. Dolinar, and D. Shnidman, "MLS Multipath Studies, Phase 3 Final Report, Volume I: Overview and Propagation Model Validation/Refinement Studies," Lincoln Laboratory, M.I.T. Project Report ATC-88 (25 April 1979), FAA-RD-79-21, DTIC AD-A08782712.

28. "Siting Criteria for Instrument Landing System," Dept. of Transportation, Federal Aviation Administration (FAA Order 7650.16A).

29. D. Shnidman, "Airport Survey for MLS Multipath Issues," Lincoln Laboratory, M.I.T. Project Report ATC-58, (Dec. 1975), FAA-RD-75-195.

30. P. Cornwell and P. Greene, "Fine Resolution Forward Scatter Measurements, IEEE Int'l Conf Radar-77, London, England (Oct 1977).

31. "Time Reference Scanning Beam Microwave Landing System," U.S. Proposal to ICAO (Dec. 1975).

32. G. Blaschke, "Reduction of Errors Caused by Echo-Signals," Presentation to the FAA/BMFT Experts Meeting (Dec 12, 1979).

33. P. Form, K. Westphal, and W. Schroer, "Progress in Measurement and Simulation of Multipath," Report of the Sonderforschungs-Bereich 58 "Flugfuhrung" of the Tech Univ. Braunschweig (Sept. 1981).

34. T. Tapsell (presenter), "A New Approach to Optimisation of the Essential Characteristics of DME/M to meet the Operation Requirements," AWOP WGM Background Information Paper to be presented in Rio de Janeiro (Sept. 1980).

35. P. Woodward, Probability and Information Theory, With Applications to Radar (Pergamon Press, London, 1964).

36. D. Barton and H. Ward, Handbook of Radar Measurement (Prentice Hall, New Jersey, 1969).

37. J. Edwards (presenter), "DME/P Flight Test Data Results," AWOP WGM Background Information Paper AWOP/WG M.5/BIP-2 (Sept. 1981).

38. M. Whitney (presenter), "An alternative ranging system in L-Band," AWOP Working Group A Background Information Paper, L. BIP/1, (Nov. 1976).

39. J. Evans, S. Dolinar, D. Shnidman, and R. Burchsted, "MLS Multipath Studies, Phase 3 Final Report Volume II: Development and Validation of Model for MLS Techniques," Lincoln Laboratory, M.I.T. Project Report ATC-88 Vol. II (Feb. 1980), FAA-RD-79-21, DTIC AD-A088001/3.

40. S. Nakamura (presenter), "Proposal for Optimized Pulse Shapes and Related System Design," AWOP Paper AWOP/WGM.4/BIP (Mar. 1981).

41. J. Hetyei, "Functioning of the DAC Trigger and P-DME Time Reference," AWOP WG-M Paper AWOP/WGM.5/WG-13 (Sept. 1981).

42. W. Kabiersch, "PDME Simulation Program Description and Discussion of Results", DFVLR Inst. Flugfuhring Draft Report presented by T. Bohr as AWOP WG-M Paper AWOP/WGM.5/BIP-3 (Sept. 1981).

43. M. Gori and M. Carnevale, "The Italian Proposal for the DME-M System," AWOP WG-M Paper, Dec. 1981.

44. D. Sun, "Experimental Measurements of Low Angle Ground Reflection Characteristics at L-Band and C-Band for Irregular Terrain," Lincoln Laboratory, M.I.T. Project Report ATC-107 (29 Dec 1981), DOT/FAA/RD-81/65.

45. J. Evans and S. Dolinar, "MLS Multipath Studies Phase 3 Final Report volume III: Comparative Assessment Results," Lincoln Laboratory, M.I.T. Project Report ATC 88, Volume III (8 June 1981), FAA-RD-79-21.

46. J. Evans, and P. Swett, "Results of L-Band Multipath Measurements at Operational United States (US) Airports in Support of the Microwave Landing System (MLS) Precision Distance Measuring Equipment (DME/P)," Lincoln Laboratory, M.I.T. Project Report ATC-109 (23 July 1981), DOT/FAA/RD-81/63.

47. P. Form and R. Springer, "Field Tests for Multipath Propagation Measurements in Mountainous Sites," ICAO AWOP/WP.101 (April 1978).

48. R. Ullrich, "Error Response of a Trapezoid Pulse DME Technique Disturbed by Multipath Effects and Noise," DFVLR report (draft) (May 1981).

49. S. Nakamura (presenter), "Long Range Echo Problem of Existing DME and TACAN," AWOP WG-M paper AWOP/WGM.5/BIP-6 (Sept. 1981) (drawn from an article in the NEC Research and Development Journal No. 39 of Oct 1975).

50. D. Carel (rapporteur), "Report of the Fifth Meeting of AWOP Working Group M," Neuilly, France (Sept. 1981).

APPENDIX A

# DERIVATION OF DME MULTIPATH PERFORMANCE FORMULAS

All multipath error formulas used in this report are derived by a common method. The procedure is to first determine the nominal arrival time ($\tilde{t}$), which is the reference time at which the DME processor would emit a range marker in the absence of multipath (i.e., the time of threshold crossing or envelope coincidence). The second step is to approximate the time ($\hat{t}$) at which the marker occurs in the presence of a single multipath component having specified parameters. The difference

$$\varepsilon = \hat{\tau} - \tilde{t} \tag{A.1}$$

is the single scan error. Motion averaging is accounted for by averaging several values of the error in which the differential phase has been incremented in accordance with a particular scalloping frequency and pulse spacing.

In most cases the processor equation cannot be solved analytically for $\hat{t}$ in the presence of arbitrary multipath; even in some of those cases for which it can be, the solution is needlessly obscure. Thus it is generally necessary to make some assumption about the multipath signal in order to complete the calculation. In the following it is assumed that the relative multipath amplitude ($\rho$) is small enough that the sum envelope (direct + multipath) can be approximated by a McLaurin expansion in $\rho$ truncated at the linear term:

$$\begin{aligned} e(t) &= \left| s(t) + \rho e^{j\phi} s(t-\tau) \right| \\ &\simeq s(t) + \rho \cos \phi \; s(t-\tau) \end{aligned} \tag{A.2}$$

Although this restriction on the size of $\rho$ is the major analytic assumption, other specialized approximations may arise from time to time in the course of the error derivation. Each receiver type is treated separately below, and the derivation illustrated with the Gaussian pulse result. Formulas are also given for the cos/cos$^2$ and trapezoidal pulses.

## A.1 Fixed Threshold Detection

The direct pulses are all normalized to have unity peak amplitude, e.g., the Gaussian pulse is

$$s(t) = e^{-\beta(\frac{t}{t_r})^2} \tag{A.3}$$

The threshold $\alpha$ ($0<\alpha<1$) is thus a fixed fraction of the peak, and the equation for the nominal leading edge crossing is

$$s(\tilde{t}) = \alpha \tag{A.4}$$

In the Gaussian case, the solution is

$$\tilde{t} = -t_r\sqrt{\frac{-\ln\alpha}{\beta}} \triangleq -vt_r \tag{A.5}$$

The parameter v expresses the nominal crossing time in risetime units.

With the multipath component added, the equation becomes

$$s(\hat{t}) + \rho \cos\phi\ s(\hat{t}-\tau) = \alpha \tag{A.6}$$

or directly in terms of the error $\varepsilon$,

$$s(\tilde{t}+\varepsilon) + \rho \cos \phi \; s(\tilde{t}+\varepsilon-\tau) = \alpha \tag{A.7}$$

e.g.,

$$e^{-\beta\left(\frac{\tilde{t}+\varepsilon}{t_r}\right)^2} \left[1 + \rho \cos \phi \; e^{-\beta\left(\frac{\tau}{t_r}\right)\left(\frac{\tau-2\tilde{t}-2\varepsilon}{t_r}\right)}\right] = \alpha \tag{A.8}$$

Since a small $\rho$ solution is being sought, it is assumed that small errors will result. Thus quadratic terms such as $\varepsilon^2$ and $\rho\varepsilon$ will be discarded in solving (A.8); taking logarithms, linearizing the logarithm (according to $\ln(1+x) \simeq x$), and discarding the quadratic terms leaves

$$-\beta\left(\frac{\tilde{t}^2 + 2\tilde{t}\varepsilon}{t_r^2}\right) + \rho \cos \phi \; e^{-\beta\left(\frac{\tau^2 - 2\tilde{t}\tau}{t_r^2}\right)} = \ln \alpha \tag{A.9}$$

Equation (A.9) can be solved exactly to give the error formula for fixed thresholding, denoted by $\varepsilon_{fix}$:

Gaussian Pulse:

$$\varepsilon_{fix} = -\frac{\rho t_r}{2\beta v} \; e^{-\beta\left(\frac{\tau}{t_r}\right)\left(\frac{\tau}{t_r} + 2v\right)} \cos \phi \tag{A.10}$$

The corresponding results for the other waveforms of interest are given below.

Cos/Cos$^2$ Pulse:

This waveform is a variant on the pedestal pulse in which the linear pedestal is deleted and the trailing edge is shaped as cos$^2$ to improve the spectrum (Fig. A-2):

$$s(t) = \begin{cases} \cos\left(\frac{2\pi t}{3T}\right) & ; \quad -\frac{3T}{4} \leq t \leq 0 \\ \cos^2\left(\frac{\pi t}{2T}\right) & ; \quad 0 \leq t \leq T \\ 0 & ; \quad \text{elsewhere} \end{cases} \tag{A.11}$$

The -6 dB pulsewidth is T and the pulse is set up to have width T/2 on either side of the peak. Following through the above procedure leads to the result:

$$\varepsilon_{fix} = \begin{cases} \frac{-3T}{2\pi\sqrt{1-\alpha^2}}\ \rho \sin(\sin^{-1}\alpha - \frac{2\pi\tau}{3T})\cos\phi; & \tau \leq \frac{3T}{2\pi}\sin^{-1}\alpha \\ 0 & ; \quad \tau > \frac{3T}{2\pi}\sin^{-1}\alpha \end{cases} \tag{A.12}$$

Trapezoidal Pulse:

$$s(t) = \begin{cases} 0 & ; \quad t < 0 \\ \frac{t}{t_r} & ; \quad 0 \leq t \leq t_r \\ 1 & ; \quad t > t_r \end{cases} \tag{A.13}$$

$$\varepsilon_{fix} = \begin{cases} -\rho(\alpha t_r - \tau)\cos\phi & ; \quad \tau < \alpha t_r \\ 0 & ; \quad \tau > \alpha t_r \end{cases} \tag{A.14}$$

A.2 Real Time Threshold Detection

The equation for the nominal crossing is the same as for fixed thresholding (A.4). The multipath-perturbed crossing is the solution of the following equation:

$$\hat{e(t)} = \alpha e(t_{max}) \tag{A.15}$$

where $t_{max}$ stands for the time at which the net envelope maximum occurs. Thus, prior to solving (A.15), one must find the peak value.

For pulses having a unique maximum (e.g., Gaussian and cos/cos$^2$), we can assume that the pulse is symmetric about t=0 and has $\dot{s}(0) = 0$. Again neglecting $\rho^2$ and higher terms, we find that

$$\dot{e}(t) \simeq \dot{s}(t) + \rho \cos \phi \, \dot{s}(t - \tau) \tag{A.16}$$

Replacing $s(t)$ and $s(t - \tau)$ by their Taylor series at $t = 0$,

$$s(t) \simeq 1 + \frac{1}{2} \ddot{s}(0)t^2 \tag{A.17}$$

$$s(t - \tau) \simeq s(-\tau) + \dot{s}(-\tau)t \tag{A.18}$$

and setting $\dot{e}(t) = 0$ yields the following equation,

$$\ddot{s}(0)t + \rho \cos \phi \, \dot{s}(-\tau) = 0 \tag{A.19}$$

whose solution is $t_{max}$:

$$t_{max} = \rho\left[\frac{\dot{s}(-\tau)}{-\ddot{s}(0)}\right] \cos \phi \ . \tag{A.20}$$

The most useful aspect of this result is the discovery that $t_{max}$ is proportion to $\rho$ for small multipath. Without even solving explicitly for $t_{max}$ we can go back to (A.15) and determine which terms are of sufficiently high order to neglect. For the Gaussian pulse, Eq. (A.15) becomes

$$e^{-\beta\left(\frac{\tilde{t}^2 + 2\tilde{t}\varepsilon}{t_r^2}\right)}\left[1 + \rho\cos\phi\, e^{-\beta\left(\frac{\tau}{t_r}\right)\left(\frac{\tau}{t_r} + 2v\right)}\right]$$

$$= \alpha\left[1 + \rho\cos\phi\, e^{-\beta\left(\frac{\tau}{t_r}\right)^2}\right] \qquad (A.21)$$

Taking logarithms, linearizing and solving for $\varepsilon$ yields the real time thresholding error.

Gaussian Pulse:

$$\varepsilon_{rt} \simeq \rho\tau e^{-\beta\left(\frac{\tau}{t_r}\right)\left(\frac{\tau}{t_r} + v\right)}\left[\frac{\sinh\frac{\beta v\tau}{t_r}}{\frac{\beta v\tau}{t_r}}\right]\cos\phi \quad . \qquad (A.22)$$

Cos/Cos$^2$ Pulse:

The time of the envelope peak can be found from Eq. (A.20). Since the waveform changes shape at t=0, the second derivative is discontinuous there, viz

$$\ddot{s}(0-) = -\frac{4}{9}\left(\frac{\pi}{T}\right)^2 \qquad (A.23)$$

$$\ddot{s}(0+) = -\frac{1}{2}\left(\frac{\pi}{T}\right)^2 \qquad (A.24)$$

We use $\ddot{s}(0-)$ in the ensuing analysis. For short delays, the multipath affects both the leading edge and the peak. The equation to be solved is

$$\cos \omega(\tilde{t}+\varepsilon) + \rho \cos \phi \cos \omega(\tilde{t}+\varepsilon-\tau) = \alpha e(t_{max}) \tag{A.25}$$

where

$$\omega = \frac{2\pi}{3T} \tag{A.26}$$

Multipath arriving later than the nominal threshold crossing time affects the peak only, i.e.,

$$\cos \omega(\tilde{t} + e) = \alpha e(t_{max}) \tag{A.27}$$

Carrying through the small $\rho$, small $\varepsilon$ solution yields

$$\varepsilon_{rt} = \begin{cases} \frac{3T}{2\pi} \rho \sin \omega\tau \cos \phi & ; \ \omega\tau \leq \sin^{-1} \alpha \\ \frac{3T}{2\pi} \left(\frac{\alpha}{\sqrt{1-\alpha^2}}\right) \cos \omega\tau \cos \phi & ; \ \sin^{-1}\alpha \leq \omega\tau \leq \pi/2 \\ 0 & ; \ \omega\tau > \pi/2 \end{cases} \tag{A.28}$$

Trapezoidal Pulse:

As for the cos/cos$^2$, two distinct expressions are found, depending on whether the multipath is before or after the nominal crossing:

$$\varepsilon_{rt} = \begin{cases} \rho \tau \cos \phi & ; \ \tau \leq \alpha t_r \\ \rho \alpha t_r \cos \phi & ; \ \tau > \alpha t_r \end{cases} \tag{A.29}$$

A.3 Delay-and-Compare

In this case the operation is governed by the choice of processor gain (G) and delay ($\tau_d$). The nominal crossing is found by solving

$$\tilde{s}(t) = G\,\tilde{s}(t - \tau_d) \tag{A.30}$$

e.g.,

$$e^{-\beta\left(\frac{\tilde{t}}{t_r}\right)^2} = G\,e^{-\beta\left(\frac{\tilde{t} - \tau_d}{t_r}\right)^2} \tag{A.31}$$

or

$$\tilde{t} = -\frac{t_r}{2}\left[\frac{\ln G}{\beta}\left(\frac{t_r}{\tau_d}\right) - \left(\frac{\tau_d}{t_r}\right)\right] \tag{A.32}$$

An equivalent specification of the processor is to give a threshold value which indicates the relative amplitude point on the undelayed pulse at the crossing point. Given $\alpha$ (or equivalently, v) and $\tau_d$, the required gain can be computed. In the Gaussian case it is

$$G = e^{\beta\left(\frac{\tau_d}{t_r}\right)\left(\frac{\tau_d}{t_r} + 2v\right)} \tag{A.33}$$

The resulting error formula is

$$\varepsilon_{dc} = \rho\,\tau\, e^{-\beta\left(\frac{\tau}{t_r}\right)\left(\frac{\tau}{t_r} + \frac{\tau_d}{t_r} + 2v\right)} \left[\frac{\sinh\left(\frac{\beta\tau_d\tau}{t_r^2}\right)}{\frac{\beta\tau_d\tau}{t_r^2}}\right] \cos\phi \tag{A.34}$$

Cos/Cos$^2$ Pulse:

Unlike the Gaussian case, in which the leading edge waveform trails off indefinitely as $t \to -\infty$ (i.e., the multipath is "always" present), the cos/cos$^2$ pulse has a sharp beginning. Thus three separate cases must be considered. For short multipath delays, both the delayed and undelayed pulses are corrupted by multipath at the envelope crossing point. For somewhat larger values of $\tau$, the delayed envelope may be free of multipath at the crossing. Finally, beyond a certain multipath delay, the crossing of two clean leading edges occurs. The result is

$$\varepsilon_{dc} = \begin{cases} \left(\frac{3T}{2\pi}\right) \rho \sin \omega\tau \cos \phi & ; \omega\tau \leq \sin^{-1}\alpha - \omega\tau_d \\ \frac{3T}{2\pi} \dfrac{\sin(\sin^{-1}\alpha - \omega\tau_d)}{\omega \sin \omega\tau_d} \sin(\sin^{-1}\alpha - \omega\tau) \cos \phi & ; \sin^{-1}\alpha - \omega\tau_d \leq \omega\tau < \sin^{-1}\alpha \\ 0 & ; \omega\tau > \sin^{-1}\alpha \end{cases} \tag{A.35}$$

The required comparator gain is

$$G = \left[\cos \omega\tau_d - \frac{\sqrt{1-\alpha^2}}{\alpha} \sin \omega\tau_d\right]^{-1} \quad ; \quad \sin \omega\tau_d < \alpha \tag{A.36}$$

Trapezoidal Pulse:

The analysis follows the pattern established in the cos/cos$^2$ case, resulting in

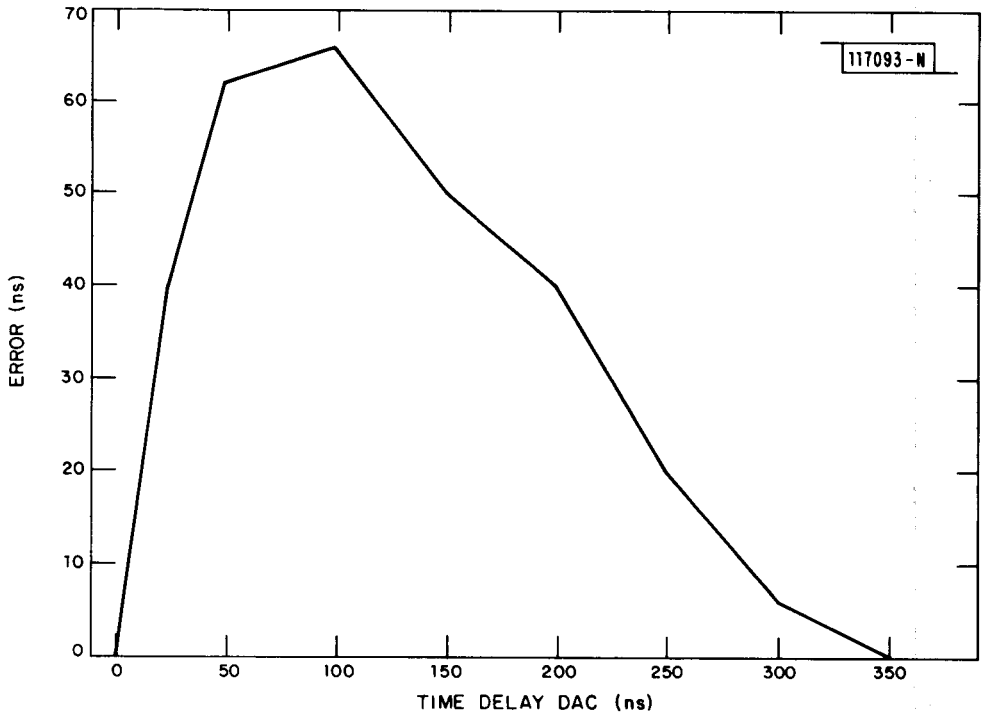


Fig.A-1. Error curve for cos-cos$^2$ pulse and DAC with IF filter.

$$\varepsilon_{dc} = \begin{cases} \rho\tau \cos\phi & ; \ \tau \leq \alpha t_r - \tau_d \\ \rho \dfrac{\alpha t_r}{\tau_d} - 1 \quad (\alpha t_r - \tau) \cos\phi & ; \ \alpha t_r - \tau_d \leq \tau < \alpha t_r \\ 0 & ; \ \tau \geq \alpha t_t \end{cases} \tag{A.37}$$

$$G = \left[1 - \frac{\tau_d}{\alpha t_r}\right]^{-1} \quad ; \ \tau_d < \alpha t_r \tag{A.38}$$

Cos - Cos$^2$ PULSE WITH IF FILTERING

The bandwidth of typical IF filters is necessarily restricted to reduce receiver noise and interference from adjacent channels. This causes the input pulse to the DAC to rise more slowly than the cosine pulse leading edge. Simulations of the DAC error characteristic suggest that the error can be approximated by:

$$\varepsilon_{DC} = \rho \, f(\tau) \cos \phi \tag{A.39}$$

where $f(\tau)$ is shown in Fig. A-1.

# APPENDIX B

## AIRPORT MAPS USED TO DETERMINE BUILDING LOCATIONS

Figures B-1 to B-24 show the airport maps used to determine building locations and orientations.

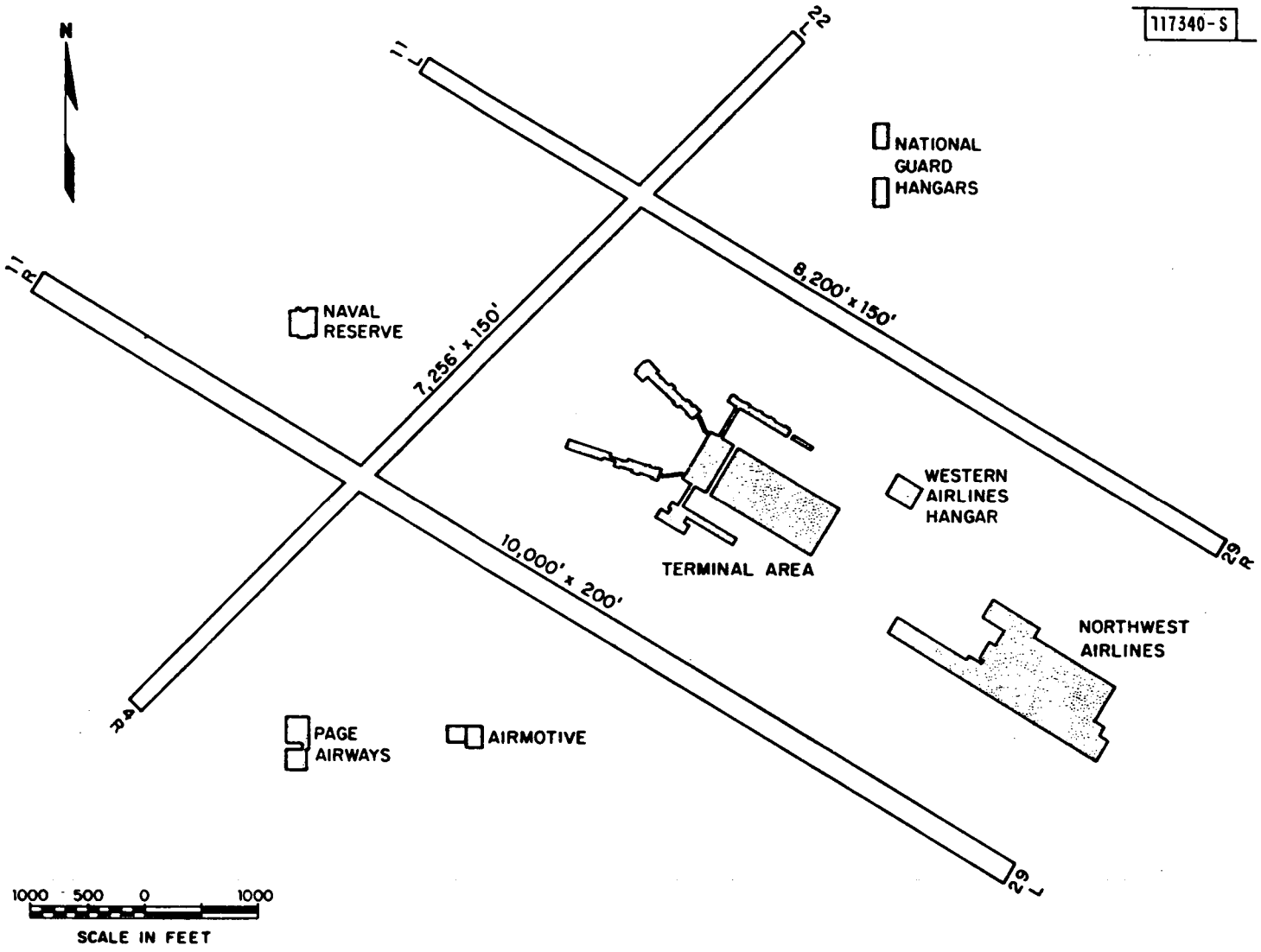


Fig.B-1. Minneapolis — St. Paul (Wold-Chamberlain Field) (MSP).

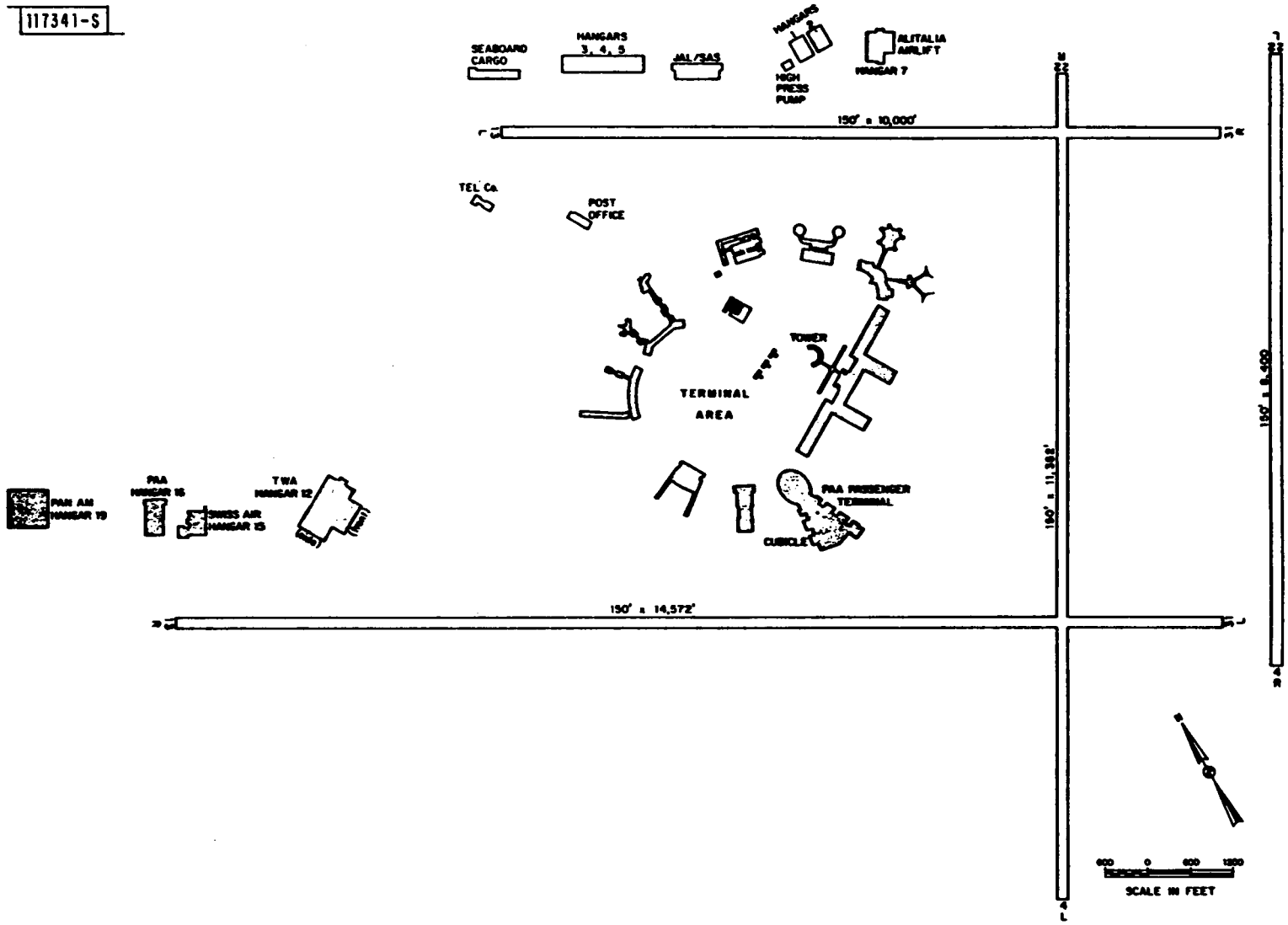


Fig.B-2. John F. Kennedy International Airport (JFK).

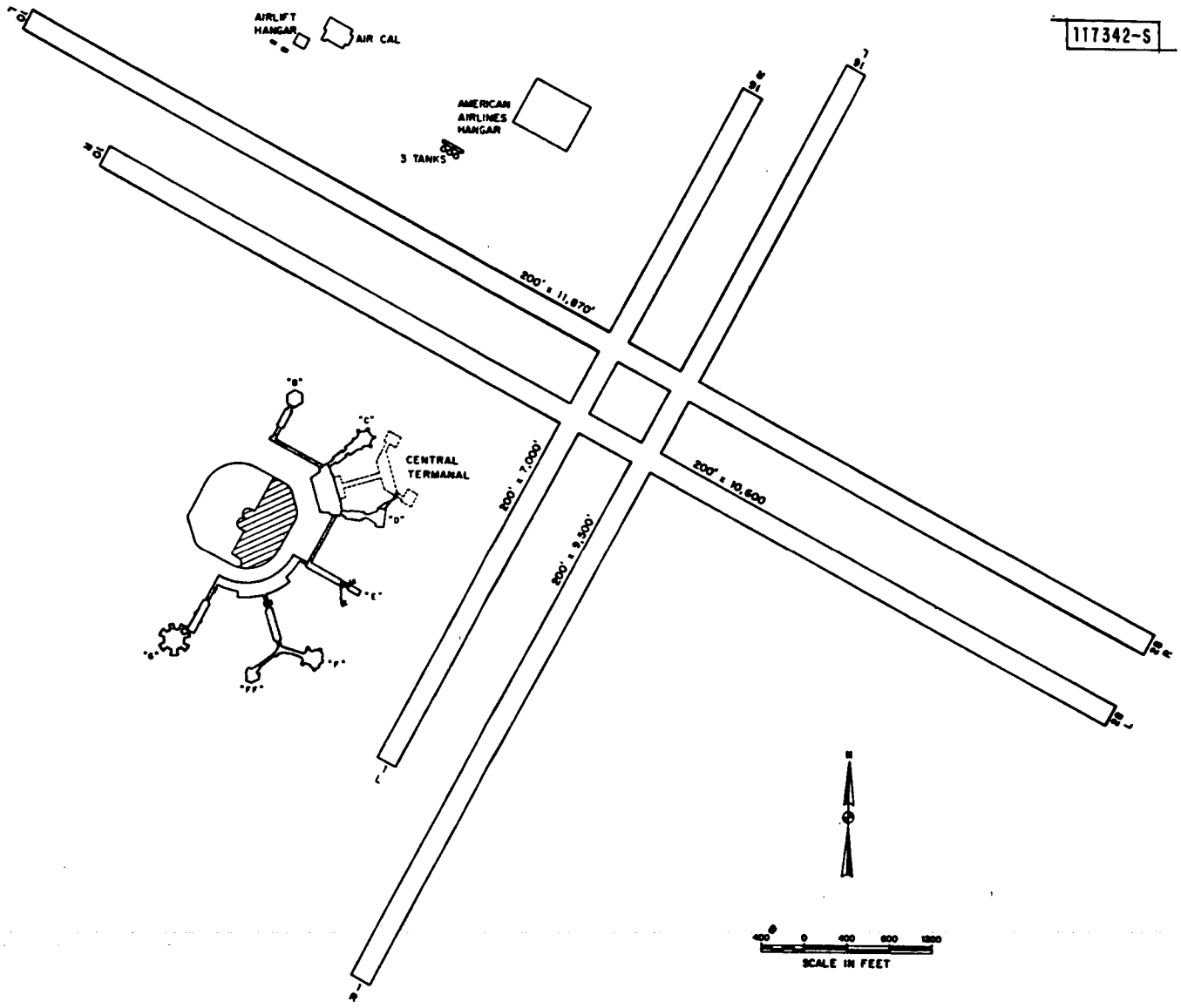


Fig.B-3. San Francisco International Airport (SFO).

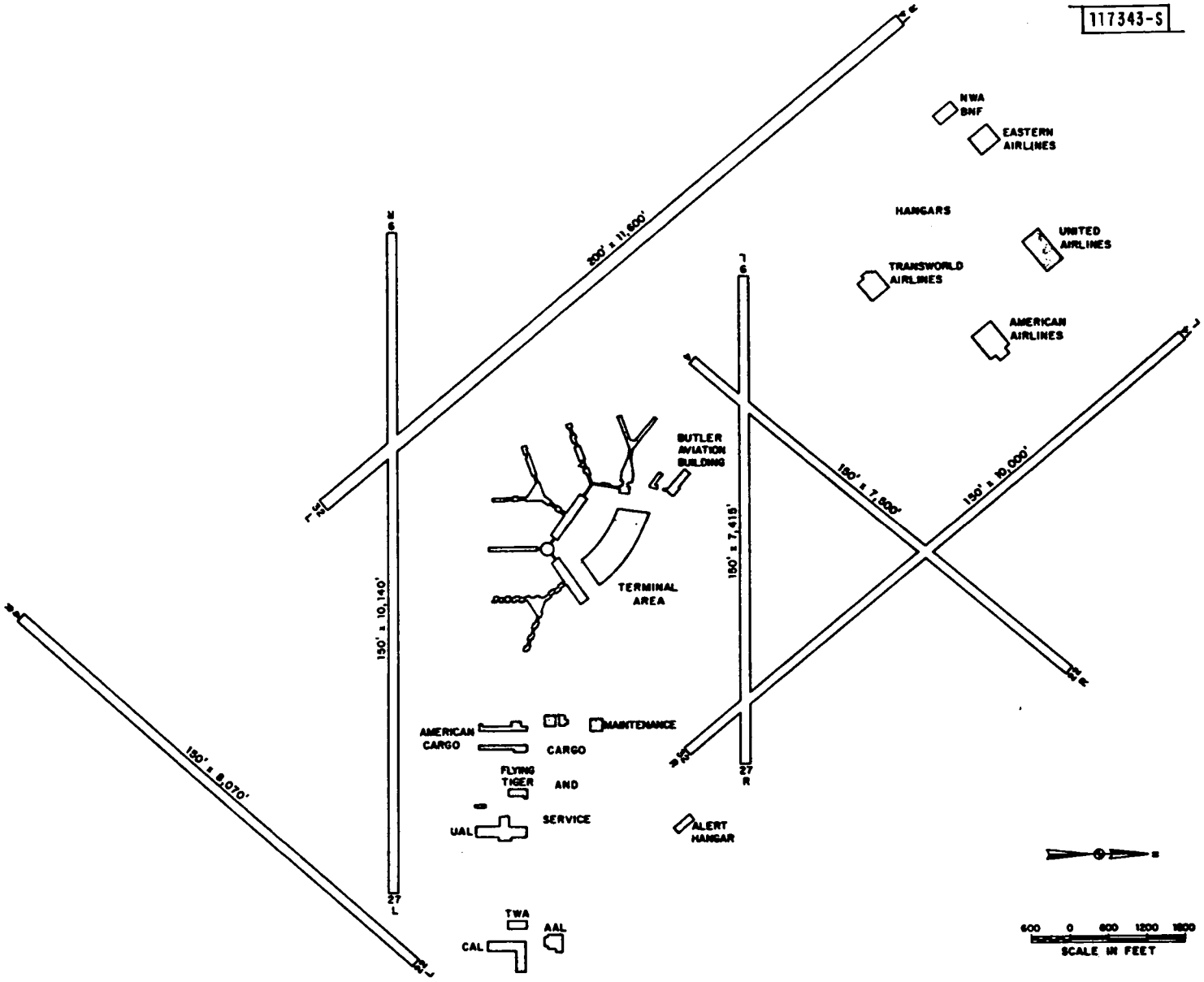


Fig.B-4. O'Hare International Airport (ORD).

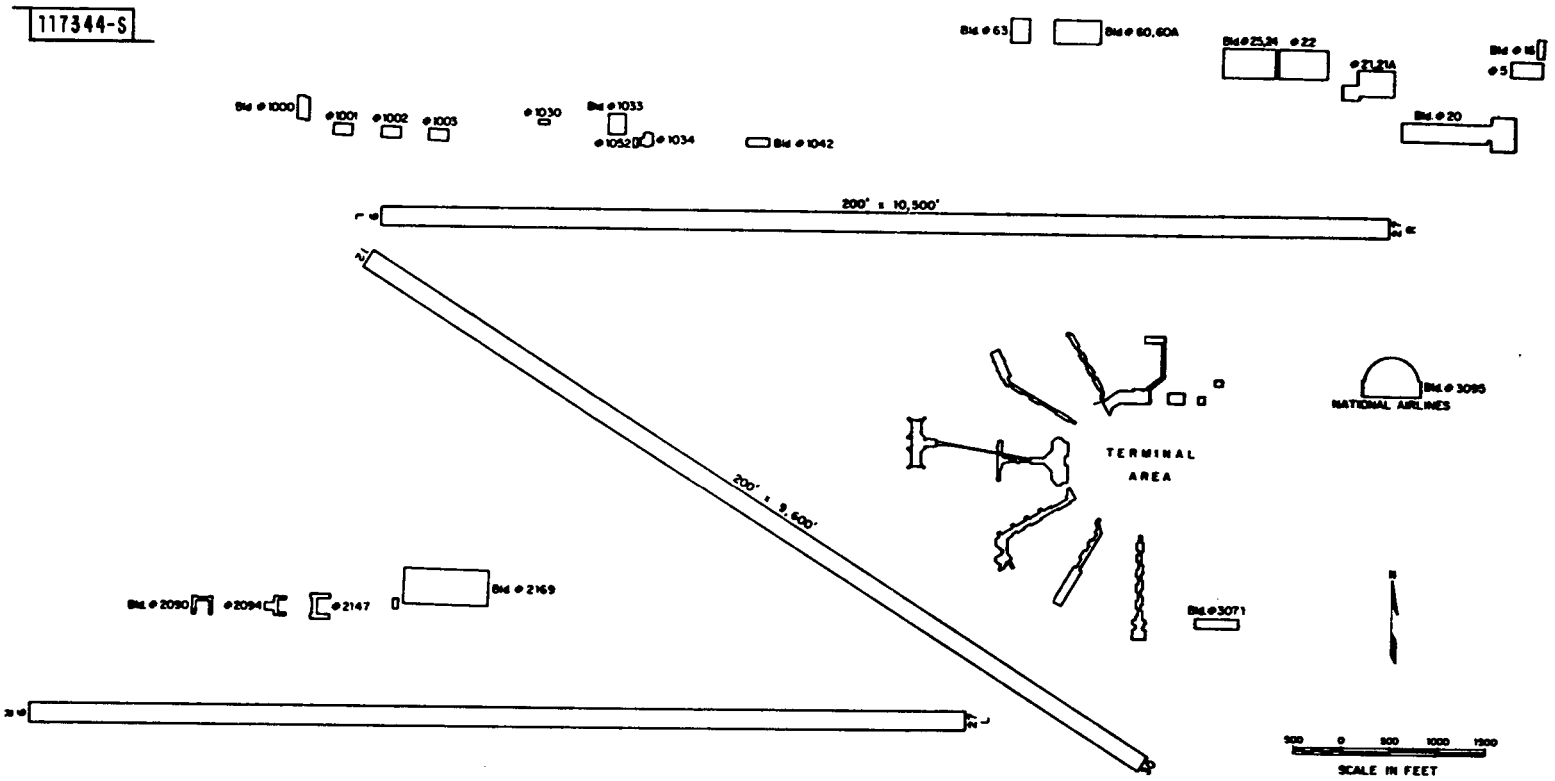


Fig.B-5. Miami International Airport.

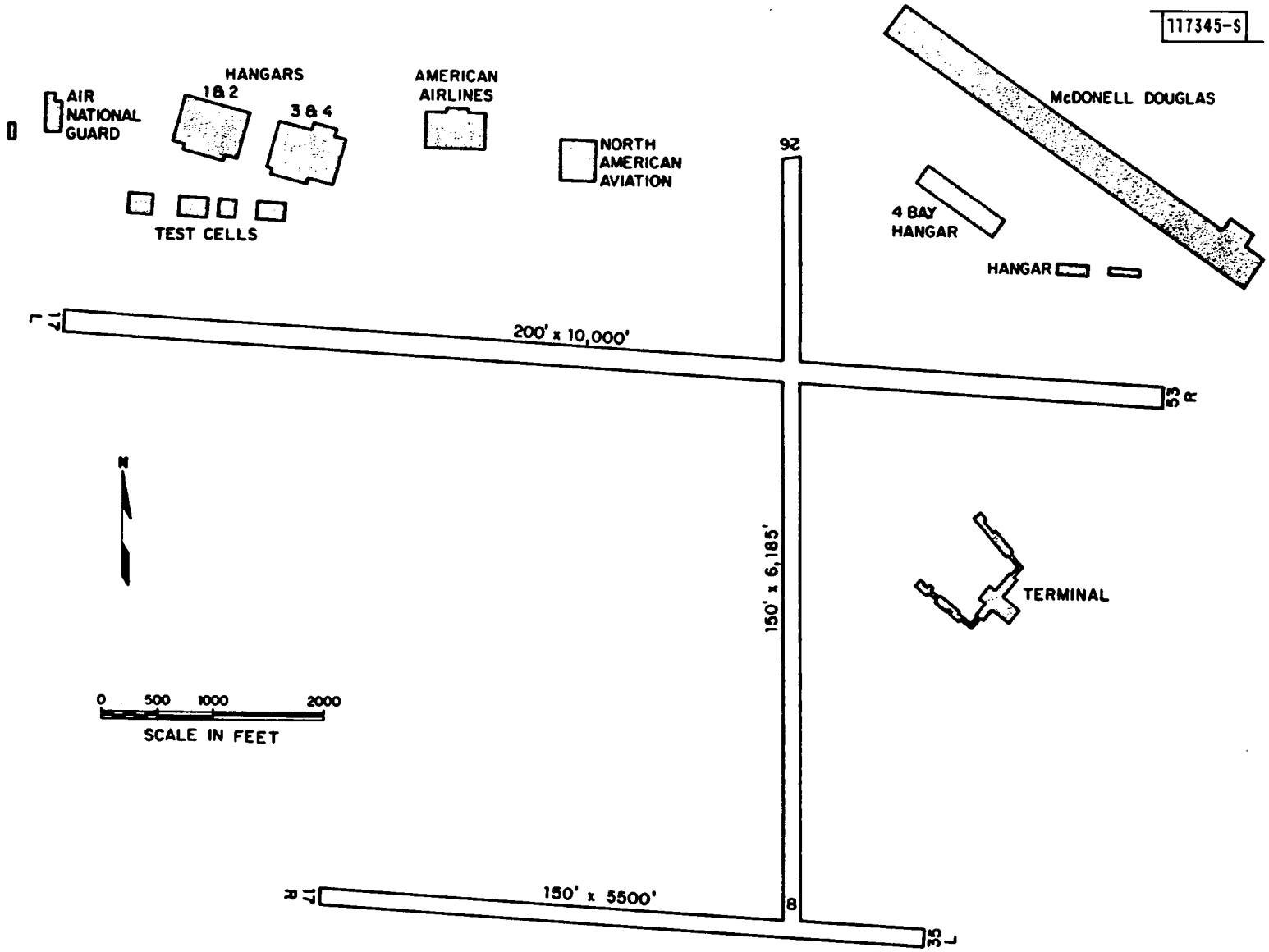


Fig.B-6. Tulsa International Airport (TUL).

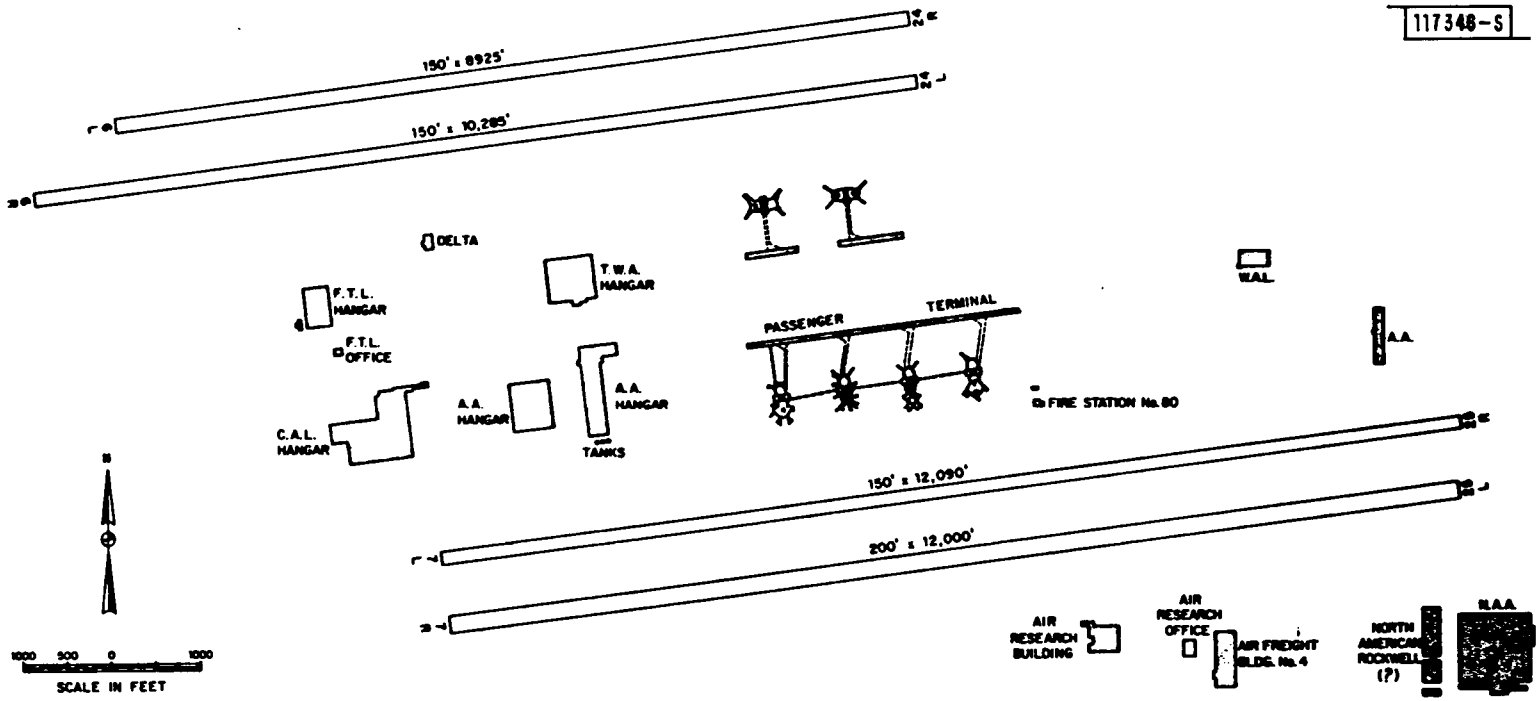


Fig.B-7. Los Angeles International Airport (LAX).

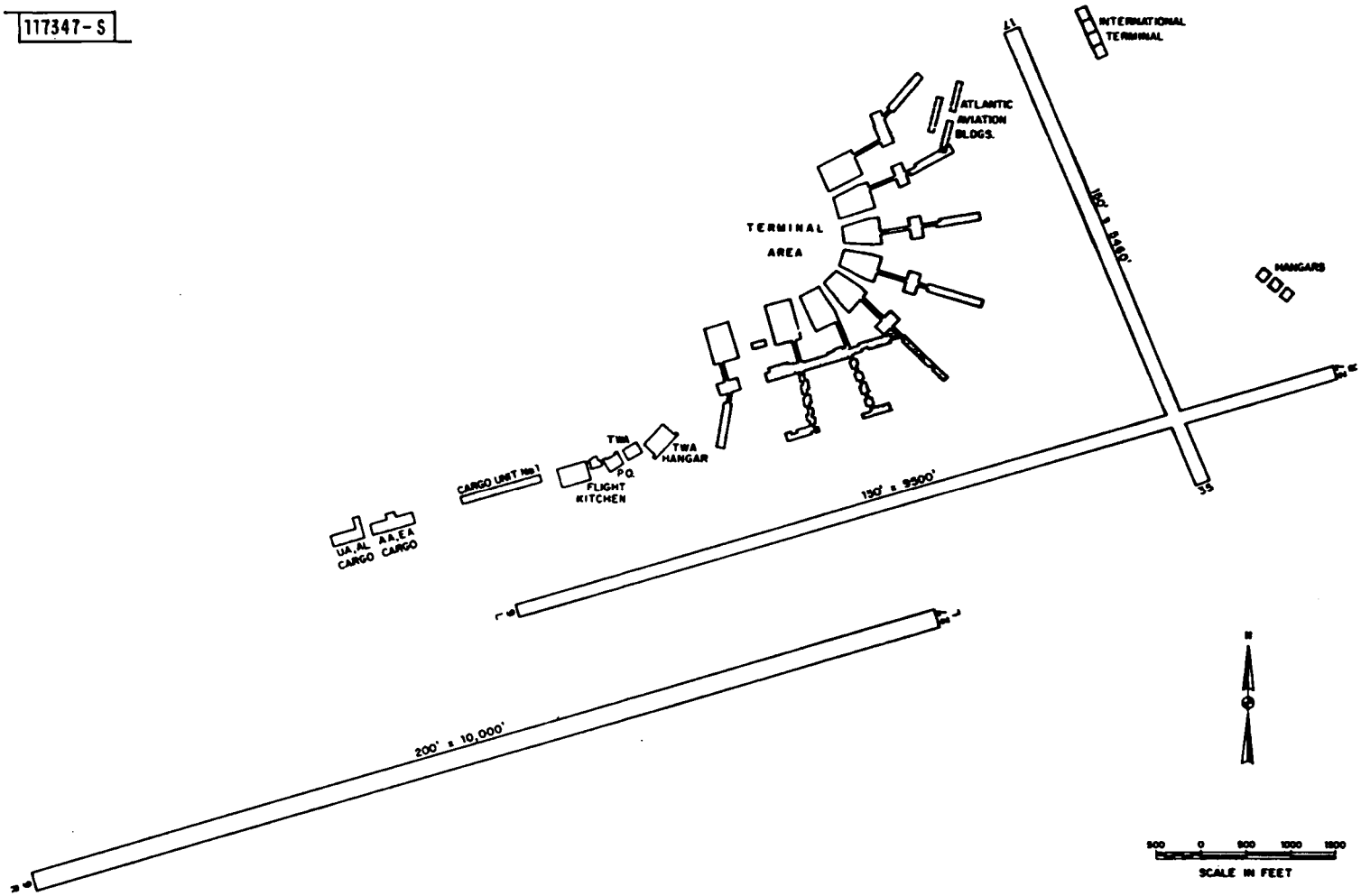


Fig.B-8. Philadelphia International Airport (PHL).

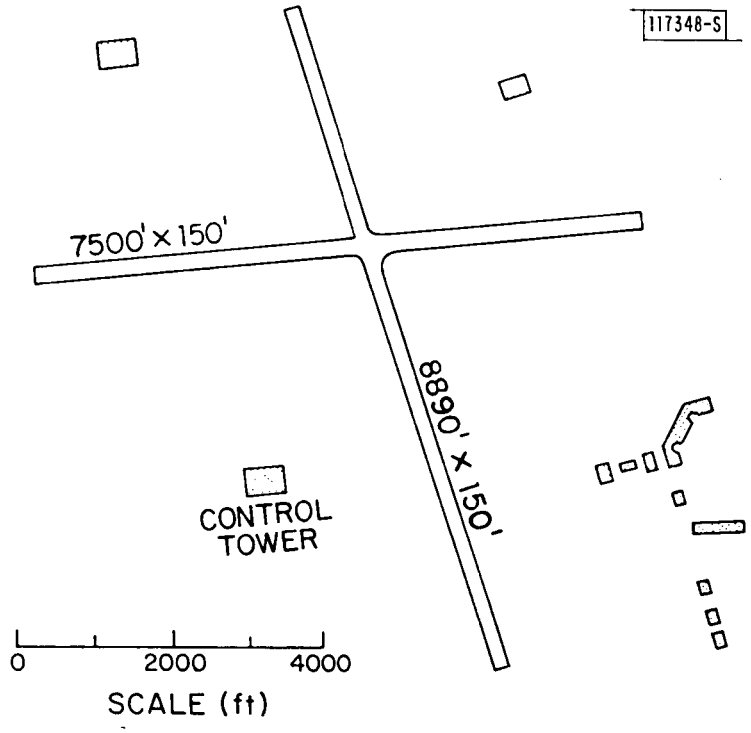


Fig.B-9. Melbourne Airport.

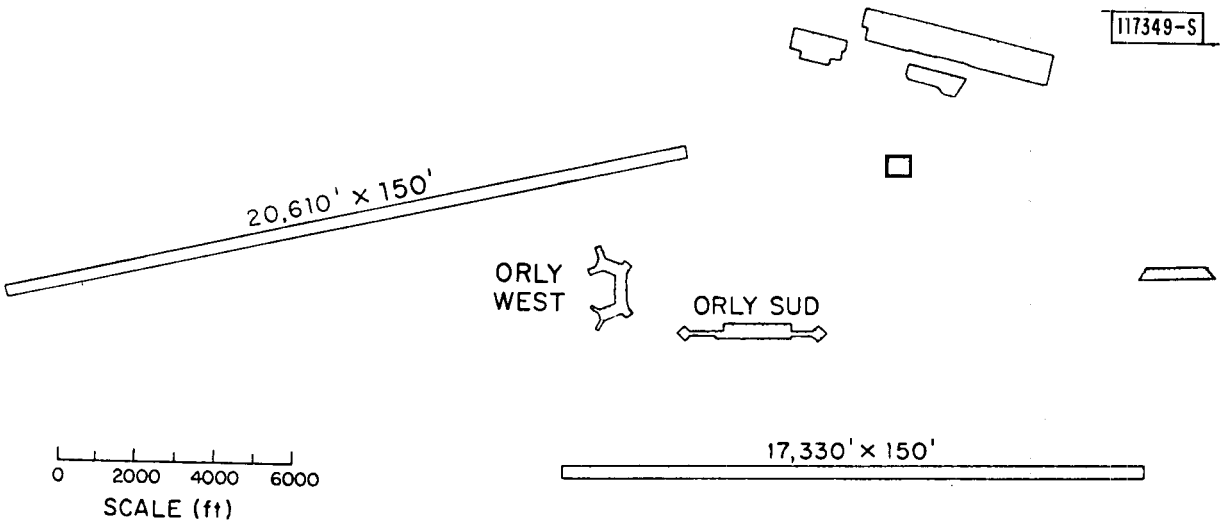


Fig.B-10. Orly Airport (Paris).

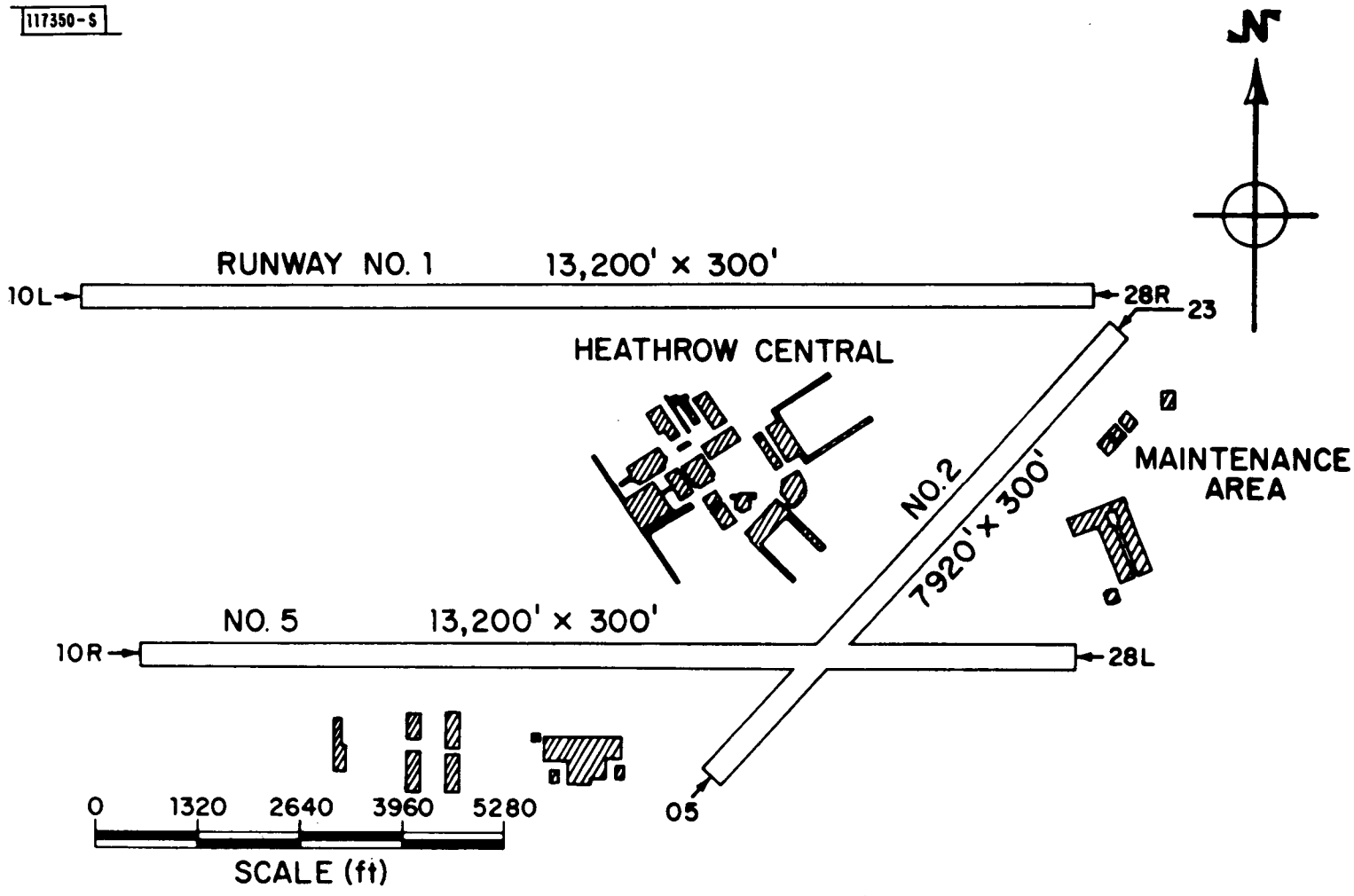


Fig.B-11. Heathrow Airport (London).

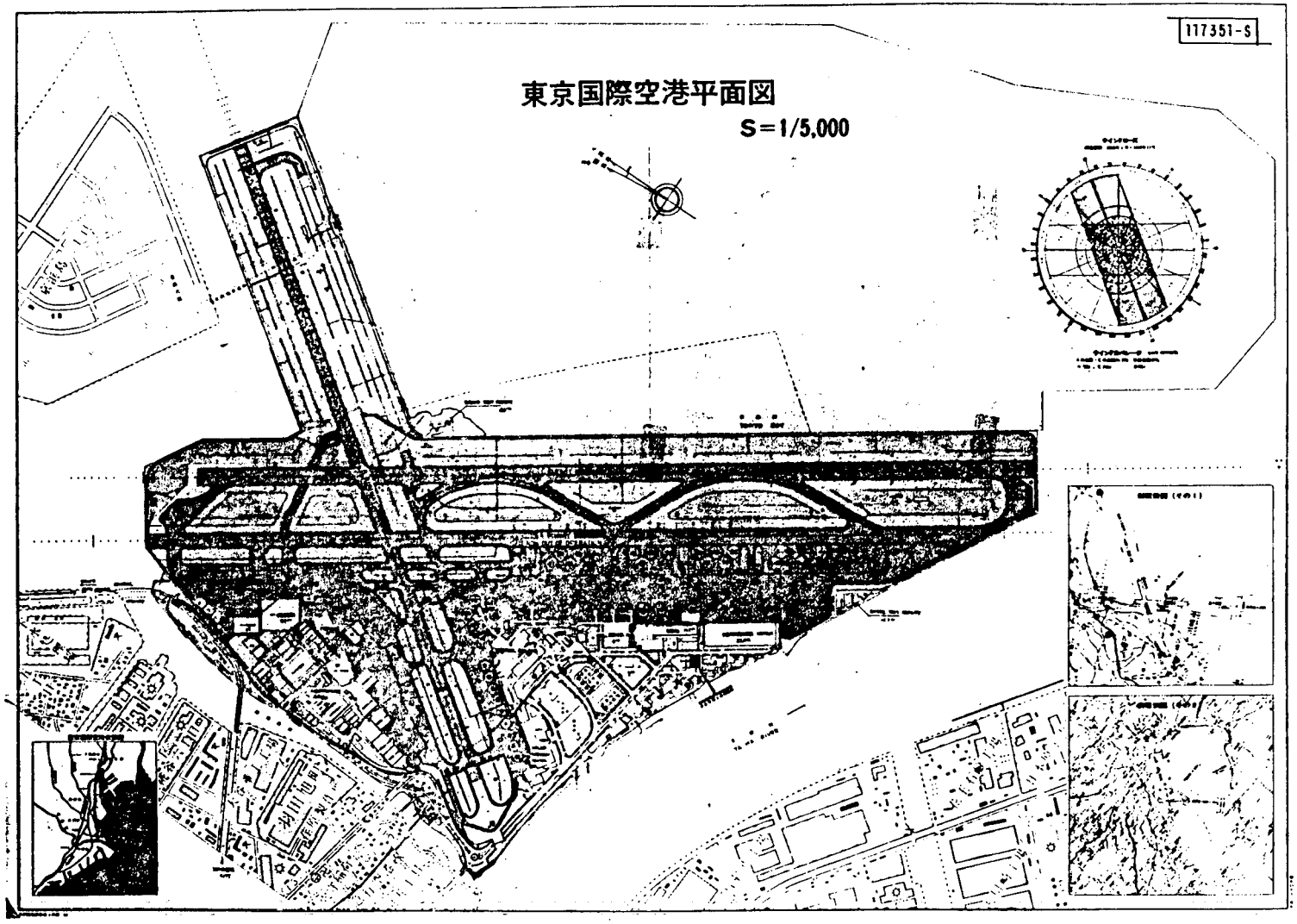


Fig.B-12. Haneda Airport (Tokyo).

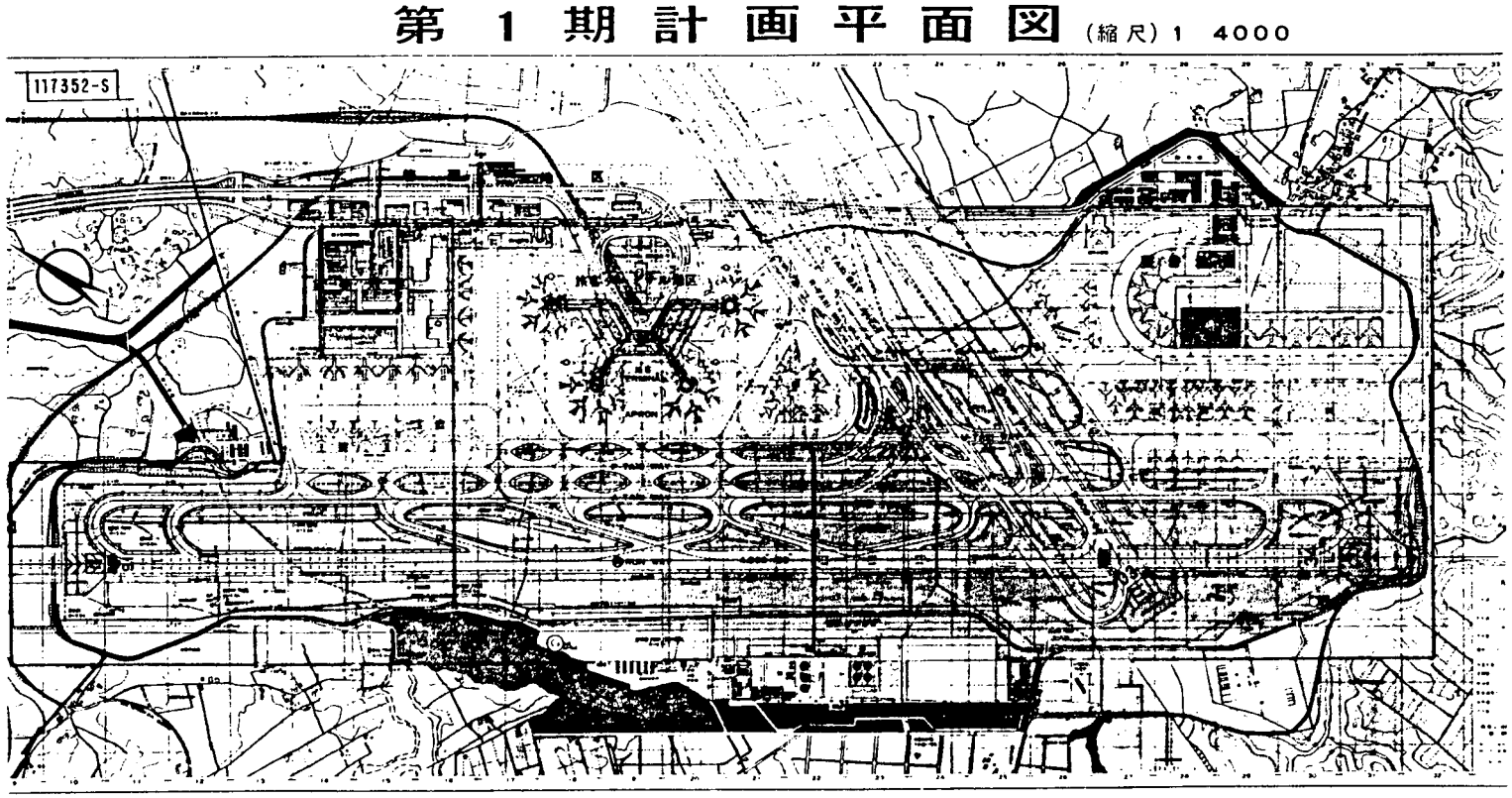


Fig.B-13. Narita Airport (Tokyo).

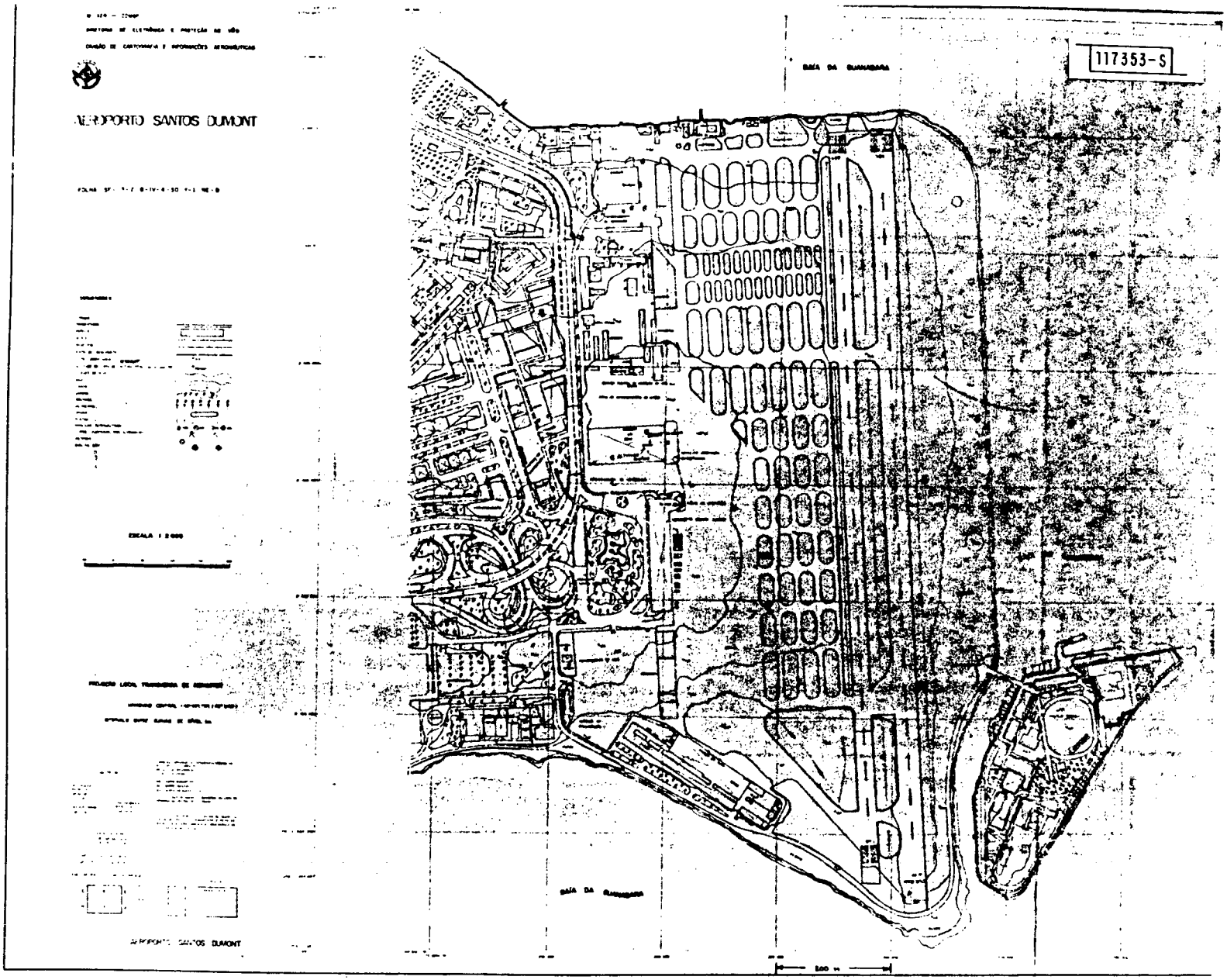


Fig.B-14. Santos Dumont Airport (Brazil).

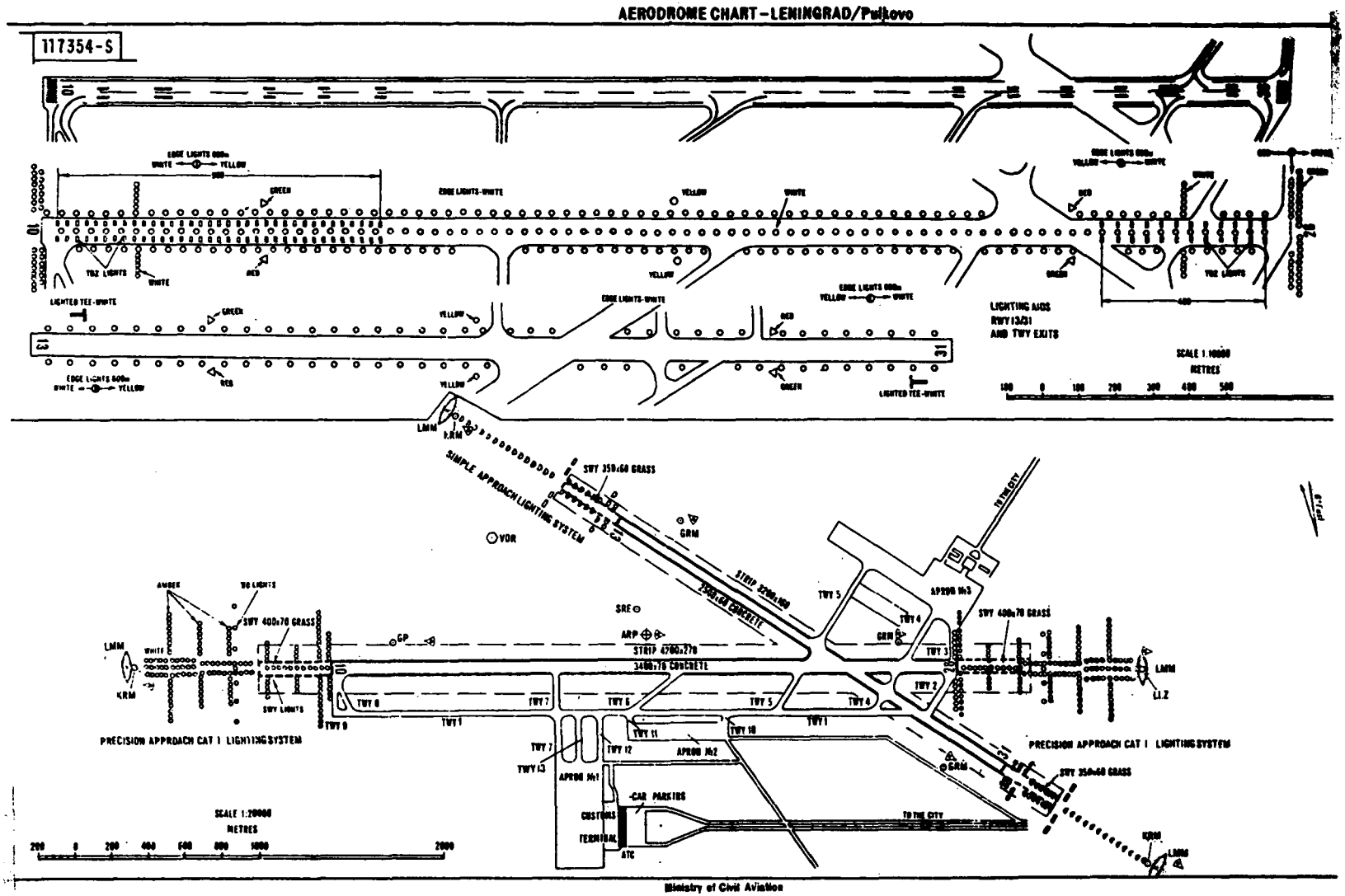


Fig.B-15. Pulkovo Airport (Leningrad).

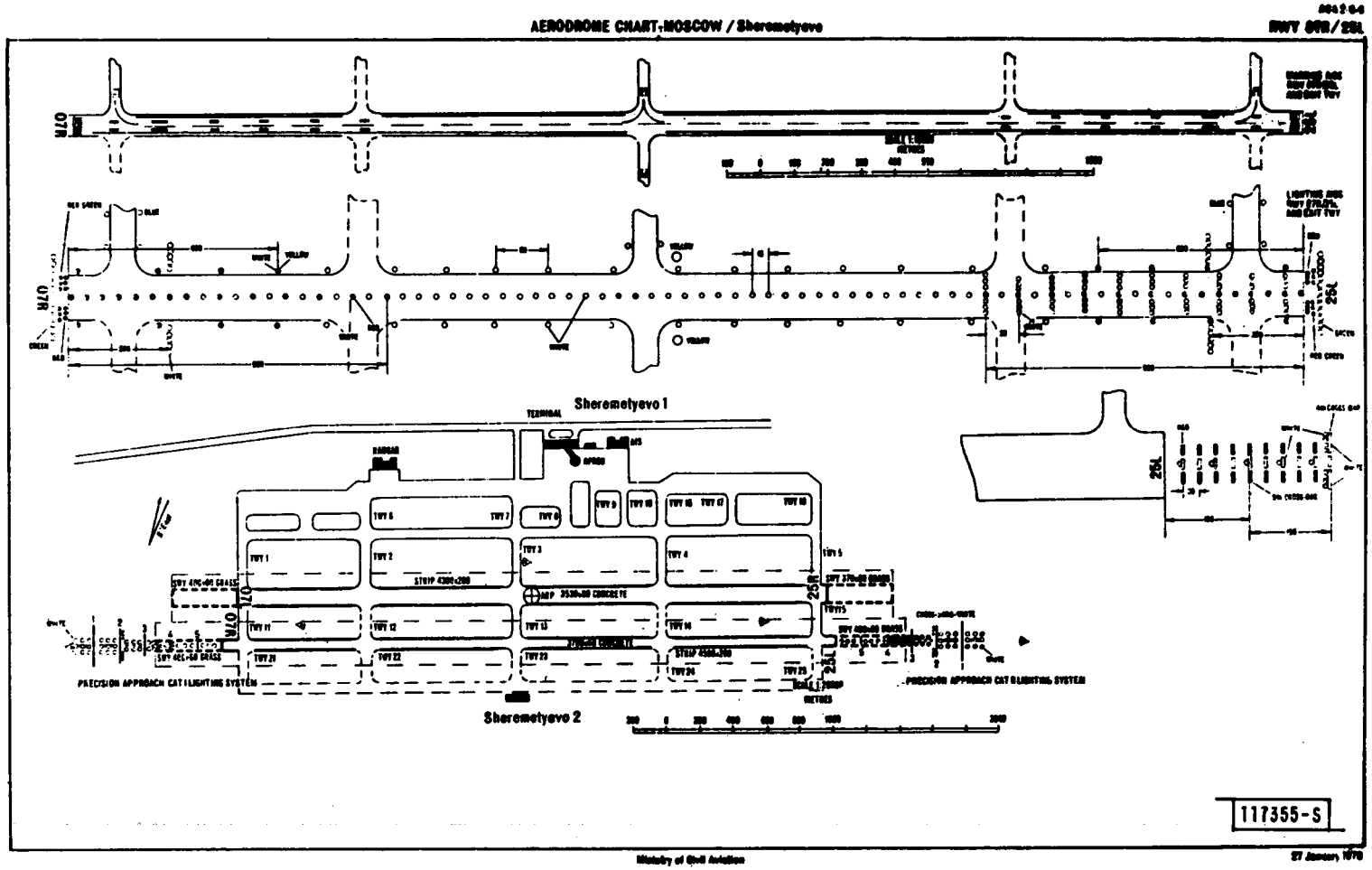


Fig.B-16. Sheremetyevo Airport (Moscow).

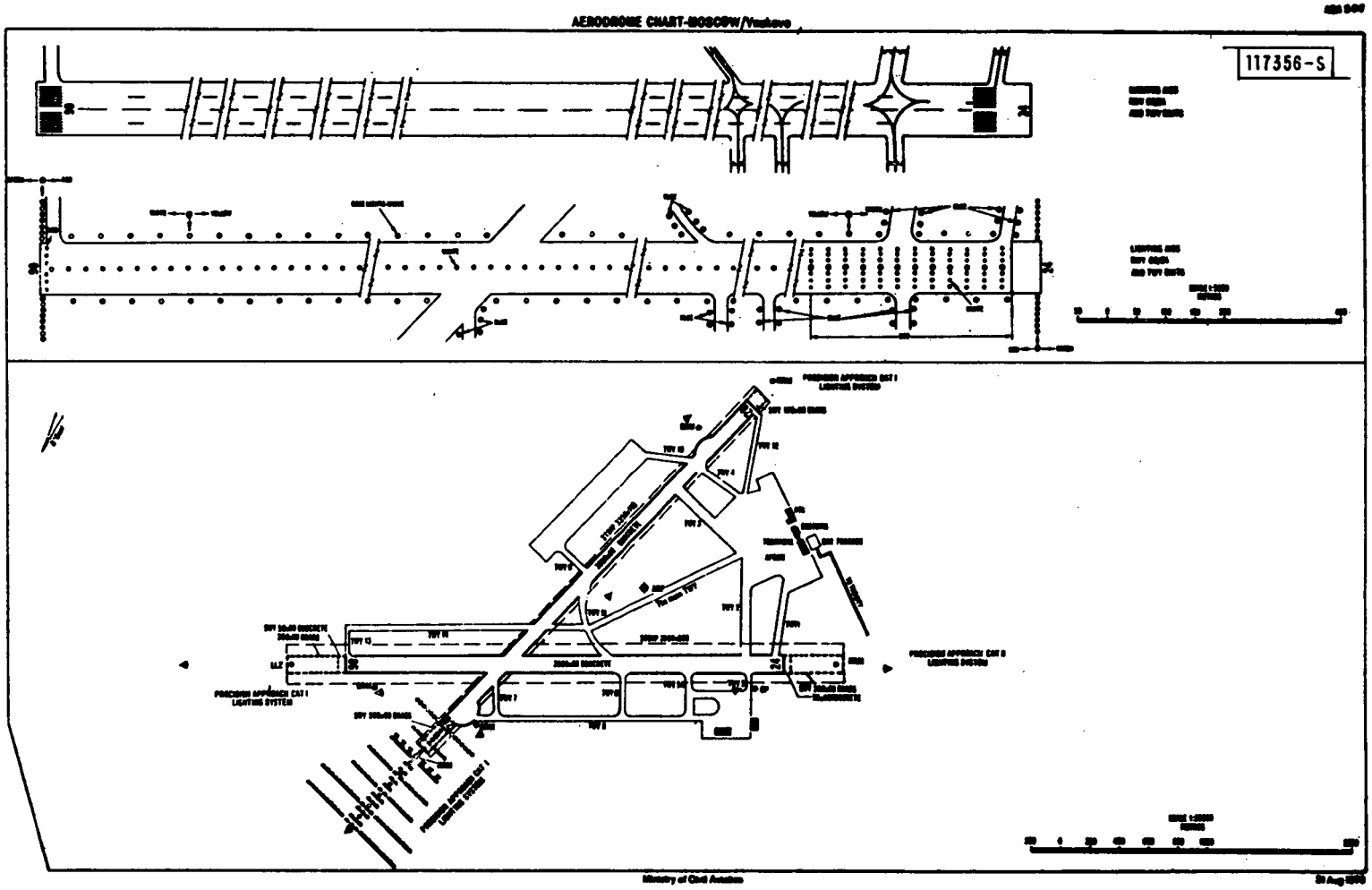


Fig.B-17. Vnukovo Airport (Moscow).

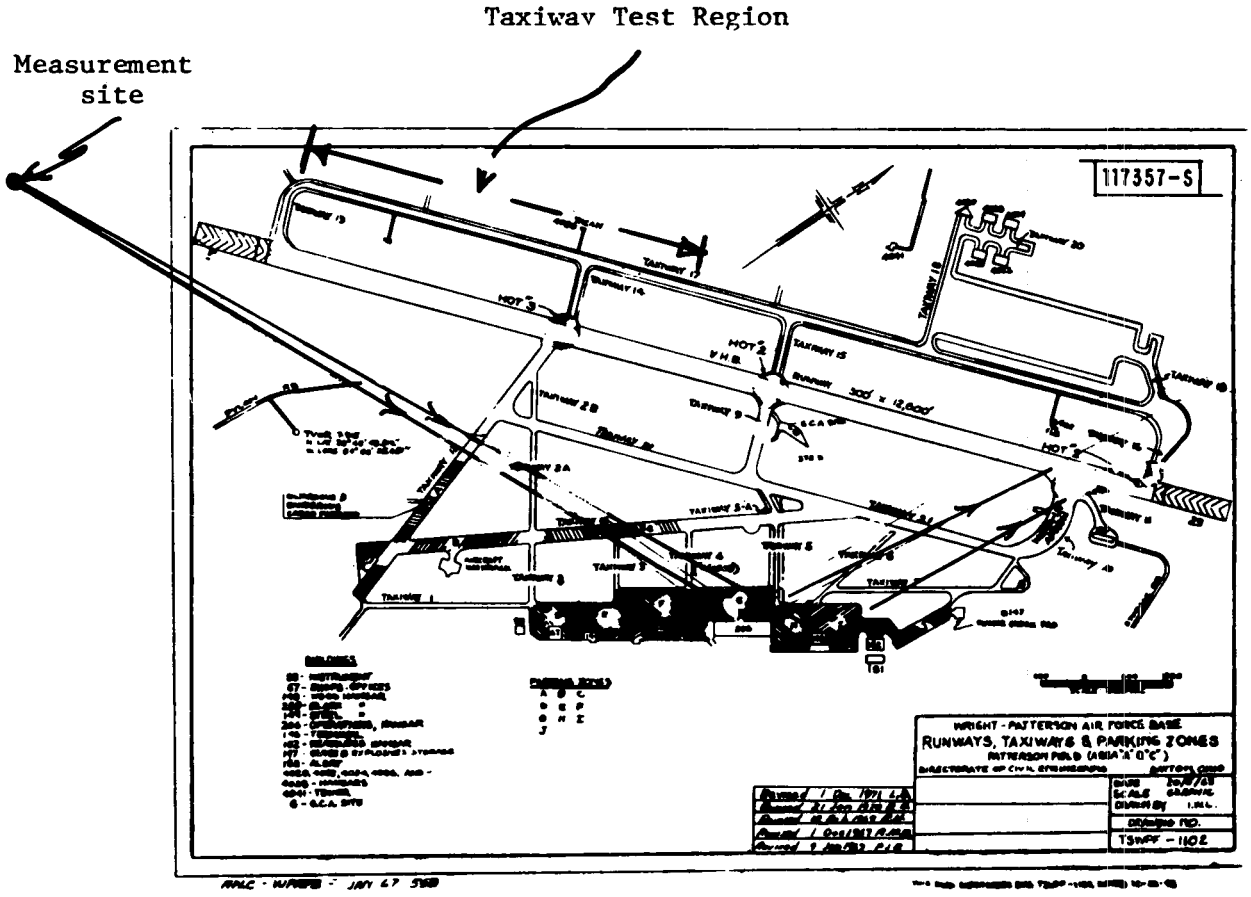


Fig.B-18. Wright Patterson AFB.

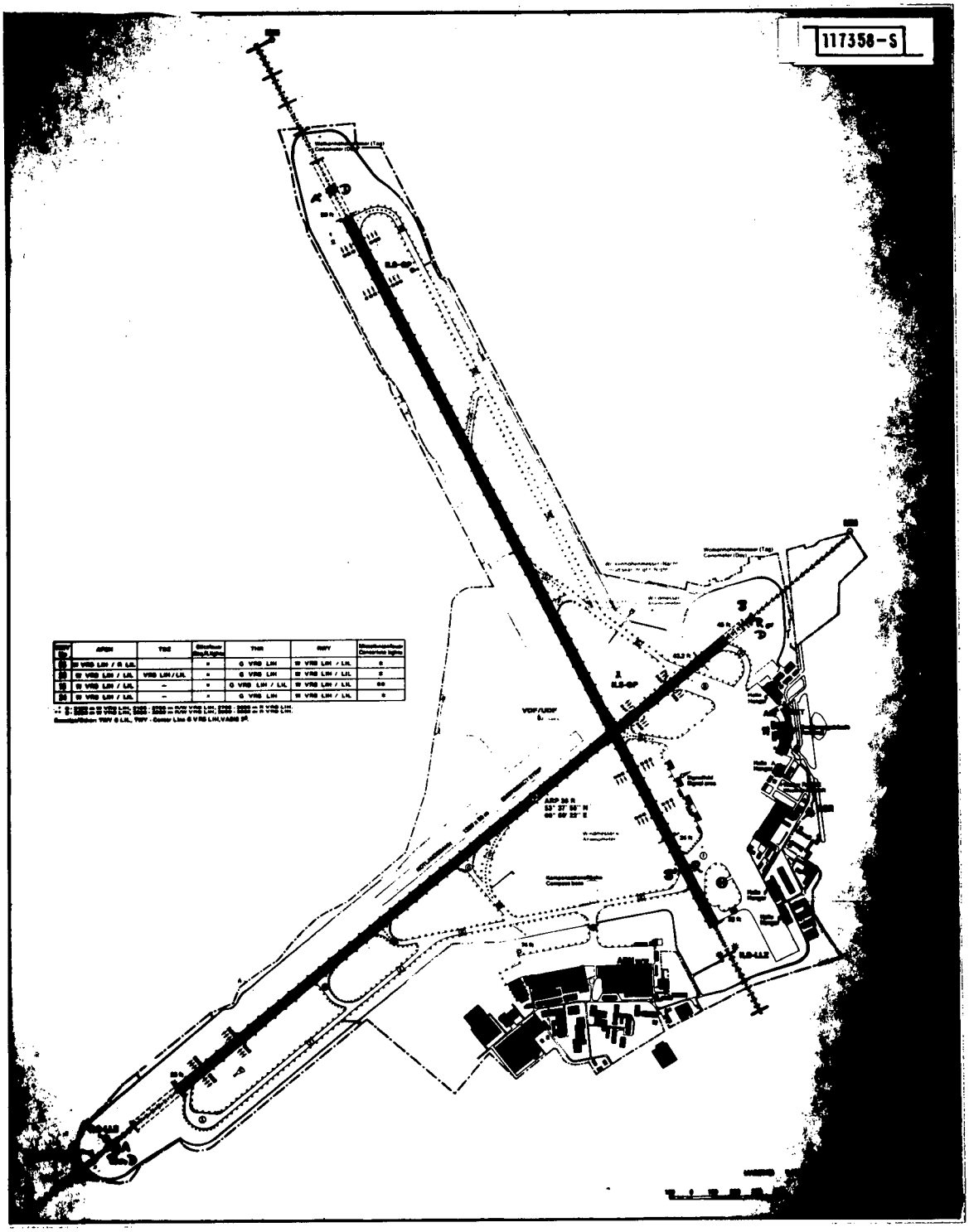


Fig.B-19. Hamburg, W. Germany Airport.

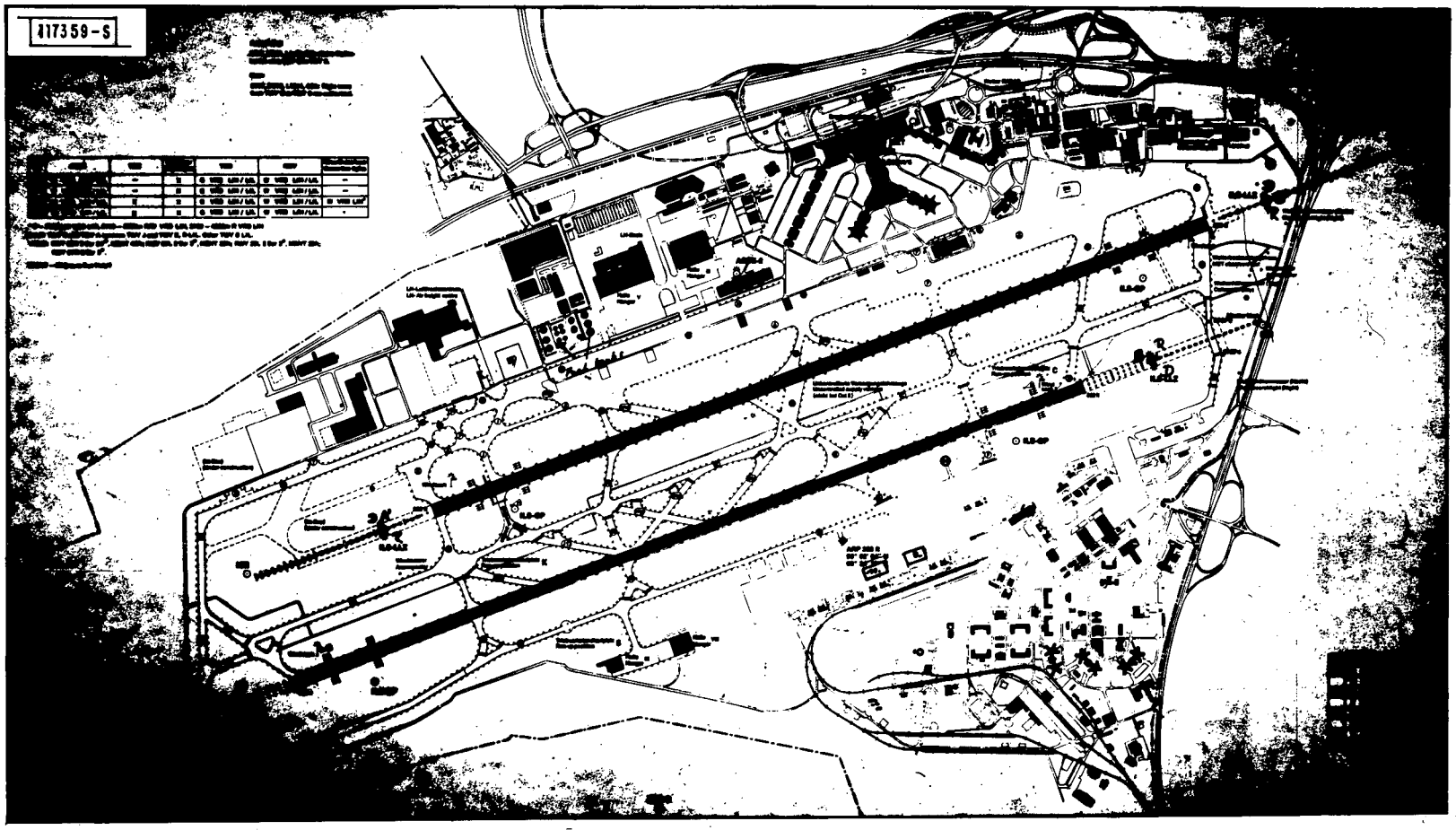


Fig.B-20. Frankfurt (Main), W. Germany Airport.

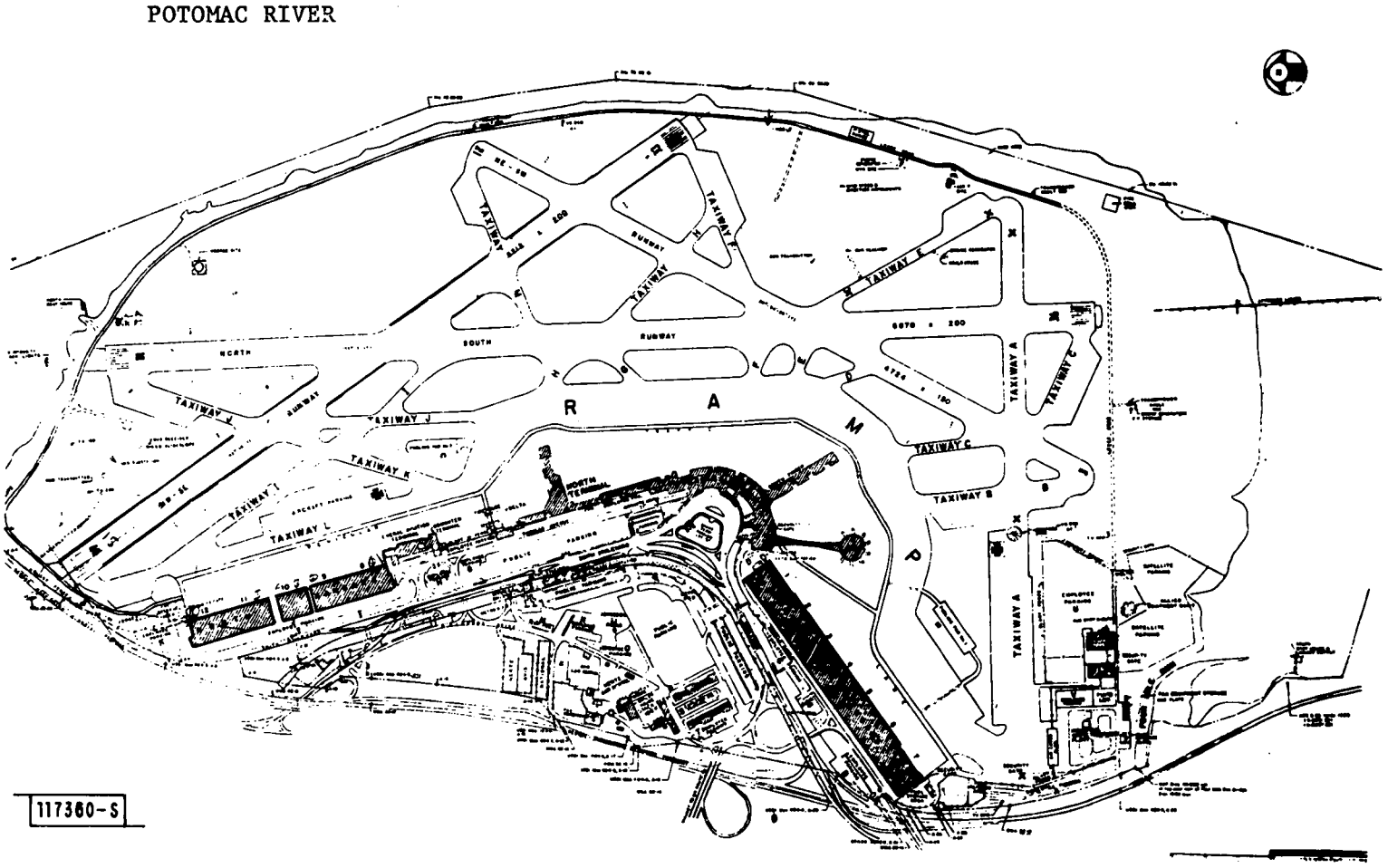


Fig.B-21. Washington National Airport (DCA).

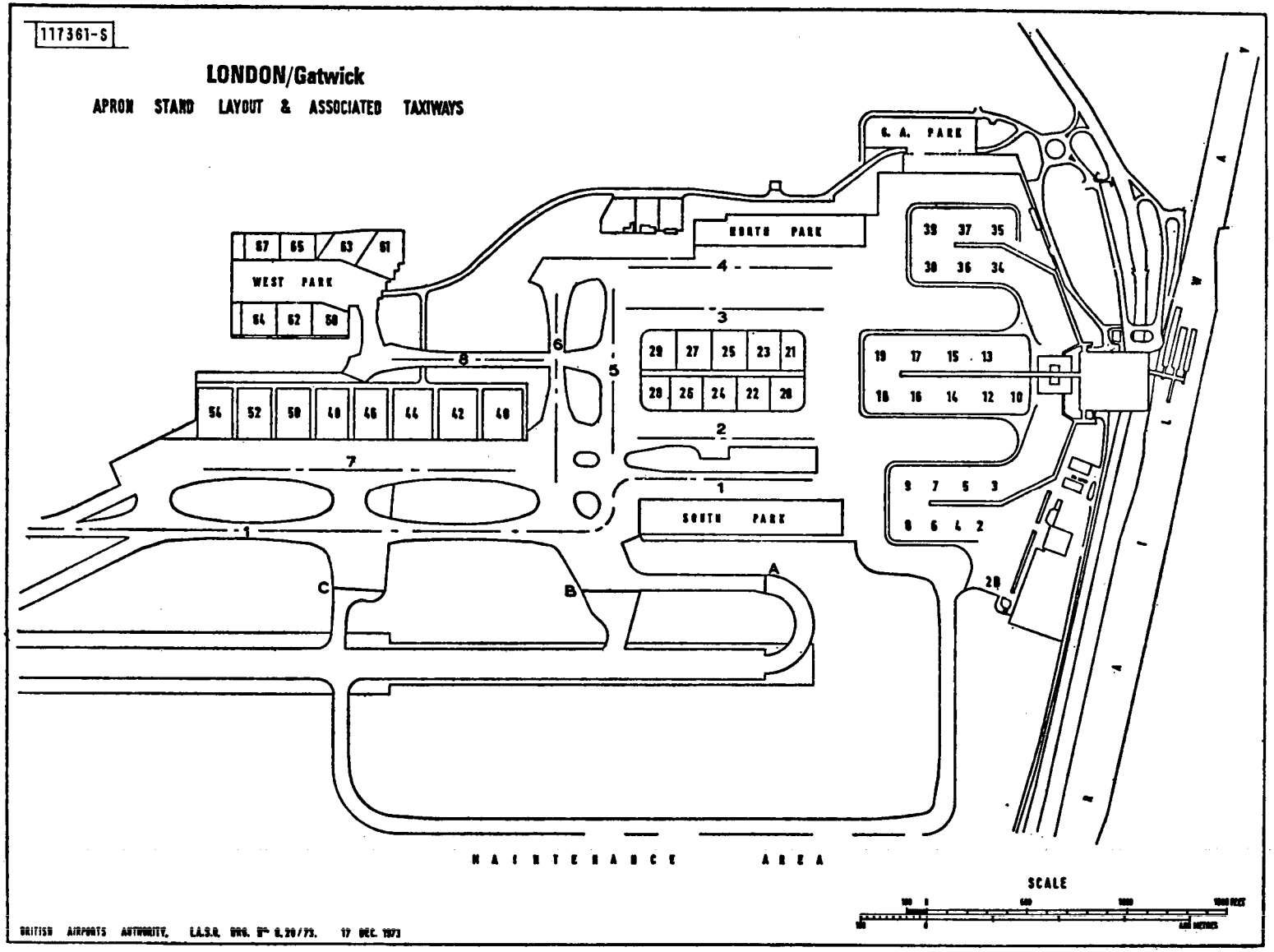


Fig.B-22. Gatwick Airport (London).

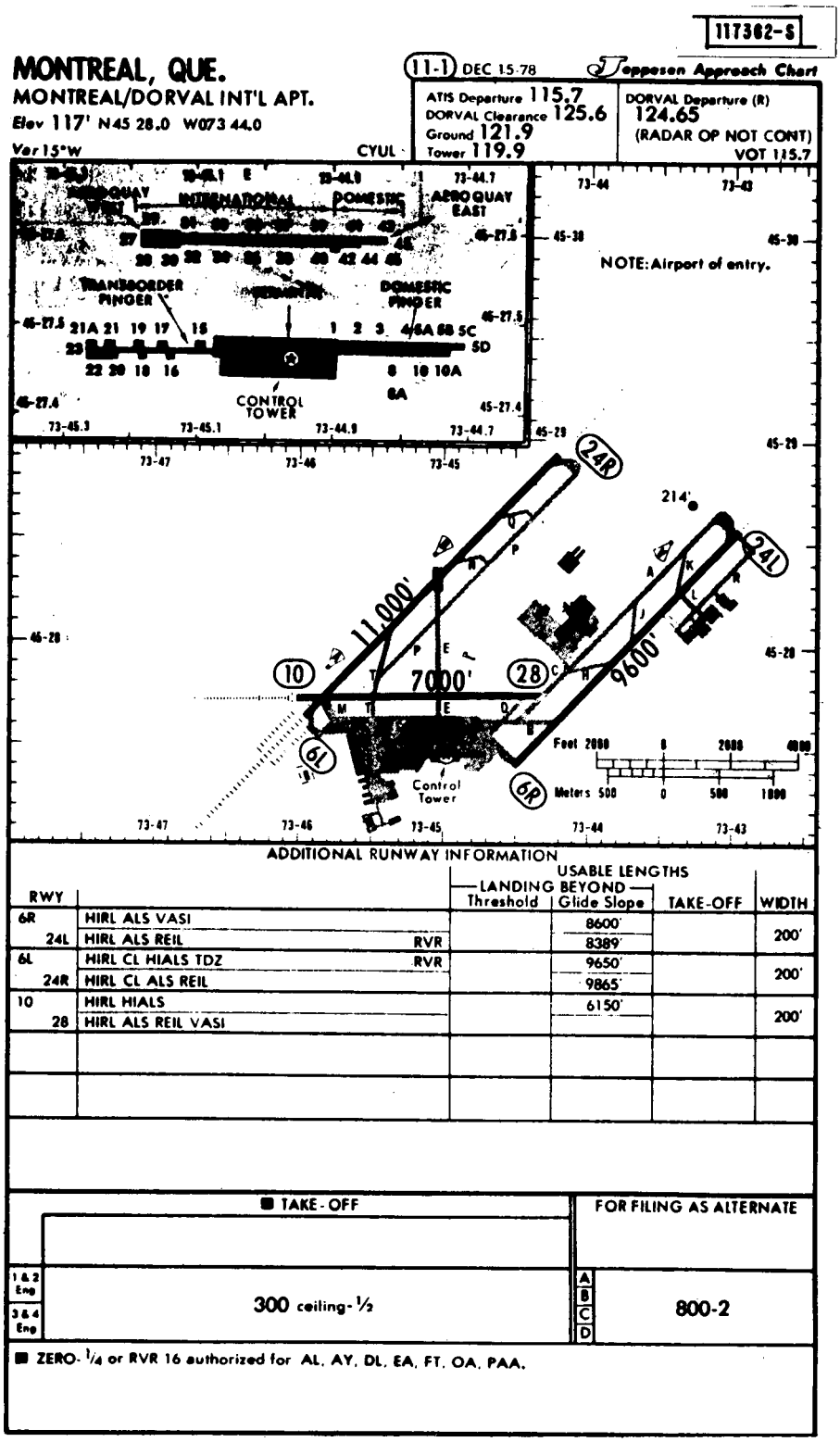


Fig.B-23. Dorval Airport (Montreal).

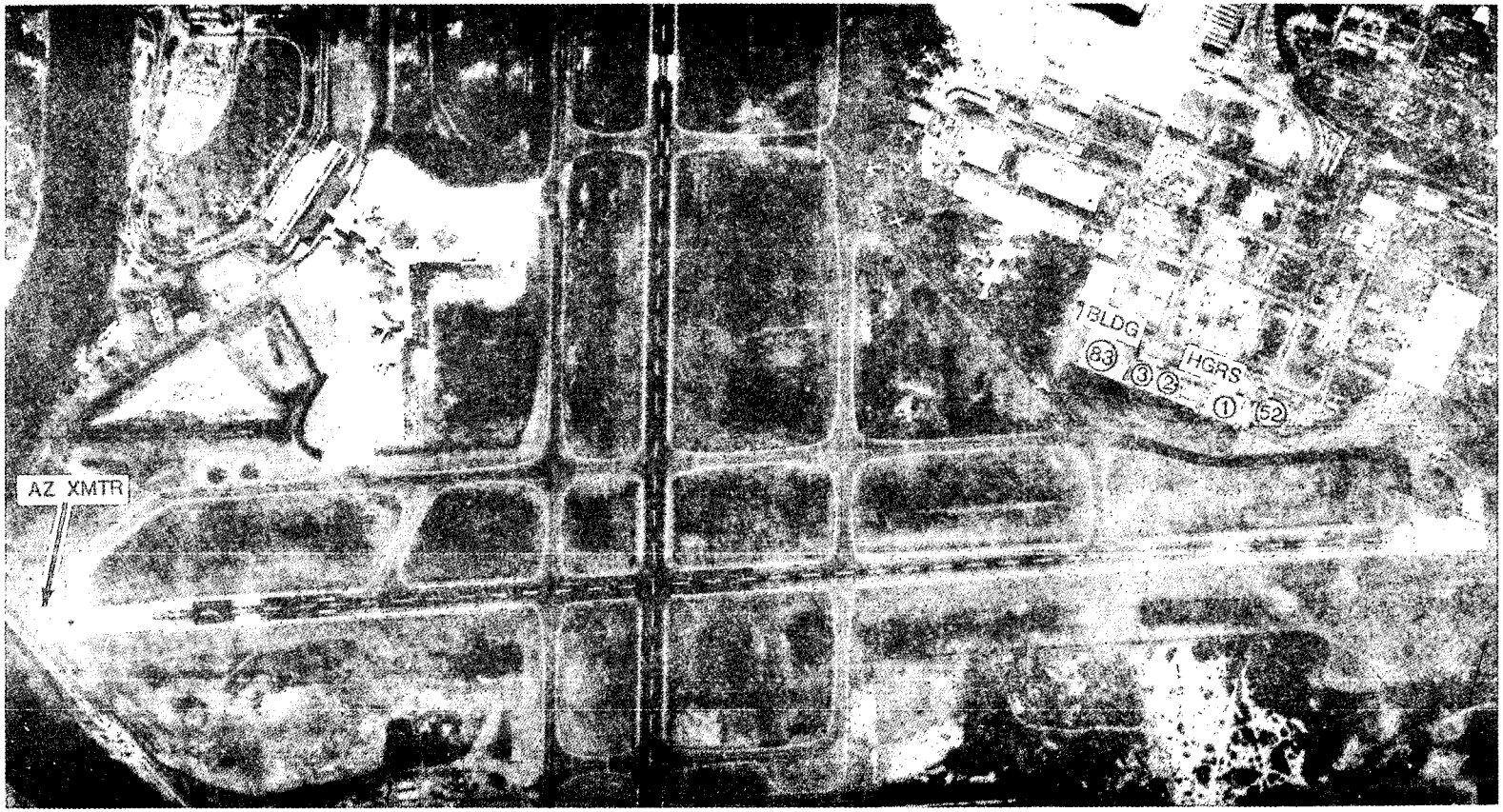


Fig.B-24. Sydney Airport (Australia).